

Targeting neurons with small molecule probes: from imaging to modulation

Umed Boltaev

Submitted in partial fulfillment of the
requirements for the degree of
Doctor of Philosophy
in the Graduate School of Arts and Sciences

COLUMBIA UNIVERSITY

2018

© 2018

Umed Boltaev

All rights reserved

ABSTRACT

Targeting neurons with small molecule probes: from imaging to modulation

Umed Boltaev

Our body is governed through a complex network of diverse set of synapses created by many different neurons, which extend throughout the body. A great progress has been made to monitor and modulate these cells using genetic methods in limited settings, while chemical approaches have not achieved comparable successful results. Yet given the versatility of chemical probes, it has been important to create platforms which would allow us to generate compounds with characteristics of neuronal targeting and modulation.

In our effort to modulate neurons and their synapses, a platform of assays was developed to find agonists and modulators of the brain derived neurotrophic factor, BDNF, and its receptor, TrkB, which is a central signaling system for neurogenesis and synaptic plasticity. These assays were used to evaluate reported TrkB agonists and perform a high throughput screen. In addition, an alternative approach in the form of phage display targeting TrkB was employed, since TrkB proved to be a challenging target for identification of small molecule agonist or modulator.

To visualize different parts as well as various types of neurons, two different platforms were developed. A diversity oriented fluorescent library coupled with high content screening provided an opportunity to identify probes that could specifically stain neurons and synapses. In the second approach a new phage display method was developed that could identify probes with the ability to bind to neuronal cell surface markers. The developed platforms that we developed have a great potential to generate promising probes for vast array of applications.

Table of Contents

List of Figures.....	iv
List of Tables.....	vii
Foreword and Acknowledgements.....	viii
1 Chapter I: Toward Pharmacological Modulation of the TrkB Receptor Tyrosine Kinase.....	1
1.1 Introduction.....	1
1.1.1 Importance of the BDNF-TrkB system.....	1
1.1.2 Signaling of BDNF-TrkB.....	4
1.1.3 TrkB agonists.....	6
1.1.4 Reproducibility of TrkB agonists.....	15
1.2 Results.....	15
1.2.1 Overview.....	15
1.2.2 Established cell lines.....	16
1.2.3 Western Blot.....	20
1.2.4 Sandwich ELISA.....	21
1.2.5 ELFI.....	24
1.2.6 DiscoverX PathHunter assay and U2OS-TrkB/p75 cell line.....	29
1.2.7 Invitrogen CellSensor assay and CHO-TrkB cell line.....	30
1.2.8 Characterization of reported compounds in developed assays.....	31
1.2.9 High throughput screen.....	34
1.2.10 Phage Display.....	54
1.3 Discussion.....	71
1.4 Conclusion.....	75
1.5 Materials and Methods.....	75

1.5.1	Materials	75
1.5.2	Western Blot	76
1.5.3	Cell lines	76
1.5.4	Sandwich ELISA:	77
1.5.5	ELFI	78
1.5.6	DiscoverX PathHunter® assay	78
1.5.7	Phage Display.....	79
1.5.8	Statistical analysis	79
1.6	References.....	80
1.7	Appendix	87
1.7.1	Compound libraries	88
1.7.2	Pilot screen	89
1.7.3	HEK-TrkB screen.....	90
1.7.4	CellSensor screen	93
1.7.5	CNC screen	96
2	Chapter II: Targeting neurons through screening platforms	101
2.1	Introduction	101
2.1.1	Central nervous system diversity of neurons and synapses	101
2.1.2	Neurons and synapses in pathologies	102
2.1.3	Genetic methods	103
2.1.4	Chemical methods.....	104
2.1.5	Phage display	106
2.2	Results	108

2.2.1	Overview.....	108
2.2.2	High content screening assay	109
2.2.3	Phage Display.....	137
2.3	Discussion.....	146
2.4	Conclusion	149
2.5	Materials and Methods.....	149
2.5.1	DNA constructs and AAV production	149
2.5.2	Neuronal culture and lentiviral transduction	150
2.5.3	Immunofluorescence on HTS microscope	150
2.5.4	Screening.....	150
2.5.5	Colocalization algorithm and hit selection	151
2.5.6	Serial dilutions	151
2.5.7	Determination of excitation/emission spectra and lipophilicity	151
2.5.8	Live imaging in cultured hippocampal and cortical neurons.....	152
2.5.9	Quantification of CX-G3 colocalization with synaptic markers in cultured hippocampal neurons	152
2.5.10	Immunofluorescence in cortical neuronal cells cultured in the grid dish	153
2.5.11	Electrical stimulation of CX-G3-labeled hippocampal neurons	153
2.5.12	Data repository and analysis.	154
2.5.13	Striatal cultures for phage display	154
2.6	References.....	155
2.7	Appendix: HCS plates	158

List of Figures

Figure 1.1.1 TrkB structure and signaling	5
Figure 1.1.2 Structure of 7,8-DHF, staurosporine, and K252a	8
Figure 1.1.3 Structure of DMAQ-B1	9
Figure 1.1.4 Structure of LM series.....	10
Figure 1.1.5 Structure of deoxygedunin, amitriptyline, deprenyl.....	11
Figure 1.1.6 Structure of ANA-12.....	13
Figure 1.2.1 CNC characterization by immunofluorescence	16
Figure 1.2.2 TrkB internalization in HEK-TrkB cells.....	17
Figure 1.2.3 SH-SY5Y culturing conditions in 96-well plates.....	17
Figure 1.2.4 TrkB and p75 expression profile in differentiated SH-SY5Y cell	18
Figure 1.2.5 DiscoverX PathHunter assay scheme	19
Figure 1.2.6 Invitrogen CellSensor assay scheme	19
Figure 1.2.7 Western blot analysis of reported agonists in cortical neuron culture	21
Figure 1.2.8 Antibody screen for sandwich ELISA	22
Figure 1.2.9 ELISA characterization in established cell lines	24
Figure 1.2.10 Stripping and re-probing in ELFI and IF	26
Figure 1.2.11 ELFI in established cell lines	28
Figure 1.2.12 DiscoverX U2OS-TrkB/p75 cells characterization	29
Figure 1.2.13 Invitrogen CellSensor CHO-TrkB cell line characterization.....	31
Figure 1.2.14 5E5 and its precursors, SR-III-003, SR-III-006.....	31
Figure 1.2.15 Reported agonists test results	32
Figure 1.2.16 Activity of 7,8-DHF and LM22a-4 in cortical neuron culture at different conditions.....	34
Figure 1.2.17 HTS outline	35
Figure 1.2.18 CellSensor screen outline.....	38
Figure 1.2.19 CellSensor screen with K252a.....	39
Figure 1.2.20 Retest of selected compounds in CNC.....	43
Figure 1.2.21 Signal variation and BDNF concentration relationship in allosteric mode.....	45

Figure 1.2.22 Phage display scheme.....	56
Figure 1.2.23 BN PAGE development	58
Figure 1.2.24 Cell-based Phage Display protocol characterization	60
Figure 1.2.25 Cell-based Phage display first run	61
Figure 1.2.26 Cell-based Phage display second run	63
Figure 1.2.27 CX7C sequences and ELFI characterization.....	67
Figure 1.2.28 CX8C sequences and ELFI characterization.....	70
Figure 2.1.1 Structure of synaptic and voltage sensitive dyes.....	105
Figure 2.1.2 FFN structure	105
Figure 2.1.3 Structures of NeuO, CDr10, and CDy5	106
Figure 2.2.1 Characterization of synaptic markers for HCS	110
Figure 2.2.2 Structural cores of the fluorescent library.	111
Figure 2.2.3 HCS outline.....	113
Figure 2.2.4 Segmentation of the representative image	114
Figure 2.2.5 Control plate plots	116
Figure 2.2.6 Quality control of the images	118
Figure 2.2.7 Bleed through correction.....	120
Figure 2.2.8 Parameters of the DAPI_DAPI plate.....	122
Figure 2.2.9 Colocalization of CX-G3 with immunostained markers, Lysotracker, Mitotracker.....	123
Figure 2.2.10 CX-G3 versus Lysotracker and Mitotracker.....	125
Figure 2.2.11 DAPI_DAPI_101_Q4 structures and properties	126
Figure 2.2.12 Spectral properties of CX-G3 and its analogs	128
Figure 2.2.13 Representative images of CX-G3 and Lysotracker	130
Figure 2.2.14 spH imaging with and without bafilomycin	132
Figure 2.2.15 spH and CX-G3 response to electrical stimulation in spH expressing hippocampal neuronal culture incubated with CX-G3.	133
Figure 2.2.16 Representative CX-G3 image analysis approaches.....	134
Figure 2.2.17 Individual punctum analysis.....	136

Figure 2.2.18 Immunofluorescence of isolated neuron and glia cultures	138
Figure 2.2.19 Ex vivo phage display scheme and outcome	139
Figure 2.2.20 CX7C sequences and numbers from the neuronal versus glia screen	143
Figure 2.2.21 CX8C sequences and numbers.....	145
Figure 2.2.22 Immunofluorescent analysis of phage specificity	146

List of Tables

Table 1.1 EC ₅₀ values of neurotrophic factors: EC ₅₀ (ng/ml) values in primary cortical neurons. Data represents the mean ± SD (n = 3-7 independent experiments).....	23
Table 1.2 S/B values of ELISA and ELFI in cortical neuron culture. Signal-to-background ratios of maximal responses to BDNF in cortical neurons culture (DIV various), data represents mean ± SD (n = 3-6).	24
Table 1.3 CellSensor inhibition screen of 17 hit compounds.....	39
Table 1.4 K54211867 characterization as allosteric agonist	46
Table 1.5 K30652576 characterization as allosteric agonist	48
Table 1.6 K46962856 characterization as allosteric agonist	50
Table 1.7 K21249854 characterization as allosteric agonist	52
Table 1.8 Recombinant TrkB phage display first approach.....	55
Table 1.9 Recombinant TrkB phage display second approach results	55
Table 1.10 Phage display on plated cell results.....	56
Table 1.11 Phage titer at every washing step.....	57
Table 1.12 Phage display on plated cell results.....	60
Table 1.13 Top 20 abundant phages found through Ion Torrent sequencing in CX7C libraries. Phages selected for ELFI analysis are in bold.	65
Table 1.14 Sanger sequencing results. Phages selected for ELFI analysis are in bold.....	66
Table 1.15 Top 20 abundant phages found through Ion Torrent sequencing in CX8C libraries. Phages selected for ELFI are in bold	68
Table 1.16 Sanger sequencing results. Phages selected for ELISA are in bold	69
Table 2.1 List of the groups for HCS.....	112
Table 2.2 Analysis of the overlap value per library groups	121
Table 2.3 Top 20 sequence in CX7C libraries identified by IonTorrent	141
Table 2.4 Sequences of CX7C round 3	142
Table 2.5 Top 20 sequence in CX8C libraries identified by IonTorrent	144
Table 2.6 Sequences of CX8C round 3 library identified by Sanger sequencing.....	145

Foreword and Acknowledgements

Current work is the summary of the several projects which produced two important publications. Publication in *Science Signaling* (ref. 125) was based on the results of TrkB agonist characterization efforts. Publication in *ACS Chemical Neuroscience* (ref. 211) was based on new small molecule synaptic probe, CX-G3. This thesis contains several passages from these papers.

I would like to thank foremost my advisor, Dalibor Sames. I would not be at Columbia University had he not recognized me as a promising candidate for graduate school. Enrolling at Columbia University, I was looking for challenging new projects related to neuroscience, which incidentally were conducted at Dali's laboratory. Under Dali's guidance I have matured professionally and became a scientist I am today. Later in my research, Dali gave me ample opportunities to expand my knowledge and skills by utilizing new exciting techniques, which emboldened me to think broader.

It would have been much harder to conduct a meaningful research without my colleagues. I want to thank Madalee Gassaway for sharing her knowledge and always being there when I would need advice or just someone to discuss complex topics with. I want to thank Yves Meyer who taught me ins and outs of the many hurdles of the cell assays. I want to thank Matt Dunn for his helpful critiques and suggestions, and Theresa Jacques for helping me adapting to the new project. I want to thank Katherine Kovalyova for helping me to develop MATLAB algorithms. And I want to thank my other lab mates, who made this journey much more fun.

Joining high content screening project, I was fortunate to meet Clarissa Waites whose enthusiasm and support helped me achieve new exciting results. Anne Beskow, Patty Sheehan, Cyndel Volmer were indispensable for me in learning primary culturing. I also want to thank Ellen Kanter for sharing her experience with striatal neurons, which greatly expended my understating of cell culturing. I want to thank Sergey Pampou for helping to perform new analysis on the images for high content screening.

While expanding my research interest and involvement in new projects, I was fortunate to meet new advisor and colleague. I would like to thank Erkki Ruoslahti and Tambet Teesalu for guiding and advising me on mastering phage display technology. Erkki was very kind to welcome me to his lab for a

brief period to let me learn phage display, where I met Aman Mann and Sazid Hussain, who showed me how to correctly conduct phage display.

I want to thank Moses Chao for his advice, support, and interest in my research: I was honored to present my work to you and your colleagues. To my thesis committee members (both present and past), thank you for your time, productive critique, and for participating in this important event of my career: Laura Kaufman, Ruben Gonzalez, Ronald Breslow, Virginia Cornish, and Tristan Lambert. I greatly appreciate your insights and advice.

I want to acknowledge my roots that instilled my interest in pursuing scientific discovery. Through the discussion of the world from distant galaxy to minute waves, my mentor, Golib Nasimov, helped me realize my interest in science. My advisor at Moscow State University, Nikolay Melik-Nubarov, is an important person to me, who helped me and guided me through the hardships of science.

I want to thank my sister, Farangis Tolibzoda, without whom I would be unable to succeed in my graduate studies: thank you for your help and demand in performing cutting-edge research and staying focused to achieve the greater goals and thank you for always being there. To my parents, Toly Bolta and Gulchehra Ahmedova, thank you for your never-ending support and advice. I also would like to thank my cousin, Firuz Mukhitdinov, for always helping me whenever I would face a challenging task. Thank you for helping to set up OMERO server, which became a very important tool in quest of image analysis. And finally, to my wife – thank you for joining me in my journey and helping me to achieve my ambitions, for the lovely kids, who are a part of me. I love you.

1 Chapter I: Toward Pharmacological Modulation of the TrkB Receptor Tyrosine Kinase

1.1 Introduction

1.1.1 Importance of the BDNF-TrkB system.

Brain derived-neurotrophic factor (BDNF) and its main receptor, tropomyosin related kinase (TrkB), has emerged as one of the key players in neuroplasticity during development and maintenance of the nervous system. Being a member of neurotrophic factor and Trk receptors (TrkA, TrkB, and TrkC) family, the interest in understanding and influencing this system has been high as the number of publications on BDNF and its receptor has increased exponentially since 2000, reaching 1,828 publications in 2017 (1). BDNF release and TrkB activation have been reported to affect genesis and function of neurons and synapses via modulation of transcription, translation, and trafficking of proteins (slow time scale, hours-days), as well as modulation of ion channels and G-protein-coupled receptors (GPCRs) (rapid events, from seconds) (2, 3). These molecular effects are generally thought to underlie the cellular, circuit-level, and physiological consequences of the BDNF/TrkB signaling system activation. Hence the role of BDNF in neuroplasticity, mood disorders, and neurodegenerative diseases has been actively studied.

1.1.1.1 *Neuroplasticity*

BDNF has been recognized as a central molecule for inducing and regulating neuroplasticity in the brain (4). The evidence for these BDNF activities has come from the observation of increased BDNF expression in the hippocampus upon electrical induction of long-term potentiation (LTP) (5) and enhanced transition of short-term potentiation to long-term potentiation upon exogenous BDNF application on a neuronal circuit. (6). Moreover, neuron activity-dependent BDNF secretion has been associated with LTP (7). In other words, the BDNF-TrkB system itself has the power to induce LTP in the brain, rendering this system to be sufficient to induce synaptic modulation. On the other hand, knocking out or scavenging BDNF by recombinant TrkB extracellular domain in the hippocampus has shown to lead to impairment in LTP induction, which was rescued by exogenous BDNF (8, 9). Interestingly, a single-nucleotide

Val66Met BDNF polymorphism has been shown to decrease activity dependent release of BDNF in humans (10) and induce impairments in synaptic and cognitive functions (11). Furthermore, humans carrying this mutation have demonstrated to display increased risk of fear generalization (12). Thus, BDNF has been shown to be necessary to induce LTP, making the BDNF-TrkB system an important target to modulate neuroplasticity.

Perhaps one of the most dramatic examples of the BDNF trophic effect has been demonstrated in visual cortex. During the formation of the visual cortex, synaptic connections segregate into eye-specific patches, called ocular dominance columns, based on competing signal input from the eye. BDNF infusion into primary visual cortex, but not nerve growth factor (NGF, a TrkA ligand) or neurotrophin-3 (NT3, TrkC and partial TrkB ligand), has inhibited formation of ocular dominance columns and orientation selectivity within infusion area without affecting other areas. In other words, exogenous BDNF has competed with activity-released BDNF and disrupted formation of the synapses based on the competing signals coming from the eyes (13). Thus, TrkB activation could support synaptogenesis and could be required for synaptic plasticity. Similar activity has been shown in the formation of glutamatergic synapses in the hippocampus (14), which in turn underlie memory (15) and cognitive enhancements (4, 11).

In addition to synaptic modulation, BDNF has been shown to rescue neurons and induce neurogenesis. For instance, BDNF treatment of the eye and visual cortex has significantly reduced ganglion cell loss following injury to the optic nerve in adult cats (16). Intraventricular infusion of BDNF into adult rats has induced formation of new neurons in the olfactory bulb, striatum, septum, and even in the thalamus and hypothalamus (17, 18), while TrkB knockout in hippocampal progenitor cells has drastically reduced the number of new neurons in postnatal and adult mice (19). TrkB activation has led to enhanced neurogenesis of different neurochemical cell types in several areas of the adult murine brain (20, 21). In addition, mice with TrkB knockout in the cortex has resulted in reduced dendritic arborization, layer thinning, and progressive elimination of neurons in the somatosensory and visual cortices (22).

Given the number of functions BDNF-TrkB activity has been reported to exert in the central nervous system (CNS), it should not be surprising that this system has important implications in various diseases of CNS, including mood disorders and neurodegenerative diseases.

1.1.1.2 *Depression and Mood disorders*

Therapeutic efficacy of common antidepressants like fluoxetine has been associated with the ability to induce neuroplasticity in relevant circuits (23), and moreover to influence activity of the BDNF-TrkB system. Indeed, chronic administration of fluoxetine and other selective serotonin reuptake inhibitors has resulted in an increased phosphorylated state of TrkB in the hippocampus and prefrontal cortex (24). Deletion of TrkB in newborn neurons has inhibited the effects of antidepressants (19) and increased anxiety-like behavior in mice (25). In addition, BDNF infusion into different brain areas of mice or rats has shown antidepressant (26–28) and anxiolytic effects (29) and has influenced other mood conditions (30) by inducing synaptic plasticity (31, 32). Furthermore, one of the mechanistic models for the fast-acting antidepressant effect of ketamine has invoked activity-dependent release of BDNF as the required downstream effect of ketamine administration (33).

An example of BDNF-TrkB's effect on neuroplasticity has been demonstrated in the visual cortex once again. Chronic treatment with fluoxetine has led to rewiring of the adult visual cortical system and effective reversal of vision loss in amblyopic animals through TrkB activation (34). Systemic fluoxetine administration or cortical infusion of BDNF has been capable of inducing plasticity seen only during the critical postnatal developmental period, enabling recovery of lost function, most likely via visual cortex rewiring.

Collectively this data has indicated that the BDNF-TrkB signaling system has been necessary for antidepressant activity, and thus has questioned the previously held monoamine hypothesis of depression pathogenesis. It has been believed that adrenergic and serotonergic activity is impaired in depression. However, a number of studies have indicated that the lack of plasticity has been more crucial in the development of depression and other disorders (35). Hence, the neurotrophin hypothesis has been proposed, which has stated that the induction of neuroplasticity through the neurotrophic factor system could have the potential to treat mood disorders (31).

1.1.1.3 *Neurodegenerative diseases*

BDNF, as a prominent neurotrophin, has also been pursued as an experimental treatment of neurodegenerative diseases (36, 37). Huntingtin protein, a protein that is linked to the cause of Huntington's disease, has been found to regulate expression and trafficking of BDNF (38), where

mutation in huntingtin has suppressed BDNF expression and disrupted normal transport of BDNF and TrkB. Delivery of BDNF into the striatum has been shown to attenuate progression of Huntington's disease in animal models (38).

BDNF has also been found to play a role in Alzheimer's disease. BDNF levels have been found to be reduced in parietal cortices and hippocampi in postmortem brains of Alzheimer's disease patients (39), and it has been suggested that amyloid-beta peptides have led to truncation of the TrkB receptor and reduction of TrkB signaling (40). Lentiviral delivery of GFP-tagged BDNF into the entorhinal cortex of aged monkeys has been reported to significantly ameliorate visuospatial performance compared to the vehicle-GFP treated controls (41), indicating the ability of BDNF to improve some symptoms of Alzheimer's disease, likely through induction of neuronal plasticity in the central nervous system (CNS), thus counteracting progression of the disease.

BDNF along with other neurotrophins and growth factors has also been explored in the context of neurological disorders. For example, BDNF treatment of the eye and visual cortex significantly reduced ganglion cell loss following injury of the optic nerve in adult cats as noted above (16). Moreover, BDNF has been shown to induce recovery of movement after spinal cord injury (42).

1.1.2 Signaling of BDNF-TrkB

1.1.2.1 *Receptor structure*

Based on sequence analysis TrkB has been classified as a membrane protein with a ligand binding domain in the extracellular domain and tyrosine kinase in the intracellular domain (Figure 1.1.1). The extracellular domain contains a leucine-rich repeat and two Ig-like domains, which could be carrying cell adhesion function, and the ligand binding immunoglobulin like domain is located at 301-379 aa. Multiple glycosylation sites have been predicted on TrkB and resolved on a related receptor TrkA (43). Following the ligand binding site, a transmembrane domain, a juxtamembrane region, and tyrosine kinase domain has been identified. Despite crystallography studies of the BDNF binding site, the extracellular domain of TrkA (43, 44), and the intracellular tyrosine kinase domain (45), the full structure of the receptor remains to be elucidated. Apart from location of the transmembrane region at 431-454 aa and the signaling tyrosine residue at 516 aa in the juxtamembrane region, little has been known about structural conformation at 382-532 aa and what conformational changes would TrkB undergo to become active.

This part of the protein most likely has played crucial roles in receptor activation as it likely transduces conformational changes upon ligand binding (46).

In addition to the full length form of TrkB, neurons have been reported to produce the truncated isoform, TrkB.t1, which lacks the cytosolic tyrosine kinase domain and has been regarded as the dominant-negative isoform (47, 48), which regulates BDNF signaling. The later notion has been supported by the inhibition of BDNF-induced downstream pathways by TrkB.t1, since it has been able to bind BDNF without inducing enzymatic kinase activity. It has also been shown to scavenge BDNF for storage or degradation in glial cells. However, TrkB.t1 has been reported to induce BDNF-independent cytoskeletal changes in glia (49). Interestingly full length TrkB and TrkB.t1 mutually could inhibit each other's activity.

1.1.2.2 Receptor activation

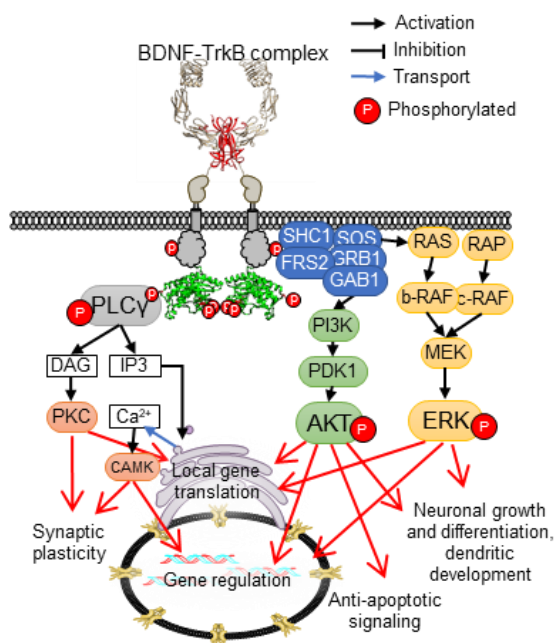


Figure 1.1.1 TrkB structure and signaling

BDNF (red structure) and TrkB (grey structure) complex formed on the cell surface leads to phosphorylation (P symbol) of TrkB, ERK, Akt, and PLCγ through recruitment of adapter proteins (SHC1, FRS2, GRB1, GAB1) and intermediate kinases (RAF, MEK, PI3K, PDK). Phosphorylated ERK and Akt through gene regulation and translation induce neuronal growth and survival. PLCγ through second messengers (DAG, IP3, Ca²⁺) activates PKC and CAMK kinase pathways, which leads synaptic plasticity and other trophic effects of BDNF.

These pathways have been associated with differentiation, proliferation, and pro-survival signaling (53,

BDNF and other neurotrophins are present as dimers at physiological conditions and concentrations. Upon binding, BDNF mediates TrkB dimerization and conformational changes. This leads to autophosphorylation of the TrkB intracellular domain at several tyrosine residues (3, 50, 51). Among them Y516, Y706/Y707, and Y816 are found to be important for signal transduction. After the receptor activation SHC adapter protein (SHC1) protein is recruited to the pY516 residue and phosphorylated by TrkB (52), which leads to activation of the extracellular signal-regulated kinase (ERK) and protein kinase B (Akt) signaling cascades (Figure 1.1.1).

54). Phospholipase C (PLC γ) has been shown to directly bind phosphorylated TrkB at pY816 site and to be activated by the receptor and trigger Protein Kinase C/Ca $^{2+}$ signaling. These pathways account for anti-apoptotic signaling, local protein synthesis and gene regulation that ultimately lead to increased neurogenesis, neuronal growth and differentiation, synaptogenesis, synaptic plasticity, and other physiological effects of BDNF(55) (Figure 1.1.1).

BDNF-induced TrkB activation has been reported to initiate internalization of the BDNF-TrkB signaling complex through clathrin-coated pits and by macropinocytosis (50). These created endosomes would still contain active TrkB, forming 'signaling endosomes', and have been shown to be retrogradely transported to the cell soma and nucleus (for the axonal receptors). Retrograde transport velocity has been estimated to be at 1 $\mu\text{m/s}$ (56), which has corresponded to the velocity of axonal active transport (0.1-2 $\mu\text{m/s}$) (57). This transportation is believed to transduce the trophic signal from the axonal terminal to the cell soma and deliver BDNF to the cell body from peripheral application.

To summarize, TrkB activation could be characterized at the receptor (e.g. receptor phosphorylation and internalization) or its downstream targets and physiological consequences (e.g. LTP induction, gene expression, neurite outgrowth, and cell survival).

1.1.3 TrkB agonists

1.1.3.1 *BDNF Pharmacokinetics*

Given the importance of TrkB activity in brain plasticity and development, as well as its role in various brain disorders and diseases, many different attempts have been made to modulate the BDNF-TrkB system. The first step would have to be to evaluate BDNF itself as a potential therapeutic agent.

A pharmacokinetic study of parenteral administration of radioiodinated BDNF into adult Sprague-Dawley rats has revealed a BDNF plasma half-life to be 0.92 min with a higher non-specific binding to brain and nerve capillaries compared to other neurotrophins (58). In another study, intravenous injection of BDNF radiolabeled with ^3H into Sprague-Dawley rats has demonstrated a plasma half-life of 2.72 min with rapid degradation measured with trichloroacetic acid precipitation, while BDNF conjugated to monoclonal antibody to transferrin receptor has shown a half-life of 12 min with slower degradation. Control protein, ^{14}C labeled rat serum albumin, has produced a 382 min half-life with no detectable

degradation. Non-conjugated BDNF has been found to be bound to capillaries and with little BBB penetration, while conjugated BDNF has shown higher BBB penetration (59).

Subcutaneous (s.c.) BDNF administration to Wistar rats has resulted in a plasma half-life of 3h measured by ELISA and has rescued choline acetyltransferase expressing neurons in sciatic and facial nerve axotomized rats (60). Human trials of s.c. injection of recombinant methionyl BDNF has increased colonic transit, relieved constipation, and has demonstrated a plasma half-life of BDNF to be on average 7h, with 2.9-14.2 h range measured by ELISA (61).

A pharmacokinetic study of intrathecal administration of methionyl BDNF into sheep spinal cord at lumbar level demonstrated 3 and 2 phase decay of BDNF concentration at injection and cranial sites respectively. First phase of the decay has shown a half-life of BDNF at 3.8-8.8 min, while at the second phase half-life has been measured to be 3.8 h. It has been hypothesized that first phase decay was a distribution phase of the injected BDNF, while the second phase appeared due to transient binding of BDNF to the meninges. Moreover, free distribution of the BDNF in spinal cord parenchyma could be observed, while in the grey matter BDNF has been detectable exclusively in the perinuclear space of motor neurons, suggestive of retrograde transport (62). These results prompted human trials. In phase I/II trial of amyotrophic lateral sclerosis (ALS) treatment with intrathecal delivery of recombinant methionyl BDNF or placebo, the measured concentration of BDNF in lumbar cerebrospinal fluid (CSF) obtained between day 11 and 24 has been 40 ng/ml at the lowest dose infusion rate (25 µg/day) (63). Lumbar-to-cisternal CSF ratio ranged from 2:1 to 20:1 in 17 individuals with average of 4:1 ratio, which would be in agreement with bulk dilution of the compounds in the CSF (64). Serum concentration of BDNF have been measured to be < 5ng/ml at any injected doses (63). In phase III clinical trials of ALS treatment, intrathecal delivery of recombinant methionyl BDNF to 1135 patients has shown no significant improvements over placebo in forced vital capacity test, survival, walking speed, or respiratory events (65). Lack of success in clinical trials of BDNF could be attributed to the pharmacokinetic properties of BDNF or to dosage of BDNF, where positive in vivo results with BDNF were observed at 5-10 mg/kg in mice, while human dosage were at 25-100 µg/kg, with max tolerance of 150 µg/kg (66).

Even though direct BDNF injection did not produce anticipated treatment outcome, a lot of effort has been put to increase bioavailability of the BDNF since pharmacokinetics of intravenous (i.v.) injected

BDNF seem to be the primary cause of lack of functional improvements (36, 67, 68). In particular, viral-based (AAV, or lentivirus, adenovirus) and cell-based (genetically engineered bone marrow stem cells, fibroblast, neural stem cell) delivery systems have been tested in animal models of different diseases (Parkinson's, Huntington's, Alzheimer's, epilepsy) and injuries (CNS lesion, spinal cord injury). Alternatively, polymer scaffolds, like polyethylene glycol chain conjugation, poly(lactic-co-glycolic acid) microsphere binding, and agarose hydrogel association, have been used to deliver and release BDNF into the targeted tissue (68).

Converting BDNF into pharmaceuticals has faced many challenges and would require more modifications and testing before moving into human trials. On the other hand, developing small molecule agonists and modulators should provide more control over pharmacokinetics and pharmacological profile (e.g. efficacy and signaling bias), which could allow for a wider range of therapeutic options.

1.1.3.2 *TrkB* small molecule agonists

Development of *TrkB* small molecule agonists and modulators has been of great importance (69). In recent years, several small molecule agonists have been reported to activate *TrkB* in living cells *in vitro* including 7,8-dihydroxyflavone (7,8-DHF) (70), deoxygedunin (71), LM22a-4 (72), desmethylasterriquinone B1 (DMAQ-B1) (73), amitriptyline (74), and deprenyl (75).

1.1.3.2.1 7,8-Dihydroxyflavone

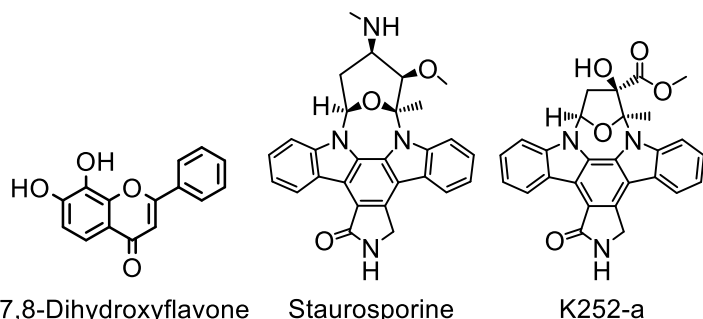


Figure 1.1.2 Structure of 7,8-DHF, staurosporine, and K252a
7,8-Dihydroxyflavone, a reported *TrkB* agonist. Staurosporine, a non-selective kinase inhibitor and apoptosis inducing agent. K252a, a *Trk* family selective kinase inhibitor derived from staurosporine.

The most studied *TrkB* agonist, 7,8-DHF (Figure 1.1.2), has been identified in a screen of 2000 biologically active compounds based on their anti-apoptotic activity in a *TrkB* expressing cell line treated with staurosporine (apoptosis inducing agent and non-specific kinase inhibitor,

Figure 1.1.2 (76, 77)). It has been reported to induce *TrkB* dimerization, rescue neurons from kainic acid induced toxicity, and exhibit neuroprotective properties in an animal model of Parkinson's disease. A 4'-dimethylamino-7,8-dihydroxyflavone derivative has been reported to be a more potent and efficacious in

TrkB activation promoting neurogenesis in the dentate gyrus and demonstrating antidepressant activity (78). Intracerebroventricular administration of 7,8-DHF dampened the development of the “depressive” phenotype in vulnerable animals with decreased serum BDNF (79). 7,8-DHF has been shown to activate TrkB in amygdala at 5 mg/kg intraperitoneal injection and enhanced fear acquisition and extinction (80). In six different publications it has caused various improvements in animal models of Alzheimer’s disease (81–86), while one publication has claimed no significant effect of 7,8-dihydroxyflavone on Alzheimer-associated phenotypes (87).

Subsequent studies have demonstrated direct binding of 7,8-DHF to the TrkB extracellular domain by surface plasmon resonance and tryptophan fluorescence quenching. It has also been reported that the agonistic activity of 7,8-DHF at TrkB in cultured rat cortical and hippocampal cultures depended on day in vitro culturing of the cells with the highest activity at DIV 13 (88). In rodents *in vivo* systemic administration of this compound has been shown to have antidepressant effects in mice (89) and improve motor function in Huntington disease models (90). All in all, approximately 100 papers have been published since the initial report of BDNF mimetic property of 7,8-DHF.

However, in addition to agonistic activity at TrkB, 7,8-DHF has been reported to possess antioxidant activity. 7,8-DHF has been found to be a potent antioxidant, it has inhibited lipoperoxidation of lysosomal membranes (EC₅₀ around 30 μ M) (91), bromobenzene-induced hepatotoxicity in mice (100-200 mg/kg) (92), and preventing H₂O₂-induced DNA damage in-vitro at 40 μ M (93). It has also been shown to activate Akt in wild type CHO cells (93). In addition, it has been shown to rescue immortalized hippocampal cells that do not express TrkB from glutamate, H₂O₂, and menadione-induced oxidative stress (94). It has been shown to induce aortic dilation through TrkB-independent endothelial nitric oxide cGMP and Ca²⁺ signaling pathways (EC₅₀ 24 μ M) (95). It should be noted that these antioxidant activities of 7,8-DHF have been detected at high concentrations (20-100 μ M).

1.1.3.2.2 Desmethylasterriquinone B1

DMAQ-B1 (Figure 1.1.3) has been reported to activate TrkA, TrkB, and TrkC in CHO cells transfected with these receptors (73). It has demonstrated a short period of TrkA activation with

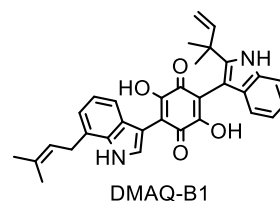


Figure 1.1.3 Structure of DMAQ-B1
DMAQ-B1, a reported Trk family receptor agonist.

maximal induced response at 3 min. It has also activated TrkB in rat cortical culture at 5 and 20 μM within 10 min of incubation. However, DMAQ-B1 has also induced ERK and Akt phosphorylation in wild-type CHO cells at 20 μM within a 10 min treatment and has induced cell death at active concentration in rat cortical neurons (73).

It has initially been identified as an insulin receptor (IR) agonist through screening of 50,000 mixtures of synthetic and natural products by assaying for tyrosine kinase activity of IR expressed in CHO cells (96). It has been reported to activate IR with similar efficacy as insulin and EC₅₀ at 3-6 μM . Moreover, at 2 μM DMAQ-B1 increases insulin potency and efficacy. It has also induced PI-3K and Akt phosphorylation in CHO. However, it activates other RTKs, like insulin-like growth factor receptor (IGF-IR) and epidermal growth factor receptor (EGFR), with lower potency and efficacy.

1.1.3.2.3 LM22a-4

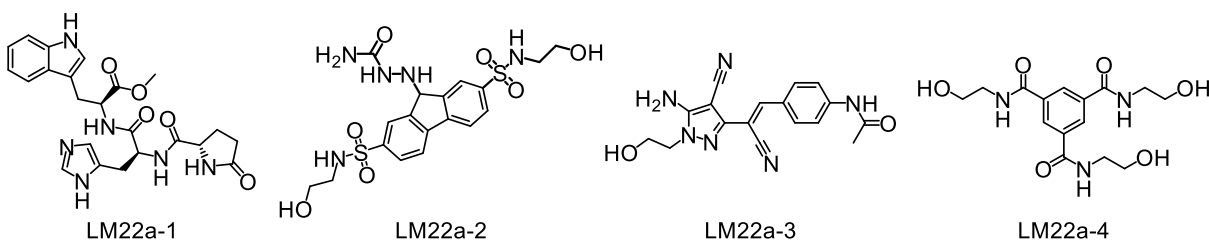


Figure 1.1.4 Structure of LM series
LM series compounds, reported TrkB agonist derived from BDNF structure modeling

Another series of compounds referenced as LM (named after the authors, Longo and Massa) has been developed through in-silico screening of more than 1,000,000 available compounds for structural resemblance to the BDNF loop IIb consisting of the SKGQL amino acid sequence (72). Several compounds (Figure 1.1.4) identified from the screen have been reported to activate TrkB and downstream targets in NIH-3T3 cells, while LM22a-4 has also shown activation of TrkB in mouse hippocampal neuronal culture (72). Further in vivo studies of LM22a-4 have demonstrated BDNF-related activities. For example, LM22a-4 has induced spinal cord injury recovery by reducing apoptosis in mice (97). LM22a-4 has improved recovery of motor functions in mice that suffered from artificially induced stroke without significant change in angiogenesis, dendritic arborization, axonal sprouting, glial scar formation, or neuroinflammation (98). Interestingly, LM22a-4 treatment has shown increased rescue of dendritic spine density of medium spiny neurons in mouse models of Huntington's diseases (99). In a

mouse model of Rett syndrome, LM22a-4 has rescued wild-type levels of TrkB phosphorylation in the medulla and pons and restored wild-type breathing frequency, eliminated spontaneous apneas in resting animals, improved hippocampal-dependent object location memory and restored hippocampal long-term potentiation (LTP) (100–102).

1.1.3.2.4 Other compounds

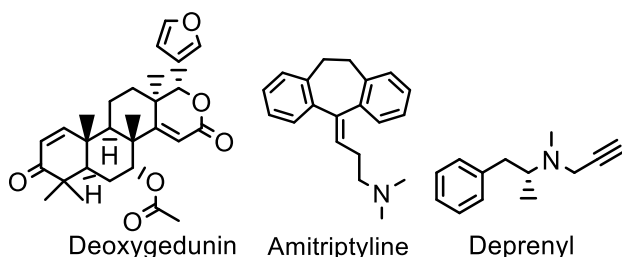


Figure 1.1.5 Structure of deoxygedunin, amitriptyline, deprenyl
Deoxygedunin, a reported TrkB agonist. Amitriptyline, a tricyclic antidepressant and reported TrkB agonist. Deprenyl, a selective irreversible monoamine oxidase inhibitor and reported TrkB agonist.

Deoxygedunin (Figure 1.1.5) has been identified as TrkB agonists along with 7,8-DHF. It has been described as orally available agent able to activate TrkB in mouse brain and even prevent degeneration of vestibular ganglion in BDNF double knockout mice (71). It has also demonstrated anti-depressant and learning

enhancement effects. Deoxygedunin was shown to promote axon regeneration (103). In Parkinson's disease animal models, it has rescued behavioral performances of the animals and decreased the extent of dopaminergic neuron loss (104).

Another TrkB agonist contender discovered in the same screen as 7,8-DHF and deoxygedunin has been amitriptyline, one of the oldest tricyclic antidepressant agents (105)(Figure 1.1.5), which has also been reported to have activity at TrkB and neuroprotective properties at 500 nM in vitro (74). It has induced TrkB phosphorylation and increased neurogenesis in the dentate gyrus in an Alzheimer's disease mouse model (106), potentiated BDNF-TrkB signaling and supported mitochondrial integrity and functionality in a Huntington's disease mouse model (107). It has induced TrkB phosphorylation in dorsal root ganglion explant at 10 μ M which has also appeared to be toxic (108). However, amitriptyline has not induced TrkB in fibroblast or rat primary hippocampal and cortical neuronal culture in another independent lab (109).

Deprenyl, a monoamine oxidase inhibitor type antidepressant (110) (Figure 1.1.5), has been reported to induce TrkB phosphorylation in the SH-SY5Y cell line at 100 μ M, however, neither ERK nor Akt have been found to be activated (75). Of downstream TrkB targets, only PI3K has been reported to

be phosphorylated in response to deprenyl stimulation. No other report on deprenyl activity has been published to date.

1.1.3.3 *TrkB peptide agonists*

An alternative approach to finding TrkB agonists has been to use part of the BDNF sequence with certain structural constraints to mimic BDNF tertiary structure. The available crystal structure of BDNF has been used to select an appropriate region as a basis for peptide synthesis. Based on a sequence of BDNF loop II, a 12-mer peptide flanked with Cys for cyclization, CEKVPVSKGQLKQC, has been selected to identify potent peptide sequence for TrkB activation (111). Modification of the sequence has led to a development of a shorter peptide, CVPVSKGQLC, which has been further altered to give a more constrained conformation by cyclizing the monomer and dimerizing through Cys-Cys and Glu-Lys coupling respectively, named tricyclic dimeric peptide 6, or TDP6 (112). This peptide has demonstrated neuroprotective properties and induced TrkB and ERK phosphorylation in primary oligodendrocyte culture but not to the same level of efficacy as BDNF (113).

Another peptide has been designed based on the neurotrophin sequence and the hypothesis that neurotrophins have not been able to promote axonal growth in the presence of myelination inhibition through interaction with p75NTR receptor (114). Constraining the peptide to the BDNF sequence that selectively interacts with TrkB and not p75 may yield a TrkB agonist that would promote myelination and axonal growth even in the presence of p75. As a start, the N terminus sequence has been synthesized as a cyclic peptide, N-Ac-CSRRGEC-NH₂, to antagonize TrkB and confirm competitive binding to the receptor, which has been shown by inhibition of neurite growth in vitro with IC100 at 125 μM. Then, a tandem repeat approach has been used to dimerize the peptide to N-Ac-CSRRGELAASRRGELC-NH₂ and thereby turning it into a TrkB agonist, which promoted axonal growth in vivo with EC100 at 6 μM. However, this peptide has not been active in the CellSensor assay (see below) (115).

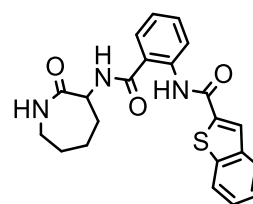
Another attempt to create a BDNF mimetic peptide has used BDNF structural analysis yielding 6 sequences originating from sequences of BDNF loops. Peptides based on these sequences have been synthesized as tetrameric dendrimers coupled to a lysine backbone (116). Out of these peptides, two peptides, Betrofin 3 (RGIDKRHWNSQ) and Betrofin 4 (SYVRALTMDSKKRIGWR) have induced ERK and Akt phosphorylation, neurite outgrowth, and neuronal survival in primary cerebellar granule neurons.

Betrofin3 has also been reported to cause differentiation of embryonic stem cells into cardiomyocytes (117).

Going smaller in scale, five tetra peptides based on different regions of BDNF have been synthesized and tested for TrkB agonism in hippocampal neuronal culture with arguably positive results (118). Peptide B-3, Ac-SKKR-NH₂, and B-5, Ac-IKRG-NH₂, have been found to be partial agonist and partial antagonist of BDNF respectively.

1.1.3.3.1 TrkB antagonists

Generating TrkB antagonist may have potential use as pharmaceuticals to treat some mood disorders as well as cancer. One approach to find antagonists could be finding a peptide that would compete with BDNF in binding to TrkB. The rational starting point would be BDNF sequences itself. As a direct approach to find BDNF sequence responsible for TrkB binding and activation, BDNF has been enzymatically cleaved into six subsequences and tested for inhibition of BDNF-induced TrkB phosphorylation (119). A BDNF specific sequence from region next to loop 3, NPMGYTKEG, has emerged as potent antagonist. This cyclic peptide of the Cys-flanked sequence has been named Cyclotraxin B and found to be potent antagonist with IC₅₀ at 12 pM. It has exhibited anxiolytic effects in mice similar to diazepam but showed no antidepressant activity.



ANA-12

Figure 1.1.6 Structure of ANA-12
ANA-12, a reported TrkB antagonist derived from BDNF structure modeling.

Continuing in-silico screening approaches, the N-terminal region of NT4 in the complex with TrkB-d5 has been modelled for BDNF-TrkB interactions (120). Using docking algorithms 12 compounds were selected for testing on cells. As the result two compounds have shown full inhibition of TrkB activity with an IC₅₀ at 200 μM. Further modifications have yielded the ANA-12 compound (Figure 1.1.6) with biphasic inhibition curve displaying IC₅₀ 50 nM and 50 μM. In vivo testing of ANA-12 has revealed anxiolytic and antidepressant activities.

BDNF mimetics in the form of cyclic pentapeptide monomer or dimer with VSK sequence core, b-Ala or Gly as 4th amino acid, and (1S,2S)-2-aminocyclohexanoic acid (BAC6c), or (S)-2-carboxylate-azetidine (Azg), or 19 (S)- and (R)-2-carboxylate-2-methylazetidine as 5th amino acid mimicking loop 2, and cyclo[Asp-Ser-Lys-Lys-Arg-BAC6c] and cyclo[Asp-Ser-Lys-Lys- Arg-Azg] mimicking loop 4 have been

synthesized and shown to be TrkB antagonist by inhibiting BDNF-induced TrkB activation in rat cortical neuronal culture at 100 μ M (121).

1.1.3.3.2 Phage display efforts

Utilization of phage display has been yet another approach to find small molecule agonists, modulators, or antagonists of TrkB. This approach has been based on library of phages that display peptides or protein on the capsid proteins. By presenting a phage library to the target, these peptides may specifically bind phage to this target in the process called biopanning. Collected bound phages have usually been amplified and presented in the next round of biopanning. A phage library has been sequenced to identify peptides that bind to the target. Before development of next generation sequencing that enables sequencing the whole phage library, the Sanger sequencing of randomly selected phages has been used limiting the information on sequences in different fractions of the biopanning process. To account for background binding two approaches have been employed: consecutive biopanning, where phage library has been biopanned against background (e.g. plate, tube, cells lacking the target) before biopanned against the target, and parallel biopanning, where same library has been biopanned against target and background. In the consecutive biopanning approach, phages with specific binding to the background are assumed to be depleted before the rest of the phage are presented to the target, thus creating a library with phage that should be specific to the target. In parallel biopanning approach, the phage library collected from target has been used for the next round. Target specific peptides then have been identified through comparison of the sequences collected from both target and background biopannings. Parallel biopanning could only be used with next generation sequencing, since the sequences of whole library has been required for comparable elimination of non-specific peptides.

In one report, a phage display with consecutive biopanning has been used to find sequences of peptides that bind to TrkB, employing TrkB-expressing NIH 3T3 cells and bacteriophage f1 CX9C library (122). After four rounds of selection 20 peptides have been identified through the Sanger sequencing. Out of 20 peptides, only one peptide, CSMAHPYFARC named C1, has been characterized more thoroughly, which has demonstrated antagonism of BDNF induced NIH 3T3 proliferation.

Another phage display using T7 phages with random peptide sequences (no constraints have been described) has been performed on recombinant TrkB-Fc chimera constructed as a pseudo-receptor dimer immobilized on Dynabeads (123). After 5 rounds of selection, BM17 peptide with NVRPRICRVRKWTLCF sequence has been selected for characterization and modification. This peptide has bound to TrkB with K_d at 17 nM, while its modified version, BM17d99 with KSLPRMCRVRKWRLCF sequence has had K_d at 0.45 nM. Dimerization of BM17d99(K1N/K11R) has produced a peptide that induced TrkB phosphorylation with EC_{50} at 10 nM and lower efficacy than BDNF.

A surprising discovery has been made in the course of *in vivo* phage display of cardiac vasculature using pSKAN Phagemid Display System with CX6C in young and aged mice. A peptide, ψ O40, with ARRQQA sequence collected from aged mice has been found to be highly homologous to BDNF N-terminus at 5-9 positions. Through this discovery it has been determined that the truncated form of TrkB is upregulated in the aged mice heart.

1.1.4 Reproducibility of TrkB agonists

Discoveries of TrkB agonist have seemed to be successful. However, there have been a number of reports, which show that *in vitro* and *in vivo* activity of these compounds as TrkB agonists could not be reproduced. For example, no TrkB, ERK, or Akt activation has been detected in CHO-TrkB cells (see below) and neurons in the presence 7,8-DHF, LM22a-4, or amitriptyline (115, 124). In another instance, 7,8-DHF has failed to alleviate learning and memory impairments in the Alzheimer's disease mouse model (87). In addition, the lack of reproducibility of these has been highlighted at conferences. Given this conflicting information, independent characterization of the reported agonist has become important.

1.2 Results

1.2.1 Overview

To thoroughly characterize potential TrkB agonists and modulators and address the reproducibility issue, a platform of various assays was developed during the course of the presented work. Specifically, several different cell lines expressing TrkB have been established, including primary neuronal culture. Using these cell lines, several cell-based assays have been developed and acquired, that reported on activation of TrkB and its downstream targets, as well as on TrkB-dependent gene

expression. These assays were then used to characterize reported agonists as well as to provide an opportunity to perform an independent high throughput screening of the small molecule library in collaboration with Dr. Holson (Broad Institute). The results of our efforts have been published in *Science Signaling* (125).

In addition to the developed assays, a new screening platform was developed based on phage display of the short cyclic peptides in collaboration with Dr. Teesalu (Sanford Burnham Prebys Medical Discovery Institute, SBP MRI), which aimed at finding peptides that would exhibit affinity to BDNF-TrkB complex, an alternative approach to the previously reported phage display efforts (see above).

1.2.2 Established cell lines

1.2.2.1 Neurons

To test endogenously expressed TrkB, primary neuron culturing was developed. Following Dr. Waites (Columbia University Medical Center, CUMC) protocol and assistance, cortical neuronal cultures (CNC) were prepared from E18 rat pups' cortices. These cultures were grown beyond 12 days in vitro (DIV 12) up to DIV25, a time period when neurons are considered to be fully mature. Typically, mature cells would create long processes overlapping with each other, creating synaptic connections. CNC contained different neuronal and glial subtypes which expressed TrkB (Figure 1.2.1). TrkB was expressed in full length and truncated forms (Figure 1.2.7).

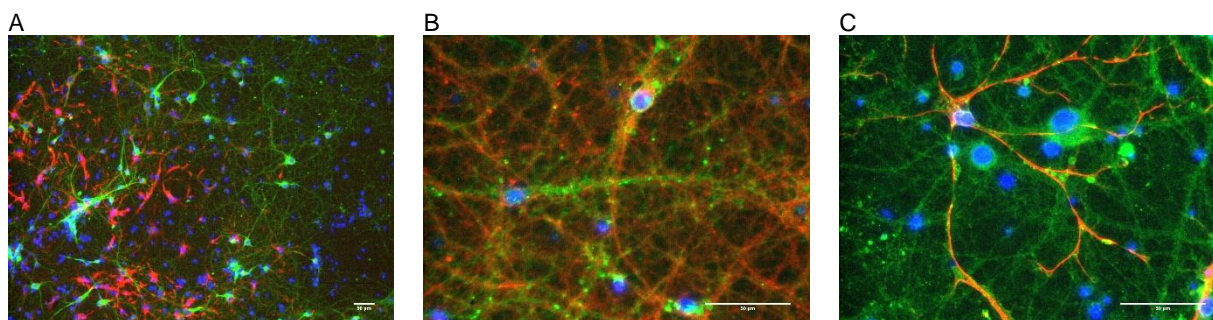


Figure 1.2.1 CNC characterization by immunofluorescence

A. CNC stained with neuronal marker b3-Tubulin (green), astrocytic marker GFAP (red), and Hoechst nuclear stain (blue) to confirm the presence of neurons, astrocytes, and other cell types (not stained) in the culture (scale 50 μ m). B. CNC stained for TrkB (green) and neuronal marker b3-Tubulin (red) to demonstrate presence of TrkB in neurons. C. CNC stained for TrkB (green) and GFAP (red), to show expression of TrkB in astrocytes and other cells (not labeled). Scale bar for B and C 50 μ m.

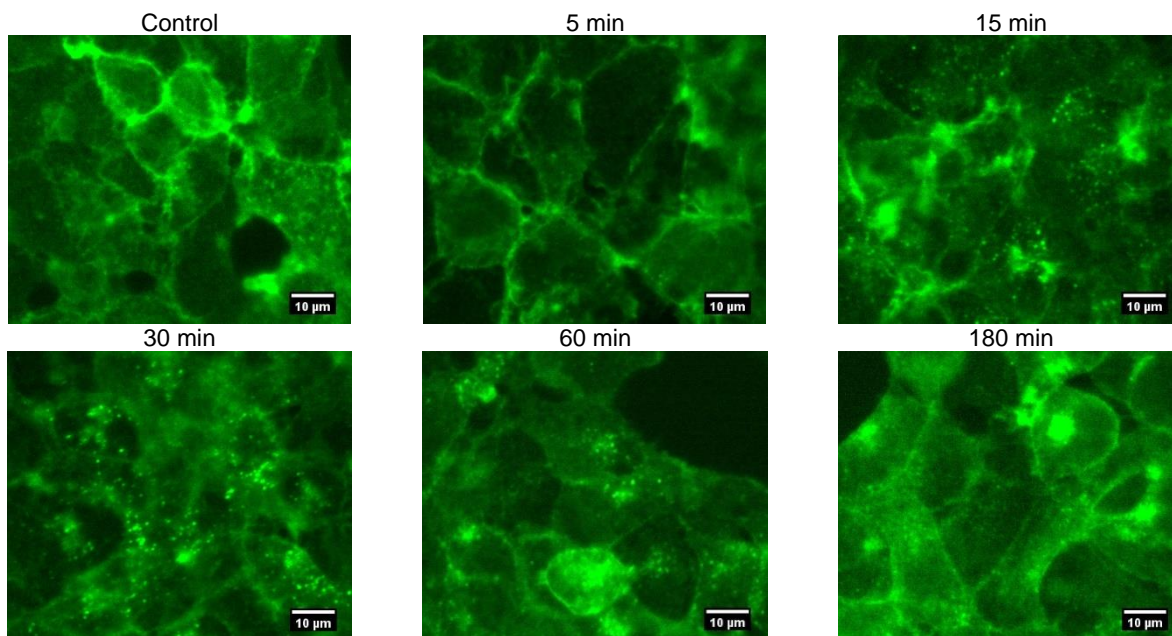


Figure 1.2.2 TrkB internalization in HEK-TrkB cells
 BDNF induced TrkB internalization in HEK-TrkB, which could be observed at different time points as the formation of vesicles (puncta stained with TrkB antibody). Excess TrkB remained on the cell surface (coronal staining by TrkB antibody).

1.2.2.2 HEK-TrkB

In order to have reliable TrkB activation in the context of human cells, a HEK cell line stably expressing TrkB was acquired from Dr. Chao (NYU). Functional activity of the receptor at several

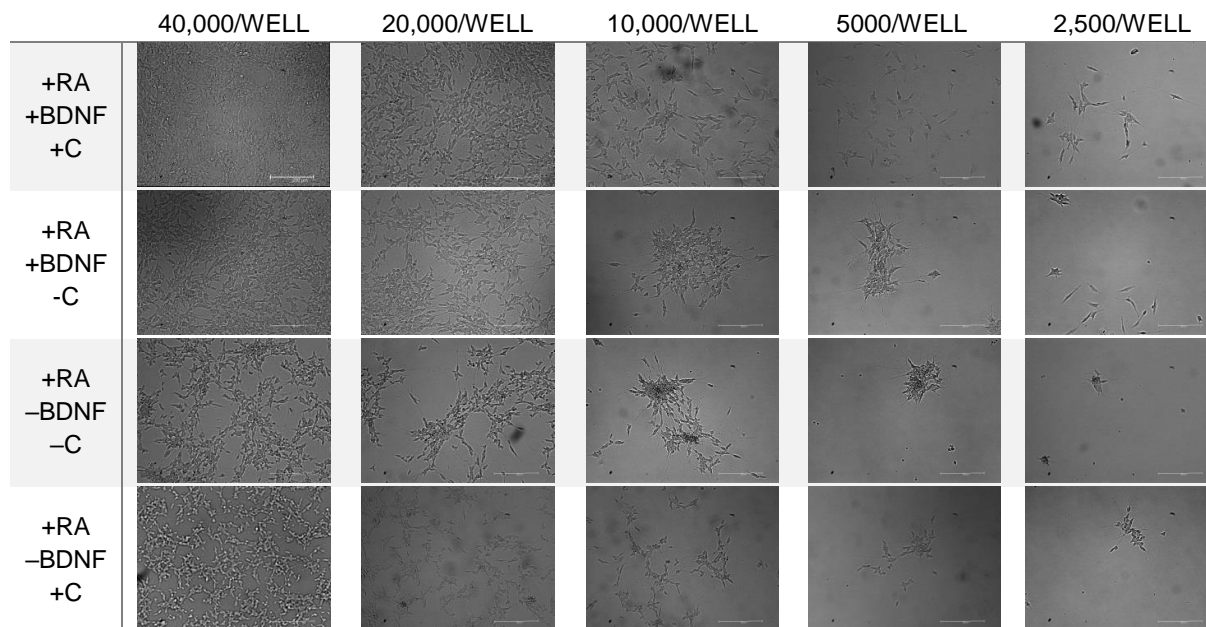


Figure 1.2.3 SH-SY5Y culturing conditions in 96-well plates
 SH-SY5Y cells seeded at different conditions in a 96-well plate to find optimal conditions for the developed assays. Scale bar is 100 µm.

signaling levels was verified by the assays developed in our laboratory (see below). Moreover, BDNF-induced TrkB internalization could be detected through immunofluorescence (IF) (Figure 1.2.2).

1.2.2.3 SH-SY5Y

To test endogenously expressed *human* TrkB, an SH-SY5Y cell line based protocol was developed. Human bone marrow derived SH-SY5Y could be differentiated using retinoic acid into neuron-like cells, which express TrkB. Using standard protocols, SH-SY5Y was used to test reported agonists. However, to increase the throughput of the assays, optimal conditions to seed and treat the cell line in a 96-well plate were explored. To this end, several different cell densities, treatment with BDNF, and surface binding agents (collagen, laminin, poly-D-lysine) were tested. Seeding the cells at 40,000/well provided better binding to the surface, while lower seeding density resulted in cell aggregation. BDNF treatment reduced the number of aggregates in the culture (Figure 1.2.3). Collagen and laminin had similar effect on the cells, while poly-D-lysine surface treatment resulted in cell aggregates. Furthermore,

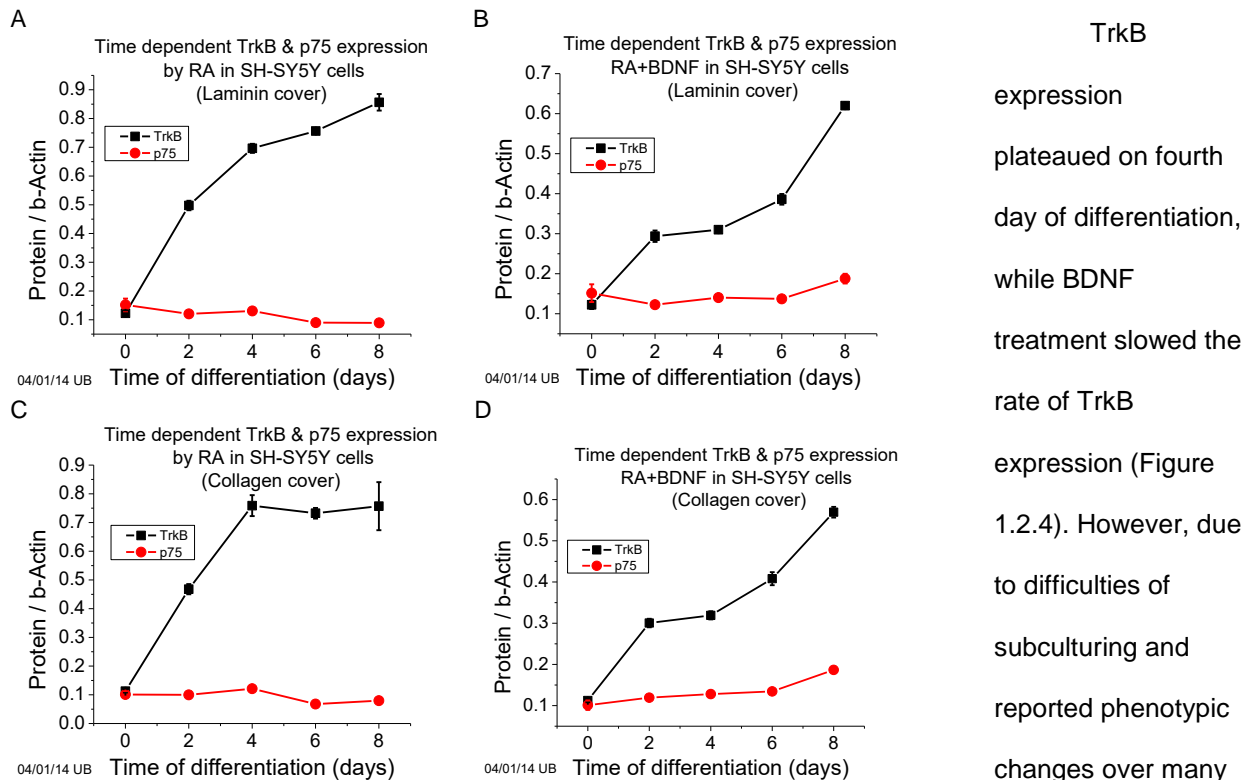


Figure 1.2.4 TrkB and p75 expression profile in differentiated SH-SY5Y cell
 A and C. Expression profile of TrkB and p75 in retinoic acid induced differentiated SH-SY5Y in laminin (A) or collagen (C) covered 96-well plate. B and D. Expression profile of TrkB and p75 retinoic acid induced differentiated SH-SY5Y cells treated with BDNF on the 2nd day of the differentiation. in laminin (B) or collagen (D) covered 96-well plate. BDNF inhibited increase of TrkB expression over 2 days.

TrkB expression plateaued on fourth day of differentiation, while BDNF treatment slowed the rate of TrkB expression (Figure 1.2.4). However, due to difficulties of subculturing and reported phenotypic changes over many passages SH-SY5Y cell assays were not pursued any further.

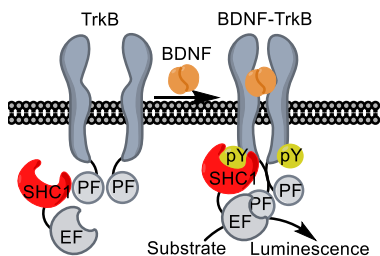


Figure 1.2.5 DiscoverX PathHunter assay scheme

The DiscoverX PathHunter® assay schematic based on U2OS cell lines transfected with TrkB and SHC1 proteins fused with parts of β -galactosidase enzyme (EF – enzyme fragment, PF – peptide fragment). This assay reports on TrkB phosphorylation through protein-protein interaction of phospho-TrkB (pTrkB) and SHC1 proteins, which leads to reconstitution of the enzyme (EF+PF). The signal is registered as luminescence produced by enzymatic activity on the reporter substrate.

enzyme in close enough proximity for enzyme reconstitution to occur. The enzyme activity has been recorded through a luminescent reaction (proprietary information). DiscoverX U2OS cell line expressing TrkB and p75 was used for primary high throughput screen.

The Invitrogen CellSensor CHO cell line expressing TrkB, which reports nuclear factor of activated T-cells (NFAT) activation, was used as a counter screen. The Invitrogen CellSensor assay has been based on β -lactamase expression under the control of NFAT in a CHO cell line. TrkB phosphorylation results in PLC γ activation leading to increased Ca²⁺ level and subsequent NFAT activation (Figure 1.2.6). β -lactamase expression is quantified by a FRET interaction between a coumarin and fluorescein derivatives connected by a β -lactam ring. Upon bond cleavage by newly expressed β -lactamase, the FRET is disrupted, leading to an increase of

1.2.2.4 Cell lines for HTS

To perform high throughput assays based on reporter gene technology, two commercially available cell lines were acquired. DiscoverX PathHunter® has been based on the reconstitution of β -galactosidase through a protein-protein interaction of TrkB and a downstream target by fusing the major fraction of β -galactosidase (EF) to the SH2 domain containing protein, SHC1, and a peptide fragment (PF) of the enzyme to the C-terminus of TrkB in human U2OS cells (Figure 1.2.5). Upon phosphorylation of TrkB, SHC1 binds to the receptor, which brings the two split portions of the

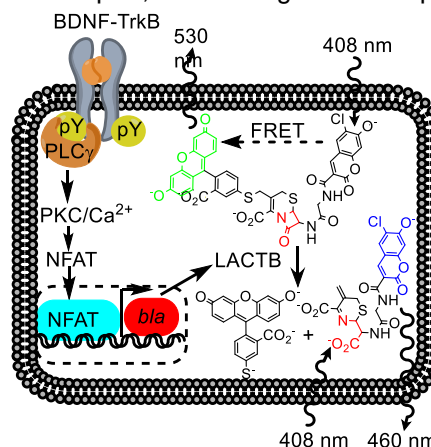


Figure 1.2.6 Invitrogen CellSensor assay scheme

The NFAT-bla-TrkB-CHO CellSensor assay schematic based on CHO cell line expressing TrkB. The assay reports on TrkB activation through the expression of the β -lactamase (LACTB) gene (BLA) under control of the receptor-PLC γ -NFAT pathway. TrkB phosphorylation results in PLC γ activation, leading to an increase of cytosolic Ca²⁺ concentration and subsequent NFAT activation (126), which controls expression of β -lactamase in the transfected construct in CHO cell line. Expression of β -lactamase is quantified by a FRET between a coumarin and fluorescein derivative connected by a β -lactam system. Upon bond cleavage by newly expressed β -lactamase, the FRET is disrupted, leading to an increase of donor fluorescence and decrease of acceptor fluorescence.

donor fluorescence and decrease of acceptor fluorescence. Therefore, TrkB activation is directly correlated to the increased level of β -lactamase. TrkB functional activity was confirmed with independent assays developed in our laboratory (see below).

1.2.3 Western Blot

Western blot was used to characterize antibodies and expressed proteins in cell lines, as well as to compare results obtained in the fluorescence assays. TrkB was expressed in full length and truncated isoforms in CNC. The expression of truncated TrkB was higher than full length at DIV 13. Phospho-TrkB (pTrkB) antibody that recognizes pY816 was used to detect TrkB phosphorylation induced by BDNF and reported compounds. It stained a band at 140 kDa. Interestingly, the level of this band in BDNF treated sample was slightly heavier than in other samples. This antibody also stained other targets indicating a low specificity to pTrkB. On the other hand, antibodies against TrkB, phospho-ERK (pERK), ERK, phospho-Akt (pAkt), and Akt produced only target specific bands at the expected MW. These antibodies were deemed reliable to be used in the developed assays.

It has been reported that Zn^{2+} transactivates TrkB through an indirect mechanism (127) in which Zn^{2+} ions inhibit the kinase CSK (C-terminal SRC kinase), thus preventing it from inhibiting the kinase SRC. Disinhibited SRC then phosphorylates TrkB at Tyr⁷⁰⁶⁻⁷⁰⁷, which in turn activates the TrkB kinase domain, leading to phosphorylation of other tyrosine residues required for signaling through the ERK and AKT pathways. SRC and TrkB have also been shown to mutually activate each other (128).

Zn^{2+} in the complex with pyrithione ionophore and reported agonists were tested in CNC in an attempt to reproduce published results. Phospho-TrkB staining as noted above contained an unexplained shift in MW of pTrkB band. Activation of ERK and Akt induced by reported compound were not conclusive. Notably, the Zn^{2+} sample in the pTrkB blot was quite noisy, while in the pAkt blot Zn-induced response had a larger signal than that of BDNF.

Western blot could not be used for thorough characterization of compounds, since the replication power of western blot was low and sample preparation was quite time consuming limiting the throughput capacity of the assay. To achieve higher throughput and a more robust response enzyme linked immunosorbent assay (ELISA) and enzyme-linked fixed-cell immunoassay (ELFI) were developed.

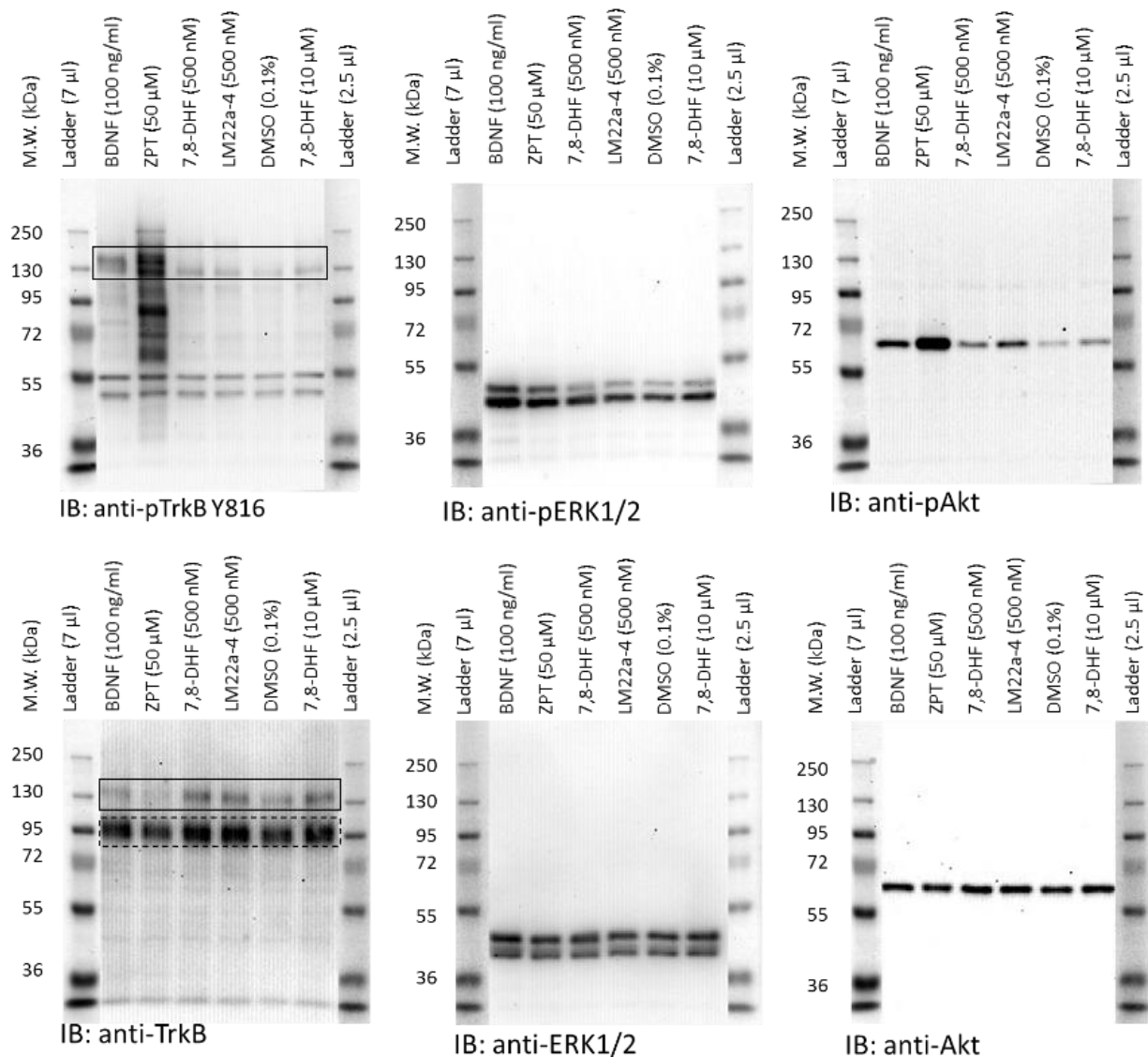


Figure 1.2.7 Western blot analysis of reported agonists in cortical neuron culture

Representative examples of western blot analysis of lysates from primary cortical neuron cultures after 13 days in vitro (DIV 13) treated for 1 hour with the compounds at indicated concentrations. The blot was immunostained with an appropriate antibody. Molecular weight of full length TrkB in native and phosphorylated states is 140 kDa and highlighted with a solid rectangle on the blots, and the truncated form of TrkB with molecular weight of 90kDa is highlighted with a dashed rectangle. Molecular weights of ERK and AKT are 44/42 kDa and 60 kDa, respectively. The antibody against pTrkB stained other non-specific targets, which resulted in noisy data. Antibodies against pERK, ERK, pAkt, and AKT had high specificity.

1.2.4 Sandwich ELISA

To robustly detect TrkB activation, a sandwich-style ELISA was developed to detect TrkB phosphorylation. ELISA, a medium throughput assay, also allowed us to test multiple experimental

conditions with several replicates within a single plate, which is not possible using western blot. Sandwich ELISA was based on immobilization of the target (TrkB) on the surface of a 96-well plate using antibodies, and detecting the target using a different antibody. Since relevant TrkB phosphorylation occurs at several tyrosine residues on the receptor, it was important to detect global TrkB tyrosine phosphorylation. To this end, pTrkB antibodies could not be used for this purpose. To detect global TrkB phosphorylation, a pan phospho-Tyrosine (pY) antibody was used, while a TrkB antibody specific to the extracellular domain was used to capture TrkB on the surface. In addition to detecting pTrkB, it was also important to detect total TrkB in CNC to account for variable levels of TrkB in the samples. To develop this assay, it was important to find a TrkB specific antibody.

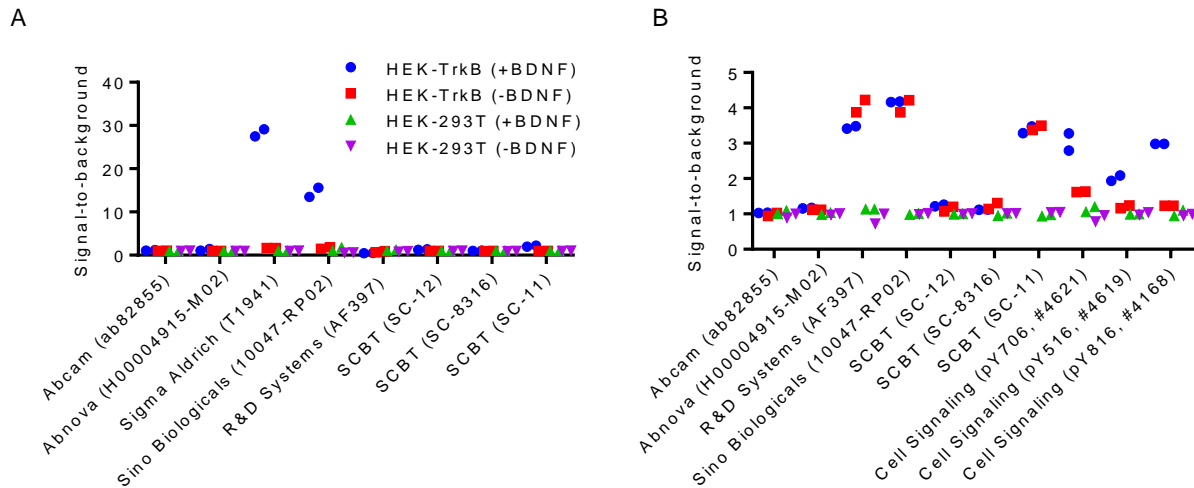


Figure 1.2.8 Antibody screen for sandwich ELISA

A small screen of commercially available TrkB antibodies for TrkB capturing in ELISA. A) Several commercially available TrkB antibodies tested as capturing antibodies for the pTrkB sandwich ELISA using a TrkB-transfected HEK cell line (HEK-TrkB) and a wild-type HEK cell line (HEK-293T). A pan-phospho-tyrosine antibody was used as the detecting antibody. Only Sigma and Sino antibodies were found to be feasible as TrkB capturing antibodies. Sino Antibody for the pTrkB sandwich ELISA were used in further experiments. B) Several commercially available TrkB antibodies tested in the ELFI on HEK-TrkB and HEK cell lines. R&D (goat pAb), Sino (rabbit pAb), and SCBT (rabbit pAb) antibodies produced significant signal. R&D as capturing antibody and Sino as detecting antibody were used in the total TrkB sandwich ELISA in further experiments. Data for each of both independent experiments (n=2) is shown.

1.2.4.1 Antibody screen for sandwich ELISA

To find a specific TrkB antibody several commercially available antibodies were screened on HEK-TrkB cells. Out of seven tested in ELFI assay (see below), three antibodies were able to detect TrkB in HEK-TrkB cell line, only two antibodies produced necessary signal for pTrkB detection. Based on these results, rabbit-derived TrkB polyclonal antibody from Sino Biologicals was selected as the capturing

antibody for pTrkB. Goat-derived TrkB polyclonal antibody from R&D as the capturing agent and Sino antibody as detecting agent were selected for total TrkB

1.2.4.2 TrkB phosphorylation in different cell lines

To test the dynamic range of the sandwich ELISA, dose-response curves of several neurotrophic factors were measured in the established cell lines (Figure 1.2.9). In CNC, BDNF ($EC_{50} = 1.1 \pm 0.4$ nM) was used as the reference for full activation (or full agonism, taken as 100% efficacy). Neurotrophic factor 4 (NT4, $EC_{50} = 1.2 \pm 0.4$ nM) was determined to be a high-efficacy agonist, while NT3 ($EC_{50} = 1.7 \pm 0.7$ nM) a low-efficacy partial agonist (maximum efficacy = $16 \pm 4\%$) at TrkB; NGF was inactive (Figure 1.2.9A, Table 1.1, reported EC_{50} values are 0.7 nM for BDNF, 4 nM for NT4, and 1.3 nM for NT3). Previously reported EC_{50} values have been 0.7 nM for BDNF, 4 nM for NT4, and 1.3 nM for NT3 (129, 130), consistent with our results.

Table 1.1 EC_{50} values of neurotrophic factors: EC_{50} (ng/ml) values in primary cortical neurons. Data represents the mean \pm SD ($n = 3-7$ independent experiments).

	BDNF		NT4		NT3	
TrkB activation (sandwich ELISA)	29	\pm 12	32.6	\pm 9.9	44.7	\pm 19.0
ERK1/2 activation (ELFI)	2.6	\pm 2.5	8.0	\pm 10.7	4.4	\pm 5.9
AKT activation (ELFI)	2.2	\pm 1.4	2.1	\pm 0.7	2.3	\pm 1.6

K252a (Figure 1.1.2) has been a well-established Trk family inhibitor. BDNF-induced activation was inhibited by K252a with an IC_{50} of 6 ± 4 nM (in CNC, Figure 1.2.9C) (reported IC_{50} is at 3 nM (131)). Zinc ions, administered as zinc pyrithione (ZPT), induced TrkB phosphorylation with similar efficacy to BDNF (Figure 1.2.9B) and was not inhibited by K252a (Figure 1.2.9C), consistent with a TrkB transactivation mechanism through Zn^{2+} mediated activation of SRC (which was not sensitive to K252a inhibition at the tested concentrations, see below) as reported (128).

Similar results were obtained in the HEK-TrkB and CellSensor cell lines. BDNF induced TrkB phosphorylation with EC_{50} at 0.9 ± 0.4 nM, while NT4 EC_{50} was at 2 ± 1 nM and NT3 induced low-efficacy response with EC_{50} at 2.13 nM in HEK-TrkB cells. In CellSensor cells, BDNF induced TrkB phosphorylation with EC_{50} 1.3 ± 0.4 nM.

This assay produced reliable signal in all established cell lines; for example, HEK-TrkB cells displayed a signal-to-background ratio (S/B) of 8 ± 1 ; CNC had $S/B = 5 \pm 2$ (Table 1.2), while the CellSensor CHO-TrkB cell line produced S/B 12 ± 5 . Moreover, ELISA allowed detection of statistically significant TrkB

activation at as low as 5-10% of BDNF efficacy in the HEK-TrkB and CellSensor cell lines (Figure 1.2.9 D and E)

Table 1.2 S/B values of ELISA and ELFI in cortical neuron culture. Signal-to-background ratios of maximal responses to BDNF in cortical neurons culture (DIV various), data represents mean \pm SD ($n = 3-6$).

	CNC		HEK-TrkB		CellSensor	
TrkB activation (sandwich ELISA)	4.6	\pm 1.9	8.1	\pm 1.2	12	\pm 5
ERK activation (ELFI)	2.0	\pm 0.4	13	\pm 7	2.0	\pm 0.2
AKT activation (ELFI)	2.3	\pm 0.3	1.27	\pm 0.06	6.0	\pm 0.7

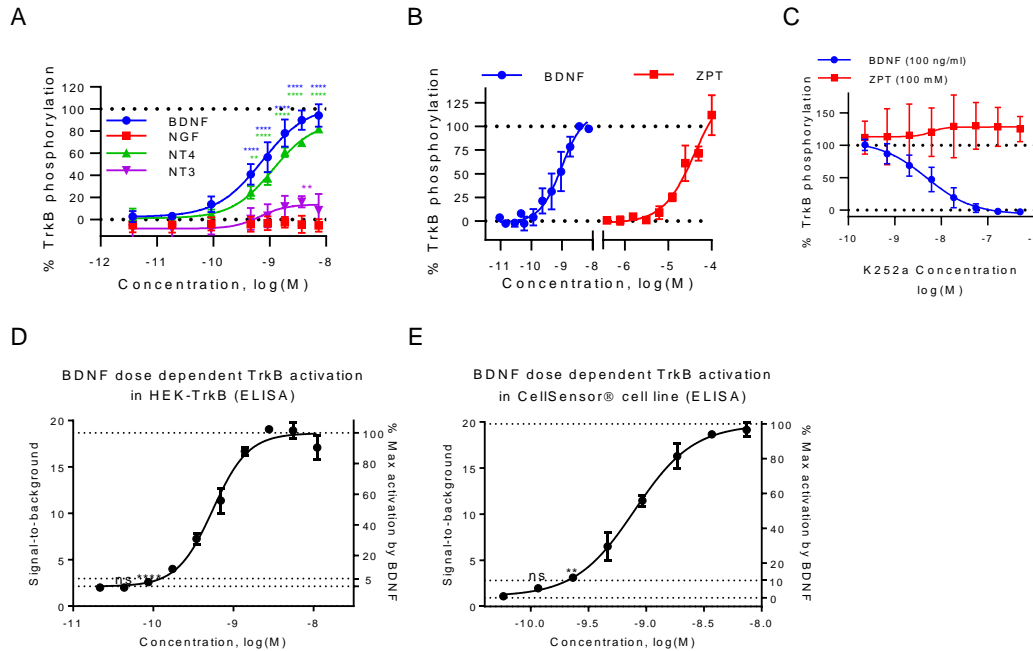


Figure 1.2.9 ELISA characterization in established cell lines

A. Neurotrophin dose response curves measured in CNC using ELISA. BDNF was considered a full agonist of TrkB and all responses were scaled based on the BDNF maximal activation of TrkB. NT4 demonstrated full agonism at TrkB, while NT3 demonstrated partial agonism. NGF did not activate TrkB, as expected. The lowest statistically significant TrkB activation level could be detected at ~20% of BDNF efficacy in CNC. B. Zinc pyrithione (ZPT) induced TrkB phosphorylation measured by ELISA. ZPT was as efficacious as the BDNF-induced response (ZPT EC_{50} 42 μ M). C. K252a inhibition of TrkB phosphorylation induced by BDNF, but not by ZPT (K252a IC_{50} 5 nM). D. BDNF dose response curve measured in HEK-TrkB using ELISA with lowest statistically significant signal at 5% BDNF efficacy. E. BDNF dose response curve was measured in CellSensor CHO using ELISA with lowest significant signal at 10% BDNF efficacy. Data in A-C represent mean \pm SD of 3 independent experiments. Data in D and E represent mean \pm SD of a representative experiment. Two-way ANOVA was used followed by Dunnett's t-test (compared to DMSO): * $p < 0.05$, ** $p < 0.01$, *** $p < 0.001$, **** $p < 0.0001$.

1.2.5 ELFI

Since TrkB activation induces ERK and Akt signaling cascades, it was necessary to develop assay for these signaling molecules as well. As in case with TrkB, phosphorylation of ERK and Akt has been accepted as indication of activation of these molecules. To detect activation of downstream

signaling cascades more reliably an ELFI was developed, similar to the immunofluorescence method, in which fixed cells were incubated with an antibody specific to native and phosphorylated forms of the target proteins (ERK1/2, Akt). The signal was developed through a chemiluminescent reaction of horseradish peroxidase attached to a secondary antibody and enhanced chemiluminescent (ECL) reagent. While ELFI is highly dependent on antibody specificity, as with the western blot assay, the chemiluminescent readout provided a more reliable and reproducible results than densitometric analysis of WB. In other words, ELFI readout could be viewed as integration of the signal from the whole lane in western blot. In order to measure a reliable signal, antibodies had to be highly specific to the target to be able to attribute the difference in signal to target response, as opposed to changes in non-specific target. Thus, there should be few differences between western blot and ELFI in terms of quality of the signal, but robustness and higher throughput of the assay would deem ELFI superior to western blot.

1.2.5.1 Stripping and re-probing

For normalization purposes, a possibility to detach antibodies from their target in fixed cells was explored. This approach would allow the detection of multiple target proteins in the same well, for example, both pERK and pAkt as well as total concentration of these proteins in one well. Stripping and re-probing of the fixed samples were reported for imaging purpose, which suggested feasibility of this approach for ELFI due to similarities to the immunofluorescence method. To this end, a guanidine-based stripping method, which was routinely used in our lab on western blots, was explored. The guanidine solution has unfolded protein, which strips protein of their functional activity, while removing guanidine causes the re-folding of some proteins into their native conformations. Thus, guanidine has acted as mild stripping agent. To test this approach, pERK and pAkt induced by BDNF at different concentrations were detected over six stripping and re-probing cycles in CNC (Figure 1.2.10 A and B). The absolute values fluctuated between cycles, while the relative value remained similar, the later observation being more crucial for quantitative assays. Moreover, stripping and re-probing could also be used for imaging. Staining of β -Tubulin over two cycles did not alter the protein localization, while other targets could be imaged in parallel (Figure 1.2.10C). Thus, stripping and re-probing could be reliably used for detection of ERK and Akt activation as well as other targets if a specific antibody was present.

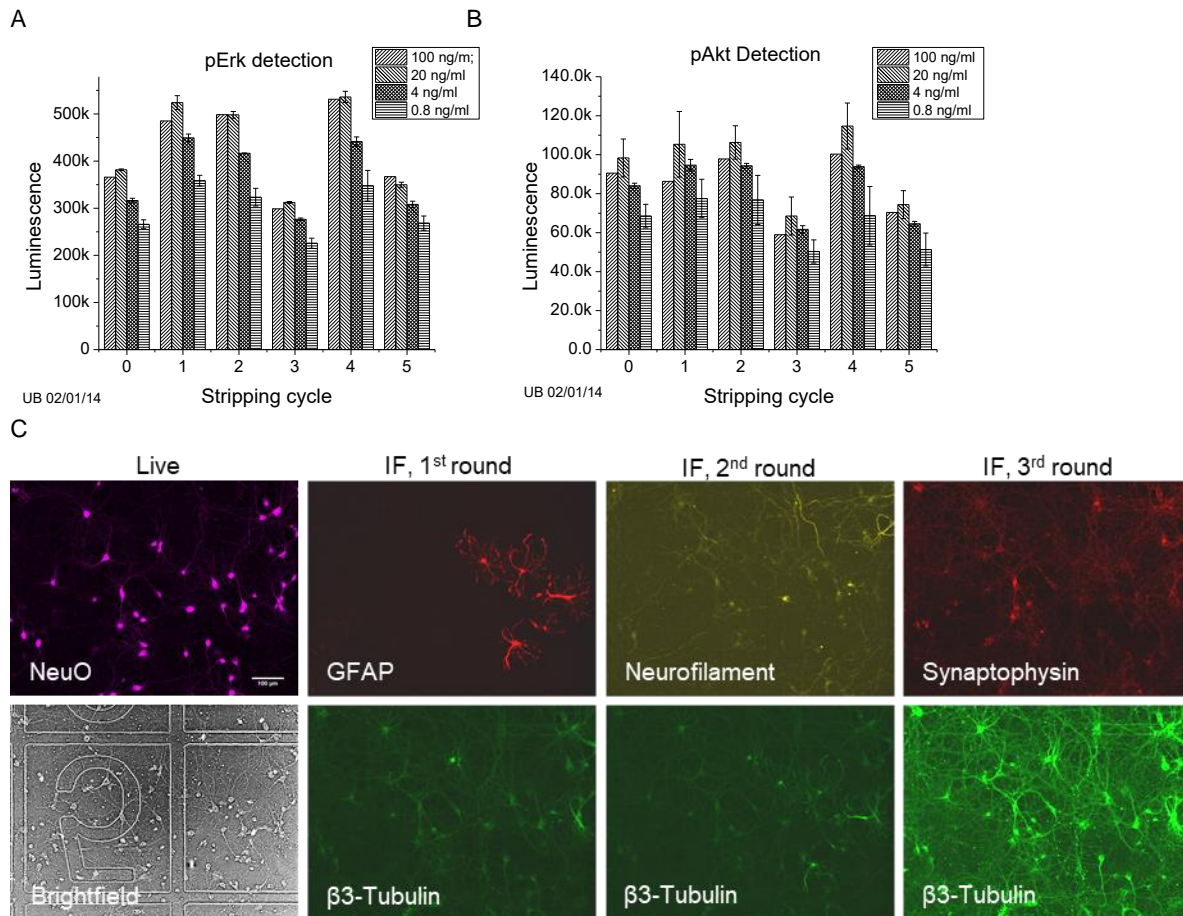


Figure 1.2.10 Stripping and re-probing in ELFI and IF
A-B. BDNF induced ERK (A) and Akt (B) phosphorylation detected in CNC over 6 stripping and re-probing cycles with similar signal ratios. CNC was treated with different concentration of BDNF to test whether stripping and re-probing cycles would alter relative readout of ERK and Akt activation. C. Fixed CNC was characterized with neuronal (NeuO, a neuron specific dye (132), β 3-Tubulin, Neurofilament), astrocytic (GFAP), and synaptic (synaptophysin) markers to check if stripping and re-probing cycles alter protein localization in fixed samples. Stripping and re-probing cycles were performed between immunofluorescent (IF) imaging.

1.2.5.2 ELFI in different cell lines

Similar to ELISA, all established cell lines were tested for ERK and Akt phosphorylation induced by neurotrophins. BDNF and NT4 induced activation of Akt (Figure 1.2.11 A) and ERK (Figure 1.2.11 B) with similar efficacies and potencies (Table 1.1) in CNC. NT3 had lower efficacy at Akt, which is consistent with observed low efficacy of TrkB phosphorylation (Figure 1.2.11 A), however, it induced ERK activation at a level similar to BDNF (Figure 1.2.11 B). The difference in efficacies of ERK and AKT activation could be due to low concentrations of the adaptor proteins, like SOS1, SOS2, and GAB1, which are mediators of the ERK signaling cascades. Under such a scenario, the highest amount of ERK activity may be induced by activation of a fraction of the available receptor pool, as shown previously (133).

When comparing activation of TrkB and downstream signaling proteins, BDNF had a higher potency at ERK and Akt than at TrkB, most likely due to the amplification of downstream signals (Figure 1.2.11 D). This result indicates that a low-level activation of TrkB would be amplified downstream and should be detected in our assays (lower than the statistical threshold of direct TrkB assays above). Interestingly, ZPT activated Akt with much higher efficacy than BDNF (Figure 1.2.11 C) while activating ERK with similar efficacy as compared to BDNF (Figure 1.2.11 C).

To provide more evidence of TrkB dependent ERK and Akt activation, K252a was used. K252a inhibited BDNF activity at downstream targets (Figure 1.2.11 E). To this end, K252a inhibition of ERK phosphorylation induced by BDNF or phorbol 12-myristate 13-acetate (PMA, PKC agonist, which can induce ERK phosphorylation independent from TrkB) was measured. K252a inhibited ERK activation induced by BDNF with IC_{50} at 7.5 nM, while at higher concentration K252a inhibited ERK phosphorylation induced by either ZPT (Zn) or PMA with much lower potency at $IC_{50} = 130$ nM. It was found that higher concentrations of K252a could inhibit PMA-induced ERK phosphorylation, thus allowing only a narrow pharmacological window of TrkB selectivity (Figure 1.2.11 E). When comparing K252 dose inhibition curve at TrkB and ERK downstream amplification effect could be observed, which results in lower K252a potency at ERK (Figure 1.2.11 F). Interestingly, K252a increased phosphorylation level of Akt with EC_{50} similar to IC_{50} at ERK, while at higher concentration at which little pERK could be detected it inhibited Akt phosphorylation, resulting in a bell-shaped dose-response curve. A similar pharmacological response at ERK could be observed in HEK-TrkB (Figure 1.2.11 H).

Signal-to-background ratios of ELFI for CNC were ~ 2–4 and higher for other established cell lines (Figure 1.2.11 G, I, and J). The HEK-TrkB cell line had an S/B for ERK around 13, while for Akt hardly 1.25, possibly due to different basal phosphorylated levels of ERK and Akt in these transfected

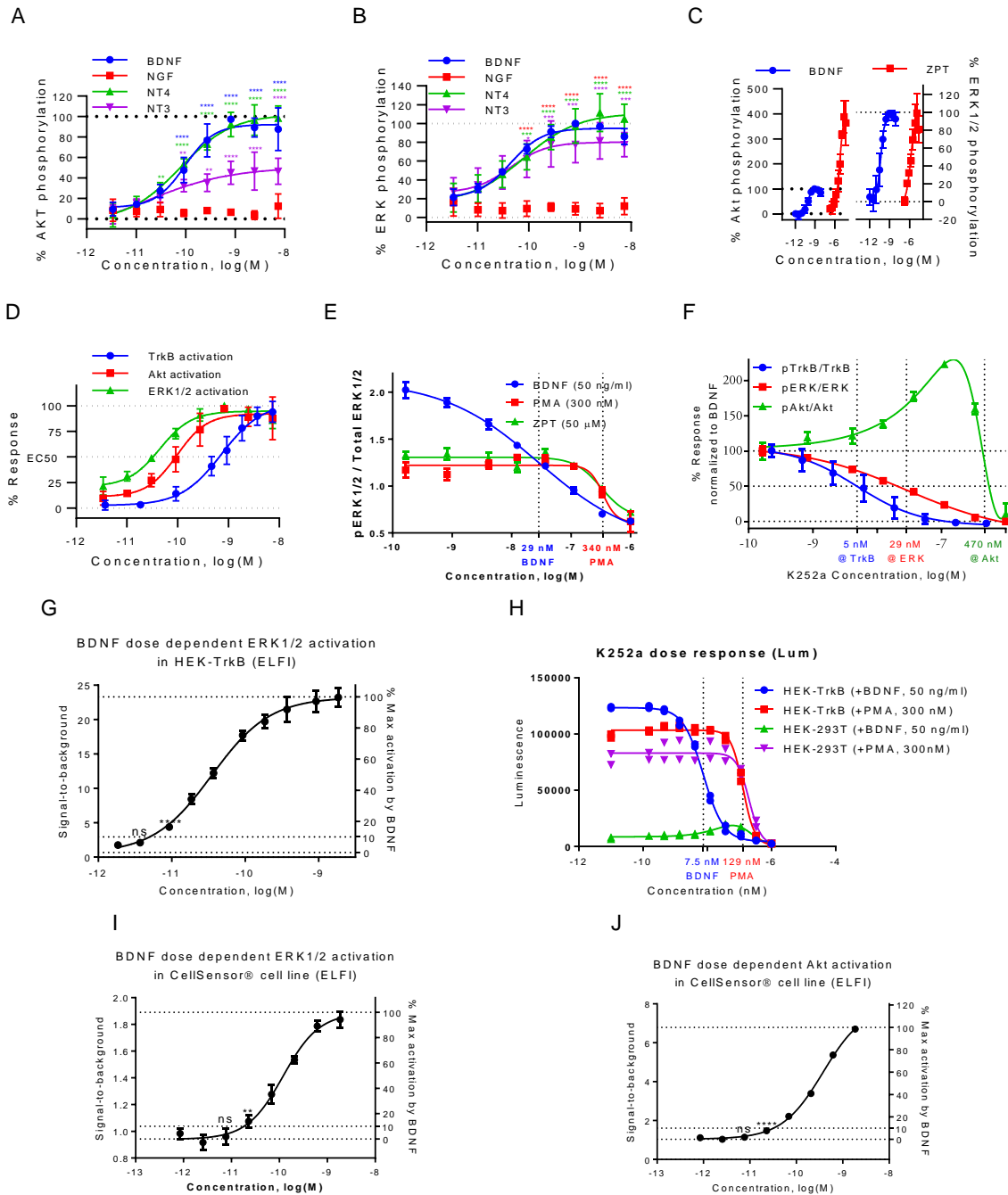


Figure 1.2.11 ELFI in established cell lines

A-B. BDNF, NT4, and NT3 (partial), but not NGF, induced Akt (A) and ERK (B) phosphorylation in CNC (DIV 13) after 1-hour incubation. C. Zn²⁺ induced Akt phosphorylation with 4x higher efficacy than BDNF and ERK phosphorylation at similar level as BDNF (1-hour treatment, CNC DIV14). D. Comparison of the TrkB, Akt, and ERK activation curve induced by BDNF. BDNF displayed higher potency at phosphorylating Akt and ERK than TrkB in CNC (DIV 13) after 1-hour incubation. E. K252a inhibition of BDNF-induced ERK phosphorylation in CNC (DIV 13). Cells were preincubated with K252a for 1 hour followed by 1-hour BDNF treatment. F. Comparison of K252a inhibition curve at TrkB, ERK, and Akt activation induced by BDNF in CNC. K252a inhibited BDNF induced TrkB and ERK activation with lower potency at ERK, while it produced bell-shaped response at Akt. Data of pTrkB inhibition curve represent mean±SD of n=4 independent experiments. G. BDNF dose response curve of ERK phosphorylation measured in HEK-TrkB using ELFI with lowest statistically significant signal at 10% BDNF efficacy. H. K252a dose response curve of ERK inhibition in the presence of BDNF or PMA measured using ELFI in HEK-TrkB and HEK-293T. IC₅₀ at TrkB was 7.5 nM, and IC₅₀ at unidentified kinase was 129 nM. I. BDNF dose

response curve of ERK phosphorylation measured in CellSensor CHO cells using ELFI with lowest statistically significant signal at 10% BDNF efficacy. J. BDNF dose response curve of ERK phosphorylation measured in DiscoverX U2OS-TrkB/p75 cells using ELFI with lowest statistically significant signal at 10% BDNF efficacy. Data in A-D represent mean \pm SD of 3 independent experiments. Data in E-J represent mean \pm SD of a representative experiment. Two-way ANOVA was used followed by Dunnett's t-test (compared to DMSO): * $p < 0.05$, ** $p < 0.01$, *** $p < 0.001$, **** $p < 0.0001$.

cells. CHO-TrkB cells showed an inverse trend with ERK S/B around 2 and Akt S/B closer to 6 (Table 1.2), further suggesting cell line variability.

1.2.6 DiscoverX PathHunter assay and U2OS-TrkB/p75 cell line

Functional activity of TrkB was confirmed in our laboratory by detecting BDNF-induced ERK activation using ELFI, with EC_{50} at 100 ± 100 pM (mean \pm SD, N=4 of independent experiments) in U2OS-TrkB/p75 (Figure 1.2.12A). As the primary screen was conducted at the Broad institute, the PathHunter assay was characterized at the HTS facility. BDNF induced a robust signal in the PathHunter[®] assay in U2OS-TrkB/p75 with EC_{50} 0.37 nM, S/B 5.4 and Z' 0.59; and in U2OS-TrkB with EC_{50} 1.1 nM, S/B 7.2

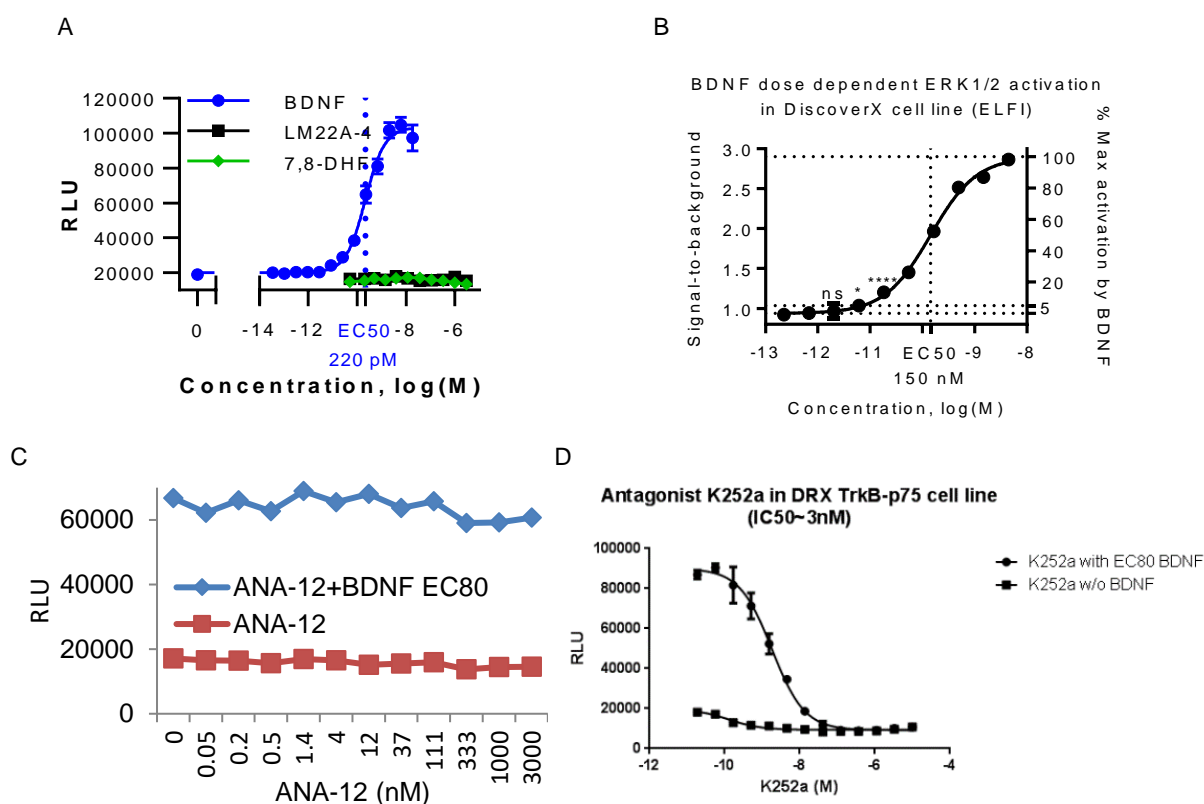


Figure 1.2.12 DiscoverX U2OS-TrkB/p75 cells characterization

A. BDNF and reported agonists tested in the PathHunter[®] assay using U2OS-TrkB/p75 cells. B. BDNF dose response curve of ERK phosphorylation measured in U2OS-TrkB/p75 using ELFI with lowest statistically significant signal at 5% BDNF efficacy. C. ANA-12 activity in PathHunter assay U2OS TrkB-p75 cells. No antagonistic activity was detected. D. K252a tested in PathHunter[®] assay to confirm TrkB dependent activation. Data represents mean \pm SD of a representative experiment. Two-way ANOVA was used followed by Dunnett's t-test (compared to DMSO): * $p < 0.05$, **** $p < 0.0001$.

and Z' 0.59 (using 384 well plate format), acceptable for high throughput screening (Figure 1.2.12A). Interestingly, BDNF EC_{50} measured with PathHunter® assay in U2OS-TrkB is similar to BDNF EC_{50} in CNC measured with ELISA, while EC_{50} in U2OS-TrkB/p75 is 3x lower. Meanwhile, BDNF EC_{50} at ERK in U2OS-TrkB/p75 measured with ELFI was similar to CNC results (Figure 1.2.12B). It was decided to perform the primary screen in the U2OS-TrkB/p75 cell lines to account for possible complex formed between TrkB and p75. To test the assay with small molecules as well as to test whether ELISA and ELFI assays were comparable to PathHunter® assay, reported agonists were tested. LM22a-4 and 7,8-DHF did not evoke any response in this assay (Figure 1.2.12B), confirming our previous ELISA and ELFI results (see Characterization of reported compounds section). ANA-12 also did not antagonize BDNF activity at TrkB (Figure 1.2.12C), while K252a inhibited activation of TrkB by BDNF at EC80 having IC_{50} 3 nM (Figure 1.2.12D), which was consistent with CNC ELISA results.

1.2.7 Invitrogen CellSensor assay and CHO-TrkB cell line

CellSensor was characterized by measuring BDNF and thapsigargin dose response curves (Figure 1.2.13A). Thapsigargin is sarco/endoplasmic reticulum Ca^{2+} ATPase inhibitor, which induces an increase in cytoplasmic Ca^{2+} concentration. BDNF induced β -lactamase expression with EC_{50} 150 ± 50 pM (mean \pm SD, N=7 of independent experiments), S/B >5.8 and $Z' \geq 0.9$, deemed highly feasible for high throughput screening. Thapsigargin with EC_{50} at 230 pM had a more steeper response than BDNF. To confirm functional activity of TrkB in these cell lines, BDNF induced phosphorylation of TrkB, ERK, Akt, and PLC γ at different time points, including the 5 hour-long CellSensor assay treatment time, and were measured using ELISA and ELFI with EC_{50} equal to 1.2 ± 0.4 nM, 0.3 ± 0.2 nM, 0.5 ± 0.3 nM, and 0.6 nM (one experiment was performed on PLC γ activation) respectively (Figure 1.2.13B-E, Figure 1.2.11 I and J). When all signaling levels are compared signal amplification was more evident in this cell line: the more downstream the signaling molecule, the more potent was BDNF response (Figure 1.2.13F). In other words, BDNF EC_{11} at TrkB was equal to EC28 at Akt, EC41 at PLC γ , EC52 at ERK, or EC90 at gene expression level. Thus, the CellSensor assay gave opportunity to record very low levels of TrkB activations that may not be significant in ELISA or ELFI. K252a could inhibit BDNF activity with IC_{50} 114 pM but not that of thapsigargin, which indicated a TrkB-dependent activation of the system (Figure

1.2.19A). Thus, the CellSensor response was in agreement with the ELISA, ELFI, and DiscoverX results provided. This assay gave the opportunity to assess the gene expression signaling level of TrkB activation as well as could be used as a reliable counter screen assay.

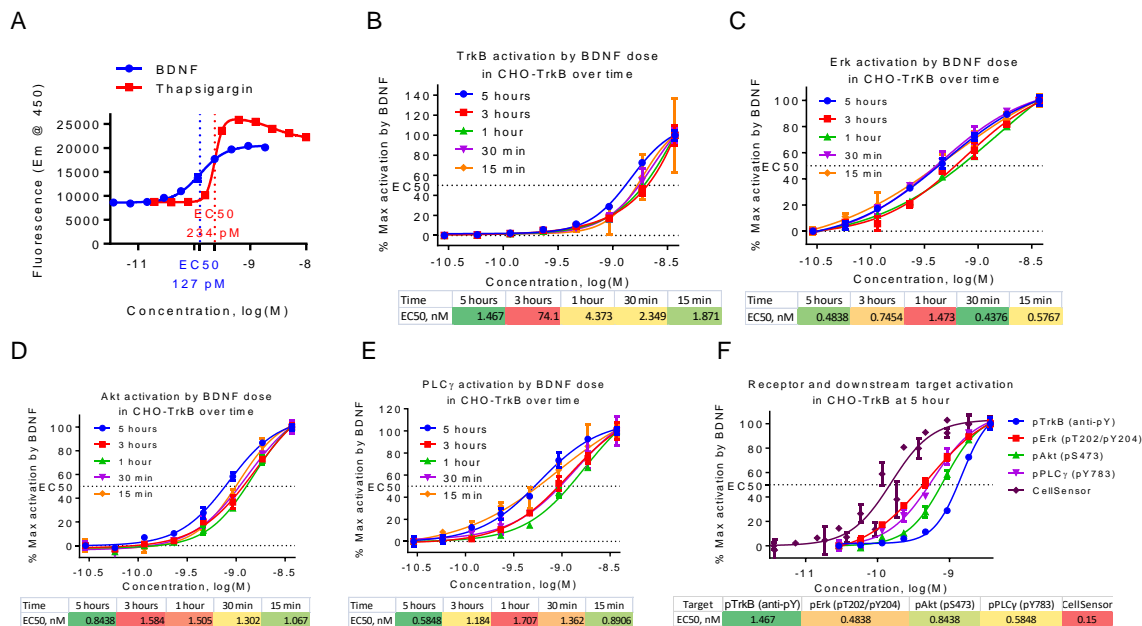


Figure 1.2.13 Invitrogen CellSensor CHO-TrkB cell line characterization

A. Dose response curve of BDNF and thapsigargin measured in the CellSensor assay to characterize the dynamic range and sensitivity. B-E. BDNF dose response curves of TrkB (B), ERK (C), Akt (D), and PLC γ (E) phosphorylation at various treatment times measured using ELISA and ELFI to characterize TrkB activity in Invitrogen CHO-TrkB cells. F. BDNF Dose response curve at different signaling levels put together to compare BDNF potency. Data represents mean \pm SD of N=3 for TrkB, ERK, and Akt, and a representative experiment for pPLC γ . Data of CellSensor represent mean \pm SD of N = 2 independent experiments

1.2.8 Characterization of reported compounds in developed assays

With the validated assays in hand, the reported small molecule agonists of TrkB were tested over a range of different concentrations and treatment times. The prominent reported small molecule agonists, except for DMAQ-B1, did not induce TrkB, AKT or ERK phosphorylation in cortical neuron culture (Figure 1.2.15 A-B), SH-SY5Y

(Figure 1.2.15 J-K), or HEK-TrkB (Figure 1.2.15 F-G) at any time or concentration measured; similarly no response was observed in the CellSensor (Figure 1.2.15I) or DiscoverX assays (Figure 1.2.12B). Most

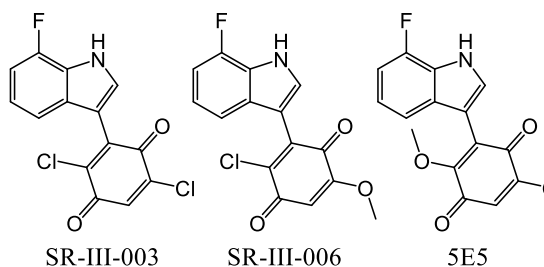


Figure 1.2.14 5E5 and its precursors, SR-III-003, SR-III-006

5E5, a reported TrkA activator. SR-III-003 and SR-III-006, 5E5 precursors

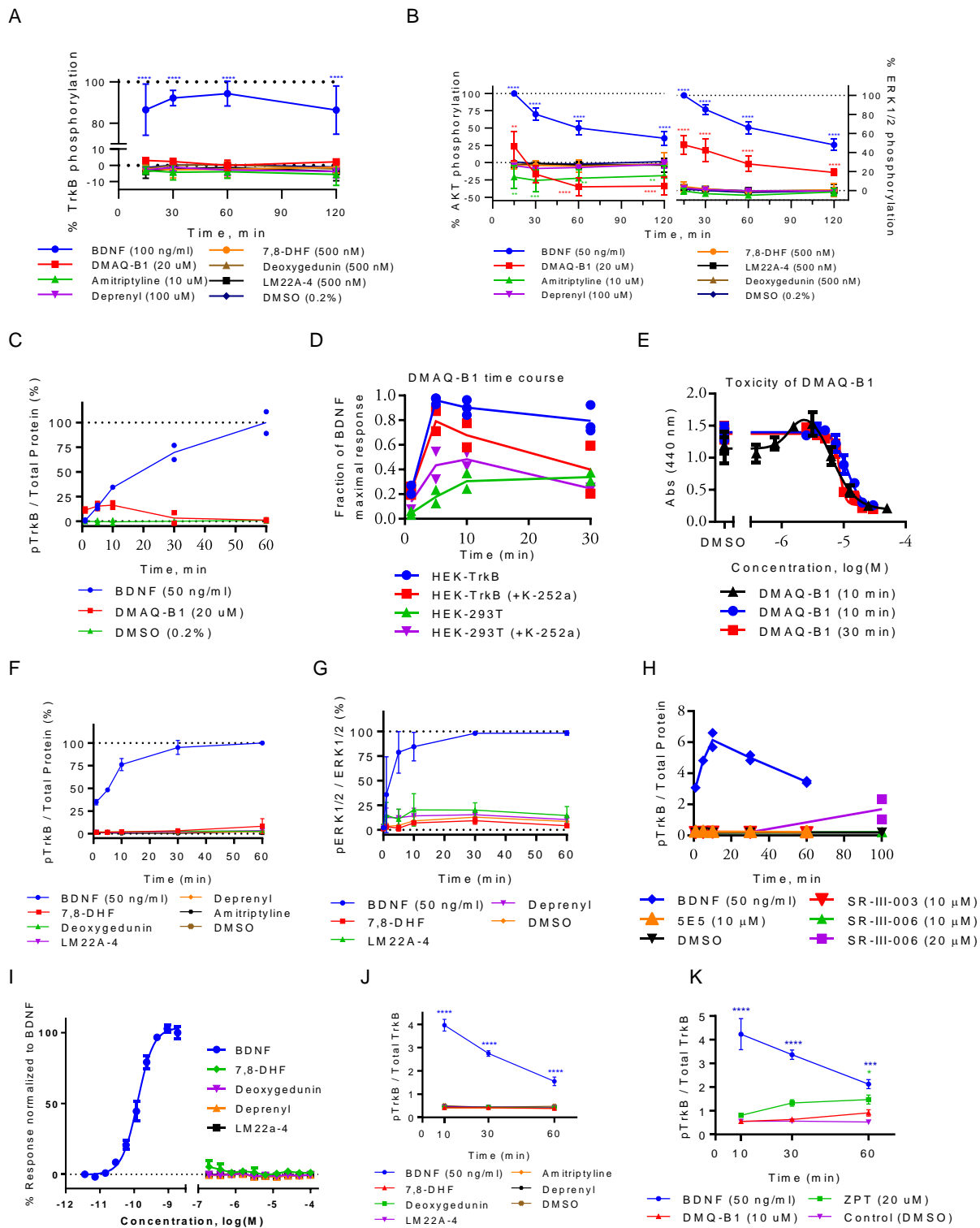


Figure 1.2.15 Reported agonists test results

A. Reported compounds tested at different time points for TrkB phosphorylation in CNC (DIV 15) at the reported concentrations. Reported small molecule agonists showed no activation of TrkB. Data represent mean \pm SD of 3 independent experiments. Two-way ANOVA was used followed by Dunnett's t-test (compared to DMSO): * $p < 0.05$,

p<0.01, *p<0.001, ****p<0.0001. B. Reported small molecule agonists tested for ERK and Akt activation at reported concentrations at different time points (CNC, DIV15). Data represent mean \pm SD of 3 independent experiments. C. Time-course of TrkB phosphorylation in HEK-TrkB upon DMAQ-B1 treatment (sandwich ELISA, data represents 2 independent experiments). D. DMAQ-B1 time course response of ERK activation in HEK-TrkB and HEK-293 in the presence of K252a measured using ELFI. E. Toxicity of DMAQ-B1 in pulse treatment measured in HEK-TrkB cells using WST-1 assay. Cells were treated with DMAQ for 10 or 30 min, then washed and incubated in the serum-free medium for 24 h before WST-1 treatment. F. Time-course of TrkB phosphorylation in HEK-TrkB cells upon compound treatment at 10 μ M measured in sandwich ELISA, data represents mean \pm SD (n=2). G. Time-course of ERK phosphorylation in HEK-TrkB cells upon compound treatment at 10 μ M measured in ELFI, data represents mean \pm SD of 3 independent experiments. H. Time course responses of 5E5 and its precursors induced TrkB activation measured in HEK-TrkB using ELISA. I. BDNF induced expression of β -lactamase in the CellSensor assay while none of the reported agonists could mimic BDNF activity. Data represent mean \pm SD of a representative experiment. Two-way ANOVA was used followed by Dunnett's t-test (compared to DMSO): *p<0.05, **p<0.01, ***p<0.001, ****p<0.0001. J-K. Time-course of TrkB phosphorylation in retinol-differentiated human neuroblastoma SH-SY5Y cells (which express TrkB upon differentiation (134)) when treated with the compounds at 10 μ M measured in sandwich ELISA, data represents mean \pm SD of 3 independent experiments, 2-way ANOVA was used followed by Dunnett's t-test (compared to DMSO): *p <0.05, ***p < 0.001, ****p < 0.0001.

notably, neither 7,8-DHF nor LM22A-4 induced time and/or dose-dependent TrkB, AKT, or ERK activation in any established cell lines in contrast to previously reported data (72, 88).

DMAQ-B1 produced weak positive signals in the assays. Even though no DMAQ-B1 induced TrkB phosphorylation was detected in CNC, downstream signaling activation was detected in cortical neurons (Figure 1.2.15 A-B). DMAQ-B1 induced maximal AKT phosphorylation at 15 min with 20% efficacy, but AKT phosphorylation decayed rapidly, eventually resulting in a lower level of phosphorylated AKT than under basal conditions, which potentially indicated toxicity of the compound. DMAQ-B1 induced maximal ERK phosphorylation at 15 min, as well, with 50% efficacy and showed a similar temporal profile as BDNF. A small amount of TrkB phosphorylation was detected in HEK-TrkB cells (maximal efficacy =16 \pm 2%, Figure 1.2.15C), consistent with the reported data (73). DMAQ-B1 has been reported to induce phosphorylation of all three Trk receptors as well as ERK and AKT kinase. However, activation of ERK and AKT also occurred in the absence of Trk receptors (Figure 1.2.15D). Further, the compound exhibited significant toxicity at concentrations (\geq 20 μ M) that induce Trk receptor phosphorylation (Figure 1.2.15E) (73). Regardless of the mechanism, which is likely complex and confounded by the toxicity, DMAQ-B1 provided additional validation of the assays described in this report by demonstrating the ability to detect low levels of receptor and downstream kinase activation.

Another validation came from the precursor of 5E5, coded as SR-III-006 (Figure 1.2.14). 5E5 has been reported as TrkA activator (135). SR-III-006 produced TrkB phosphorylation at 100 min treatment in

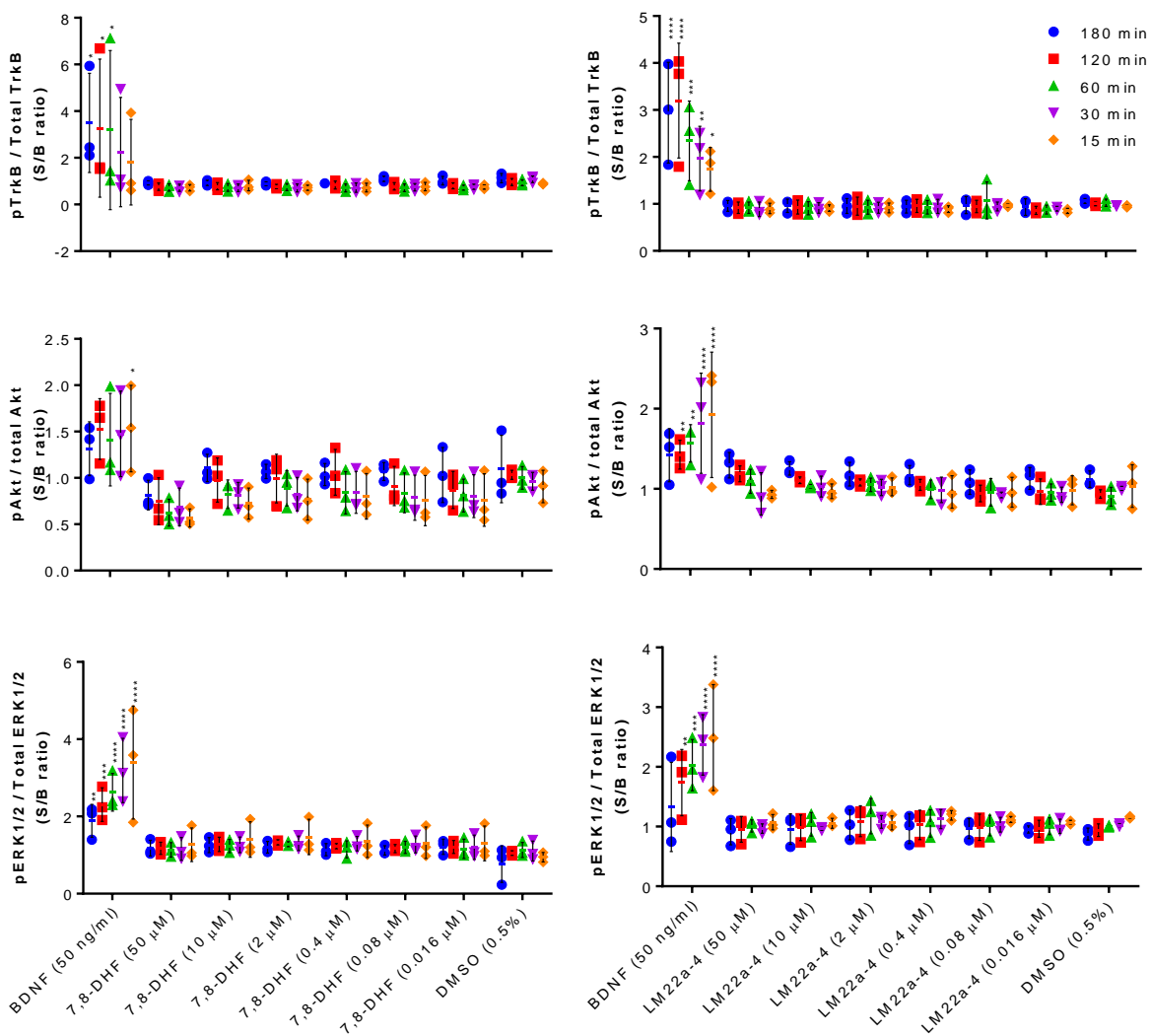


Figure 1.2.16 Activity of 7,8-DHF and LM22a-4 in cortical neuron culture at different conditions

Time-course and dose-response of TrkB, AKT, and ERK1/2 phosphorylation in primary cortical neuron cultures after 13-19 days in vitro (DIV13-19) upon 7,8-DHF and LM22A-4 treatment (Data represents mean \pm SD of 3 independent experiments normalized to average DMSO response, 2-way ANOVA was used followed by Dunnet's t-test (compared to DMSO): * $p < 0.05$, ** $p < 0.01$, **** $p < 0.0001$).

HEK-TrkB (Figure 1.2.15H). However, due to its oxidative properties as well as chemically labile group (chloride on quinone) this compound was not thoroughly characterized.

1.2.9 High throughput screen

Based on these negative results, it was decided to perform a high-throughput screen using a large library of small molecule. To identify possible agonists or modulators of BDNF-induced TrkB activation, we performed a primary screen of 40,000 compounds from the Broad CNS Diversity Oriented

Synthesis (DOS) library. This DOS library contains compounds with CNS drug-like properties, which were selected using *in silico* analysis and *in vitro*, cellular and *in vivo* assays and models (136).

In collaboration with the Broad Institute, it was planned to test each compound for the ability to increase TrkB activation in the absence and presence of BDNF at EC₁₅ using the DiscoverX PathHunter cell system in 384-well format, searching for both TrkB agonists and positive allosteric modulators. The screen consisted of two main stages: primary screen at Broad Institute and counter screen in our laboratory. The first stage further consisted of single point screen with the follow-up retest of compounds in dose response in the DiscoverX PathHunter assay using U2OS-TrkB/p75 cells and counter screen in the U2OS TrkB-null cell line. In the second stage, compounds were tested in a dose-dependent manner in the CellSensor assay and ELISA and ELFI on HEK-TrkB and CNC (Figure 1.2.17). Selection criterion of the hits was a signal higher than 3x the standard deviation of the background (BDNF at EC₁₅ or DMSO).

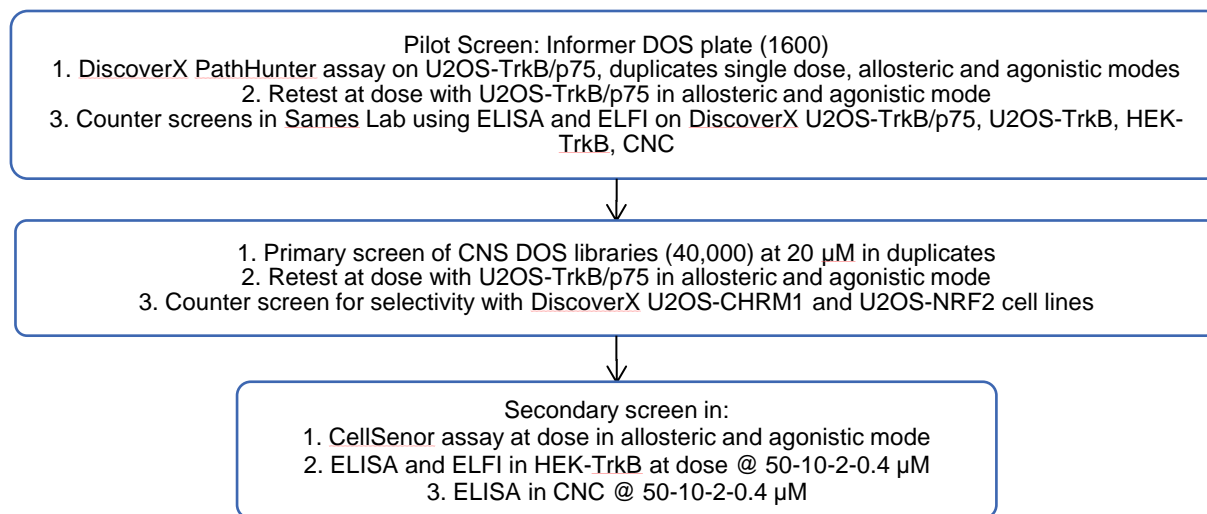


Figure 1.2.17 HTS outline

1.2.9.1 Pilot screen compounds

A pilot screen of 1600 compounds was performed to characterize the HTS assay in the context of compound screening. To this end, five informer DOS plates were used in allosteric and agonistic screen modes as duplicated plates at a 6 µM single dose. As the result, 38 compounds were found to be active in allosteric mode (2.4% hit rate), and 8 compounds were found to be active in agonistic mode of which 7

were also active in allosteric mode. Upon retest in a dose response screen two compounds in agonistic mode and three compounds in allosteric mode demonstrated full activation curves. These compounds and their inactive enantiomers were sent to our lab for further evaluation.

These hit compounds were tested in the DiscoverX U2OS-TrkB/p75 and U2OS-TrkB for ERK and Akt activation in a time-dependent manner at a 10 μ M single dose using ELFI (see Pilot screen in Appendix). Compound K93930139 and K76756739 induced weak activation of ERK and Akt at 10 min treatment, which then declined at later time points in contrast to BDNF-induced activation. Next, these compounds were tested for TrkB activation in HEK-TrkB and CNC, which revealed no activation of the receptor. However, K93930139 and K76756739 induced weak activity at ERK in CNC similar to the DiscoverX cell lines.

1.2.9.2 *Primary screen*

The primary screen of the entire library identified 355 compounds as potential hits based on selection criterion (3x standard deviation above DMSO or BDNF at EC15 response), 192 of which were active in both duplicate plates, while 163 were active in one of them. These compounds were tested in duplicate plates at dose starting at 50 μ M followed with 2x dilution to reach 10 different concentrations. Compounds were identified as hits if the induced responses met selection criteria at a 20 μ M concentration. As the result, 52 allosteric (27% of the primary active hit list) and 29 agonistic hits (23 of which overlap with allosteric hits) were identified. Hits were not potent and contained most of the hits from pilot screen. These identified compounds were counter screened in the DiscoverX PathHunter assay using U2OS-CHRM1 and U2OS-NRF2 cell lines of which 22 compounds were active only at 50 μ M in these cell lines, indicating that these compounds were more active in U2OS-TrkB/p75 cells.

1.2.9.3 *HEK-TrkB screen*

Based on these results 83 compounds were selected for further characterization using the secondary assays in our laboratory. The first batch of 42 compounds were tested in HEK-TrkB for TrkB and ERK activation (see HEK-TrkB screen in Appendix). To test for TrkB activation, ELISA was conducted in agonistic and allosteric mode at four serially diluted concentrations in duplicate with 30 min treatment time. ELFI assays for ERK activation were conducted at four concentrations in quadruplets with 30 min treatment time. Compounds K74587389, K80786583, K74405511 were found to be weak agonists

and active in allosteric mode at TrkB and ERK in initial screen. K61473003 and K21249854 were active only in allosteric mode at TrkB and ERK level. The K32712332, K21471155, and K09140990 activities were inconclusive. The rest of the compounds were not active in HEK-TrkB screen. The eight promising compounds were retested again in HEK-TrkB and CNC for TrkB activation, but their activity was not reproduced (see HEK-TrkB screen on in Appendix).

1.2.9.4 *CellSensor screen*

Upon receiving the second batch of compounds, the entire 83-compound library was tested in the CellSensor assay (Figure 1.2.18). During the first screen cells were treated with compounds at four serially diluted concentrations ranging from 50 μM to 0.4 μM in quadruplet in agonistic and allosteric modes. From the experiments 38 compounds were found to be active and were retested. It was observed that most of the compounds were more active at higher concentrations while at 50 μM many of the compounds precipitated out of solution. Given the sporadic nature of precipitation, some compounds exhibited inconsistent activity at high concentrations. To focus more on higher concentrations and avoid compound precipitation, the retest was conducted under similar conditions at four serially diluted concentrations ranging from 30 μM to 3.25 μM . Out of 83 compounds, 9 compounds were active in agonistic mode in both screens, while 20 compounds exhibited activity in allosteric mode, prompting another round of testing (see CellSensor screen in Appendix).

In the third round, compounds were diluted to yield 8 concentrations ranging from 50 μM to 0.2 μM and were tested in quadruplet in both agonistic and allosteric modes using CellSensor (see CellSensor screen in Appendix). This screen revealed three compounds that were active in allosteric mode, but not as agonists. These compounds were tested in the CellSensor assay for the 4th re-test as well as in ELISA using the same CHO cell line. K54211867 and K30652576 were active at the two highest concentrations (50 and 25 μM) in allosteric mode in both assays. K46962856 was not active in any of the assays (see below).

The remaining 17 compounds of the third round of screening were active in both modes. To verify these results compounds were retested with K252a in agonistic mode to rule out TrkB independent activation of the system, since CellSensor reported TrkB activation at gene expression level (see below), which could also be triggered by other kinases.

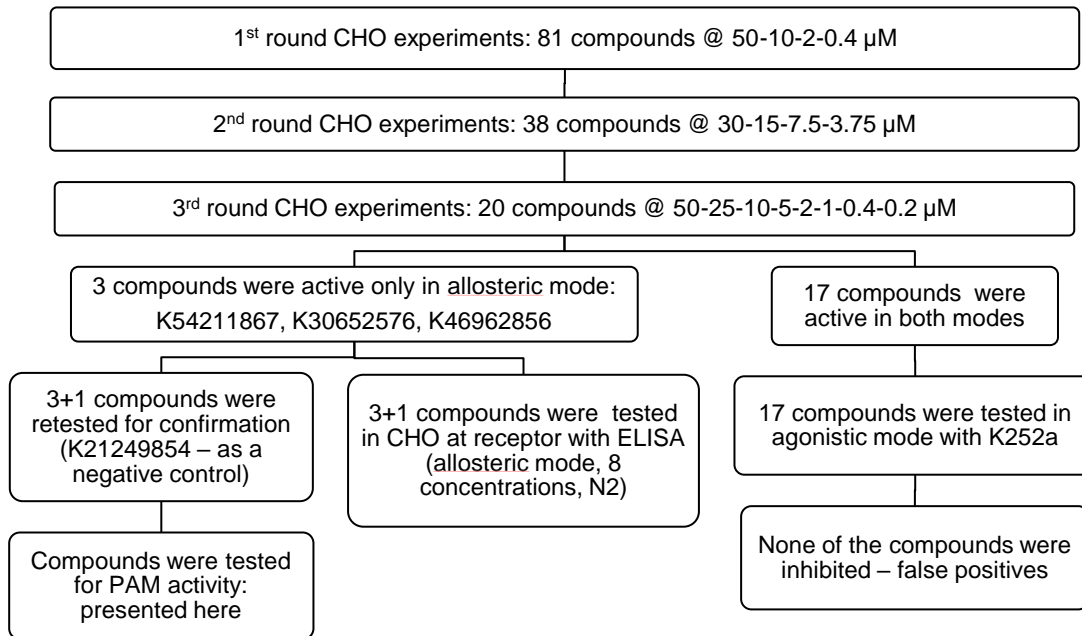


Figure 1.2.18 CellSensor screen outline

1.2.9.4.1 Inhibition screen by K252a.

K252a inhibition in the Invitrogen CHO-TrkB cell line was published (IC_{50} 11 nM(126)) and tested by Dr. Meyers in our group (IC_{50} 35 nM). As it was previously shown in HEK-TrkB and CNC that K252a inhibited TrkB and ERK with a narrow pharmacological window for TrkB selectivity (Figure 1.2.11 H), it was important to test whether K252a was capable of inhibiting TrkB while keeping activity of downstream targets intact. For this purpose, cells were pretreated with K252a 30 min prior to Thapsigargin (10 nM, EC100) or BDNF (50 ng/ml, EC100) treatments (Figure 1.2.19 A). The IC_{50} was 113.5 nM at TrkB, which is 10x higher than reported. One of the probable explanations of the discrepancy with previous results could be the old batch of K252a. For the inhibition screen, IC_{80} of K252a was selected (200 nM). The BDNF (50 ng/ml, EC100) control was inhibited by K252a by 35%-40% (Figure 1.2.19B) in the screened plates.

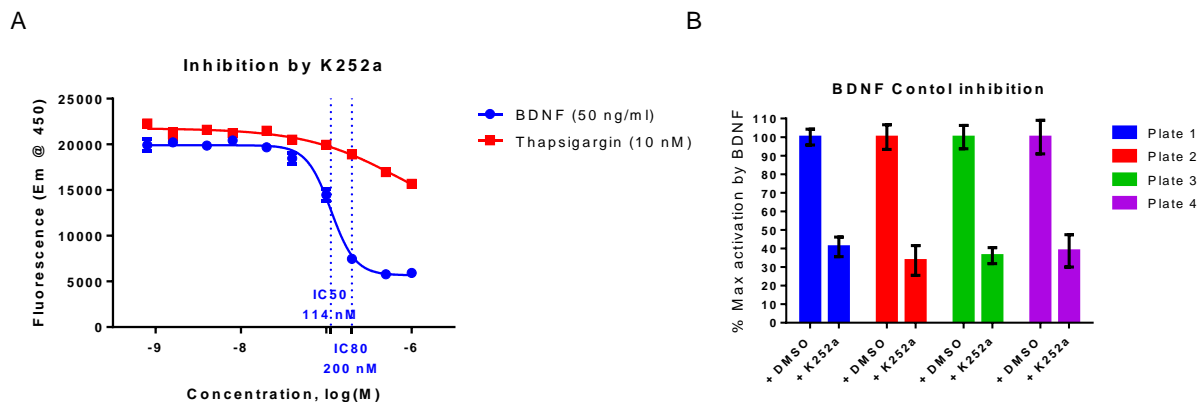
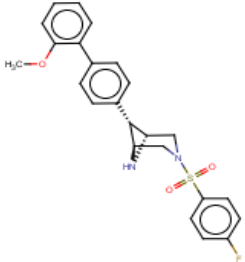
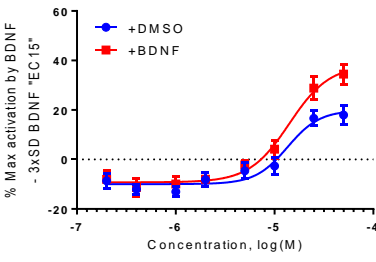
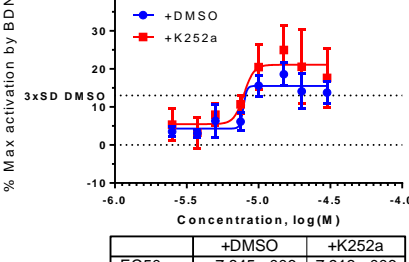
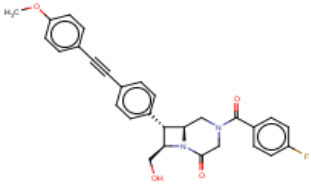
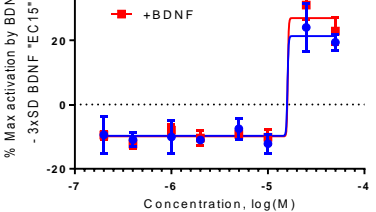
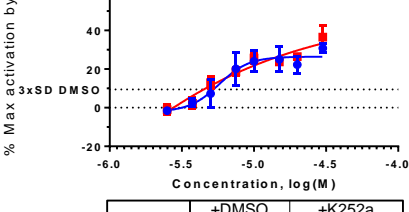
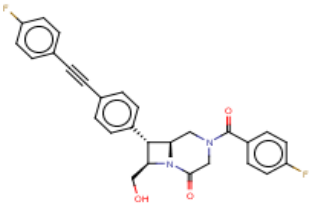
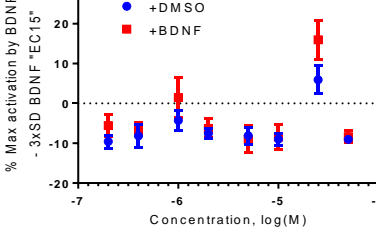
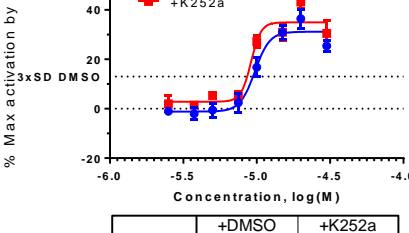
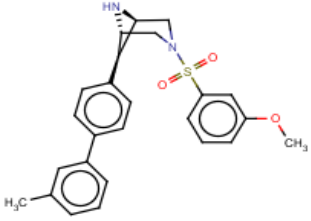
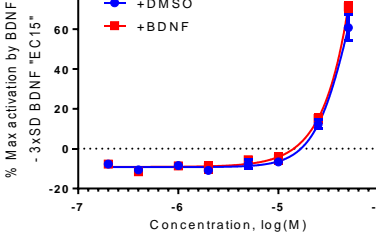
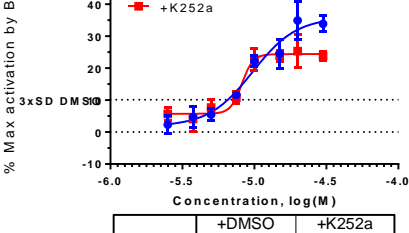
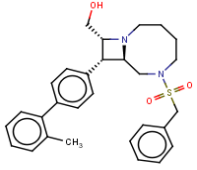
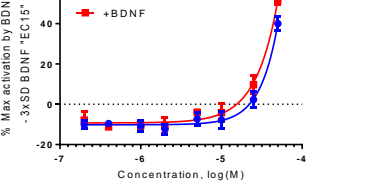
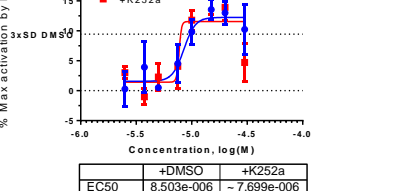


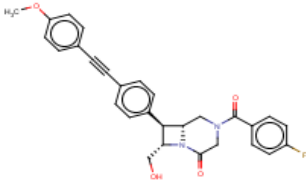
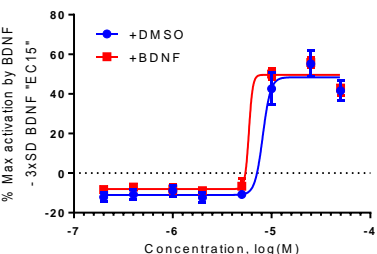
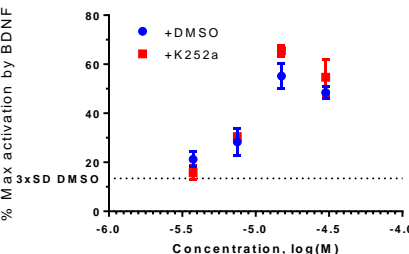
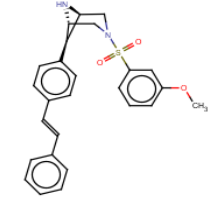
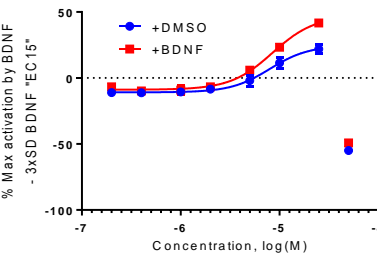
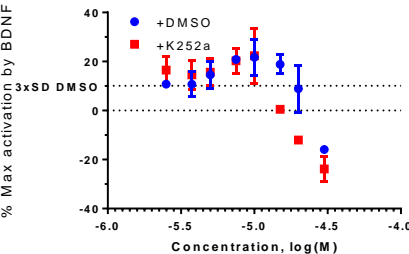
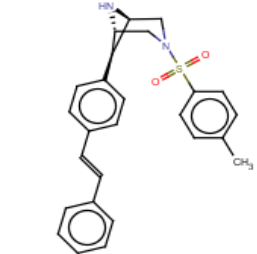
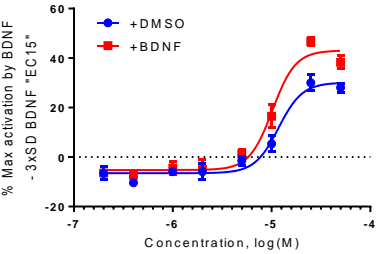
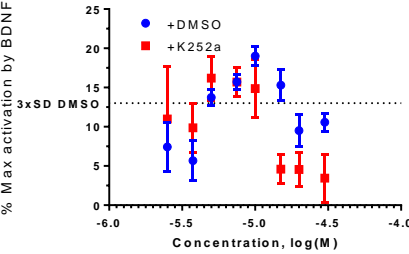
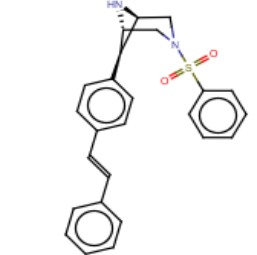
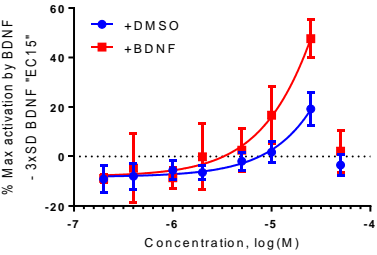
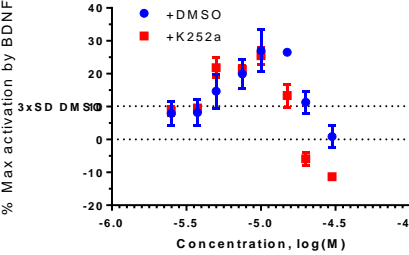
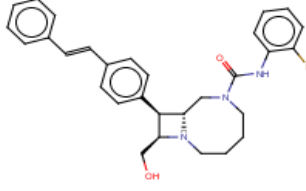
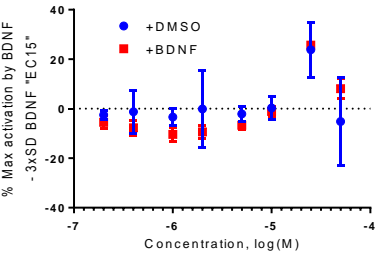
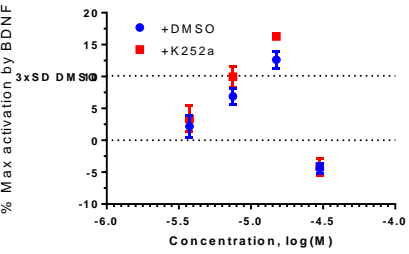
Figure 1.2.19 CellSensor screen with K252a
 A. K252a inhibition curve of BDNF and thapsigargin activity measured by CellSensor to identify IC80 value of K252a to use in the inhibition tests. B. Inhibition control in plates used for inhibition screen with K252a at IC80

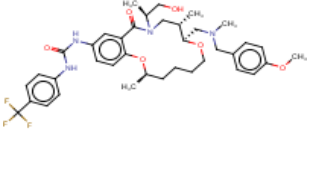
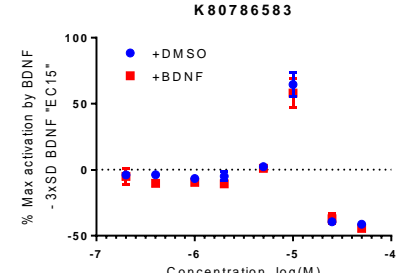
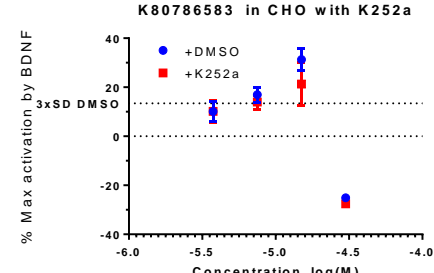
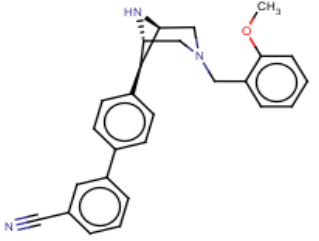
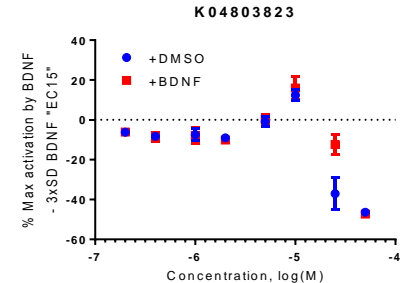
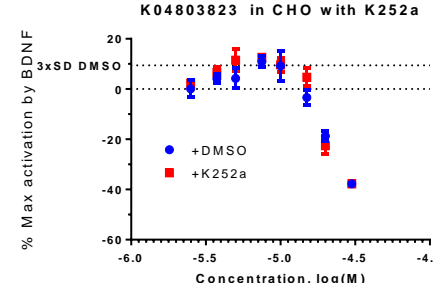
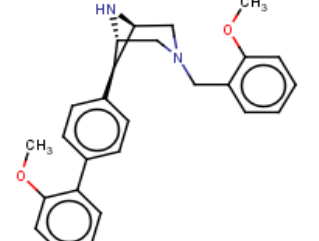
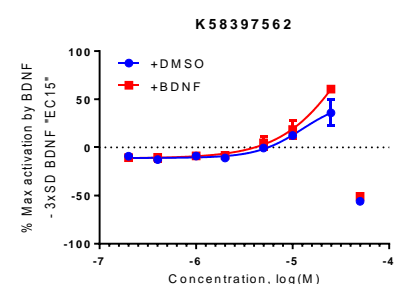
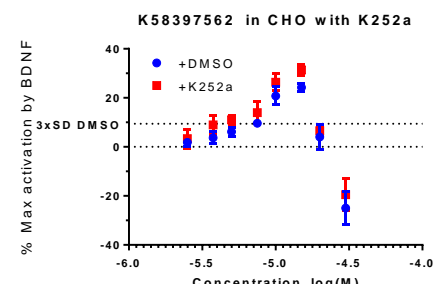
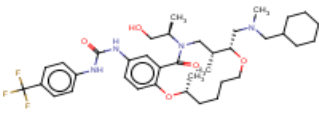
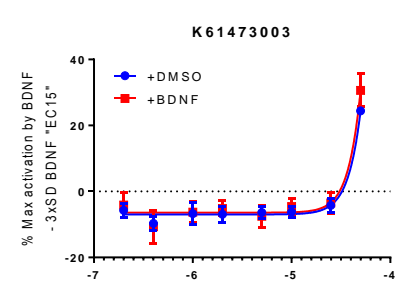
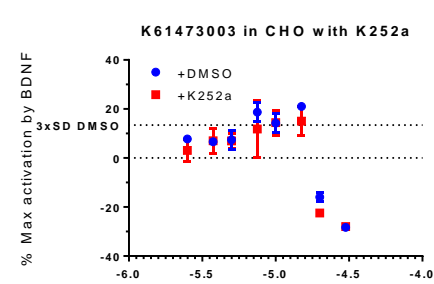
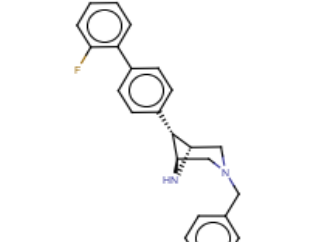
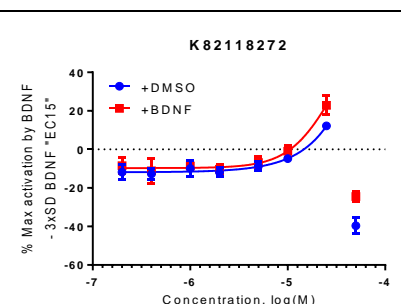
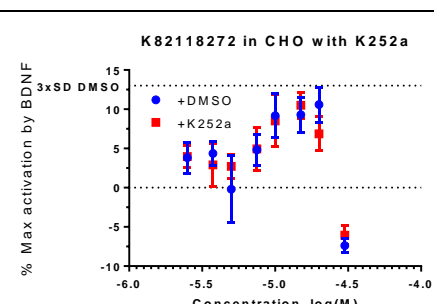
Compounds were used at eight concentrations (30-20-15-10-7.5-5-3.75-2.5 μM) in quadruplet. Some compounds were tested at four concentrations (30-15-7.5-3.75 μM) due to the small amount of material that was available. The results of the screen are presented in Table 1.3.

Table 1.3 CellSensor inhibition screen of 17 hit compounds

Compound and structure	3 rd screening round (agonistic mode)	Inhibition experiments
BRD-K21249854-001-01-8 	K21249854 	K21249854 in CHO with K252a
BRD-K21471155-001-01-4 	K21471155 	K21471155 in CHO with K252a

Compound and structure	3 rd screening round (agonistic mode)	Inhibition experiments						
<p>BRD-K60174045-019-01-2</p> 	<p>K60174045</p> 	<p>K60174045 in CHO with K252a</p>  <table border="1" data-bbox="1149 520 1450 562"> <thead> <tr> <th></th> <th>+DMSO</th> <th>+K252a</th> </tr> </thead> <tbody> <tr> <td>EC50</td> <td>~ 7.845e-006</td> <td>7.913e-006</td> </tr> </tbody> </table>		+DMSO	+K252a	EC50	~ 7.845e-006	7.913e-006
	+DMSO	+K252a						
EC50	~ 7.845e-006	7.913e-006						
<p>BRD-K50330857-001-01-7</p> 	<p>K50330857</p> 	<p>K50330857 in CHO with K252a</p>  <table border="1" data-bbox="1149 867 1450 909"> <thead> <tr> <th></th> <th>+DMSO</th> <th>+K252a</th> </tr> </thead> <tbody> <tr> <td>EC50</td> <td>5.734e-006</td> <td>~ 3.294e-008</td> </tr> </tbody> </table>		+DMSO	+K252a	EC50	5.734e-006	~ 3.294e-008
	+DMSO	+K252a						
EC50	5.734e-006	~ 3.294e-008						
<p>BRD-K10432698-001-01-3</p> 	<p>K10432698</p> 	<p>K10432698 in CHO with K252a</p>  <table border="1" data-bbox="1149 1232 1450 1274"> <thead> <tr> <th></th> <th>+DMSO</th> <th>+K252a</th> </tr> </thead> <tbody> <tr> <td>EC50</td> <td>9.711e-006</td> <td>9.152e-006</td> </tr> </tbody> </table>		+DMSO	+K252a	EC50	9.711e-006	9.152e-006
	+DMSO	+K252a						
EC50	9.711e-006	9.152e-006						
<p>BRD-K70388087-019-01-5</p> 	<p>K70388087</p> 	<p>K70388087 in CHO with K252a</p>  <table border="1" data-bbox="1149 1581 1450 1623"> <thead> <tr> <th></th> <th>+DMSO</th> <th>+K252a</th> </tr> </thead> <tbody> <tr> <td>EC50</td> <td>9.726e-006</td> <td>8.186e-006</td> </tr> </tbody> </table>		+DMSO	+K252a	EC50	9.726e-006	8.186e-006
	+DMSO	+K252a						
EC50	9.726e-006	8.186e-006						
<p>BRD-K02764896-019-01-1</p> 	<p>K02764896</p> 	<p>K02764896 in CHO with K252a</p>  <table border="1" data-bbox="1125 1864 1352 1896"> <thead> <tr> <th></th> <th>+DMSO</th> <th>+K252a</th> </tr> </thead> <tbody> <tr> <td>EC50</td> <td>8.503e-006</td> <td>~ 7.699e-006</td> </tr> </tbody> </table>		+DMSO	+K252a	EC50	8.503e-006	~ 7.699e-006
	+DMSO	+K252a						
EC50	8.503e-006	~ 7.699e-006						

Compound and structure	3 rd screening round (agonistic mode)	Inhibition experiments
<p>BRD-K32712332-001-01-4</p> 	<p>K32712332</p> 	<p>K32712332 in CHO with K252a</p> 
<p>BRD-K50931717-019-01-4</p> 	<p>K50931717</p> 	<p>K50931717 in CHO with K252a</p> 
<p>BRD-K53212675-019-01-6</p> 	<p>K53212675</p> 	<p>K53212675 in CHO with K252a</p> 
<p>BRD-K27145031-019-01-0</p> 	<p>K27145031</p> 	<p>K27145031 in CHO with K252a</p> 
<p>BRD-K75724375-001-01-5</p> 	<p>K75724375</p> 	<p>k75724375 in CHO with K252a</p> 

Compound and structure	3 rd screening round (agonistic mode)	Inhibition experiments
<p>BRD-K80786583-001-02-3</p> 	<p>K80786583</p> 	<p>K80786583 in CHO with K252a</p> 
<p>BRD-K04803823-019-01-3</p> 	<p>K04803823</p> 	<p>K04803823 in CHO with K252a</p> 
<p>BRD-K58397562-019-01-6</p> 	<p>K58397562</p> 	<p>K58397562 in CHO with K252a</p> 
<p>BRD-K61473003-001-01-5</p> 	<p>K61473003</p> 	<p>K61473003 in CHO with K252a</p> 
<p>BRD-K82118272-019-01-7</p> 	<p>K82118272</p> 	<p>K82118272 in CHO with K252a</p> 

None of the compounds were inhibited by K252a. These results indicated that none of the compounds agonized TrkB. Probably, these compounds induced the increase of cytosolic calcium which led to the expression of β -lactamase in CHO cells independently from TrkB.

1.2.9.5 CNC screen

All the 83 compounds were also screened in CNC for TrkB activation under the same condition as the CellSensor screen. Each compound was tested at four concentrations prepared by 5x serial dilution in quadruplet for 1h treatment in both agonistic and allosteric mode (see CNC screen in Appendix). Most of the compounds did not satisfy the selection criterion in CNC screen, however 19 compounds exhibited an upward trend at higher concentrations in allosteric mode. Hits found in the CHO screen (20 compounds) also contained 14 of these compounds. These 19 compounds were retested in CNC more thoroughly. To this end, compounds were tested at eight concentrations ranging from 50 μ M to

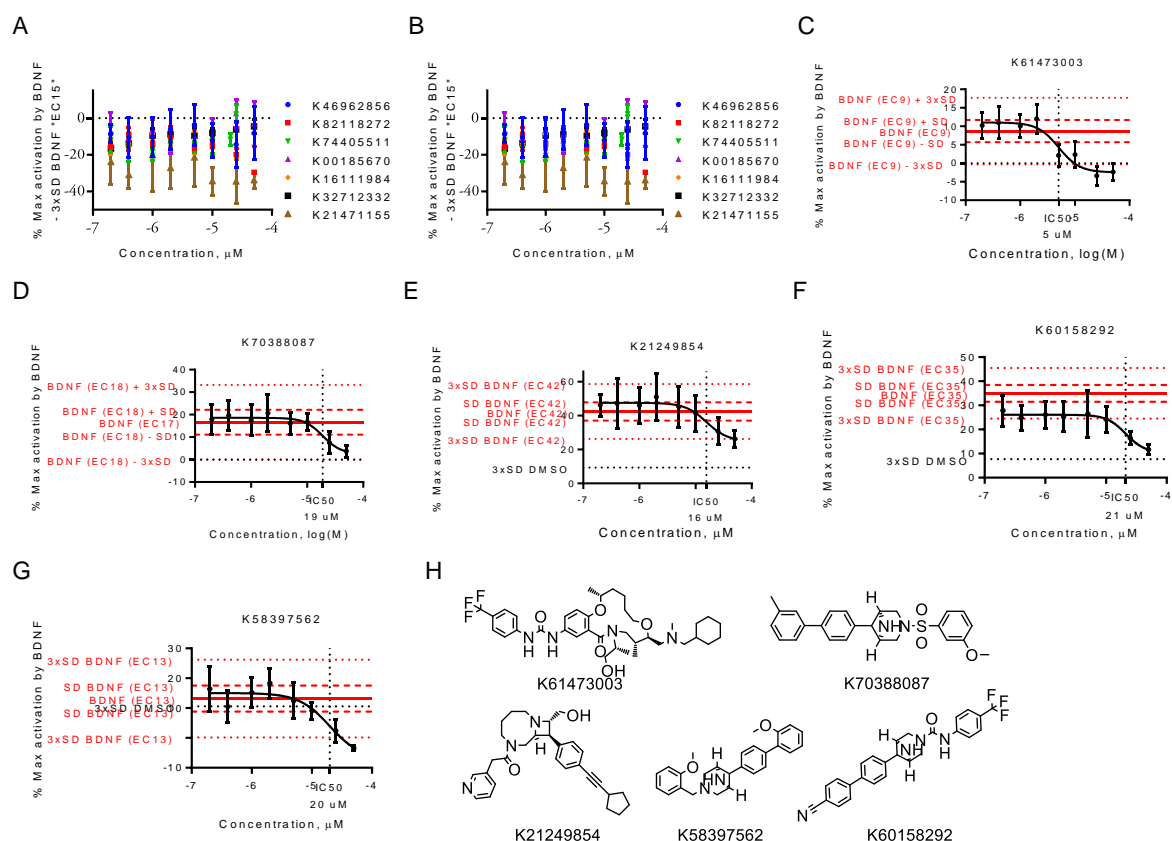


Figure 1.2.20 Retest of selected compounds in CNC

A-B. Compounds selected from CNC screen retested for TrkB activation in CNC in allosteric mode, 14 out of 19 compounds presented. C-G. Remaining compounds' inhibition curves of TrkB activation by BDNF; 5 compounds were measured in CNC in allosteric mode. IC₅₀ values are presented in the x-axis. H. Structure of the 5 compounds with inhibition activity. Data represents mean \pm SD of a representative experiment.

0.2 μ M in allosteric mode. None of the compounds exhibited any statistically significant activation of the receptor.

On the other end, five compounds exhibited inhibition activity at TrkB (Figure 1.2.20 C-H). The most potent compound, K61473003, inhibited TrkB phosphorylation in CNC with IC_{50} at 5 μ M. However, this compound did not induce any activity (agonistic, or antagonistic) in HEK-TrkB cells at TrkB or ERK, while in the CellSensor assay, it produced significant activation signal in allosteric mode at 10 μ M and was toxic at 50 μ M. Similar discrepancies could be observed for other compounds, so further characterization was not pursued.

1.2.9.6 *Allosteric hits*

Based on the 3rd round of the CellSensor screening, three compounds were active in allosteric, but not in agonistic mode. These compounds were retested for the 4th round. As these compounds were active in allosteric mode, TrkB inhibition experiments would not be useful to determine whether these compounds were directly activating TrkB. In order to detect TrkB activation at the receptor level ELISA was conducted on CellSensor CHO-TrkB cells in allosteric mode at eight concentrations with 1h treatment time. Allosterically active compounds had 6% activation over basal level activity in the CellSensor assay. Since ELISA on CellSensor CHO-TrkB proved to be sensitive with a S/B = 10, it provided an opportunity to measure low levels of TrkB activations.

An important aspect of the allosteric mode was BDNF concentration. BDNF concentrations in the CellSensor assays used for allosteric mode would correspond to EC 0.3 level in CHO-TrkB ELISA experiments. This low concentration of BDNF produced $3xSD \leq 2\%$, which was not significantly different from DMSO signal. Having these low ECs was beneficial for allosteric experiments as the smaller SD could help detect weak signals. For example, BDNF at EC31 with $3xSD = 24\%$ the significant signal of the compound would be at 55% of TrkB activation, while at EC2.5 with $3xSD 8.7\%$ it would be at 11% (see Figure 1.2.21 A) in CellSensor assay, which produces a larger dynamic range to detect significant activation of TrkB. This relation could be easily explained if one analyzes the dose dependent activation of the system by BDNF. BDNF at 3.5 ± 0.5 ng/ml yields in $28 \pm 5\%$ activation, while BDNF at 1 ± 0.5 ng/ml yields in $8 \pm 2\%$. Thus, $3xSD$ values were 15% and 6% respectively (see Figure 1.2.21B). The later $3xSD$

is smaller, which lowers the cut-off value, and allows identification of possible weaker compounds. In other words, small variations in BDNF concentrations at higher levels resulted in noisier results.

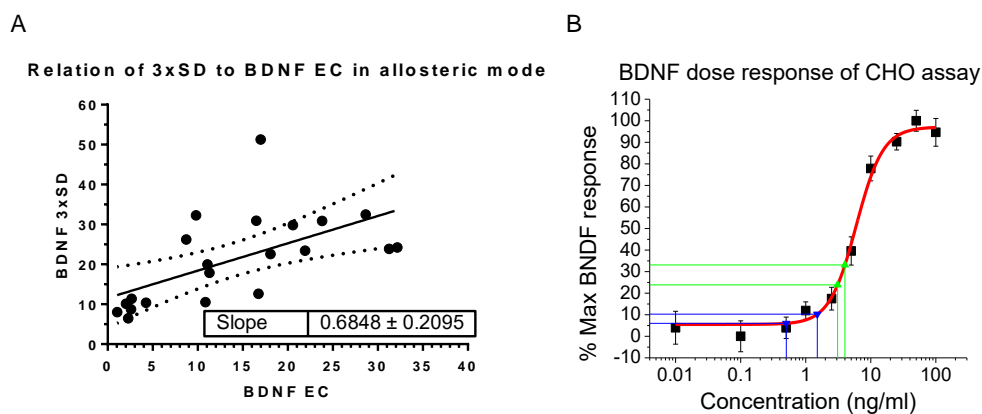


Figure 1.2.21 Signal variation and BDNF concentration relationship in allosteric mode
A. Relation between 3xSD threshold of BDNF and BDNF EC. 3xSD linearly increases with the increase of the EC (solid line represents fitted line function, dashed curve represents 95% confidence band). Data gathered from 21 experiments in CHO Invitrogen assay. B. BDNF at 3.5 ± 0.5 ng/ml yields in $28 \pm 5\%$ activation (green line), while BDNF at 1 ± 0.5 ng/ml yields in $8 \pm 2\%$ (blue line)

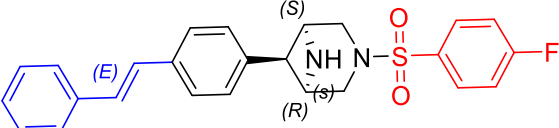
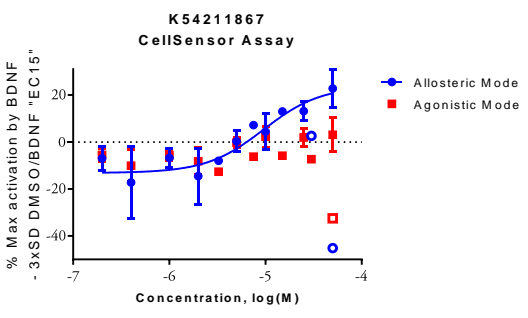
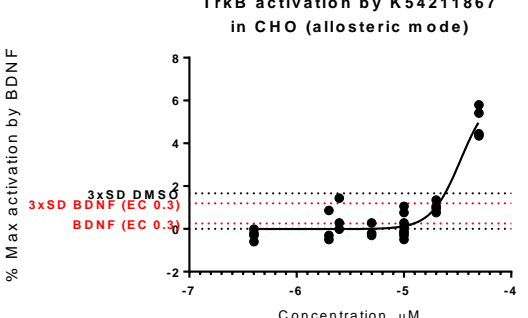
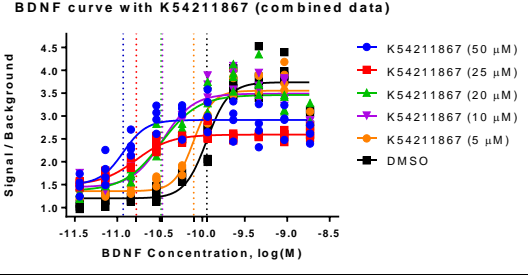
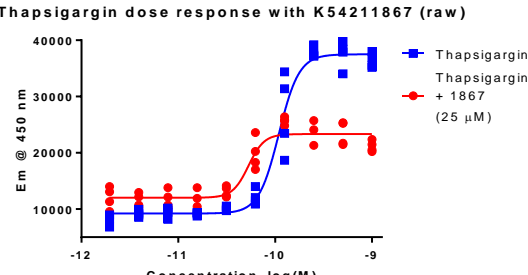
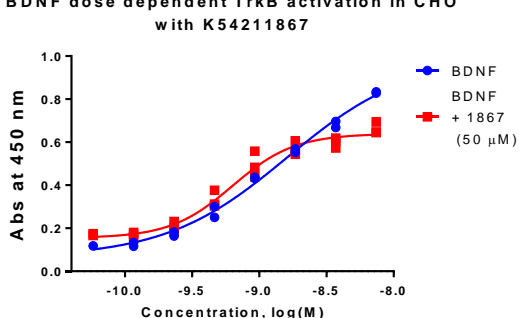
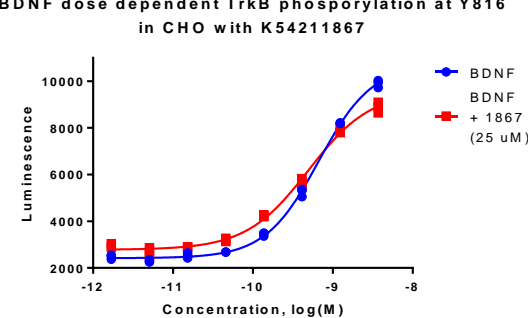
Since allosteric modulators influenced the response of the receptor to its ligand, these molecules at active concentrations should be able to influence the dose-response curve of BDNF. To demonstrate this, the BDNF dose response curve was measured in the presence of hit compounds at active concentrations. Selected compounds at different concentrations were added to cells prior to treating them with BDNF. Using CellSensor, ELISA, and ELFI assays on CellSensor CHO-TrkB, HEK-TrkB, and CNC cells, BDNF dose response curves were measured for TrkB, Akt, and ERK activation, as well as reporter gene expression. As a control in the CellSensor assay, a dose response curve of thapsigargin in the presence of the compounds was also measured.

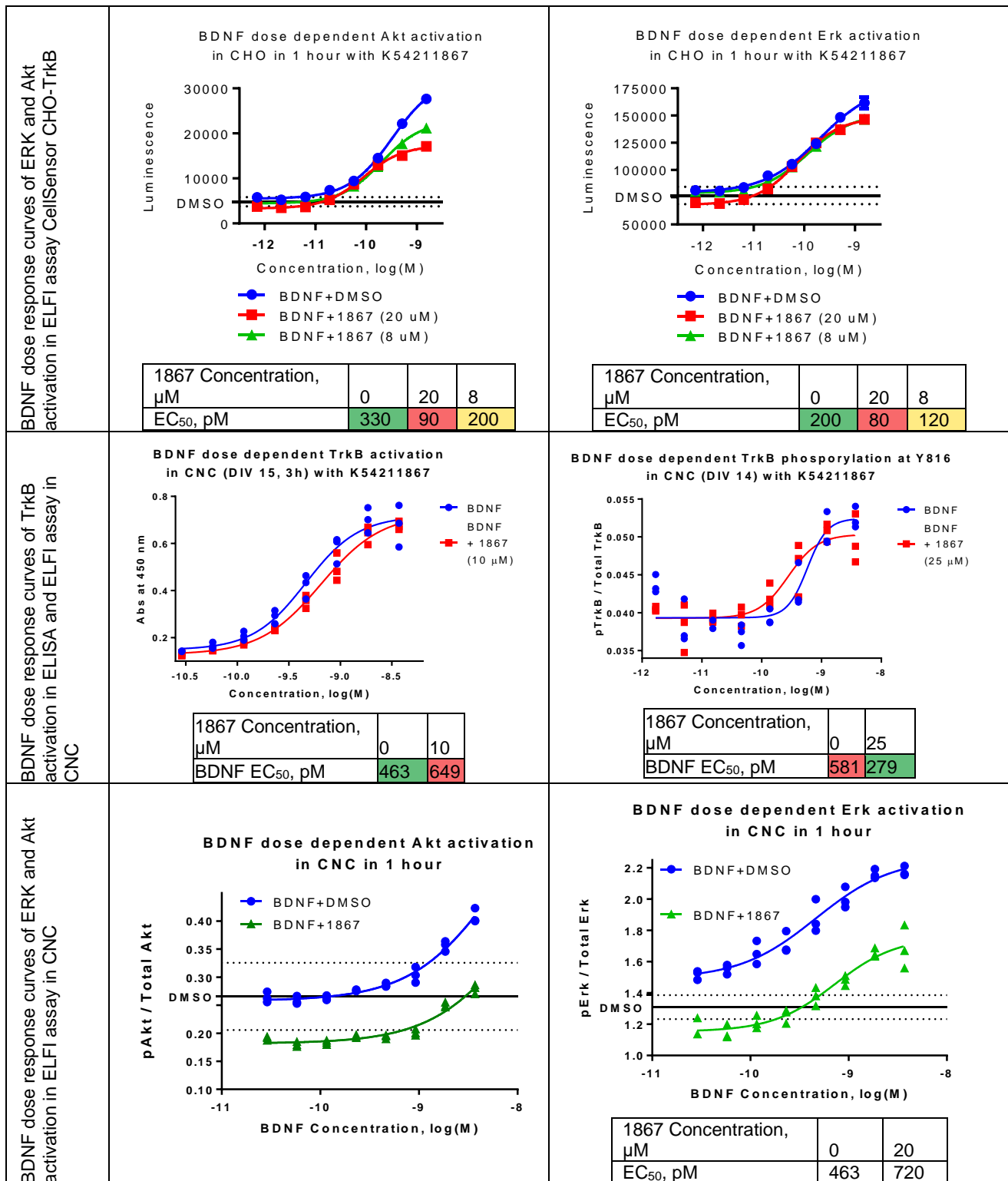
1.2.9.6.1 BRD-K54211867-019-01-5

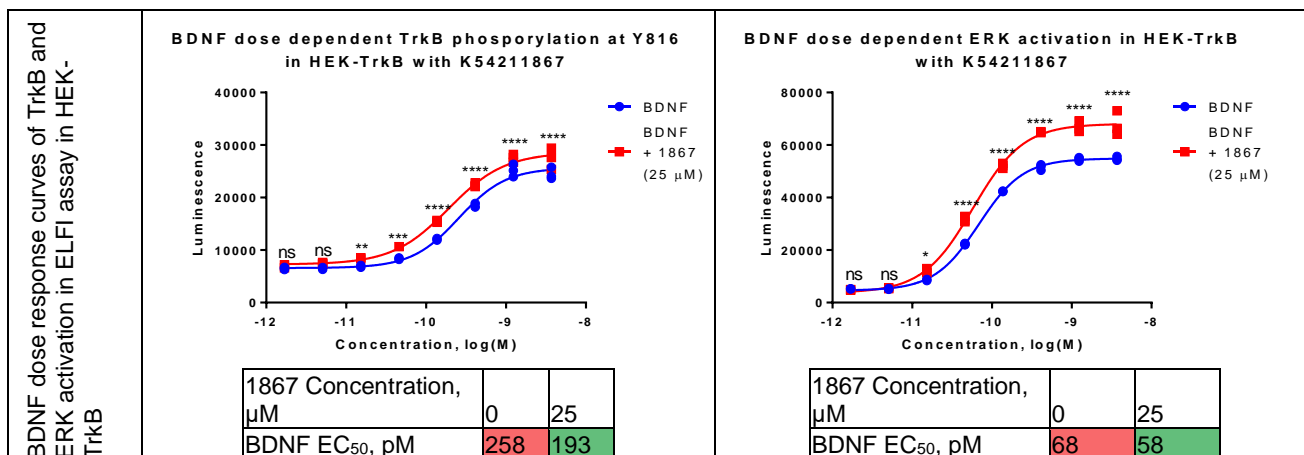
All the experimental results are presented in Table 1.4. In the CellSensor assay, K54211867 potentiated BDNF in a dose-dependent manner, with 10x decrease of BDNF EC₅₀ at a 50 μ M concentration. However, higher concentrations of the compound decreased efficacy of BDNF. At 50 μ M, K54211867 did not potentiate thapsigargin as much, however it did lower the efficacy of thapsigargin similar to BDNF response. At the TrkB, ERK, and Akt levels in CHO, HEK-TrkB, and CNC cells, K54211867 had no significant influence on BDNF EC₅₀ values. At the Akt level in CHO efficacy of BDNF

was reduced by the compound, while at ERK level in HEK-TrkB an increase in efficacy of BDNF could be observed.

Table 1.4 K54211867 characterization as allosteric agonist

Compound structure																						
K54211867 dose response curve in CellSensor and ELISA	<p>K54211867 CellSensor Assay</p> 	<p>TrkB activation by K54211867 in CHO (allosteric mode)</p> 																				
BDNF and thapsigargin dose response curves in CellSensor assay	<p>BDNF curve with K54211867 (combined data)</p>  <table border="1" data-bbox="337 1165 878 1283"> <tr> <td>K54211867 Concentration, μM</td> <td>50</td> <td>25</td> <td>20</td> <td>10</td> <td>5</td> <td>0</td> </tr> <tr> <td>BDNF EC₅₀, pM</td> <td>18</td> <td>28</td> <td>65</td> <td>72</td> <td>125</td> <td>170</td> </tr> </table>	K54211867 Concentration, μM	50	25	20	10	5	0	BDNF EC ₅₀ , pM	18	28	65	72	125	170	<p>Thapsigargin dose response with K54211867 (raw)</p>  <table border="1" data-bbox="938 1186 1398 1283"> <tr> <td>K54211867 Concentration, μM</td> <td>0</td> <td>25</td> </tr> <tr> <td>Thapsigargin EC₅₀, pM</td> <td>53</td> <td>109</td> </tr> </table>	K54211867 Concentration, μM	0	25	Thapsigargin EC ₅₀ , pM	53	109
K54211867 Concentration, μM	50	25	20	10	5	0																
BDNF EC ₅₀ , pM	18	28	65	72	125	170																
K54211867 Concentration, μM	0	25																				
Thapsigargin EC ₅₀ , pM	53	109																				
BDNF dose response curves of TrkB activation in ELISA and ELFI assay in CellSensor CHO-TrkB	<p>BDNF dose dependent TrkB activation in CHO with K54211867</p>  <table border="1" data-bbox="423 1648 792 1734"> <tr> <td>1867 Concentration, μM</td> <td>0</td> <td>50</td> </tr> <tr> <td>BDNF EC₅₀, pM</td> <td>1611</td> <td>630</td> </tr> </table>	1867 Concentration, μM	0	50	BDNF EC ₅₀ , pM	1611	630	<p>BDNF dose dependent TrkB phosphorylation at Y816 in CHO with K54211867</p>  <table border="1" data-bbox="906 1648 1317 1734"> <tr> <td>1867 Concentration, μM</td> <td>0</td> <td>25</td> </tr> <tr> <td>BDNF EC₅₀, pM</td> <td>668</td> <td>495</td> </tr> </table>	1867 Concentration, μM	0	25	BDNF EC ₅₀ , pM	668	495								
1867 Concentration, μM	0	50																				
BDNF EC ₅₀ , pM	1611	630																				
1867 Concentration, μM	0	25																				
BDNF EC ₅₀ , pM	668	495																				

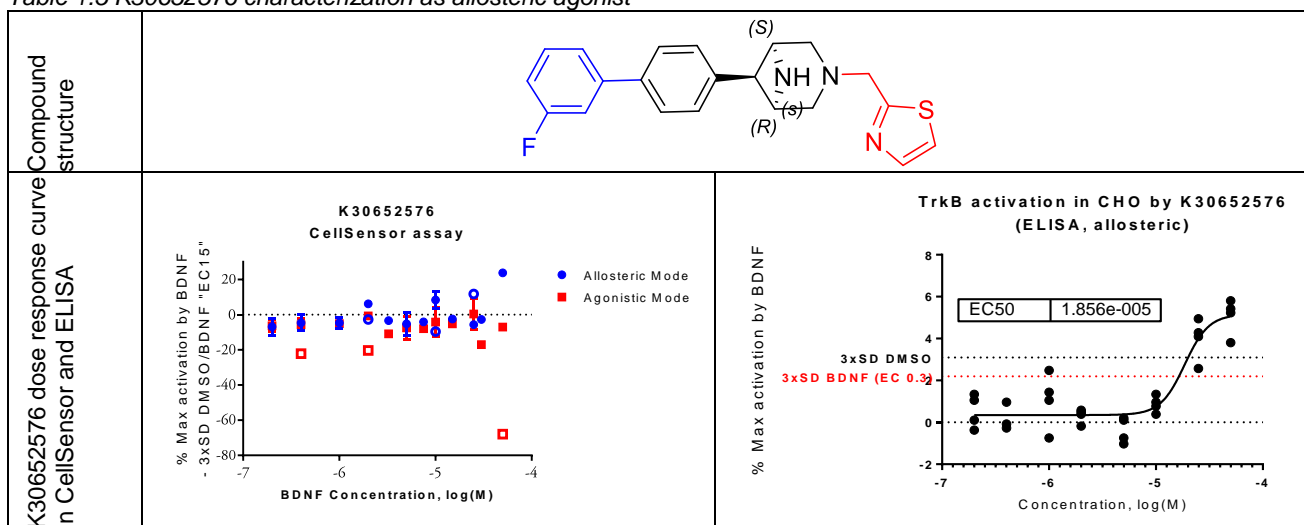


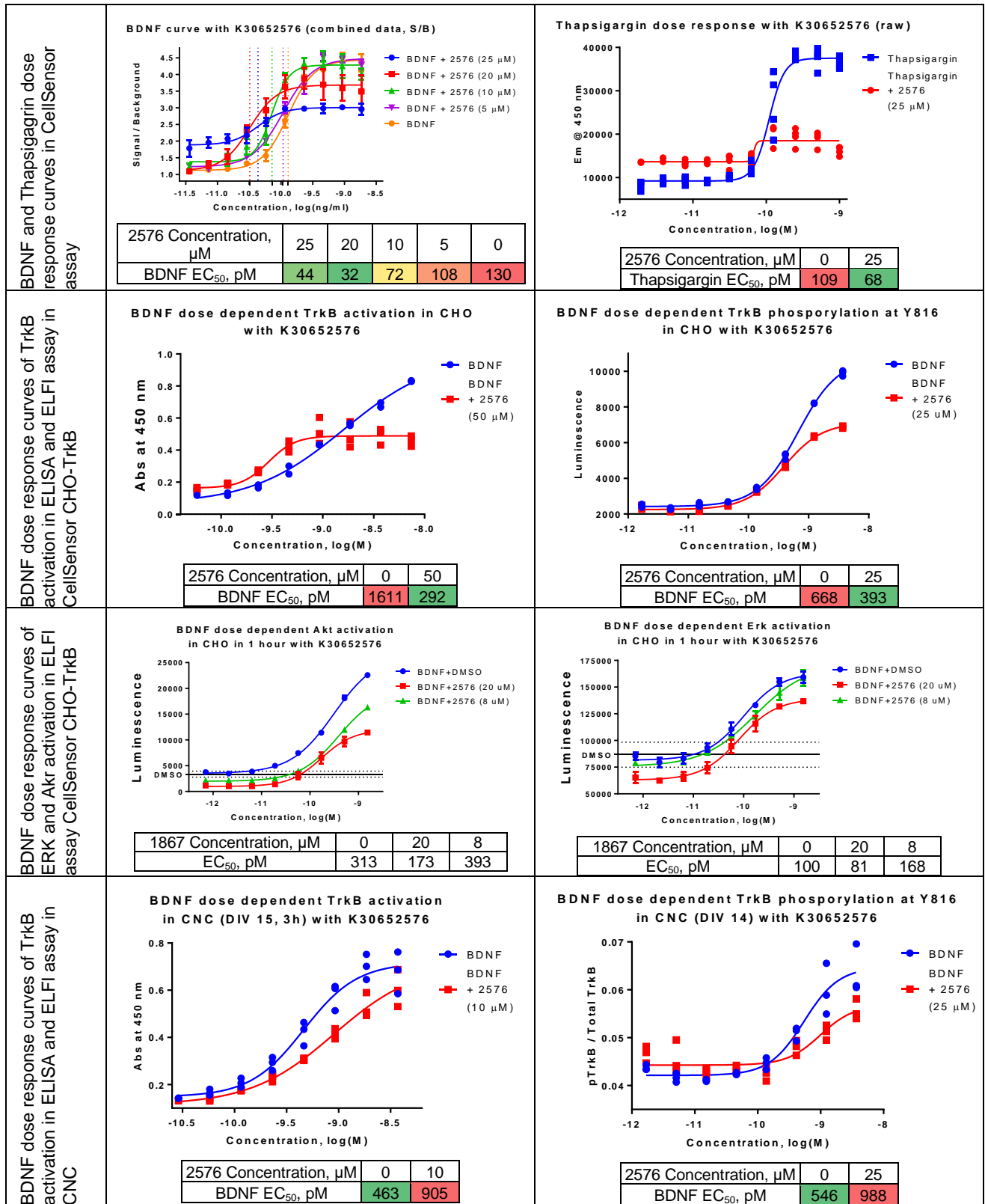


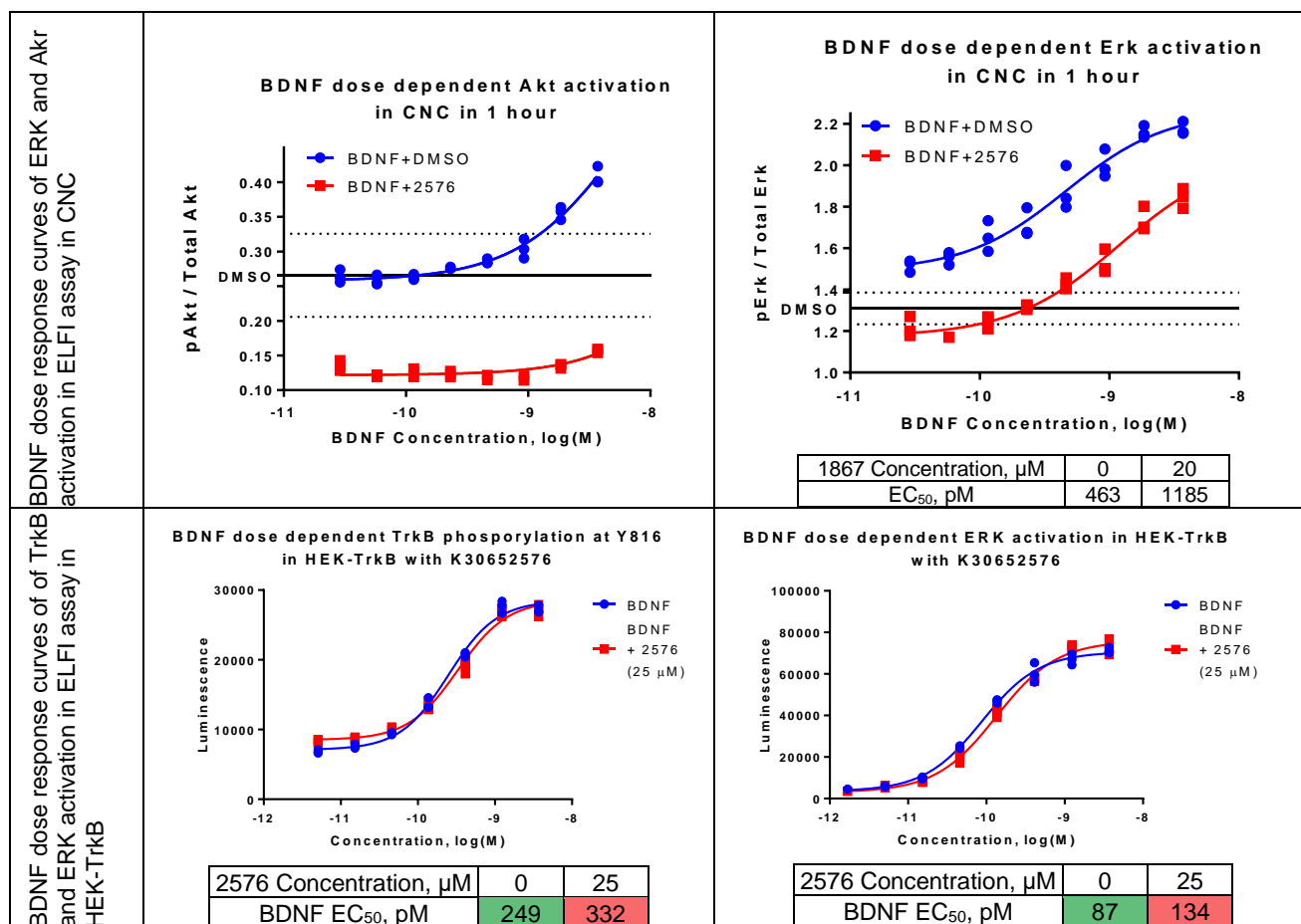
1.2.9.6.2 BRD-K30652576-019-01-1

All the experimental results are presented in Table 1.5. Similar to K54211867, K30652576 also potentiated BDNF while decreasing its efficacy in the CellSensor assay. Interestingly, K30652576 almost completely inhibited thapsigargin in CellSensor. At 50 μM it also potentiated the BDNF-induced TrkB activation, while decreasing BDNF's efficacy in CHO-TrkB as measured by ELISA. At 25 μM only inhibition of BDNF-induced TrkB activation was measured by ELFI. Akt was also inhibited to a lesser degree, while the response at the ERK level was not influenced by the compound. In CNC, an inhibition of BDNF-induced TrkB and Akt activation could be measured with no influence on ERK. No potentiation or inhibition was observed in HEK-TrkB.

Table 1.5 K30652576 characterization as allosteric agonist



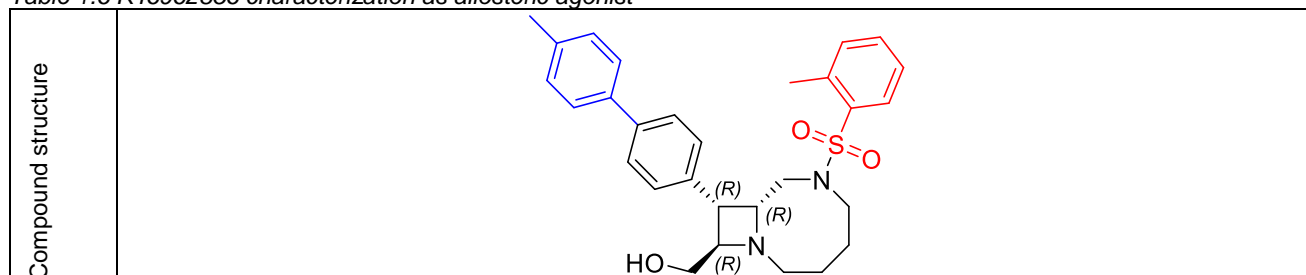


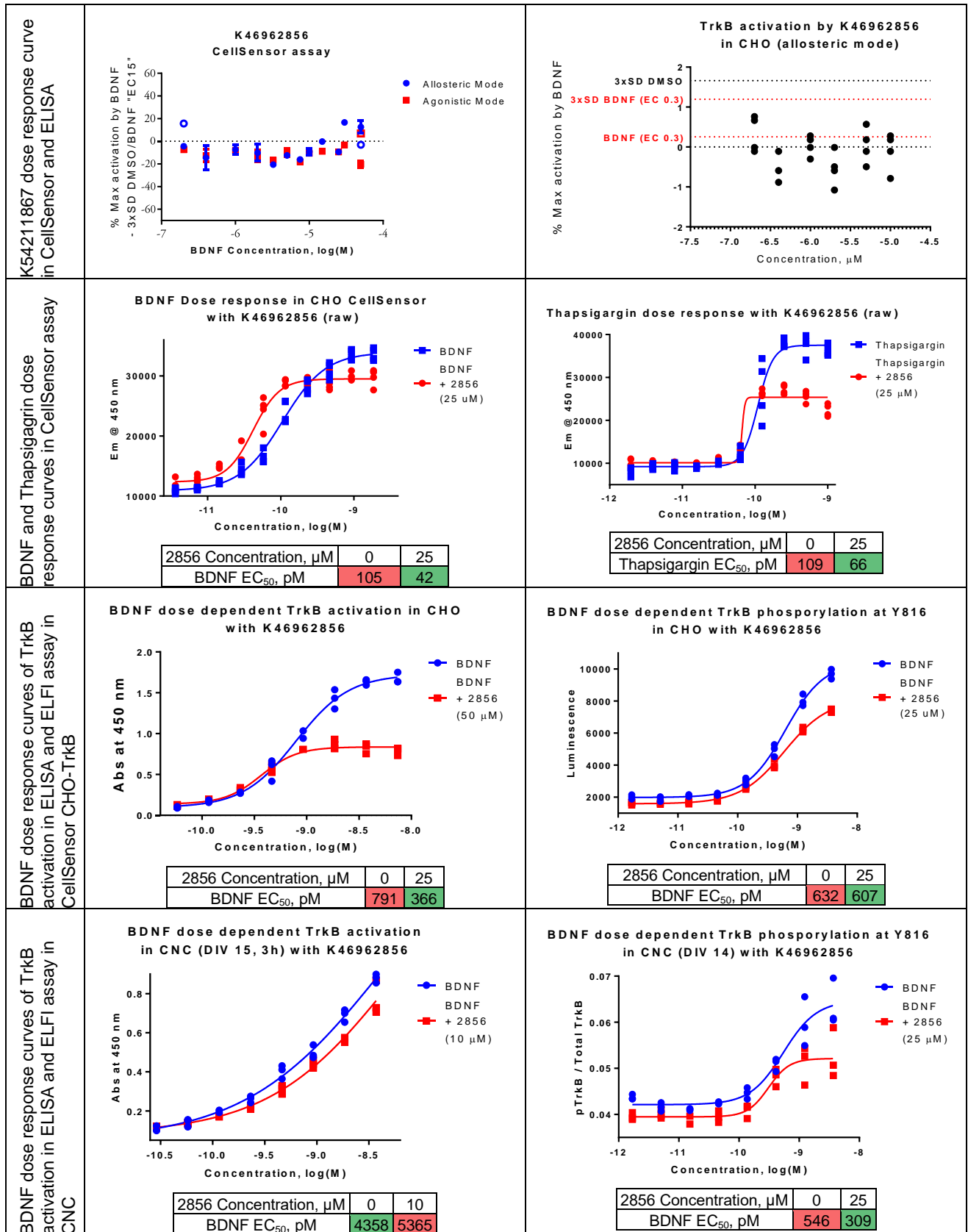


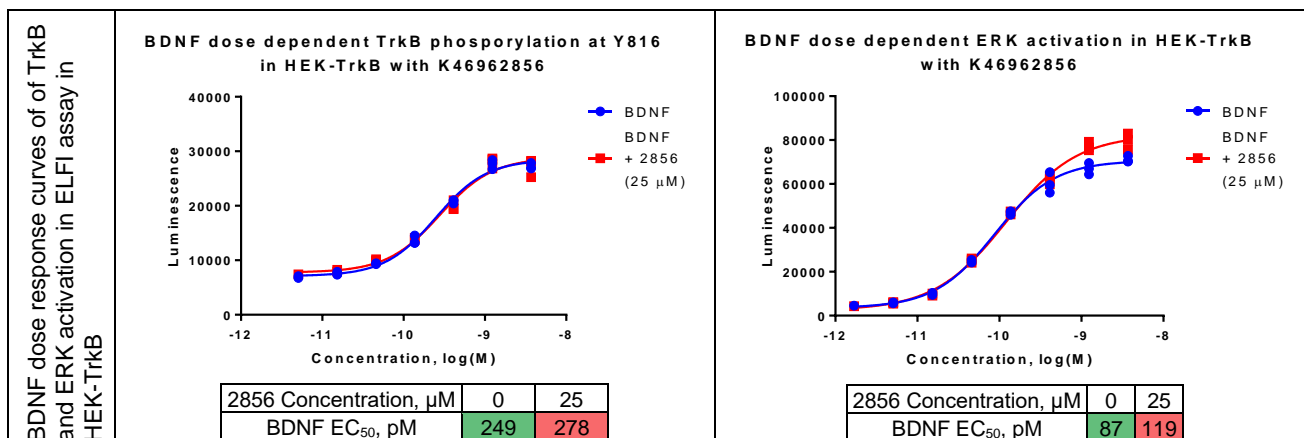
1.2.9.6.3 BRD-K46962856-001-01-5

All the experimental results are presented in Table 1.6. K46962856 had a much less pronounced BDNF potentiation with little influence on BDNF efficacy. It inhibited thapsigargin similar to K54211867. At 50 and 25 μM it also inhibited BDNF-induced TrkB activation in CHO measured by ELISA and ELFI. In CNC, an inhibition of TrkB activity could be measured. No potentiation or inhibition was observed in HEK-TrkB.

Table 1.6 K46962856 characterization as allosteric agonist



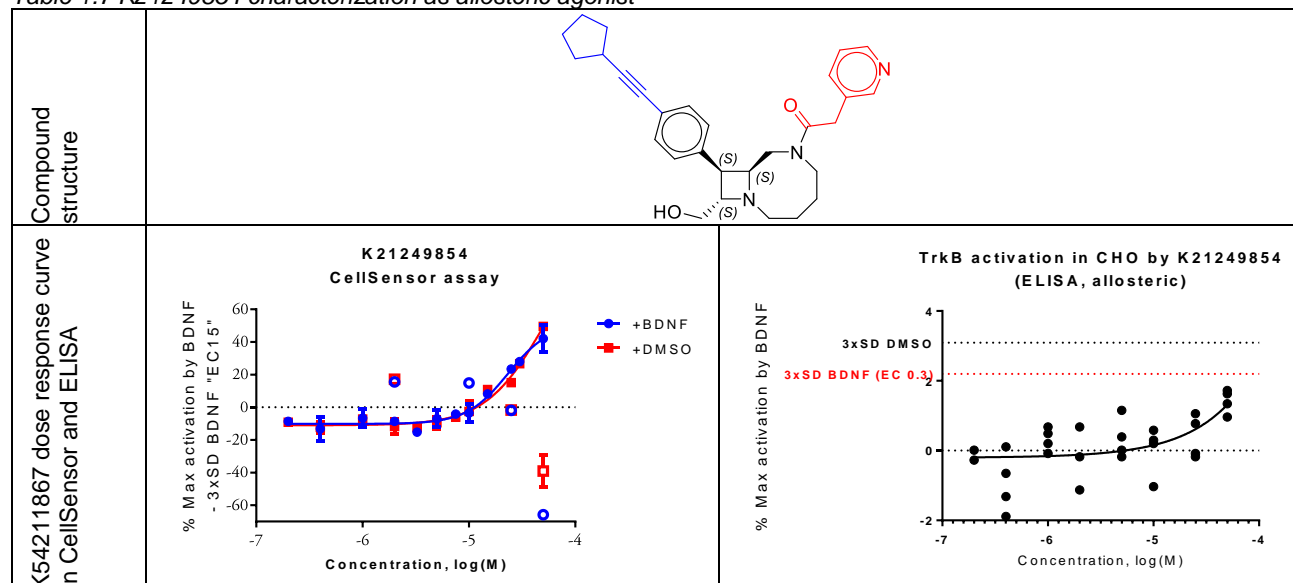


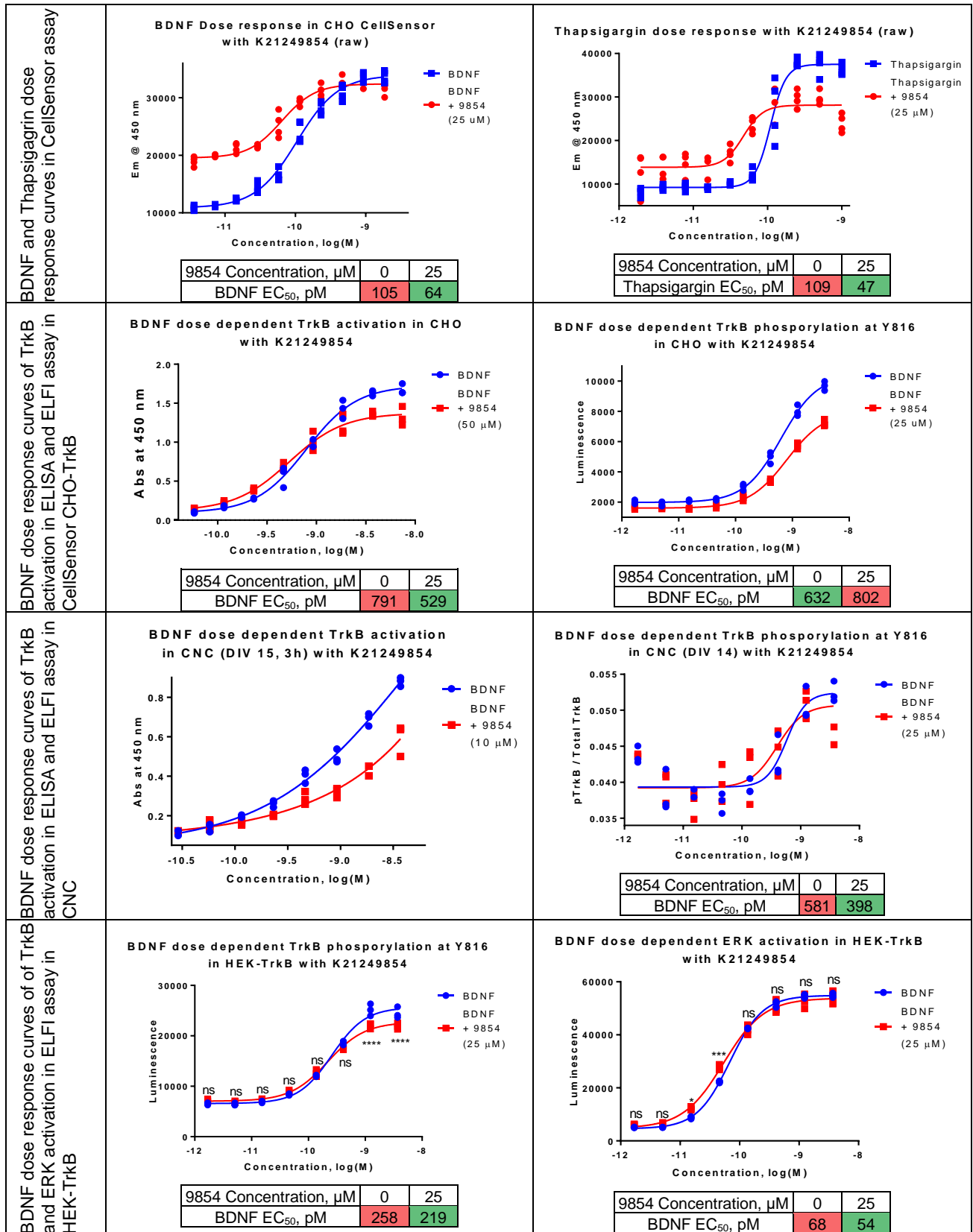


1.2.9.6.4 BRD-K21249854-001-01-8

All the experimental results are presented in Table 1.7. K21249854 acted as an agonist by increasing the background signal of the BDNF dose curve in the CellSensor assay. This compound was used as a control to show no influence on BDNF activity. Thapsigargin on the other hand was potentiated at the expense of efficacy by the compound. At 50 and 25 μM it inhibited BDNF-induced TrkB phosphorylation in CHO measured by ELISA and ELFI. Inhibition was also measured in CNC with ELISA, while ELFI contradicted this result. Little influence on BDNF curve could be measured in HEK-TrkB cells.

Table 1.7 K21249854 characterization as allosteric agonist





1.2.9.7 Conclusion of HTS

In the course of the HTS, 40,000 compounds were tested as agonists and allosteric modulators. The primary screen identified 355 potential hits, the number of which was reduced to 83. All these compounds were tested in secondary assays. No true TrkB agonists were identified in the secondary assays. All identified hits were thoroughly tested in all our assays in all established cell lines. Compounds acting as a PAM were not convincingly active at the receptor level and likely influenced unidentified downstream targets to elicit their activity.

1.2.10 Phage Display

Based on these negative results in terms of finding a TrkB agonist or modulator, alternative screening platforms were researched. It was hypothesized that the large ligand binding surface in TrkB would require a larger ligand to influence the activity of this receptor class. Hence, a DNA, protein, or peptide-based library could be used to find sequences that act as agonists/modulators at TrkB. A peptide library and the phage display screening approach were chosen. Moreover, multiple peptides displayed on the surface of a phage could act as BDNF mimics and induce TrkB dimerization. To perform phage display, T7 bacteriophage libraries displaying peptides with the composition of CX7C (C=cysteine; X= random amino acid; ~ 200 peptides per phage particle) were used. The two cysteines provided a cyclizing disulfide bond, which restricts the conformation of the peptide and provide higher affinity to the receptor than linear peptide (137, 138).. In case linear peptide is favored for binding, the library can still provide with such peptides due to random DNA sequences. A successful identification of linear peptide in cyclic library which has been reported (139). The diversity of phage library can reach theoretical levels and thus cover a large space of peptide structures.

An arguable activation mechanism of TrkB could be through conformational change of extracellular domain upon ligand binding. Thus, to find agonistic or allosteric peptide, phage display on the extracellular domain of TrkB should be performed. There were two strategies explored: phage display on the recombinant extracellular domain of TrkB immobilized on the surface and phage on TrkB presented on the surface of the cell.

1.2.10.1 Recombinant TrkB

Table 1.8 Recombinant TrkB phage display first approach

Peptide sequence	% of total in the 3rd round
CKSEHSH	47.7
CKNRHSH	12.5
CKSHHH	6.1
CHKH	5.5
CAGAHVH	2.9
CKSHQH	1.9

Phage display on recombinant TrkB was performed in Dr. Teesalu laboratory (Tartu university, Estonia). To perform phage display on isolated TrkB, a recombinant extracellular domain of TrkB was acquired (Met1-His430) with a His-tag at the C-terminus. The standard

protocol for in vitro biopanning on a protein was performed using Ni-NTA agarose beads for H7 tagged protein. TrkB immobilization on a plate surface was not chosen to avoid enrichment of phages that bind to plastic surface of a plate which could result in low selection or high background. The biopanning was performed several times on TrkB and had enrichment ~1000 fold, but the same amount of phage also bound to naked beads. It means that the enriched pool had a lot of His-containing phages as it came out from the Ion Torrent sequencing (Table 1.8) – it was unexpected. The screen was repeated and troubleshooted multiple times without success.

As a second approach another method to immobilize proteins was used. PureProteome™ NHS FlexiBind Magnetic Bead System from Merck Millipore was tested. This system covalently binds a protein on the bead surface through a free amine on a protein. A screen was conducted in duplicate for three rounds with both CX7C and CX8C phage libraries and sequenced with Ion Torrent. Finding the same or similar phages found in both duplicates was a good confirmation of a successful screen. Table 1.9 contains results from the CX8C and CX7C screens. The top list of peptides had fairly good overlap between duplicates. The most prominent peptide sequences after the third round are listed in Table 1.9:

Table 1.9 Recombinant TrkB phage display second approach results

CX8C Library	1 torrent count	2 torrent count
CLWTKKGKKC	234	390
CAKGSKWNC	85	163
CTDAKGRKRC	80	115
CRGKKASREC	87	109
CSKGPKKKPC	78	85
CERSSKSKC	69	68

CX7C Library	1 torrent count	2 torrent count
CHPGKGKRC	455	107
CRKSKRGEC	363	133
CLQKKKSKC	141	177
RLCKKGKPC	135	176
CMYKGGKKC	173	88
CFKGKKAVC	78	114
CEGKRRKGC	105	91
CKDKKGRPC	100	73

Table 1.10 Phage display on plated cell results

Phage library	Input		Output			
	+ BDNF	- BDNF	+ BDNF	O/I	- BDNF	O/I
CX8C	4.00E+08	3.00E+08	7.10E+06	1.8%	7.00E+06	2.3%
CX7C	3.50E+08	4.00E+08	6.10E+06	1.7%	7.70E+06	1.9%
G7	2.70E+08	2.80E+08	3.60E+06	1.3%	3.60E+06	1.3%

Most of these peptides contained multiple positively charged amino acids, specifically lysine. Even though sequences found in the parallel

control naked bead screen did not overlap with the primary screen, these results raised questions whether recombinant TrkB produced true binders to the receptor. It was decided to conduct phage display on TrkB expressed on the cell surface. Found sequences could be compared to the recombinant TrkB screen, which would validate the results of both screens.

1.2.10.2 Cell based Phage Display

Since the main purpose of the TrkB phage display was to identify peptides that would act as TrkB agonists or allosteric modulators, it was decided to conduct the screen against the activated form of TrkB, which should be present in a BDNF-TrkB complex. Therefore, the general strategy of the cell-based phage display was to form a BDNF-TrkB complex on cell surface and biopan against this complex (Figure 1.2.22). Typically, the first round of selection could be performed overnight at 4°C. Subsequent rounds required more strict conditions, to reduce non-specific and low affinity peptides. To ensure diversity collapse of the initial library 3-5 rounds of selection were conducted.

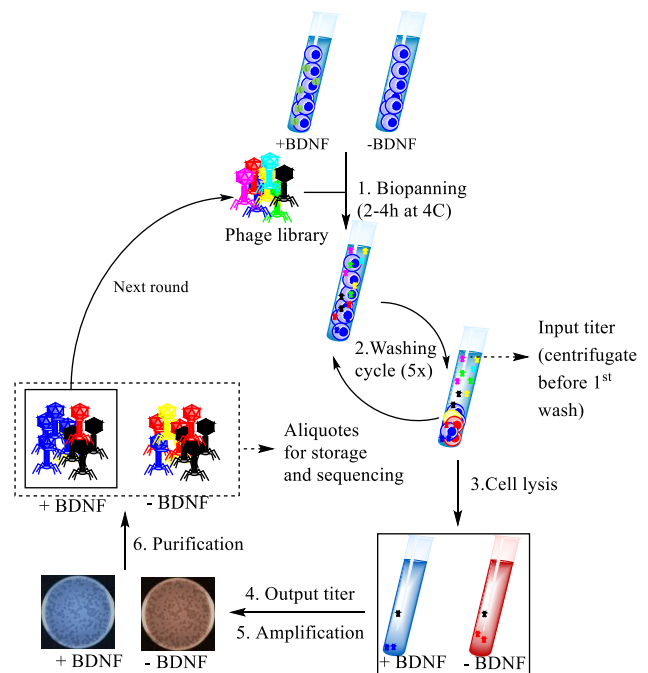


Figure 1.2.22 Phage display scheme

Phage display consisted of several steps reminiscent of a catalytic cycle. 1. Cells were incubated with phage library and BDNF (+BDNF) or Phage vehicle (-BDNF) for 2h or overnight at 4°C with rocking. 2. After biopanning cell medium was collected for input titer, and cells were washed 5 times. 3. Cells were lysed. 4. The number of phages were counted in the lysate. 5-6. Collected phages were amplified and purified for sequencing and next round of selection.

1.2.10.2.1 Phage display on cultured HEK-TrkB cells

Since protein conformation at 37°C was considered to be more relevant to physiological conditions as well as binding of phage could be faster, it was decided to perform biopanning on seeded HEK-TrkB at 37°C for 2 h incubation in the presence of BDNF at EC100 (100 ng/ml). To test the feasibility of the outlined approach, CX8C and CX7C libraries and CG7C control phages were added to HEK-TrkB, which then was treated with BDNF. After the biopanning, cells were washed with medium five times and lysed. Lysates were collected and analyzed for phage content. The results of the test run results are present in Table 1.10.

Table 1.11 Phage titer at every washing step

Washing steps		
Input	2.70E+08	100.00%
1	3.45E+06	1.28%
2	2.75E+05	0.10%
3	1.50E+05	0.06%
4	8.00E+04	0.03%
5	8.80E+04	0.03%
Output	3.60E+06	1.33%

The output-to-input ratio was too high, indicating high background. To characterize whether the five washing steps were enough to wash off excess phages, each washing step aliquots were collected and analyzed for phage content (Table

1.11). On the fifth washing step the number of phages was almost two orders of magnitude lower than the output sample, indicating that increasing steps or the volume of medium of washing had not decreased the number of phages in the output sample. Lowering the temperature had not yielded more favorable results, so an alternative approach was explored.

1.2.10.2.2 BDNF-TrkB complex detection: Blue-native PAGE (BN PAGE)

Since phage display on the plate produced high background, biopanning was performed in cell suspension (Figure 1.2.22). HEK-TrkB is an adherent cell line so several questions were raised:

1. Did the BDNF-TrkB complex form in suspension?
2. Was it present in the course of phage display?
3. Did phosphorylation of TrkB takes place at 4°C?
4. Did cells survive in suspension?

To answer the first question a method for detecting protein-protein interactions was used. The common method is co-immunoprecipitation, which requires BDNF-specific antibody for precipitation and

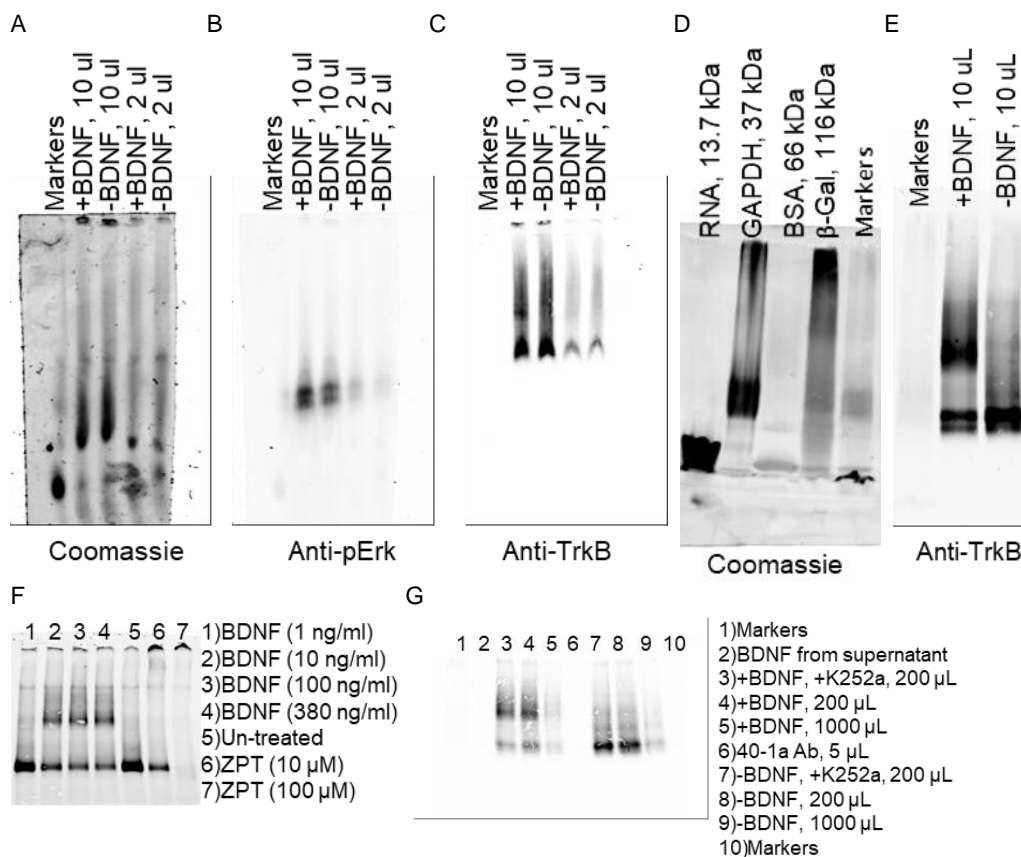


Figure 1.2.23 BN PAGE development

A. A test run of CBG250 stained marker proteins and cell lysate of U2OS-TrkB treated with BDNF performed on 4-20% Mini Protean pre-cast gel. To test the detection limit two loads of lysate were tested. The Coomassie stained blot was imaged on the 700 nm channel on a NIR Licor Odyssey imaging station. B-C. Coomassie stained membrane blotted against pERK and TrkB to test protein migration in the gel and detection of ERK phosphorylation and BDNF-TrkB complex. D. Coomassie stained blot of different recombinant proteins imaged to visualize protein migration in manually prepared 4-20% BN PAGE Bis-Tris gel. Markers sample contained lower concentration of recombinant proteins used on other lanes. E. Lysates of BDNF treated and control U2OS-TrkB cells blotted against TrkB imaged to visualize TrkB migration in BN PAGE gel and detect formation of the complex. F. BN PAGE blot of U2OS-TrkB treated with BDNF and K252a stained against TrkB to test formation of the complex in the presence of K252a. G. BN-PAGE blot of BDNF dose response of BDNF-TrkB complex formation and Zn activity at TrkB in U2OS-TrkB at 37°C 1-hour treatment was stained against TrkB to demonstrate BDNF dose dependent complex formation and whether Zn²⁺ induced any TrkB dimerization.

detection, which was not available. Other potential in vitro methods use purified protein or require genetic tagging of the proteins in the cells. One other method that could be used with cell lysates has been native electrophoresis. However, PAGE electrophoresis could only be used to resolve negatively charged proteins. To solve this issue in native PAGE, Coomassie Brilliant Blue G-250 (CBG250) has been used to give proteins negative charge (140, 141). This dye has stained proteins non-specifically without disrupting protein complexes and has given negative charge to proteins proportional to the size. This method has been called Blue-native PAGE (BN PAGE).

To test the principle of BN PAGE as well as to develop this method, the SDS PAGE method was adjusted as necessary by substituting SDS to CBG250, while using SDS PAGE buffers and Tris-glycine gel. Different recombinant proteins (RNase, GAPDH, BSA, alkaline phosphatase, β -galactosidase) were mixed to prepare BN PAGE markers. DiscoverX U2OS-TrkB cells, which were readily available at the time of the experiments, were used. BN PAGE on 4-20% gradient Mini Protean gel produced protein electrophoresis with long streaks, broad bands and poor front stacking (Figure 1.2.23A). CBG250 stained proteins could be visualized in the 700 nm channel of near-IR on the Lycor Odyssey dual channel imaging station. Cell lysates had one continuous droplet-shaped band and contained large proteins that did not travel into the gel. CBG250 could not be effectively destained from the blot rendering the 700 nm channel useless for further staining. Thus, target proteins could only be visualized in the 800 nm channel. Phospho-ERK and TrkB were detected using corresponding antibodies (Figure 1.2.23B-C). The pERK band appeared to be broad, while TrkB contained a long streak and one major band. There was a second TrkB band in the BDNF-treated lysate which was barely detectable. These results indicated that BN PAGE in principle does work, however SDS PAGE gel was not suitable for this method.

BN PAGE has been performed on Bis-Tris - ϵ -aminocaproic acid or tricine-imidazole gels. Based on reagent availability 4-20% gradient Bis-Tris gel was manually prepared by layering 20-15-12-10-8-7-6-5-4% acrylamide/bisacrylamide solutions. To test how proteins of different size and charge travel in BN PAGE, RNase (13.7 kDa), GAPDH (37 kDa), BSA (66 kDa), and β -galactosidase (116 kDa) were used (Figure 1.2.23D). The protein front was stacked, however streaks remained. Rf values of RNA, GAPDH, and β -galactosidase correlated with MW, while BSA had a higher Rf than expected. Lysates of DiscoverX U2OS-TrkB cells treated with BDNF were used in BN PAGE to identify whether the BDNF-TrkB complex could be detected. Untreated cells contained one band, while BDNF treated lysates contained two TrkB bands, with one corresponding to similar band in untreated cells with lower absorbance (Figure 1.2.23E). The second band most likely represented the BDNF-TrkB complex. To confirm a BDNF-dependent complex formation U2OS-TrkB cells were treated with BDNF at various concentrations for 1h at 37°C (Figure 1.2.23F). A second TrkB band indeed formed at active concentrations of BDNF. Interestingly, Zn did not form a TrkB dimer and at high concentration and probably caused TrkB degradation. To test whether formation of the complex could be inhibited, DiscoverX U2OS-TrkB were treated with BDNF and

K252a and subjected to BN PAGE analysis (Figure 1.2.23G). The BDNF and K252a treated sample contained the same bands as BDNF treated sample, indicating the formation of the complex even in the presence of K252a. The results were not surprising, since BDNF have caused TrkB dimerization through extracellular domains even though K252a inhibited activity of TrkB kinase domain, which might not play a role in complex formation and stability.

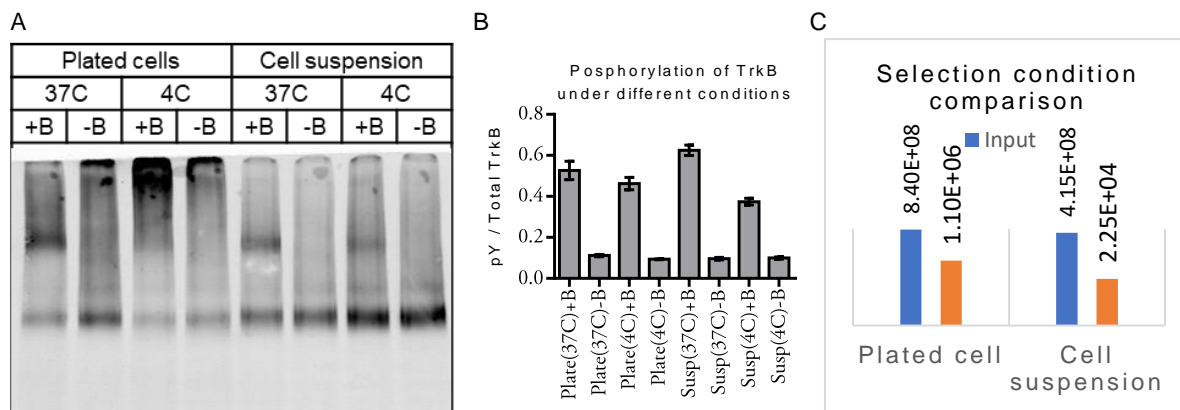


Figure 1.2.24 Cell-based Phage Display protocol characterization
 A BN PAGE of HEK-TrkB cells treated with BDNF under different conditions. B. Phosphorylation of TrkB in BDNF treated HEK-TrkB cells under different conditions measured by ELISA. C. O/I ratio of phage in plate and suspension format of phage display.

Having developed a new method to verify complex formation, the first and second stated questions above could be answered. To this end, HEK-TrkB cells were treated with BDNF at 100 ng/ml (EC100) for 1h at 4°C or 37°C on the plate or in suspension. Free TrkB and BDNF-TrkB complex were resolved on 4-20% BN PAGE and visualized using a TrkB antibody. BDNF treated cells on plate and in suspension at 37°C and 4°C contained two resolved TrkB bands indicating the formation of a BDNF-TrkB complex (Figure 1.2.24A). Lysate of cells treated on the plate at 4°C did not, however, contain clear BDNF-TrkB bands as the whole lane was noisy with a lot protein at the start.

Table 1.12 Phage display on plated cell results

Phage library	Input		Output			
	+ BDNF	- BDNF	+ BDNF	O/I	- BDNF	O/I
CX8C	4.00E+08	3.00E+08	7.10E+06	1.8%	7.00E+06	2.3%
CX7C	3.50E+08	4.00E+08	6.10E+06	1.7%	7.70E+06	1.9%
G7	2.70E+08	2.80E+08	3.60E+06	1.3%	3.60E+06	1.3%

To test whether TrkB is phosphorylated under phage display conditions, similar lysates used for BN PAGE were analyzed in ELISA (Figure

1.2.24B). TrkB phosphorylation was higher than control under all conditions where cells were treated with BDNF, which answered the third and fourth stated questions. Surprisingly even at 4°C signaling processes of cells was not inhibited. Lastly, it was important to find the output-to-input ratio of phage

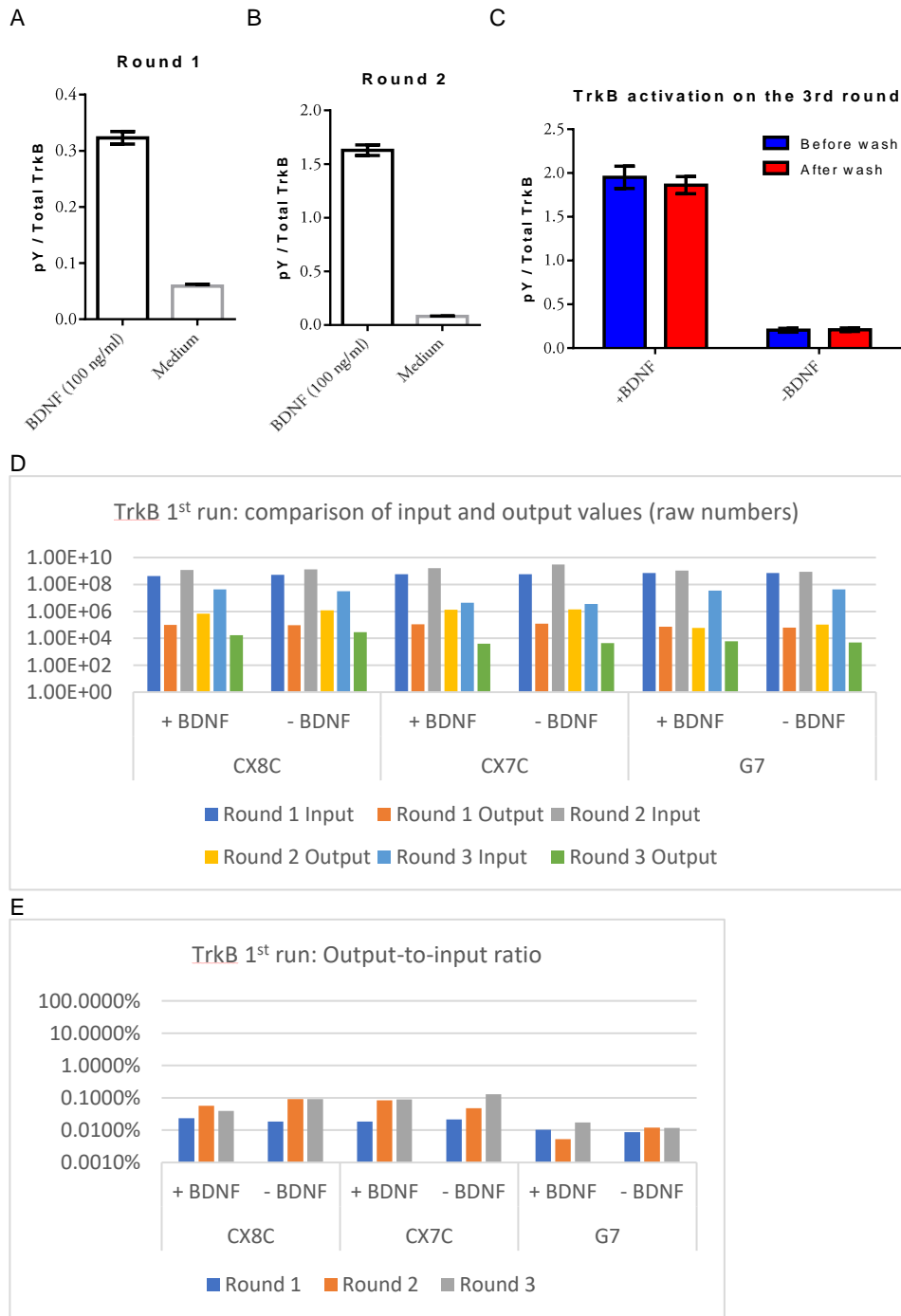


Figure 1.2.25 Cell-based Phage display first run

A-C. Phosphorylation of TrkB in the course of the screening measured using ELISA and control samples from round 1 (A), round 2 (B), and round 3 (C). TrkB phosphorylation was also measured before and after washing steps in the third round (C). D. Input and output values from each round and each library counted by titring. E. O/I ratio was calculated to track enrichment of the libraries.

display protocol (Figure 1.2.22). To this end G7 phages were added to cells and incubated for 2 h at 4°C on plate and in suspension. The output-to-input (O/I) ratio of suspension sample was 0.005%, or

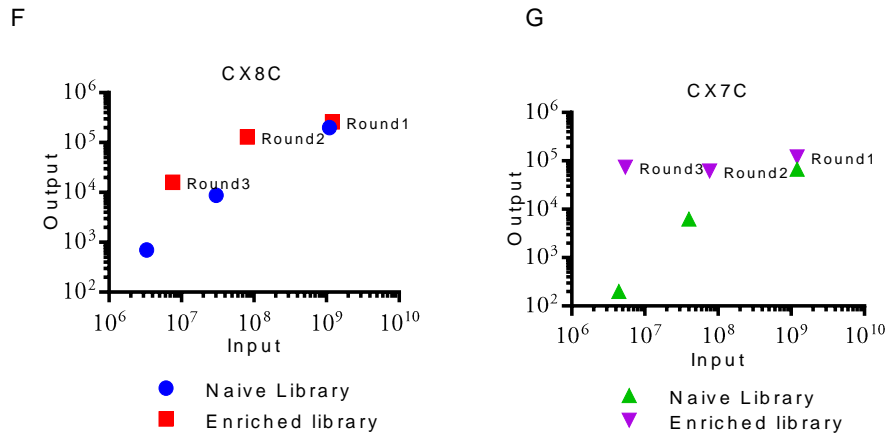
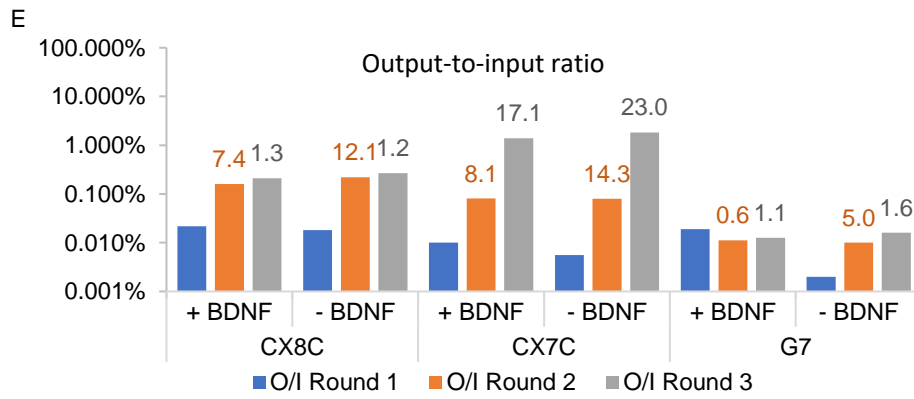
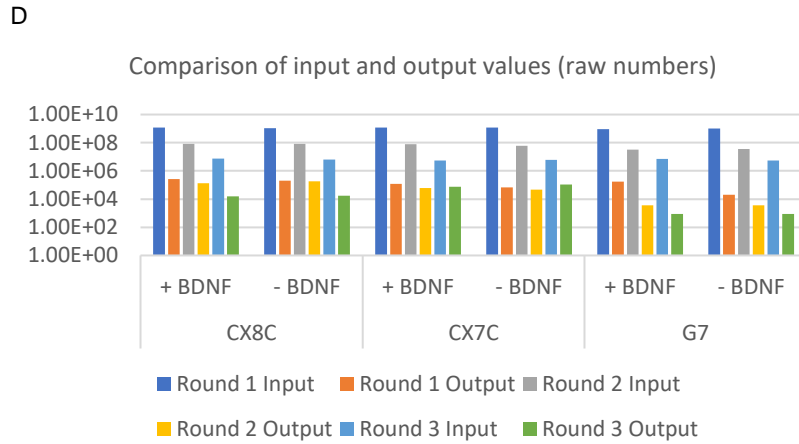
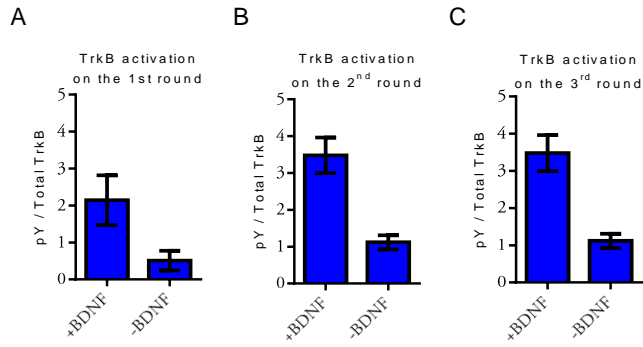


Figure 1.2.26 Cell-based Phage display second run

A-C. Phosphorylation of TrkB in the course of the screening was measured using ELISA and control samples from round 1 (A), round 2 (B), and round 3 (C). D. Input and output values from each round and each library was counted by titering. E. Output-to-input ratio was calculated to track enrichment of the libraries. F-G. Output-input graphs for CX8C (F) and CX7C (G) were drawn to compare output values of naïve and collected libraries.

20,000 times less phages in the output than in the input, while plate sample retained 0.1% of phages, or 800 times less phage in the output than the input (Figure 1.2.24C). In other words, selection in suspension was better, thus improving the protocol.

1.2.10.2.3 Phage Display in cell suspension

Using the developed phage display protocol, three rounds of selection were performed with both phage libraries and G7 phage as a control. To control for TrkB activity each round contained a sample that was later used for ELISA to identify the phosphorylation level of TrkB. In all rounds, BDNF treated cells contained phosphorylated TrkB (Figure 1.2.25A-C). In the first round, 5×10^8 phages were added to cells with and without BDNF, incubated for 4h at 4°C with rocking, and about 10^5 phages were collected after five washing rounds (Figure 1.2.25D). The O/I was 0.02% while the O/I for control G7 phage was around 0.01% (Figure 1.2.25E). In the second round 2×10^9 of library phages were input, incubated for 2 hours at 4°C rocking, and 10^5 phages were collected resulting in O/I equal to 0.07%. G7 control sample had O/I equal to 0.01%, which indicated successful enrichment of the libraries. In the third round, CX8C input and output was around 4×10^7 and 2×10^4 respectively, yielding 0.05% O/I in BDNF treated sample and 0.09% in untreated sample. CX7C input and output values were an order magnitude lower than CX8C, yielding 0.09% O/I in BDNF treated sample and 0.13% in untreated sample. G7 O/I was 0.014% which was consistent throughout the screen (Figure 1.2.25E). The O/I of the third round was similar to second round, raising the question of whether the enrichment was good, and should the current screen be pursued any further. As it was noted by Dr. Teesalu, second and subsequent rounds should have lower input than the first input to increase stringency of the screen. Therefore, it was decided to do another screen and correct conditions to increase stringency.

A second phage display run was performed with necessary modifications. The first round of biopanning was conducted rocking overnight at 4°C with 10^9 phages in the input. TrkB was phosphorylated during the first round of biopanning (Figure 1.2.26A). The output contained 2×10^5 in CX8C sample and 1×10^5 phages in CX7C, with O/I equal to 0.02% and 0.01% respectively (Figure 1.2.26 D and

E). In the second round an order of magnitude less input of phages was biopanned for 4 hours, with a similar level of the output as in the first round. As the result, second round O/I was an order of magnitude higher than first round and G7 control, indicating successful enrichment. In the third round 7×10^6 phages were input for 4h biopanning at 4°C . The output of CX8C phages were also lower at 1.6×10^4 phages, while CX7C output was similar to previous rounds. The O/I for CX8C was similar to second round while O/I for CX7C reached 1%. G7 control remained low throughout the screen. Between first and second round the O/I was improved in CX8C library screen, but no further improvement was observed in the third round. CX7C O/I throughout the phage display screen was much better, with reaching 1% from 0.01%. To determine whether the output value of each round indicated an enrichment of the target specific phages, a naïve library output value as the function of input was measured. The output was directly proportional to input, while collected libraries output deviated from this relationship, indicating a higher affinity toward the target and confirming the enrichment (Figure 1.2.26 F and G). These results were encouraging and prompted further analysis of collected phages. TrkB was phosphorylated in all rounds (Figure 1.2.26 B and C).

1.2.10.2.4 CX7C library sequence analysis and characterization

Collected libraries were sequenced in Ion Torrent sequencing. In CX7C library collected in the first round of selection the number of unique phages had been reduced from 4.14×10^6 in the naïve library to 88098 (2% of unique phages from naïve library) in the BDNF treated sample, and 49139 (1.2% of unique phages from naïve library) in the untreated one, giving a ratio of 1.8 between the samples. The total number of phages recovered was 260067 in BDNF treated sample, and 115243 in untreated, with 2.3 ratio between the samples. These numbers did not take into account phages that expressed non-cyclic peptides and the one that do not start with C amino acid, and thus these numbers could not be accurately compared with values found by titering during the screening.

In the second round the number of unique phages was 26455 from BDNF-treated sample and 14397 from untreated sample, with a ratio of 1.8 which was consistent with the first round of selection. The total number of phages in BDNF treated and untreated samples reached 259856 and 62494 giving a ratio of 4.2, which was higher than in the first round indicating a better selection in the second round. The top 20 abundant phages are presented Table 1.13. The most abundant sequence, CYKIGRVKC,

amounted to 4% of total phage number in BDNF treated sample and 2% in untreated sample, providing a selection ratio of 2, which is consistent with unique phage number ratio and lower than the total number phage ratio. CRLDVC was the second most abundant with 1.41% and 1.58% of total phages present in BDNF-treated and untreated sample respectively with a 0.90 selection ratio, indicating to lack of specificity.

Table 1.13 Top 20 abundant phages found through Ion Torrent sequencing in CX7C libraries. Phages selected for ELFI analysis are in bold.

Round 2					Round 3				
Peptides	Count		% of total		Peptides	Count		% of total	
	+BDNF	-BDNF	+BDNF	-BDNF		+BDNF	-BDNF	+BDNF	-BDNF
CYKIGRVKC	10364	1309	3.99%	2.09%	CYKIGRVKC	78356	100772	67.51%	66.97%
CRLDVC	3673	989	1.41%	1.58%	CRLDVC	10550	13184	9.09%	8.76%
CRLDFCS	1462	544	0.56%	0.87%	CRLDFCS	2760	3374	2.38%	2.24%
CQAWAISTC	549	226	0.21%	0.36%	CQAWAISTC	1694	1956	1.46%	1.30%
CGVPDGITC	429	49	0.17%	0.08%	CHEWVLEPC	1334	1753	1.15%	1.17%
CHEWVLEPC	418	160	0.16%	0.26%	CVTWEVSSC	441	722	0.38%	0.48%
CPGSEGRRC	404	50	0.16%	0.08%	CPTWEVSQC	340	400	0.29%	0.27%
CTIGEYEH	333	100	0.13%	0.16%	CHRRGDQIC	231	316	0.20%	0.21%
CRRTSRGMC	320	40	0.12%	0.06%	CKRRGDHTC	192	254	0.17%	0.17%
CGNKTKVTC	296	53	0.11%	0.08%	CPTWEVSLC	184	261	0.16%	0.17%
CGTAPLNGC	288	75	0.11%	0.12%	CEAWEVSSC	132	225	0.11%	0.15%
CSPYKVNAC	283	91	0.11%	0.15%	CEEVVSAC	111	193	0.10%	0.13%
CASEWDEGC	282	58	0.11%	0.09%	CVAEGVERC	109	93	0.09%	0.06%
CHRRGDQIC	276	59	0.11%	0.09%	CITWEVSSC	100	120	0.09%	0.08%
CGNTGVVVC	275	63	0.11%	0.10%	CAFRGDHTC	97	101	0.08%	0.07%
CRNTRTKTC	274	0	0.11%	0.00%	CKRRGDGTC	95	95	0.08%	0.06%
CVTWEVSSC	265	101	0.10%	0.16%	CISQGRRIC	70	0	0.06%	0.00%
CRQGRTKGC	244	23	0.09%	0.04%	CASTLTGAC	70	0	0.06%	0.00%
CNHSGRSKC	240	61	0.09%	0.10%	CADISDSHC	66	14	0.06%	0.01%
CRRRNVGVC	235	33	0.09%	0.05%	CNVLAKSEC	65	0	0.06%	0.00%
CVSRSEGNC	234	52	0.09%	0.08%	CHNVLDKC	64	0	0.06%	0.00%
Total	259856	62494	-	-	Total	116065	150466		
Unique	26455	14397	-	-	Unique	4175	4878		

In the third round the number of unique phages was 4175 from BDNF-treated sample and 4878 from untreated sample, with a ratio of 0.86 which was lower than in first and second rounds of selection. The total number of phages in BDNF-treated and untreated samples reached 116065 and 150466, giving a ratio of 0.77, which was in agreement with the unique phage number ratio and lower than in the first and

second rounds, indicating a worse selection in the third round. On the other hand, the diversity of the library was greatly reduced, so no further selection rounds were required. The most abundant sequence, CYKIGRVKC, amounted to 68% and 67% of total phage number in BDNF treated sample and untreated samples respectively, with selection ratio of 1 with no specificity toward BDNF treated sample that was observed in the second round. CRLDVC phage total number was also higher, up to 10550 and 13184 amounting to 9% and 8.8% in BDNF-treated and untreated samples, the selection ratio of which did not change between second and third rounds. The higher than expected number of phages in the untreated sample could be attributed to less stringent biopanning condition of the third round. However, a lower number of unique phages did not support this assumption.

Table 1.14 Sanger sequencing results.
Phages selected for ELFI analysis are in bold

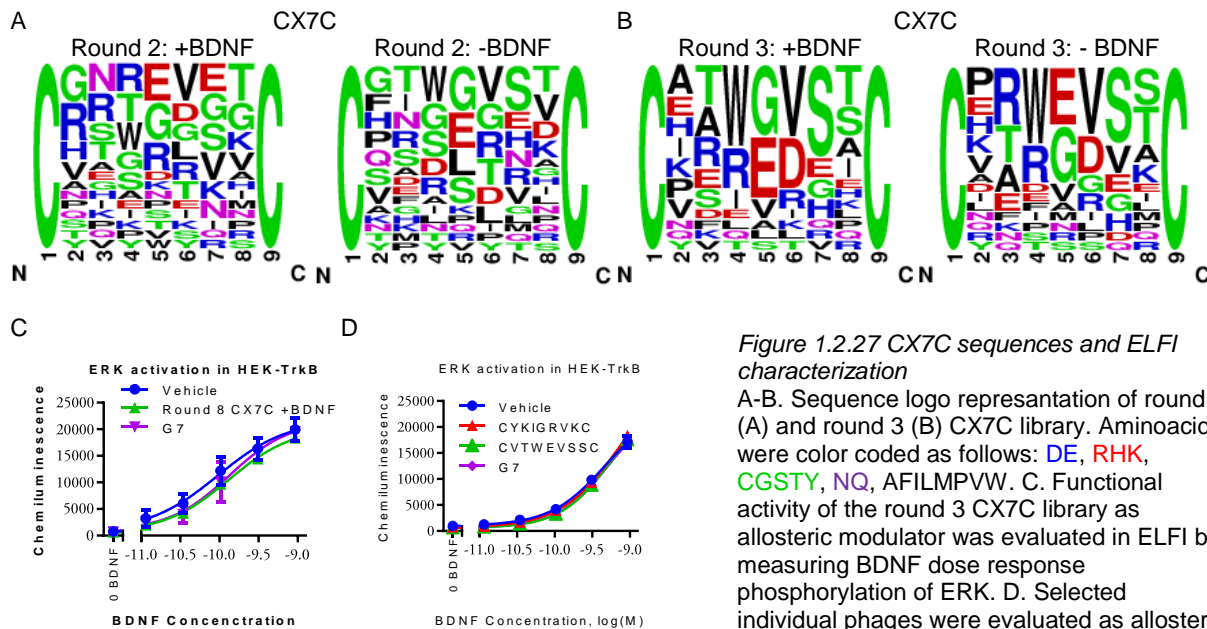
Sequence	Number
CYKIGRVKC	28
CQAMD	1
CRLDFCS	2
CRLDVC	2
CERQY	1
CNDFITPNC	1
CVTWEVSSC	1
CHRRGDQIC	1
Total	46

Sequence analysis of the round two library top 20 CX7C peptides (excluding peptides with less than 7 amino acids between C) (Figure 1.2.27A) showed a prevalence of charged amino acids like Arg and Glu at 2-4 and 5-7 positions, respectively in the BDNF-treated sample. Amino acids were color coded as follows: **DE**, **RHK**, **CGSTY**, **NQ**, **AFILMPVW**. The sequence made up from the most

frequently occurring amino acids were **CGNREVE**TC and **CRRTGDGGC** (Figure 1.2.27 A). In contrast, untreated samples contained peptides with more frequent occurrences of Gly at various positions, and less amount of charged amino acids. This library also contained Trp at fourth position quite frequently. The sequence made from the two most frequent amino acids was **CGTWGVSTC** and **CFIGEGEVC**. In all sequenced libraries Thr was present at the seventh position. In the third round, the BDNF-treated library contained **TWGVST** sequence, that was the prominent in the second round untreated library, and **RREDE** motif (Figure 1.2.27B). The third round untreated library sequences were slightly different from the second round library with the most frequent motif being **RWEVS(S/T)**.

For Sanger sequencing random phage plaques from amplified plates of round three BDNF-treated library were collected and submitted to sequencing (Table 1.14). **CYKIGRVKC** phage was in 61% of all selected plaques and **CRLDFCS** and **CRLDVC** were the next most abundant phages at 4%. Sanger

sequencing results mirrored the Ion Torrent sequencing outcome. Selection parameters for functional characterization of the phages were abundance of the peptide, low number of charged amino acids (D, E, R, H, K), and high number of amino acids with heteroatoms (S, T, N, Q, Y, W, M, F). Based on these parameters CYKIGRVKC and CVTWEVSSC were selected.



The entire round 3 CX7C BDNF treated library and selected phages were tested for allosteric modulation of BDNF activity at ERK in HEK-TrkB cells (Figure 1.2.27C-D). No significant influence of the library or individual phages were measured. Due to low concentration of phages that could be achieved in the cell medium the phages could not exert their activity. Indeed, the typical concentration of phages were at 10^{11} pfu/ml, which would be equal to 1.6 nM in stock and 20 pM in cell experiments. The EC₁₀ of BDNF at ERK was 23 pM, thus the phage concentration was likely too low to elicit any significant response in ELFI.

1.2.10.2.5 CX8C library sequence analysis and characterization

CX8C library collected in the first round of selection contained 26499 number of unique phages out of 2×10^8 in the naïve library in the BDNF-treated sample, and 82397 in the untreated one, giving a

ratio of 0.32 between the samples. The total number of phages recovered was 34143 in the BDNF-treated sample, and 199880 in untreated, with a 0.17 ratio between the samples. The outcome of the BDNF-treated sample was surprising given the output value found by titering (2.6×10^5), while the total number of phages in the untreated sample were similar to the titering. Most likely the most abundant phages in round 1 BDNF-treated library were either insertless or lacking Cys at the expected location of the coat protein, thus reducing the total number of CX8C phages.

Table 1.15 Top 20 abundant phages found through Ion Torrent sequencing in CX8C libraries. Phages selected for ELFI are in bold

Peptides	Round 2		Round 3	
	Count	% of total	Count	% of total
	+BDNF	-BDNF	+BDNF	-BDNF
CVDSTGERWC	287	299	0.653%	0.659%
CRLDFC	137	23	0.312%	0.051%
CRLDVCSP	108	48	0.246%	0.106%
CRGDRRALNC	103	42	0.234%	0.093%
CAVRDNTTTC	76	11	0.173%	0.024%
CRMFTNRSKC	58	36	0.132%	0.079%
CVGTLIGEC	47	22	0.107%	0.048%
CSIVSNSKDC	44	0	0.100%	0.000%
CRKTRSNQEC	42	2	0.096%	0.004%
CSQHRTRSKC	40	19	0.091%	0.042%
CLEESTRRAC	39	11	0.089%	0.024%
CAKRGDVGPC	39	20	0.089%	0.044%
CAGNKTHGRC	38	10	0.086%	0.022%
CTKKRC	38	0	0.086%	0.000%
CKVNKSTKCC	37	7	0.084%	0.015%
CVSDSCNPSC	36	11	0.082%	0.024%
CNSGSASSKC	36	4	0.082%	0.009%
CANSTGKRRC	36	23	0.082%	0.051%
CTRTDGIDTC	35	29	0.080%	0.064%
CNRSRTSKVC	35	12	0.080%	0.026%
CPTGDSYKCC	34	2	0.077%	0.004%
CDGYRMQGSC	8	0	0.018%	0.000%
CLGQNLDNSC	2	5	0.005%	0.011%
CLSLKHTTSC	8	3	0.018%	0.007%
Total	43972	45403	-	-
Unique	13464	16467		

Peptides	Round 3		Round 3	
	Count	% of total	Count	% of total
	+BDNF	-BDNF	+BDNF	-BDNF
CRLDFC	4015	6859	12.632%	12.760%
CRGDRRALNC	3742	5473	11.773%	10.182%
CRLDVCSP	1102	1856	3.467%	3.453%
CSQEIVYELC	1071	1578	3.370%	2.936%
CVGTLIGEC	862	1180	2.712%	2.195%
CVDSTGERWC	773	1176	2.432%	2.188%
CRLDVC	600	802	1.888%	1.492%
CRGDRRSTEC	557	1236	1.752%	2.299%
CARIRGDMAC	418	781	1.315%	1.453%
CNEIVYDLSC	228	356	0.717%	0.662%
CDRVFELNPC	212	303	0.667%	0.564%
CQKQEYCNP	158	292	0.497%	0.543%
CTAFDAVNIC	150	114	0.472%	0.212%
CDVVYELTSC	144	153	0.453%	0.285%
CGLQSYCDPC	141	284	0.444%	0.528%
CEWTLTPPAC	117	122	0.368%	0.227%
CFDLTFTQDC	109	76	0.343%	0.141%
CAVRDNTTTC	108	121	0.340%	0.225%
CVGGGC	102	1	0.321%	0.002%
CRDNKTWPPC	98	209	0.308%	0.389%
CFDGVESYEC	97	103	0.305%	0.192%
CDGYRMQGSC	5	3	0.016%	0.006%
CLGQNLDNSC	7	0	0.022%	0.000%
CLSLKHTTSC	11	1	0.035%	0.002%
Total peptides	31784	53752	-	-
Unique peptides	3006	3642	-	-

In the second round the number of unique phages was 13464 in BDNF-treated sample and 16467 from the untreated sample, with a ratio of 0.82, which indicated reduced discrepancies between the libraries observed in the first round. The total number of phages in the BDNF-treated and untreated samples reached 43972 and 45403 giving ratio of 0.97. The top 20 most abundant phages are presented in Table 1.15. The most abundant sequence, CVDSTGERWC, amounted to 0.65% of the total phage number in the BDNF-treated sample and 0.66% in the untreated sample, with a selection ratio of 1, which is consistent with a unique phage number ratio and lower than total phage number ratio. CRLDFC was the second most abundant peptide with 0.31% and 0.05% of total phages number in the BDNF-treated and untreated sample respectively with a 6.2 selection ratio, which indicates specificity toward the target sample. Moreover, this peptide shared similar RLDV(F) motif with the third most abundant peptide in the current library, CRLDVCSP, as well as second and third most abundant peptides in second round CX7C library, CRLDVC and CRLDFCS.

Table 1.16 Sanger sequencing results.
Phages selected for ELISA are in bold

Sequence	Number
CGKX TNR VSC	1
CRLDFC	4
CSLL VE SFD	1
C NK ST SGL NC	1
CS QEI V YEL C	3
CRG DRR AL NC	2
CL SS SR AIV C	1
C GL GR EN LEC	1
CF DG VE FY QC	1
C N VE GV TVIC	1
CRL T KG K H PC	1
CDG Y RM Q G SC	1
CLG Q NLD NSC	1
CLDV SPY	1
CE II EG SA	1
CLS L KHT TSC	1
CL KIK K G PGC	1
CKT D VR K M PC	1
Total	48

In the third round the number of unique phages was 3006 from the BDNF-treated sample and 3642 from the untreated sample, with a ratio of 0.83 which was similar to the previous rounds. The total number of phages in the BDNF-treated and untreated samples reached 31784 and 53752, giving a ratio of 0.59. The diversity of library was greatly reduced in the third round as with CX7C, so no further selection rounds were required. The most abundant sequence, CRLDFC, amounted to 13% of the total phage number in both BDNF-treated and untreated sample, with a selection ratio of 1, indicating no specificity toward the BDNF-treated sample that was observed in the second round. CRLDVCSP phage total number was also higher, up to 1102 and 1856, amounting to 3.5% in both BDNF-treated and untreated samples. Round 3

CX8C results were similar to CX7C in terms of specificity.

Sequence analysis of the round 2 library top 20 CX7C peptides (excluding peptides with less than 7 amino acids between C) (Figure 1.2.28A) showed a prevalence of charged amino acids like Arg and Lys at 2, 3, 5, and 7-9 positions, and Gly and Ser/Thr at 3-8 positions in the BDNF-treated library. Sequences made from the two most frequent amino acids were CAGS**R**TRK**K**C and CR**K**T**S**GS**G**EC. In contrast, untreated samples contained peptides with more frequent occurrences of Asp at various positions. The sequences of the two most frequent amino acids were CR**S**D**G**DAL**K**C and CAD**N**T**N**GV**T**C. In both libraries Ala and Arg were present at the second position, while Lys at the ninth. In the third round BDNF-treated library negatively charged amino acids Asp and Glu became more frequent in contrast to the second round BDNF-treated library, while Arg became more prominent in the untreated library (Figure 1.2.28B).

For Sanger sequencing random plaques from the amplified plates of round 3 BDNF-treated library were collected and submitted to sequencing (Table 1.16). C**R**L**D**F**C** phage was in 8% of all selected plaques and C**S**Q**E**I**V**Y**E**L**C** and C**R**G**D**R**R**A**L**N**C** were the next most abundant phages at 6.25% and 4.2% respectively. Sanger sequencing results were not similar to the Ion Torrent sequencing outcome, as very rare peptides were gathered with only 3 peptides collected in the top 20 sequences. Based on the selection parameters C**D**G**Y**R**M**Q**G**S**C**, C**L**G**Q**N**L**D**N**S**C**, and C**L**S**L**K**H**T**T**S**C** were selected.

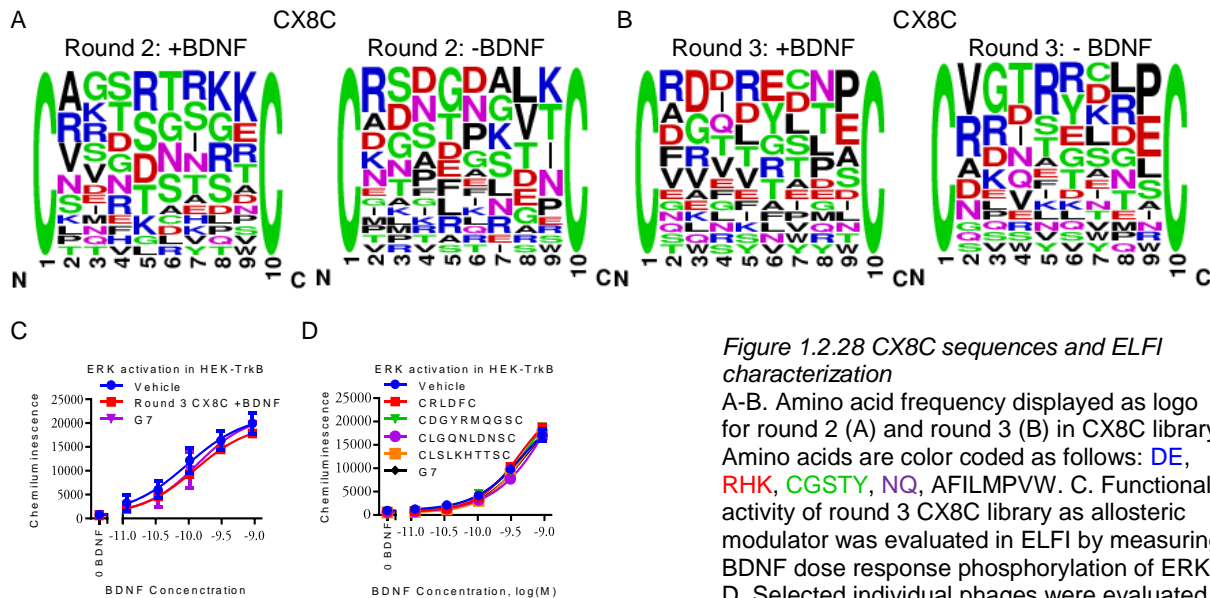


Figure 1.2.28 CX8C sequences and ELFI characterization
 A-B. Amino acid frequency displayed as logo for round 2 (A) and round 3 (B) in CX8C library. Amino acids are color coded as follows: DE, RHK, CGSTY, NQ, AFILMPVW. C. Functional activity of round 3 CX8C library as allosteric modulator was evaluated in ELFI by measuring BDNF dose response phosphorylation of ERK. D. Selected individual phages were evaluated as allosteric modulators in ELFI measuring BDNF dose response phosphorylation of ERK.

The entire round 3 CX8C BDNF-treated library and selected phages were tested for allosteric modulation of BDNF activity at ERK in HEK-TrkB cells (Figure 1.2.28C-D). No significant influence of the library or individual phages were measured probably for the same reason as with CX7C phages.

1.2.10.3 Conclusion of Phage Display

Our efforts to utilize phage display platform for finding structures to modulate TrkB activity showed promising results based on the enrichments of the libraries. Initial testing of the sequences, identified in the course of the selection, were focused the most abundant peptides. Moving forward, a more sophisticated sequence analysis should be applied to find TrkB selective sequences. In the future, optimization and improvement of the phage display protocol should allow us to identify more specific sequences.

1.3 Discussion

BDNF and TrkB are important pharmacological targets. The neurotrophin based therapy has shown promise in the treatment of many treatment-resistant diseases. It is no wonder that significant effort has been put into developing probes that could influence this system. Given the positive results of BDNF infusion into animals, it has been surprising that BDNF injection has shown little effect in the treatment of ALS. There have been several hypotheses into why intrathecal injection has not yielded the expected results. One possibility has been the dose of injected BDNF. In animal models, the effects of BDNF have been detected at 5-10 mg/kg dose, while human trials have hardly exceeded 150 µg/kg without inducing adverse reaction to the injection and side effects such as the relieved constipation. The other hypothesis has been poor pharmacokinetics of the neurotrophic factors. In mice, it has been demonstrated that BDNF was readily cleared from blood following i.v. injections. Even though BDNF has shown affinity to brain vasculature, it has had little penetration of BBB shown by 2 independent experiments: i.v. injection did not produce high concentration of BDNF in CSF, while intrathecal injections have had produced little dose of BDNF in the serum. S.c. injection did produce a longer half-life of BDNF in the blood stream, but the BDNF dose did not exceed 16 ng/ml dose in the serum, making it ineffective (61). Another hypothesis is based on BDNF interaction with p75NTR. Several reports have shown that in

the presence of p75 BDNF did not produce the expected neurotrophic effects such as axonal growth and myelination (142), which could explain the lack of positive results in ALS studies.

All these shortcomings have left little room to argue against developing alternative agonists or modulators of TrkB. Having a lead compound, it would be possible to modify the structure to penetrate BBB and have longer a half-life in the serum. Moreover, such a lead compound could be specific to TrkB over p75NTR and thus would presumably induce a neurotrophic response even in the presence of p75NTR. Alternatively, having a positive allosteric modulator might open the possibility of attenuating the side effects encountered in the BDNF infusion studies, while potentiating endogenously released BDNF. For example, physical activity has been shown to induce BDNF release (143). In the depressed brain BDNF release has been low, so having a PAM might help to overcome BDNF shortage in depressed patients performing exercises.

To examine the key pharmacological and signaling properties of reported small molecule TrkB agonists, a number of quantitative and complementary *in vitro* cell assays were developed. BDNF, NT4, and NT3 robustly activated TrkB in these assays, whereas to our surprise and disappointment, activation of TrkB by any of the reported small molecule TrkB agonists could not be reproduced (125). A recent report by the authors who introduced 7,8-DHF as a TrkB agonist suggested that its activity in CNC *in vitro* has been dependent on days *in vitro* (DIV) of culture and have reported significant activation of the receptor beyond DIV 13 (88). Also, several other protocol modifications have been suggested by the author (personal communication; e.g., preparing 7,8-DHF stock solution in DMSO immediately before the experiments as 7,8-DHF may not be stable in solution). However, none of these protocol adjustments have altered the negative outcomes in our laboratory. The positive controls have worked reliably in multiple assays, while 7,8-DHF (and the other reported compounds) have not activated our TrkB system *in vitro*. This compound along with deoxygedunin and amitriptyline have been found as TrkB agonist using survival assay from staurosporine-induced apoptosis in TrkB expressing cells, while K252a has been used to inhibit TrkB as evidence of TrkB-dependent activity of the compounds. Interestingly, staurosporine is a parent compound of K252a and has inhibited non-specifically many kinases. Moreover, K252a potentiated AKT phosphorylation induced by BDNF and Zn in cortical neuronal culture (Figure 1.2.11). Similar activity of staurosporine could be hypothesized. Then, staurosporine at 100 μM may have

potentiated Akt phosphorylation induced by BDNF and other compounds activity, and support anti-apoptotic activity of these compounds, while still inhibiting other kinases (Trk family, c-MEK). It has also been reported that staurosporine has induced neurite outgrowth (144, 145). Although the difficulty of reproducing the *in vitro* results have been discussed at conferences for several years, only recently has an independent research group reported a study that failed to confirm some of the reported small molecule compounds as TrkB agonists (115), consistent with our own results described here.

One plausible explanation for the observed discrepancies could be methodological in nature. Although western blot has been one of the standard core methods used in life sciences and has been widely utilized for the detection of phosphorylation states of receptors and kinases, it must be used cautiously for quantification, particularly of dynamic processes like kinase phosphorylation. Western blot requires a number of procedural steps (e.g., sample preparation, electrophoresis, transfer to blot), which make it impractical to perform multiple repeats for each experimental condition (including controls). Moreover, densitometry is quite dependent on the analysis procedure, which may lead to biased results, especially with the low level of phosphorylation of the protein of interest. Specificity of the antibody has played an important role as well (146, 147). While we could confidently use pERK and pAkt antibodies, as they have provided highly specific staining in blot (Figure 1.2.7), it has been more difficult finding a specific antibody for pTrkB, as these antibodies tend to stain other targets.

For example, 7,8-DHF has been tested *in vivo* in many different disease models (see introduction) by several independent laboratories. The behavioral or physiological outcomes have been consistent with what would be expected for a TrkB agonist (plasticity inducer, repair enhancer). However, most of the *in vivo* reports of the molecular mechanism have been based on post mortem western blot. In some reports western blot results were not strictly analyzed. For example, in one report pTrkB has been falsely identified at 92 kDa, while in the other paper densitometric analysis did not account for the background on the lane and measured larger density than should have been. Most of these papers have also failed to provide full blots, most likely due to procedural chopping of the blot to streamline the analysis. Given the drawbacks of this method, alternative, more robust assays should be used to directly confirm a TrkB-mediated mechanism of action.

Complementary methods should be applied to confirm the western blot results. In our view, the described ELISA and ELFI provide sufficient throughput for controls and repeats to be used along with the blot to more accurately characterize drug activity. We have recommended western blots to be used as a qualitative (or semi-quantitative) complementary method to the quantitative ELISA assays, as confirmation that the ELISA indeed detects the desired phosphorylation reaction (125). Alternative methods should also be considered that are independent from antibodies, like those methods based on enzymatic activity of reporter proteins as the readout mechanism.

In methodological terms, even though *in vitro* assays afford the necessary probing power to characterize the mechanism of action of compounds on a molecular level (e.g., induction of TrkB receptor phosphorylation), these assays are often challenging to adjust for *in vivo* application. In mechanistic terms, the *in vitro* experimental system might not represent the native *in vivo* receptor complex and or recapitulate the possibilities of circuit-level effects. Indeed, activity of antidepressant drug, imipramine, *in vivo* has been associated with TrkB phosphorylation in hippocampus and medial prefrontal cortex of mice, however, *in vitro* no TrkB phosphorylation has been detected in cortical or hippocampal neuronal culture, leading to conclusion that imipramine indirectly induced TrkB phosphorylation (109). Thus, 7,8-DHF might have indirectly activated TrkB *in vivo* through the mechanisms that might not be available *in vitro*. Pharmacokinetics might have also played a role in the activity of the compound. 7,8-DHF has likely been converted in the body into a number of metabolites that could have induced the observed effects *in vivo* (89). It has also been known that TrkB could have undergone transactivation through the activation of several GPCRs, RTKs, or kinases, e.g. EGFR and Src (127, 128, 148, 149). Therefore 7,8-DHF and/or its metabolite might have also in theory induced transactivation of TrkB through other pathways that have not been present *in vitro*. Although the *in vivo* activity of a compound has been ultimately what has mattered for drugs and molecular probes, *in vitro* assays have been an important tool typically required for detailed characterization and further development of compound leads (150)

Efforts to find TrkB agonist or allosteric modulator has proven to be a challenging task. Compounds reported in literature or found through a high throughput screen have not activated or modulated TrkB in our lab. Moreover, receptor tyrosine kinase agonists have seemed to be hard to develop in general, as little example of successful agonists of RTK proteins could have been found in

literature to date. Most of the compounds have appeared to be inhibitors or protein-based agonists, like antibodies. Pharmacologically, RTK structure has not favored small molecule interactions in the ligand binding domain for activation or modulation, while the kinase domain possesses ATP binding site that has typically been targeted by small molecule inhibitors. Targeting BDNF-TrkB complex might prove to be favorable for finding modulators, as this complex might create binding pockets for small molecule interactions. It could also be beneficial to use peptides or larger molecules that possess larger surface area available for interacting with the receptor.

1.4 Conclusion

BDNF and TrkB represent a new frontier for addressing treatment of many CNS diseases and conditions. However, being the part of RTK superfamily, development of agonists or modulators of TrkB remains to be challenging. Prominent reported agonists failed to reproduce their activity at TrkB in different assays. HTS had not led to any small molecule structures that activate the receptor in vitro. New innovative approaches must be developed to find true, therapeutically applicable agonists.

1.5 Materials and Methods

1.5.1 Materials

Chemicals were purchased from different commercial sources: 7,8-dihydroxyflavone from TCI America, #D1916; LM22A-2 and LM22A-3 from eMolecules; amitriptyline hydrochloride (#A8404), deprenyl (M003), zinc with 2 equivalents pyrithione ionophore (Zn-2PT, ZPT) (H6377) from Sigma Aldrich; L-783,281 (DMAQ-B1) (#1819) and K252a (#1683) from Tocris; thapsigargin from Cayman Chemical (#10522). Deoxygedunin was synthesized from gedunin (Tocris, #3387)(151). LM22A-4, 5E5 and its precursors were synthesized in-house (see below). A list of antibodies is presented in the table below:

Target	Vendor	Cat. #	Source
Pan-pTyr	R&D Systems	HAM1676	Mouse IgG ₁
TrkB	Abnova	H00004915-M02	Mouse mAb
	Abcam	ab82855	Rabbit pAb
	SCBT	H-181	Rabbit pAb
	SCBT	SC-11	Rabbit pAb
	SCBT	SC-12	Rabbit pAb
	Sigma Aldrich	T1941	Goat pAb
	R&D Systems	AF397	Goat pAb
	Sino Biologicals	10047-RP02	Rabbit pAb
pTrkB (pY516)	Cell Signaling	#4619	Rabbit mAb
pTrkB (pY706/707)	Cell Signaling	#4621	Rabbit mAb
pTrkB (pY816)	Cell Signaling	#4168	Rabbit mAb

p-AKT (pS473)	Cell Signaling	#4060	Rabbit mAb
AKT1	Cell Signaling	#2938	Rabbit mAb
p-ERK	Cell Signaling	#4370	Rabbit mAb
ERK	Cell Signaling	#9102	Rabbit pAb
Rabbit IgG	Cell Signaling	#7074	Goat Ab

1.5.2 Western Blot

CNC were seeded in PDL-coated 12-well plated at 3×10^5 cell/well. After the experiment, cells were lysed with 100 μ L of lysis buffer (Pierce RIPA buffer with 1:100 protease inhibitor cocktail, phosphatase inhibitor 2 and 3 cocktails (Sigma, P5726, P0044), and 0.5M EDTA solution, or ELISA lysis buffer) and incubated over ice for 15 minutes to an hour, after which time cells were scraped and the lysates transferred into microcentrifuge tubes. The tubes were centrifuged at 14,500 rpm for 10 minutes, the supernatant was transferred to fresh tubes, and the protein content was measured using the Pierce BCA assay. Lysates were diluted with 5x loading buffer (50% glycerol, 313 mM Tris, 10% SDS, bromophenol for color, pH 6.8), β -mercaptoethanol (5% final concentration), and any necessary amount of water to bring all samples to the same volume. Equal quantities of protein (typically 10 μ g/lane) were added to each well of a 10% bis-tris acrylamide gel and were blotted onto Immobilon P PVDF transfer membranes. Blots were blocked in 3% BSA in TBS for at least 30 min, followed by an hour incubation with the primary antibody with rocking at RT. The blots were washed 3 x 5 minutes with TBST (0.05% Tween20), incubated for 30 min with secondary antibody (typically 1:1000) in the buffer indicated on the antibody's corresponding data sheet, then washed again for 3 x 5 minutes prior to development with the ECL kit (ThermoScientific, PI34079). Chemiluminescence and light absorbance (for protein ladder) was visualized with a Kodak Image Station 440CF imager. Membranes were stripped and re-probed with the stripping buffer used in the in-cell ELISA followed by the same detection procedure for the next target protein. The chemiluminescent image was overlaid to the absorbance image for representation.

1.5.3 Cell lines

A HEK cell line stably transfected with human TrkB was a generous gift of Prof. Moses Chao (NYU). Cells were cultured in a 5% CO₂ atmosphere at 37 °C in Dulbecco's Modified Eagle Medium (DMEM) with GlutaMAX (Life Technologies, Grand Island, NY, USA, 10569, 10569044) supplemented with 10% Fetal Bovine Serum (FBS) (Premium Select, Atlanta Biologicals; Atlanta, GA, USA, S11550) and 100 Uml⁻¹ penicillin and 100 μ gml⁻¹ streptomycin (Life Technologies, 15140) and 200 μ g/ml G418

sulfate (MP Biomedicals, 091672548). Invitrogen CHO K1 cell line with CellSensor® construct (TrkB-NFAT-bla, K1491) was obtained from Life Technologies and cultured in growth medium (DMEM with GlutaMax) supplemented with 10% dialyzed FBS (Invitrogen, 26400-044), 1x MEM NEAA (Sigma, M7145), 25 mM HEPES (Sigma, H0887), 5 µg/mL Blasticidin (Life Technologies, R21001) and 200 µg/ml Zeocin (Life Technologies, R25001). Cortical neurons were isolated from E18 rat embryos and were seeded on flat-bottom white 96-well plates (4×10^4 cells/well) or 12-well plates ($2-3 \times 10^5$ cells/well) coated with poly-D-lysine (PDL) (Sigma, P6407) and cultured in Neurobasal medium (1/50 dilution, Life Technologies, 21103-049) supplemented with B27 supplement (1/100 dilution, Life Technologies, 17504) and GlutaMAX (Life Technologies, 35050) without changing medium until the experiment day. SH-SY5Y cells were seeded in 24-well plates (2×10^5 cells/well) and incubated for 48 hours in DMEM/F12 1:1 (Invitrogen, 11330057) supplemented with 10% FBS and 100 Uml⁻¹ penicillin and 100 µgml⁻¹ streptomycin. Then cells were washed with PBS and incubated for 48 hours in DMEM/F12 1:1 supplemented with 4% FBS, 100 Uml⁻¹ penicillin, 100 µgml⁻¹ streptomycin, and 10 µM all-trans retinoic acid (Sigma, R2625). Prior to treatment with compounds, cells were incubated for at least 6 hours in medium without all-trans retinoic acid.

1.5.4 Sandwich ELISA:

TrkB phosphorylation level was quantified using the previously described KIRA-ELISA (152) with slight modification. On the day of experiment cells were washed and incubated with culturing medium without proteins (FBS or B-27 supplement) for 0.5-1 hour. Compounds at 5x of working concentrations were delivered in medium with $\leq 2.5\%$ DMSO (to accommodate $\leq 0.5\%$ DMSO in culture). Cells were treated for various times. Experiments were stopped by removing medium on ice and cells were lysed in 100 µl of ELISA lysis buffer (0.15 M NaCl, 10 mM Trizma, 10 mM Tris base, 2 mM EDTA, 1% TritonX-100, 10% glycerol, pH 8.0, 1:100 phosphatase inhibitor cocktail 2 (Sigma Aldrich, P5726), 1:100 protease inhibitor cocktail (Sigma Aldrich, P8340)). Experimental plates were kept at -20 °C or -80 °C until transferred to ELISA plate (NUNC Immulon 4 HBX) coated overnight at 4°C with appropriate capturing antibody (PBS, 0.8 µg/mL rabbit polyclonal anti-TrkB Sino Biologicals #10047-RP02, or 1 µg/mL goat polyclonal anti-TrkB Sigma Aldrich T1941 for phosphorylation assay; 1 µg/mL goat polyclonal anti-hTrkB R&D Systems AF397 for total TrkB assay) for 2-3 hours at RT or overnight at 4 °C. ELISA plates were

washed 5 times with 150 µl of washing buffer (PBS, 0.05% Tween-20) and blocked (PBS, 1% BSA) for 1 hour at RT before transfer of 80 and 20 µl of lysate for phosphorylation and total TrkB assays respectively for overnight incubation at 4 °C. On the next day, ELISA plates were washed and incubated with an appropriate detecting antibody. Tyrosine phosphorylation was quantified by 1-hour incubation with HRP-conjugated monoclonal anti-pY antibody (1/2500 R&D systems #HAM1676) in washing buffer with 0.1% BSA followed by 30 min color development of TMB One solution (Promega #G7431) The plates was then quenched with 1N HCl and absorbance was measured at 450 nm on a plate reader (BMG Labtech, Cary, NC, USA). Total TrkB was quantified similarly using anti-TrkB antibody (0.8 µg/mL Sino Biologicals #10047-RP02, 1.5 hours incubation) and HRP conjugated anti-rabbit IgG (1:1000 Cell Signaling Technologies #7074).

1.5.5 ELFI

Phosphorylation levels of TrkB at specific tyrosine residues and downstream signaling proteins were quantified using in-Cell ELISA. Cells were treated similarly as in sandwich ELISA. Experiments were stopped by fixing the cells in 4% formaldehyde (Sigma, F8775) for 20 min. Cells were permeabilized with washing buffer, blocked in washing buffer with 10% BSA, and incubated with detecting antibody for protein of interest for 2 hours at RT or overnight at 4 °C. Appropriate HRP-linked secondary antibody was applied and luminescence (SuperSignal® ELISA Pico Chemiluminescent Substrate, ThermoScientific #37070) was detected on the plate reader. To quantify different proteins in the same plate, antibodies were stripped using stripping buffer (153) (6M Guanidine*HCl, 0.2% Triton X-100, 20 mM Tris*HCl, pH 7.5) for 5 min, washed, blocked, and treated with another antibody. Stripping and re-probing cycles were done up to 6 times.

1.5.6 DiscoverX PathHunter® assay

PathHunter® U2OS TrkB-P75 Cells were detached by detachment reagent (DiscoverX) and resuspended in Plating 16 reagent (DiscoverX). Cells (5000 cells/well) were plated into 384-well plate (Corning). Plates were incubated at 37 °C in 5% CO₂ for about 20 hours. Compounds were pin-transferred to the cells. For agonist assay, cells with compounds were incubated for 3 hours at 37°C. For allosteric agonist assay, cells were treated with compounds first and after three minutes EC₁₅ BDNF (DiscoverX) was added for 3 hours (incubation at 37 °C). Detection reagent (DiscoverX) was added for

incubation 1 hour at room temperature in the dark. The luminescence was measured in the Envision plate reader (Perkin Elmer).

Invitrogen CellSensor assay: Assay was performed according to the Invitrogen protocol. Briefly, cells were seeded in 384-well plates at 1.2×10^4 cells/well in medium without Blasticidin and Zeocin overnight. On the next day, cells were treated with compounds for 5 h. After treatment, wells were loaded with β -lactamase LiveBLazer™-FRET B/G substrate (CCF4-AM, Invitrogen, K1095) for 2 hours. Fluorescence at 450 nm and 510 nm was recorded on a plate reader (excitation wavelength 410 nm).

1.5.7 Phage Display

T7-select phage display system (EMD Biosciences, Gibbstown, NJ) was used for individual peptide-phage cloning according the manufacturer's instructions. Phage was purified by precipitation with PEG-8000 (Sigma, St. Louis, MO). The sequences of displayed peptides were determined from the DNA encoding the insert-containing region at the C-terminus of the T7 major coat protein gp10.

For cell-based phage display (154), cultured cells were dissociated with trypsin, centrifuged, and resuspended in 1% bovine serum albumin (BSA) PBS (Lonza) medium. Typically, 1 million cells were resuspended in 1 ml of the medium in 15 ml tubes, then phage libraries were added, followed by BDNF at 100 ng/ml. Biopanning was performed in 15 ml tubes placed in angled magnetic holder on rocker at 4°C. After the biopanning, cells were washed 5 times with the medium and transferred to a new tube after each washing round, lysed in LB bacterial growth medium containing 1% NP-40, and phage was titrated.

1.5.8 Statistical analysis

Statistical analysis was performed using GraphPad Prism software 2-way ANOVA analysis followed by Dunnett's t-test (compared to DMSO). Statistical significance was assigned by stars: * $p < 0.05$, ** $p < 0.01$, *** $p < 0.001$, **** $p < 0.0001$. Dose response curves were fit using built-in GraphPad function non-linear function log[agonists] vs response with variable slope and four parameters. Signal-to-background ratios were calculated by dividing the highest positive response value by the negative control value (typically DMSO).

1.6 References

1. Machado Dias, A. 2011. Bioinformatics Approach to BDNF and BDNF-Related Disorders. *Curr. Neuropharmacol.* 9: 318–329.
2. Yoshii, A., and M. Constantine-Paton. 2010. Postsynaptic BDNF-TrkB signaling in synapse maturation, plasticity, and disease. *Dev. Neurobiol.* 70: 304–322.
3. Huang, E. J., and L. F. Reichardt. 2001. Neurotrophins: roles in neuronal development and function. *Annu. Rev. Neurosci.* 24: 677–736.
4. Lu, B., G. Nagappan, and Y. Lu. 2014. BDNF and synaptic plasticity, cognitive function, and dysfunction. *Handb. Exp. Pharmacol.* 220: 223–50.
5. Castrén, E., M. Pitkänen, J. Sirviö, A. Parsadanian, D. Lindholm, H. Thoenen, and P. J. Riekkinen. 1993. The induction of LTP increases BDNF and NGF mRNA but decreases NT-3 mRNA in the dentate gyrus. *Neuroreport* 4: 895–8.
6. Figurov, A., L. D. Pozzo-Miller, P. Olafsson, T. Wang, and B. Lu. 1996. Regulation of synaptic responses to high-frequency stimulation and LTP by neurotrophins in the hippocampus. *Nature* 381: 706–709.
7. Edelmann, E., V. Leßmann, and T. Brigadski. 2014. Pre- and postsynaptic twists in BDNF secretion and action in synaptic plasticity. *Neuropharmacology* 76: 610–627.
8. Korte, M., P. Carroll, E. Wolf, G. Brem, H. Thoenen, and T. Bonhoeffer. 1995. Hippocampal long-term potentiation is impaired in mice lacking brain-derived neurotrophic factor. *Proc. Natl. Acad. Sci. U. S. A.* 92: 8856–60.
9. Patterson, S. L., T. Abel, T. A. Deuel, K. C. Martin, J. C. Rose, and E. R. Kandel. 1996. Recombinant BDNF rescues deficits in basal synaptic transmission and hippocampal LTP in BDNF knockout mice. *Neuron* 16: 1137–45.
10. Egan, M. F., M. Kojima, J. H. Callicott, T. E. Goldberg, B. S. Kolachana, A. Bertolino, E. Zaitsev, B. Gold, D. Goldman, M. Dean, B. Lu, and D. R. Weinberger. 2003. The BDNF val66met polymorphism affects activity-dependent secretion of BDNF and human memory and hippocampal function. *Cell* 112: 257–69.
11. Ninan, I. 2014. Synaptic regulation of affective behaviors; role of BDNF. *Neuropharmacology* 76 Pt C: 684–95.
12. Mühlberger, A., M. Andreatta, H. Ewald, E. Glotzbach-Schoon, C. Tröger, C. Baumann, A. Reif, J. Deckert, and P. Pauli. 2013. The BDNF Val66Met Polymorphism Modulates the Generalization of Cued Fear Responses to a Novel Context. *Neuropsychopharmacology* 1–9.
13. Cabelli, R. J., a Hohn, and C. J. Shatz. 1995. Inhibition of ocular dominance column formation by infusion of NT-4/5 or BDNF. *Science* 267: 1662–1666.
14. Minichiello, L. 2009. TrkB signalling pathways in LTP and learning. *Nat. Rev. Neurosci.* 10: 850–60.
15. Bekinschtein, P., M. Cammarota, and J. H. Medina. 2014. BDNF and memory processing. *Neuropharmacology* 76 Pt C: 677–83.
16. Weber, A. J., and C. D. Harman. 2013. BDNF treatment and extended recovery from optic nerve trauma in the cat. *Investig. Ophthalmol. Vis. Sci.* 54: 6594–6604.
17. Zigova, T., V. Pencea, S. J. Wiegand, and M. B. Luskin. 1998. Intraventricular administration of BDNF increases the number of newly generated neurons in the adult olfactory bulb. *Mol. Cell. Neurosci.* 11: 234–45.
18. Pencea, V., K. D. Bingaman, S. J. Wiegand, and M. B. Luskin. 2001. Infusion of brain-derived neurotrophic factor into the lateral ventricle of the adult rat leads to new neurons in the parenchyma of the striatum, septum, thalamus, and hypothalamus. *J. Neurosci.* 21: 6706–6717.
19. Li, Y., B. W. Luikart, S. Birnbaum, J. Chen, C.-H. H. Kwon, S. G. Kernie, R. Bassel-Duby, and L. F. Parada. 2008. TrkB regulates hippocampal neurogenesis and governs sensitivity to antidepressive treatment. *Neuron* 59: 399–412.
20. Wei, Z., J. Liao, F. Qi, Z. Meng, and S. Pan. 2015. Evidence for the contribution of BDNF-TrkB signal strength in neurogenesis: An organotypic study. *Neurosci. Lett.* 606: 48–52.
21. Bath, K. G., and F. S. Lee. 2010. Neurotrophic Factor Control of Adult SVZ Neurogenesis. *Dev Neurobiol* 70: 339–349.
22. Ceni, C., N. Unsain, M. P. Zeinieh, and P. A. Barker. 2014. Neurotrophins in the regulation of cellular survival and death. *Handb. Exp. Pharmacol.* 220: 193–221.
23. Castrén, E., and T. Rantamäki. 2010. The role of BDNF and its receptors in depression and antidepressant drug action: Reactivation of developmental plasticity. *Dev. Neurobiol.* 70: 289–97.
24. Rantamäki, T., P. Hendolin, A. Kankaanpää, J. Mijatovic, P. Piepponen, E. Domenici, M. V Chao, P. T. Männistö, and E. Castrén. 2007. Pharmacologically diverse antidepressants rapidly activate brain-derived neurotrophic factor receptor TrkB and induce phospholipase-Cgamma signaling pathways in mouse brain. *Neuropsychopharmacology* 32: 2152–62.
25. Bergami, M., R. Rimondini, S. Santi, R. Blum, M. Götz, and M. Canossa. 2008. Deletion of TrkB in adult progenitors alters newborn neuron integration into hippocampal circuits and increases anxiety-like behavior. *Proc. Natl. Acad. Sci. U. S. A.* 105: 15570–5.
26. Siuciak, J. A., D. R. Lewis, S. J. Wiegand, and R. M. Lindsay. 1997. Antidepressant-like effect of brain-

- derived neurotrophic factor (BDNF). *Pharmacol. Biochem. Behav.* 56: 131–7.
27. Saarelainen, T., P. Hendolin, G. Lucas, E. Koponen, M. Sairanen, E. MacDonald, K. Agerman, A. Haapasalo, H. Nawa, R. Aloyz, P. Ernfors, and E. Castrén. 2003. Activation of the TrkB neurotrophin receptor is induced by antidepressant drugs and is required for antidepressant-induced behavioral effects. *J. Neurosci.* 23: 349–57.
 28. Pittenger, C., and R. S. Duman. 2008. Stress, depression, and neuroplasticity: a convergence of mechanisms. *Neuropsychopharmacology* 33: 88–109.
 29. Martinowich, K., H. Manji, and B. Lu. 2007. New insights into BDNF function in depression and anxiety. *Nat. Neurosci.* 10: 1089–93.
 30. Boulle, F., G. Kenis, M. Cazorla, M. Hamon, H. W. M. Steinbusch, L. Lanfumey, and D. L. a van den Hove. 2012. TrkB inhibition as a therapeutic target for CNS-related disorders. *Prog. Neurobiol.* 98: 197–206.
 31. Castrén, E. 2014. Neurotrophins and psychiatric disorders. *Handb. Exp. Pharmacol.* 220: 461–79.
 32. Hashimoto, K. 2010. Brain-derived neurotrophic factor as a biomarker for mood disorders: an historical overview and future directions. *Psychiatry Clin. Neurosci.* 64: 341–57.
 33. Duman, R. S., N. Li, R. J. Liu, V. Duric, and G. Aghajanian. 2012. Signaling pathways underlying the rapid antidepressant actions of ketamine. *Neuropharmacology* 62: 35–41.
 34. Maya Vetencourt, J. F., A. Sale, A. Viegi, L. Baroncelli, R. De Pasquale, O. F. O’Leary, E. Castrén, and L. Maffei. 2008. The antidepressant fluoxetine restores plasticity in the adult visual cortex. *Science* 320: 385–8.
 35. Palazidou, E. 2012. The neurobiology of depression. *Br. Med. Bull.* 101: 127–45.
 36. Lu, B., G. Nagappan, X. Guan, P. J. Nathan, and P. Wren. 2013. BDNF-based synaptic repair as a disease-modifying strategy for neurodegenerative diseases. *Nat. Rev. Neurosci.* 14: 401–416.
 37. Gupta, V. K., Y. You, V. B. Gupta, A. Klistorner, and S. L. Graham. 2013. TrkB Receptor Signalling: Implications in Neurodegenerative, Psychiatric and Proliferative Disorders. *Int. J. Mol. Sci.* 14: 10122–42.
 38. Zuccato, C., and E. Cattaneo. 2014. Huntington’s disease. *Handb. Exp. Pharmacol.* 220: 357–409.
 39. Hock, C., K. Heese, C. Hulette, C. Rosenberg, and U. Otten. 2000. Region-Specific Neurotrophin Imbalances in Alzheimer Disease. *Arch. Neurol.* 57: 846.
 40. Jerónimo-Santos, A., S. H. Vaz, S. Parreira, S. Rapaz-Lérias, A. P. Caetano, V. Buée-Scherrer, E. Castrén, C. A. Valente, D. Blum, A. M. Sebastião, and M. J. Diógenes. 2015. Dysregulation of TrkB Receptors and BDNF Function by Amyloid- β Peptide is Mediated by Calpain. *Cereb. Cortex* 25: 3107–21.
 41. Nagahara, A. H., D. a Merrill, G. Coppola, S. Tsukada, B. E. Schroeder, G. M. Shaked, L. Wang, A. Blesch, A. Kim, J. M. Conner, E. Rockenstein, M. V Chao, E. H. Koo, D. Geschwind, E. Masliah, A. a Chiba, and M. H. Tuszynski. 2009. Neuroprotective effects of brain-derived neurotrophic factor in rodent and primate models of Alzheimer’s disease. *Nat. Med.* 15: 331–337.
 42. Boyce, V. S., and L. M. Mendell. 2014. Neurotrophic Factors in Spinal Cord Injury. In *Handbook of experimental pharmacology* vol. 220. 443–460.
 43. Wehrman, T., X. He, B. Raab, A. Dukipatti, H. Blau, and K. C. Garcia. 2007. Structural and Mechanistic Insights into Nerve Growth Factor Interactions with the TrkA and p75 Receptors. *Neuron* 53: 25–38.
 44. Ultsch, M. H., C. Wiesmann, L. C. Simmons, J. Henrich, M. Yang, D. Reilly, S. H. Bass, and A. M. de Vos. 1999. Crystal structures of the neurotrophin-binding domain of TrkA, TrkB and TrkC. *J. Mol. Biol.* 290: 149–59.
 45. Bertrand, T., M. Kothe, J. Liu, A. Dupuy, A. Rak, P. F. Berne, S. Davis, T. Gladysheva, C. Valtre, J. Y. Crenne, and M. Mathieu. 2012. The crystal structures of TrkA and TrkB suggest key regions for achieving selective inhibition. *J. Mol. Biol.* 423: 439–53.
 46. Lemmon, M. a., and J. Schlessinger. 2010. Cell signaling by receptor tyrosine kinases. *Cell* 141: 1117–1134.
 47. Fenner, B. M. 2012. Truncated TrkB: Beyond a dominant negative receptor. *Cytokine Growth Factor Rev.* 23: 15–24.
 48. Deinhardt, K., and M. V Chao. 2014. Shaping neurons: Long and short range effects of mature and proBDNF signalling upon neuronal structure. *Neuropharmacology* 76 Pt C: 603–9.
 49. Ohira, K., and M. Hayashi. 2009. A new aspect of the TrkB signaling pathway in neural plasticity. *Curr. Neuropharmacol.* 7: 276–85.
 50. Huang, E. J., and L. F. Reichardt. 2003. Trk receptors: roles in neuronal signal transduction. *Annu. Rev. Biochem.* 72: 609–42.
 51. Chao, M. V. 2003. Neurotrophins and their receptors: a convergence point for many signalling pathways. *Nat. Rev. Neurosci.* 4: 299–309.
 52. De Vries, L., F. Finana, F. Cachoux, B. Vacher, P. Sokoloff, and D. Cussac. 2010. Cellular BRET assay suggests a conformational rearrangement of preformed TrkB/Shc complexes following BDNF-dependent activation. *Cell. Signal.* 22: 158–65.
 53. Numakawa, T., S. Suzuki, E. Kumamaru, N. Adachi, M. Richards, and H. Kunugi. 2010. BDNF function and intracellular signaling in neurons. *Histol. Histopathol.* 25: 237–58.
 54. Kaplan, D. R., and F. D. Miller. 2000. Neurotrophin signal transduction in the nervous system. *Curr. Opin. Neurobiol.* 10: 381–91.
 55. Minichiello, L., A. M. Calella, D. L. Medina, T. Bonhoeffer, R. Klein, and M. Korte. 2002. Mechanism of

- TrkB-mediated hippocampal long-term potentiation. *Neuron* 36: 121–37.
56. Zhao, X., Y. Zhou, A. M. Weissmiller, M. L. Pearn, W. C. Mobley, and C. Wu. 2014. Real-time imaging of axonal transport of quantum dot-labeled BDNF in primary neurons. *J. Vis. Exp.* 51899.
57. van Horck, F. P. G., and C. E. Holt. 2009. Axonal mRNA Transport and Functions. In *Encyclopedia of Neuroscience* Elsevier. 1123–1131.
58. Poduslo, J. F., and G. L. Curran. 1996. Permeability at the blood-brain and blood-nerve barriers of the neurotrophic factors: NGF, CNTF, NT-3, BDNF. *Mol. Brain Res.* 36: 280–286.
59. Pardridge, W. M., Y. S. Kang, and J. L. Buciak. 1994. Transport of human recombinant brain-derived neurotrophic factor (BDNF) through the rat blood-brain barrier in vivo using vector-mediated peptide drug delivery. *Pharm. Res.* 11: 738–46.
60. Kishino, A., N. Katayama, Y. Ishige, Y. Yamamoto, H. Ogo, T. Tatsuno, T. Mine, H. Noguchi, and C. Nakayama. 2001. Analysis of effects and pharmacokinetics of subcutaneously administered BDNF. *Neuroreport* 12: 1067–1072.
61. Coulie, B., L. A. Szarka, M. Camilleri, D. D. Burton, S. McKinzie, N. Stambler, and J. M. Cedarbaum. 2000. Recombinant human neurotrophic factors accelerate colonic transit and relieve constipation in humans. *Gastroenterology* 119: 41–50.
62. Dittrich, F., G. Ochs, A. Große-Wilde, U. Berweiler, Q. Yan, J. A. Miller, K. V. Toyka, and M. Sendtner. 1996. Pharmacokinetics of intrathecally applied BDNF and effects on spinal motoneurons. *Exp. Neurol.* 141: 225–239.
63. Ochs, G., R. D. Penn, M. York, R. Giess, M. Beck, J. Tonn, J. Haigh, E. Malta, M. Traub, M. Sendtner, and K. V. Toyka. 2000. A phase I/II trial of recombinant methionyl human brain derived neurotrophic factor administered by intrathecal infusion to patients with amyotrophic lateral sclerosis. *Amyotroph. Lateral Scler.* 1: 201–206.
64. Kroin, J. S. 1992. Intrathecal drug administration. Present use and future trends. *Clin. Pharmacokinet.* 22: 319–26.
65. E.J. Kasarskis, J.M. Shefner, R.A. Smith, J. Licht, H. Mitsumoto, L.C. Hopkins, J. Rosenfeld, R. P. 1999. A controlled trial of recombinant methionyl human BDNF in ALS. *Neurology* 52: 1427–1427.
66. Thoenen, H., and M. Sendtner. 2002. Neurotrophins: From enthusiastic expectations through sobering experiences to rational therapeutic approaches. *Nat. Neurosci.* 5: 1046–1050.
67. Zuccato, C., and E. Cattaneo. 2009. Brain-derived neurotrophic factor in neurodegenerative diseases. *Nat. Rev. Neurol.* 5: 311–322.
68. Géral, C., A. Angelova, and S. Lesieur. 2013. From molecular to nanotechnology strategies for delivery of neurotrophins: Emphasis on brain-derived neurotrophic factor (BDNF). *Pharmaceutics* 5: 127–167.
69. Longo, F. M., and S. M. Massa. 2013. Small-molecule modulation of neurotrophin receptors: a strategy for the treatment of neurological disease. *Nat. Rev. Drug Discov.* 12: 507–525.
70. Jang, S.-W., X. Liu, M. Yepes, K. R. Shepherd, G. W. Miller, Y. Liu, W. D. Wilson, G. Xiao, B. Bianchi, Y. E. Sun, and K. Ye. 2010. A selective TrkB agonist with potent neurotrophic activities by 7,8-dihydroxyflavone. *Proc. Natl. Acad. Sci. U. S. A.* 107: 2687–92.
71. Jang, S.-W., X. Liu, C. B. Chan, S. a France, I. Sayeed, W. Tang, X. Lin, G. Xiao, R. Andero, Q. Chang, K. J. Ressler, and K. Ye. 2010. Deoxygedunin, a natural product with potent neurotrophic activity in mice. *PLoS One* 5: e11528.
72. Massa, S. M., T. Yang, Y. Xie, J. Shi, M. Bilgen, J. N. Joyce, D. Nehama, J. Rajadas, and F. M. Longo. 2010. Small molecule BDNF mimetics activate TrkB signaling and prevent neuronal degeneration in rodents. *J. Clin. Invest.* 120: 1774–85.
73. Wilkie, N., P. B. Wingrove, J. G. Bilsland, L. Young, S. J. Harper, F. Hefti, S. Ellis, and S. J. Pollack. 2001. The non-peptidyl fungal metabolite L-783,281 activates TRK neurotrophin receptors. *J. Neurochem.* 78: 1135–45.
74. Jang, S.-W., X. Liu, C.-B. Chan, D. Weinschenker, R. a Hall, G. Xiao, and K. Ye. 2009. Amitriptyline is a TrkA and TrkB receptor agonist that promotes TrkA/TrkB heterodimerization and has potent neurotrophic activity. *Chem. Biol.* 16: 644–56.
75. Nakaso, K., C. Nakamura, H. Sato, K. Imamura, T. Takeshima, and K. Nakashima. 2006. Novel cytoprotective mechanism of anti-parkinsonian drug deprenyl: PI3K and Nrf2-derived induction of antioxidative proteins. *Biochem. Biophys. Res. Commun.* 339: 915–22.
76. Ohmichi, M., L. Pang, A. R. Saltiel, and S. J. Decker. 1992. Inhibition of the Cellular Actions of Nerve Growth Factor by Staurosporine and K252A Results from the Attenuation of the Activity of the trk Tyrosine Kinase. *Biochemistry* 31: 4034–4039.
77. Nakano, H., and S. Ōmura. 2009. Chemical biology of natural indolocarbazole products: 30 years since the discovery of staurosporine. *J. Antibiot. (Tokyo).* 62: 17–26.
78. Liu, X., C.-B. Chan, S.-W. Jang, S. Pradoldej, J. Huang, K. He, L. H. Phun, S. France, G. Xiao, Y. Jia, H. R. Luo, and K. Ye. 2010. A Synthetic 7,8-Dihydroxyflavone Derivative Promotes Neurogenesis and Exhibits Potent Antidepressant Effect. *J. Med. Chem.* 8274–8286.
79. Blugeot, A., C. Rivat, E. Bouvier, J. Molet, A. Mouchard, B. Zeau, C. Bernard, J.-J. Benoliel, and C.

- Becker. 2011. Vulnerability to depression: from brain neuroplasticity to identification of biomarkers. *J. Neurosci.* 31: 12889–99.
80. Andero, R., S. A. Heldt, K. Ye, X. Liu, A. Armario, and K. J. Ressler. 2011. Effect of 7,8-dihydroxyflavone, a small-molecule TrkB agonist, on emotional learning. *Am. J. Psychiatry* 168: 163–72.
81. Devi, L., and M. Ohno. 2012. 7,8-Dihydroxyflavone, a Small-Molecule TrkB Agonist, Reverses Memory Deficits and BACE1 Elevation in a Mouse Model of Alzheimer's Disease. *Neuropsychopharmacology* 37: 434–444.
82. Zhang, Z., X. Liu, J. P. Schroeder, C.-B. Chan, M. Song, S. P. Yu, D. Weinschenker, and K. Ye. 2014. 7,8-dihydroxyflavone prevents synaptic loss and memory deficits in a mouse model of Alzheimer's disease. *Neuropsychopharmacology* 39: 638–50.
83. Bollen, E., T. Vanmierlo, S. Akkerman, C. Wouters, H. M. W. Steinbusch, and J. Prickaerts. 2013. 7,8-Dihydroxyflavone improves memory consolidation processes in rats and mice. *Behav. Brain Res.* 257: 8–12.
84. Castello, N. a., M. H. Nguyen, J. D. Tran, D. Cheng, K. N. Green, and F. M. LaFerla. 2014. 7,8-dihydroxyflavone, a small molecule TrkB agonist, improves spatial memory and increases thin spine density in a mouse model of alzheimer disease-like neuronal loss. *PLoS One* 9: 17–19.
85. Gao, L., M. Tian, H.-Y. Zhao, Q.-Q. Xu, Y.-M. Huang, Q.-C. Si, Q. Tian, Q.-M. Wu, X.-M. Hu, L.-B. Sun, S. M. McClintock, and Y. Zeng. 2016. TrkB activation by 7, 8-dihydroxyflavone increases synapse AMPA subunits and ameliorates spatial memory deficits in a mouse model of Alzheimer's disease. *J. Neurochem.* 136: 620–636.
86. Aytan, N., J.-K. Choi, I. Carreras, L. Crabtree, B. Nguyen, M. Lehar, J. K. Blusztajn, B. G. Jenkins, and A. Dedeoglu. 2018. Protective effects of 7,8-dihydroxyflavone on neuropathological and neurochemical changes in a mouse model of Alzheimer's disease. *Eur. J. Pharmacol.* .
87. Zhou, W., X. Li, D. Huang, W. Zhou, T. Li, and W. Song. 2015. No significant effect of 7,8-dihydroxyflavone on APP processing and Alzheimer-associated phenotypes. *Curr. Alzheimer Res.* 12: 47–52.
88. Liu, X., O. Obianyo, C. B. Chan, J. Huang, S. Xue, J. J. Yang, F. Zeng, M. Goodman, and K. Ye. 2014. Biochemical and Biophysical Investigation of the Brain-derived Neurotrophic Factor Mimetic 7,8-Dihydroxyflavone in the Binding and Activation of the TrkB Receptor. *J. Biol. Chem.* 289: 27571–84.
89. Liu, X., Q. Qi, G. Xiao, J. Li, H. R. Luo, and K. Ye. 2013. O-methylated metabolite of 7,8-dihydroxyflavone activates TrkB receptor and displays antidepressant activity. *Pharmacology* 91: 185–200.
90. Jiang, M., Q. Peng, X. Liu, J. Jin, Z. Hou, J. Zhang, S. Mori, C. a. Ross, K. Ye, and W. Duan. 2013. Small-molecule TrkB receptor agonists improve motor function and extend survival in a mouse model of huntington's disease. *Hum. Mol. Genet.* 22: 2462–2470.
91. Decharneux, T., F. Dubois, C. Beauloye, S. Wattiaux-De Coninck, and R. Wattiaux. 1992. Effect of various flavonoids on lysosomes subjected to an oxidative or an osmotic stress. *Biochem. Pharmacol.* 44: 1243–8.
92. Payá, M., M. L. Ferrandiz, M. J. Sanz, and M. J. Alcaraz. 1993. Effects of phenolic compounds on bromobenzene-mediated hepatotoxicity in mice. *Xenobiotica.* 23: 327–33.
93. Zhang, R., K. A. Kang, M. J. Piao, D. O. Ko, Z. H. Wang, W. Y. Chang, H. J. You, I. K. Lee, B. J. Kim, S. S. Kang, and J. W. Hyun. 2009. Preventive effect of 7,8-dihydroxyflavone against oxidative stress induced genotoxicity. *Biol. Pharm. Bull.* 32: 166–71.
94. Chen, J., K. W. Chua, C. C. Chua, H. Yu, A. Pei, B. H. L. Chua, R. C. Hamdy, X. Xu, and C. F. Liu. 2011. Antioxidant activity of 7,8-dihydroxyflavone provides neuroprotection against glutamate-induced toxicity. *Neurosci. Lett.* 499: 181–185.
95. Huai, R., X. Han, B. Wang, C. Li, Y. Niu, R. Li, and Z. Qu. 2014. Vasorelaxing and antihypertensive effects of 7,8-dihydroxyflavone. *Am. J. Hypertens.* 27: 750–760.
96. Zhang, B., G. Salituro, D. Szalkowski, Z. Li, Y. Zhang, I. Royo, D. Vilella, M. T. Díez, F. Pelaez, C. Ruby, R. L. Kendall, X. Mao, P. Griffin, J. Calaycay, J. R. Zierath, J. V. Heck, R. G. Smith, and D. E. Moller. 1999. Discovery of a small molecule insulin mimetic with antidiabetic activity in mice. *Science* 284: 974–977.
97. Yu, G., and W. Wang. 2015. Protective effects of LM22A-4 on injured spinal cord nerves. 8: 6526–6532.
98. Han, J., J. Pollak, T. Yang, M. R. Siddiqui, K. P. Doyle, K. Taravosh-Lahn, E. Cekanaviciute, A. Han, J. Z. Goodman, B. Jones, D. Jing, S. M. Massa, F. M. Longo, and M. S. Buckwalter. 2012. Delayed Administration of a Small Molecule Tropomyosin-Related Kinase B Ligand Promotes Recovery After Hypoxic-Ischemic Stroke. *Stroke* 43: 1918–1924.
99. Simmons, D. A., N. P. Belichenko, T. Yang, C. Condon, M. Monbureau, M. Shamloo, D. Jing, S. M. Massa, and F. M. Longo. 2013. A small molecule TrkB ligand reduces motor impairment and neuropathology in R6/2 and BACHD mouse models of Huntington's disease. *J. Neurosci.* 33: 18712–27.
100. Schmid, D. A., T. Yang, M. Ogier, I. Adams, Y. Mirakhur, Q. Wang, S. M. Massa, F. M. Longo, and D. M. Katz. 2012. A TrkB small molecule partial agonist rescues TrkB phosphorylation deficits and improves respiratory function in a mouse model of Rett syndrome. *J. Neurosci.* 32: 1803–10.
101. Kron, M., M. Lang, I. T. Adams, M. Sceniak, F. Longo, and D. M. Katz. 2014. A BDNF loop-domain mimetic acutely reverses spontaneous apneas and respiratory abnormalities during behavioral arousal in a mouse model of Rett syndrome. *Dis. Model. Mech.* 7: 1047–1055.
102. Li, W., A. Bellot-Saez, M. L. Phillips, T. Yang, F. M. Longo, and L. Pozzo-Miller. 2017. A small-molecule TrkB ligand restores hippocampal synaptic plasticity and object location memory in Rett syndrome mice. *Dis. Model. Mech.* 10: 837–845.

103. English, A. W., K. Liu, J. M. Nicolini, A. M. Mulligan, and K. Ye. 2013. Small-molecule trkB agonists promote axon regeneration in cut peripheral nerves. *Proc. Natl. Acad. Sci. U. S. A.* 110: 16217–22.
104. Nie, S., Y. Xu, G. Chen, K. Ma, C. Han, Z. Guo, Z. Zhang, K. Ye, and X. Cao. 2015. Small molecule TrkB agonist deoxygedunin protects nigrostriatal dopaminergic neurons from 6-OHDA and MPTP induced neurotoxicity in rodents. *Neuropharmacology* 99: 448–458.
105. Barbui, C., and M. Hotopf. 2001. Amitriptyline v. the rest: still the leading antidepressant after 40 years of randomised controlled trials. *Br. J. Psychiatry* 178: 129–44.
106. Chadwick, W., N. Mitchell, J. Carroll, Y. Zhou, S.-S. Park, L. Wang, K. G. Becker, Y. Zhang, E. Lehrmann, W. H. Wood, B. Martin, and S. Maudsley. 2011. Amitriptyline-Mediated Cognitive Enhancement in Aged 3xTg Alzheimer's Disease Mice Is Associated with Neurogenesis and Neurotrophic Activity. *PLoS One* 6: e21660.
107. Cong, W.-N., W. Chadwick, R. Wang, C. M. Daimon, H. Cai, J. Amma, W. H. Wood, K. G. Becker, B. Martin, and S. Maudsley. 2015. Amitriptyline Improves Motor Function via Enhanced Neurotrophin Signaling and Mitochondrial Functions in the Murine N171-82Q Huntington Disease Model. *J. Biol. Chem.* 290: 2728–2743.
108. Zheng, X., F. Chen, T. Zheng, F. Huang, J. Chen, and W. Tu. 2016. Amitriptyline Activates TrkA to Aid Neuronal Growth and Attenuate Anesthesia-Induced Neurodegeneration in Rat Dorsal Root Ganglion Neurons. *Medicine (Baltimore)*. 95: e3559.
109. Rantamäki, T., L. Vesa, H. Antila, A. Lieto, P. Tammela, A. Schmitt, K. P. Lesch, M. Rios, and E. Castren. 2011. Antidepressant drugs transactivate trkb neurotrophin receptors in the adult rodent brain independently of bdnf and monoamine transporter blockade. *PLoS One* 6: 2–9.
110. Quitkin, F. M., M. R. Liebowitz, J. W. Stewart, P. J. McGrath, W. Harrison, J. G. Rabkin, J. Markowitz, and S. O. Davies. 1984. I-Deprenyl in atypical depressives. *Arch. Gen. Psychiatry* 41: 777–81.
111. O'Leary, P. D., and R. a. Hughes. 1998. Structure-activity relationships of conformationally constrained peptide analogues of loop 2 of brain-derived neurotrophic factor. *J. Neurochem.* 70: 1712–21.
112. O'Leary, P. D., and R. a. Hughes. 2003. Design of potent peptide mimetics of brain-derived neurotrophic factor. *J. Biol. Chem.* 278: 25738–25744.
113. Wong, A. W., L. Giuffrida, R. Wood, H. Peckham, D. Gonsalvez, S. S. Murray, R. a. Hughes, and J. Xiao. 2014. TDP6, a brain-derived neurotrophic factor-based trkB peptide mimetic, promotes oligodendrocyte myelination. *Mol. Cell. Neurosci.* 63: 132–140.
114. Williams, G., E. J. Williams, P. Maison, M. N. Pangalos, F. S. Walsh, and P. Doherty. 2005. Overcoming the inhibitors of myelin with a novel neurotrophin strategy. *J. Biol. Chem.* 280: 5862–5869.
115. Todd, D., I. Gowers, S. J. Dowler, M. D. Wall, G. McAllister, D. F. Fischer, S. Dijkstra, S. a. Fratantoni, R. van de Bospoort, J. Veenman-Koepke, G. Flynn, J. Arjomand, C. Dominguez, I. Munoz-Sanjuan, J. Wityak, and J. a. Bard. 2014. A monoclonal antibody TrkB receptor agonist as a potential therapeutic for Huntington's disease. *PLoS One* 9: e87923.
116. Fobian, K., S. Owczarek, C. Budtz, E. Bock, V. Berezin, and M. V Pedersen. 2010. Peptides derived from the solvent-exposed loops 3 and 4 of BDNF bind TrkB and p75(NTR) receptors and stimulate neurite outgrowth and survival. *J. Neurosci. Res.* 88: 1170–81.
117. Xu, R., S. P. Srinivasan, P. Sureshkumar, E. N. Nembo, C. Schäfer, J. Semmler, M. Matzkies, M. Albrechtsen, J. Hescheler, and F. Nguemo. 2015. Effects of Synthetic Neural Adhesion Molecule Mimetic Peptides and Related Proteins on the Cardiomyogenic Differentiation of Mouse Embryonic Stem Cells. *Cell. Physiol. Biochem.* 35: 2437–2450.
118. Cardenas-Aguayo, M. D. C., S. F. Kazim, I. Grundke-Iqbal, and K. Iqbal. 2013. Neurogenic and neurotrophic effects of BDNF peptides in mouse hippocampal primary neuronal cell cultures. *PLoS One* 8: e53596.
119. Cazorla, M., A. Jouvenceau, C. Rose, J.-P. Guilloux, C. Pilon, A. Dranovsky, and J. Prémont. 2010. Cyclotraxin-B, the First Highly Potent and Selective TrkB Inhibitor, Has Anxiolytic Properties in Mice. *PLoS One* 5: 17.
120. Cazorla, M., J. Prémont, A. Mann, N. Girard, C. Kellendonk, and D. Rognan. 2011. Identification of a low-molecular weight TrkB antagonist with anxiolytic and antidepressant activity in mice. *J. Clin. Invest.* 121: 1846–1857.
121. Baeza, J. L., B. G. de la Torre, C. M. Santiveri, R. D. Almeida, M. T. García-López, G. Gerona-Navarro, S. R. Jaffrey, M. Á. Jiménez, D. Andreu, R. González-Muñiz, and M. Martín-Martínez. 2012. Cyclic amino acid linkers stabilizing key loops of brain derived neurotrophic factor. *Bioorg. Med. Chem. Lett.* 22: 444–8.
122. Ma, Z., X. Wu, M. Cao, W. Pan, F. Zhu, J. Chen, and Z. Qi. 2003. Selection of trkB-binding peptides from a phage-displayed random peptide library. *Sci. China. C. Life Sci.* 46: 77–86.
123. Ohnishi, T., K. Sakamoto, A. Asami-Odaka, K. Nakamura, A. Shimizu, T. Ito, T. Asami, T. Ohtaki, and H. Inooka. 2017. Generation of a novel artificial TrkB agonist, BM17d99, using T7 phage-displayed random peptide libraries. *Biochem. Biophys. Res. Commun.* 483: 101–106.
124. Engle, Sandra J., Kimmel, Lida H., Lanz, Thomas A., Friedrich, A., I. M., Weber, Mark, Prior, Faith, Lazzaro Jr, John T., Efremov, and R. J. Kleiman. 2011. DEVELOPMENT OF AN ASSAY TO IDENTIFY ACTIVATORS OF TRKB SIGNALING USING HUMAN INDUCED PLURIPOTENT STEM CELL DERIVED NEURONS. In *ISSCR 9th Annual Meeting* 42–43.
125. Boltaev, U., Y. Meyer, F. Tolibzoda, T. Jacques, M. Gassaway, Q. Xu, F. Wagner, Y. Zhang, M. Palmer, E. Holson, and D. Sames. 2017. Multiplex quantitative assays indicate a need for reevaluating reported

small-molecule TrkB agonists. *Sci. Signal.* 10.

126. Wang, J., M. K. Hancock, J. M. Dudek, and K. Bi. 2008. Cellular assays for high-throughput screening for modulators of Trk receptor tyrosine kinases. *Curr. Chem. Genomics* 1: 27–33.

127. Huang, Y. Z., E. Pan, Z.-Q. Q. Xiong, and J. O. McNamara. 2008. Zinc-mediated transactivation of TrkB potentiates the hippocampal mossy fiber-CA3 pyramid synapse. *Neuron* 57: 546–58.

128. Huang, Y. Z., and J. O. McNamara. 2010. Mutual regulation of Src family kinases and the neurotrophin receptor TrkB. *J. Biol. Chem.* 285: 8207–17.

129. Sadick, M. D., a Galloway, D. Shelton, V. Hale, S. Weck, V. Anicetti, and W. L. Wong. 1997. Analysis of neurotrophin/receptor interactions with a gD-flag-modified quantitative kinase receptor activation (gD.KIRA) enzyme-linked immunosorbent assay. *Exp. Cell Res.* 234: 354–61.

130. Antila, H., H. Autio, L. Turunen, K. Harju, P. Tammela, K. Wennerberg, J. Yli-Kauhaluoma, H. J. Huttunen, E. Castrén, and T. Rantamäki. 2014. Utilization of in situ ELISA method for examining Trk receptor phosphorylation in cultured cells. *J. Neurosci. Methods* 222: 142–146.

131. Tapley, P., F. Lamballe, and M. Barbacid. 1992. K252a is a selective inhibitor of the tyrosine protein kinase activity of the trk family of oncogenes and neurotrophin receptors. *Oncogene* 7: 371–81.

132. Er, J. C., C. Leong, C. L. Teoh, Q. Yuan, P. Merchant, M. Dunn, D. Sulzer, D. Sames, A. Bhinge, D. Kim, S.-M. Kim, M.-H. Yoon, L. W. Stanton, S. H. Je, S.-W. Yun, and Y.-T. Chang. 2015. NeuO: a Fluorescent Chemical Probe for Live Neuron Labeling. *Angew. Chemie Int. Ed.* 54: 2442–2446.

133. Shi, T., M. Niepel, J. E. McDermott, Y. Gao, C. D. Nicora, W. B. Chrisler, L. M. Markillie, V. A. Petyuk, R. D. Smith, K. D. Rodland, P. K. Sorger, W.-J. Qian, and H. S. Wiley. 2016. Conservation of protein abundance patterns reveals the regulatory architecture of the EGFR-MAPK pathway. *Sci. Signal.* 9: 1–14.

134. Kaplan, D. R., K. Matsumoto, E. Lucarelli, and C. J. Thiele. 1993. Induction of TrkB by retinoic acid mediates biologic responsiveness to BDNF and differentiation of human neuroblastoma cells. Eukaryotic Signal Transduction Group. *Neuron* 11: 321–31.

135. Lin, B., M. C. Pirrung, L. Deng, Z. Li, Y. Liu, and N. J. G. Webster. 2007. Neuroprotection by Small Molecule Activators of the Nerve Growth Factor Receptor □. .

136. Lowe, J. T., M. D. L. Iv, L. B. Akella, E. J. Donckele, L. Durak, J. R. Duvall, B. Gerard, E. B. Holson, A. Joliton, S. Kesavan, B. C. Lemerrier, H. Liu, J. Marie, C. a Mulrooney, G. Muncipinto, M. W. Shea, L. M. Panko, A. Rowley, B. Suh, M. Thomas, F. F. Wagner, J. Wei, M. a Foley, and L. a Marcaurelle. 2012. Synthesis and Pro fi ling of a Diverse Collection of Azetidone-Based Sca ff olds for the Development of CNS-Focused Lead-like Libraries. *J. Org. Chem.* 77: 7187–7211.

137. Ruoslahti, E., and M. D. Pierschbacher. 1987. New perspectives in cell adhesion: RGD and integrins. *Science* 238: 491–7.

138. Ruoslahti, E. 2012. Peptides as targeting elements and tissue penetration devices for nanoparticles. *Adv. Mater.* 24: 3747–56.

139. Simberg, D., T. Duza, J. H. Park, M. Essler, J. Pilch, L. Zhang, A. M. Derfus, M. Yang, R. M. Hoffman, S. Bhatia, M. J. Sailor, and E. Ruoslahti. 2007. Biomimetic amplification of nanoparticle homing to tumors. *Proc. Natl. Acad. Sci. U. S. A.* 104: 932–936.

140. Wittig, I., H.-P. Braun, and H. Schägger. 2006. Blue native PAGE. *Nat. Protoc.* 1: 418–428.

141. Fiala, G. J., W. W. A. Schamel, and B. Blumenthal. 2011. Blue native polyacrylamide gel electrophoresis (BN-PAGE) for analysis of multiprotein complexes from cellular lysates. *J. Vis. Exp.* e2164.

142. Lykissas, M. G., A. K. Batistatou, K. a Charalabopoulos, and A. E. Beris. 2007. The role of neurotrophins in axonal growth, guidance, and regeneration. *Curr. Neurovasc. Res.* 4: 143–151.

143. Phillips, C., M. A. Baktir, M. Srivatsan, and A. Salehi. 2014. Neuroprotective effects of physical activity on the brain: a closer look at trophic factor signaling. *Front. Cell. Neurosci.* 8: 170.

144. Lazarovici, P., D. Rasouly, L. Friedman, R. Tabekman, H. Ovadia, and Y. Matsuda. 1996. K252a and staurosporine microbial alkaloid toxins as prototype of neurotropic drugs. *Adv. Exp. Med. Biol.* 391: 367–77.

145. Thompson, A. F., and L. A. Levin. 2010. Neuronal differentiation by analogs of staurosporine. *Neurochem. Int.* 56: 554–560.

146. Gassmann, M., B. Grenacher, B. Rohde, and J. Vogel. 2009. Quantifying Western blots: Pitfalls of densitometry. *Electrophoresis* 30: 1845–1855.

147. Taylor, S. C., T. Berkelman, G. Yadav, and M. Hammond. 2013. A defined methodology for reliable quantification of Western blot data. *Mol. Biotechnol.* 55: 217–26.

148. Domeniconi, M., and M. V Chao. 2010. Transactivation of Trk receptors in spinal motor neurons. *Histol. Histopathol.* 25: 1207–13.

149. Puehringer, D., N. Orel, P. Lüningschrör, N. Subramanian, T. Herrmann, M. V Chao, and M. Sendtner. 2013. EGF transactivation of Trk receptors regulates the migration of newborn cortical neurons. *Nat. Neurosci.* 16: 407–15.

150. Arrowsmith, C. H., J. E. Audia, C. Austin, J. Baell, J. Bennett, J. Blagg, C. Bountra, P. E. Brennan, P. J. Brown, M. E. Bunnage, C. Buser-Doepner, R. M. Campbell, A. J. Carter, P. Cohen, R. a Copeland, B. Cravatt, J. L. Dahlin, D. Dhanak, A. M. Edwards, S. V Frye, N. Gray, C. E. Grimshaw, D. Hepworth, T. Howe, K. V. M. Huber, J. Jin, S. Knapp, J. D. Kotz, R. G. Kruger, D. Lowe, M. M. Mader, B. Marsden, A. Mueller-Farnow, S. Müller, R. C.

- O'Hagan, J. P. Overington, D. R. Owen, S. H. Rosenberg, B. Roth, R. Ross, M. Schapira, S. L. Schreiber, B. Shoichet, M. Sundström, G. Superti-Furga, J. Taunton, L. Toledo-Sherman, C. Walpole, M. a Walters, T. M. Willson, P. Workman, R. N. Young, and W. J. Zuercher. 2015. The promise and peril of chemical probes. *Nat. Chem. Biol.* 11: 536–541.
151. Kehrl, A. R. H., and D. a. H. Taylor. 1990. A synthesis of methyl 2 α -acetoxy-3-deoxy-3 α -hydroxyangolensate. *J. Chem. Soc. Perkin Trans. 1* 2067.
152. Sadick, M. D., a Intintoli, V. Quarmby, a McCoy, E. Canova-Davis, and V. Ling. 1999. Kinase receptor activation (KIRA): a rapid and accurate alternative to end-point bioassays. *J. Pharm. Biomed. Anal.* 19: 883–91.
153. Yeung, Y. G., and E. R. Stanley. 2009. A solution for stripping antibodies from polyvinylidene fluoride immunoblots for multiple reprobng. *Anal. Biochem.* 389: 89–91.
154. Teesalu, T., K. N. Sugahara, and E. Ruoslahti. 2012. Mapping of vascular ZIP codes by phage display. *Methods Enzymol.* 503: 35–56.

1.7 Appendix

All the screen data performed in our lab is presented on individual plate basis. Compound libraries were named as BRD## based on the availability of the compounds and necessary conditions (single or multiple doses).

Data presents as mean \pm SD of the single experiment. Color coded solid and dotted lines represent mean and 3xSD of the controls (DMSO, BDNF at low EC, BDNF at max EC). Low EC of BDNF varied between the experiments and were calculated post-factum.

BRD01-06 contained compounds at 5050-10-2-0.4 μ M concentrations and were used in HEK-TrkB screen

BRD07-17 contained compounds at 50-10-2-0.4 μ M concentrations and were used in CellSensor (1st round) and CNC screens.

BRD18-22 contained compounds at 30-15-7.5-3.25 μ M concentrations and were used in CellSensor screen (2nd round)

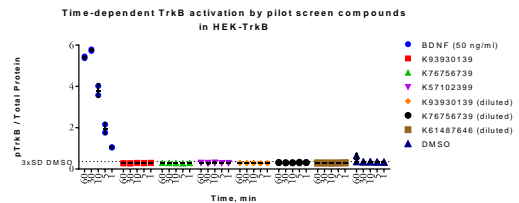
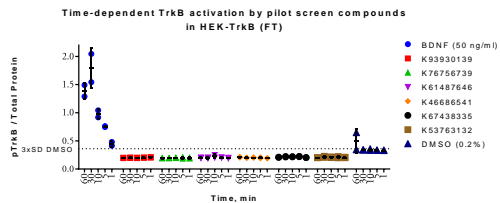
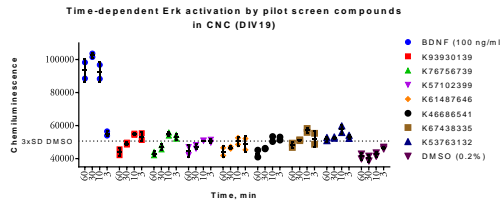
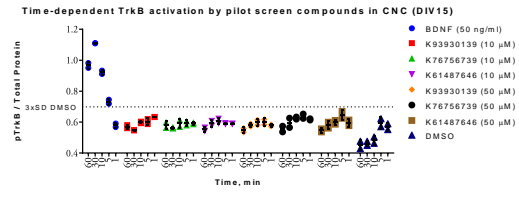
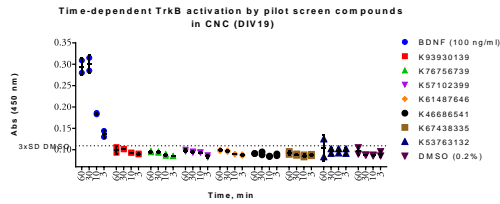
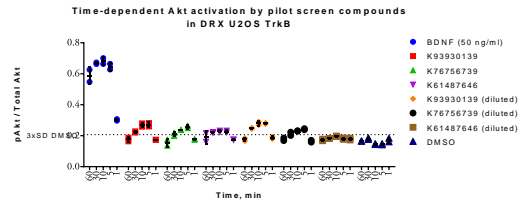
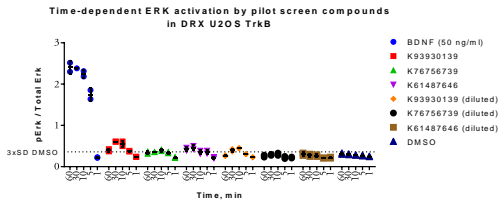
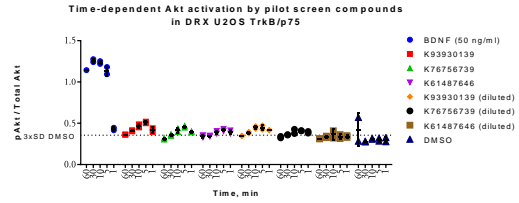
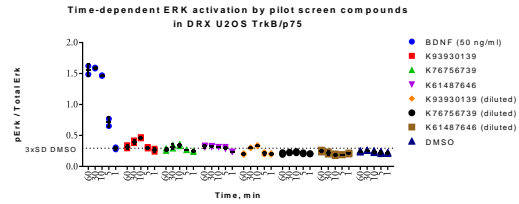
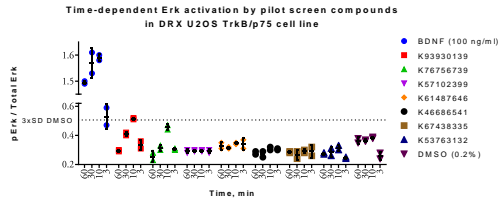
1.7.1 Compound libraries

BRD01	BRD02	BRD03	BRD04	BRD05	BRD06
K80274451	K37526858	K80786583	K74587389	K61473003	K80786583
K13752834	K54211867	K75724375	K80764150	K21249854	K09140990
K93930139	K97073606	K41945164	K00185670	K65757418	K32712332
K76756739	K25704484	K16111984	K74405511	K10432698	K74587389
K57102399	K30161335	K32712332	K46962856	K26613565	K74405511
K61487646	K61479519	K60158292	K21471155	K30877586	K21471155
K46686541	K47086760	K14188824	K70362473		K21249854
K67438335	K71944937	K09140990	K95266828		K61473003
K53763132	Naloxonazine	K51942702	K60873820		

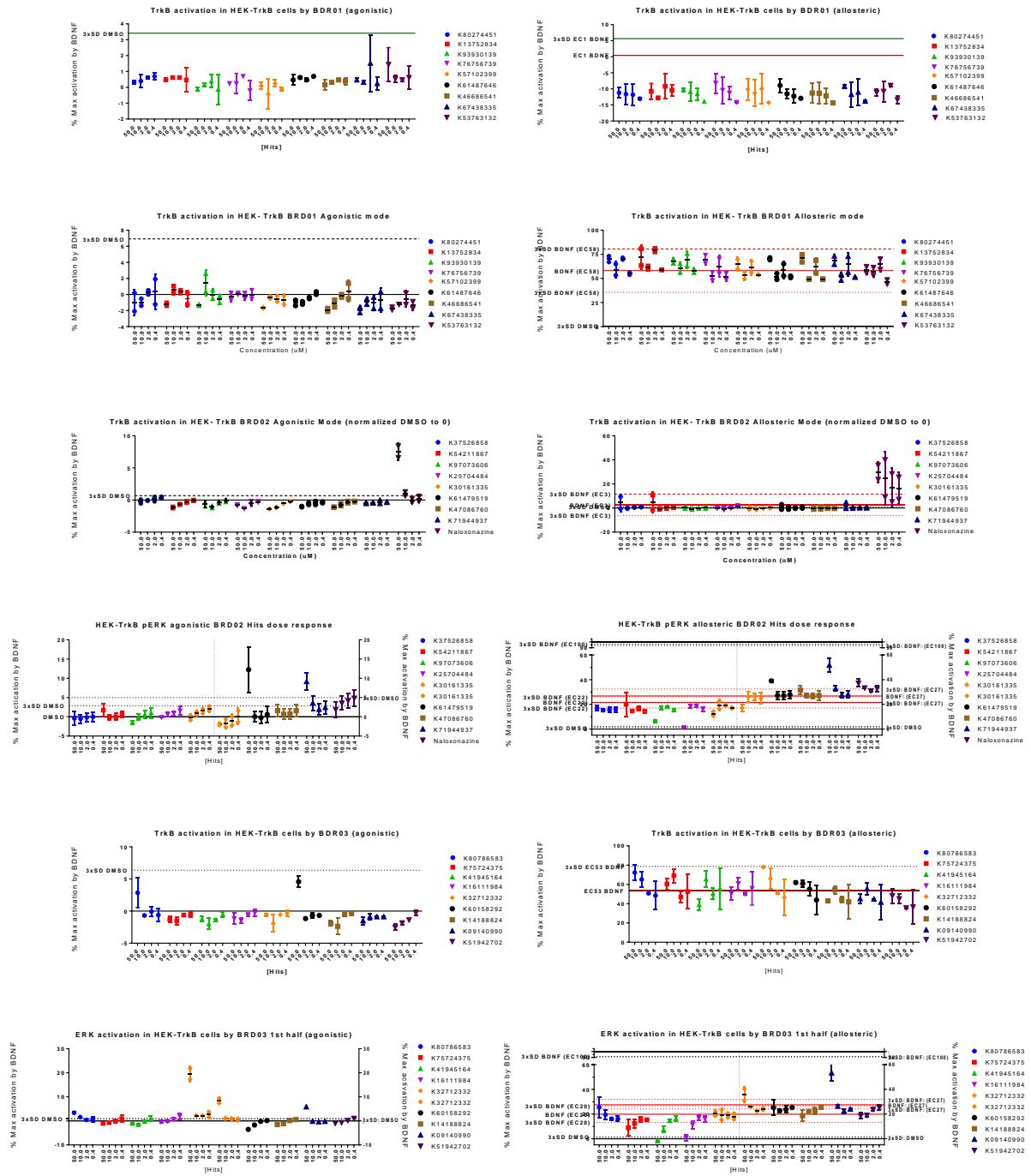
BRD07	K10432698	K65603112	K71944937	K02595530	K35151998	K13683125	K93930139	K53212675
BRD08	K70507343	K58397562	K03887292	K95361366	K82118272	K04803823	K22568370	K80274451
BRD09	K60174045	K01880422	K88581921	K22878659	K41719870	K34914110	K87640196	K26613565
BRD10	K30958256	K62850984	K10189663	K61487646	K70388087	K50330857	K30652576	K02764896
BRD11	K27145031	K15187228	K25401439	K20075659	K52427821	K63404341	K50931717	K41636894
BRD12	K78133682	K72840764	K51079083	K16329066	K44844695	K00140310	K65757418	K30877586
BRD13	K13752834	K76756739	K57102399	K46686541	K67438335	K53763132	K37526858	K47086760
BRD14	K54211867	K97073606	K25704484	K30161335	K61479519	K80786583	K75724375	K41945164
BRD15	K16111984	K32712332	K60158292	K14188824	K09140990	K51942702	K74587389	K80764150
BRD16	K00185670	K74405511	K46962856	K21471155	K70362473	K95266828	K60873820	K21249854
BRD17	K61473003							

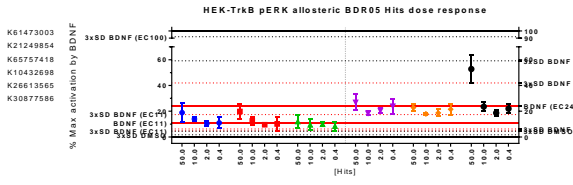
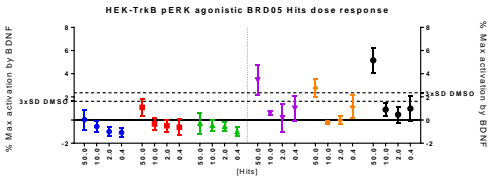
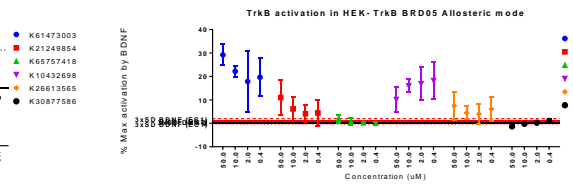
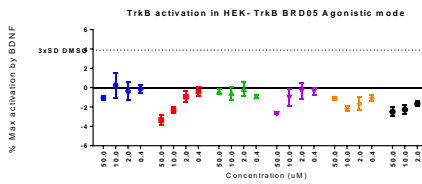
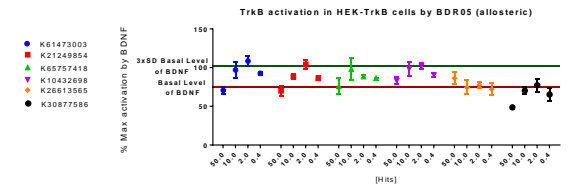
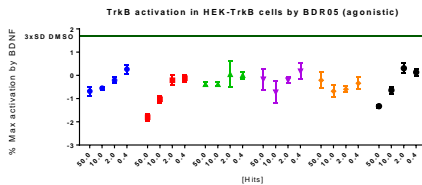
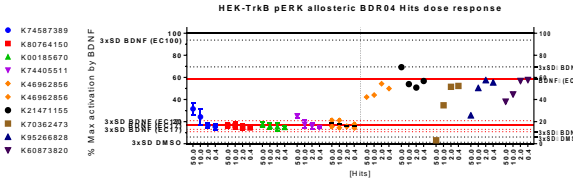
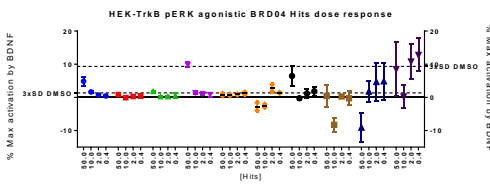
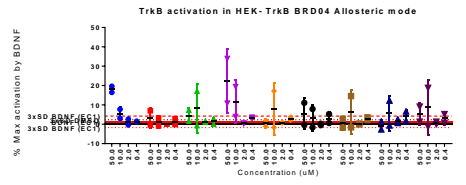
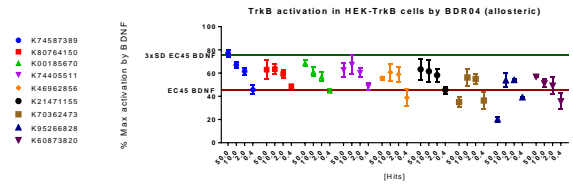
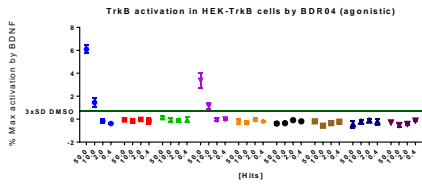
BRD18	BRD19	BRD20	BRD21	BRD22
K10432698	K58397562	K30958256	K54211867	K74405511
K71944937	K04803823	K70388087	K61479519	K21471155
K13683125	K60174045	K61487646	K80786583	K61473003
K53212675	K41719870	K25401439	K32712332	K51713105
K95361366	K22878659	K27145031	K60158292	K94669964
K22568370	K50330857	K50931717	K80764150	
K82118272	K02764896	K78133682	K21249854	
K65603112	K30652576	K75724375	K46962856	

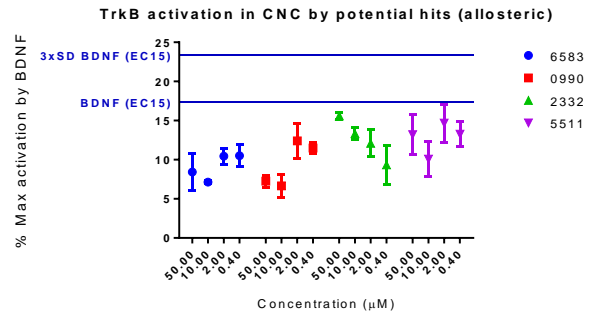
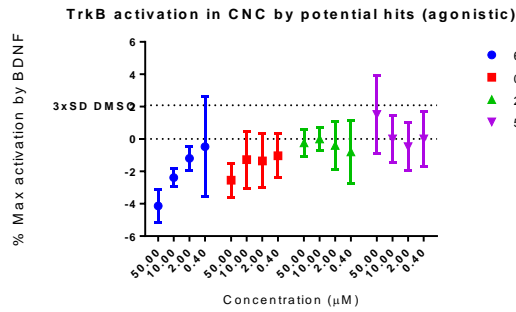
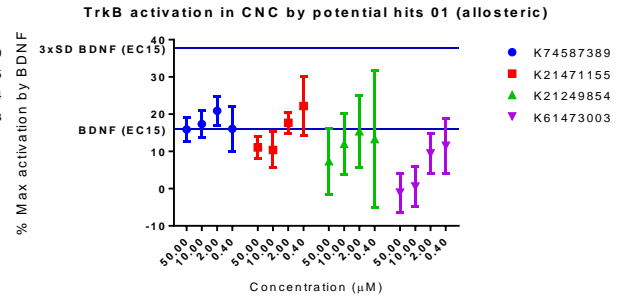
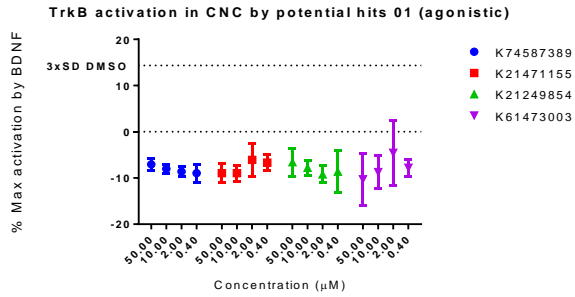
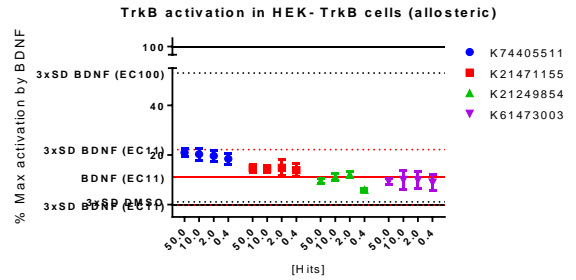
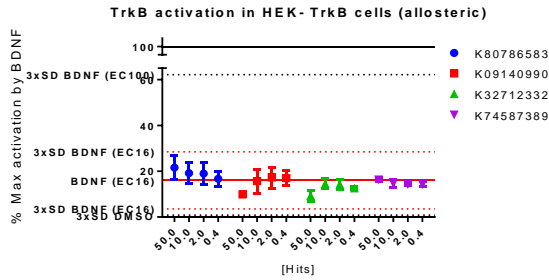
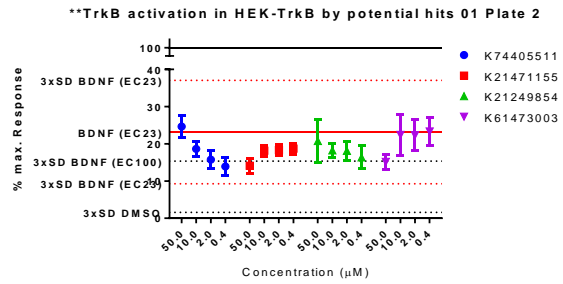
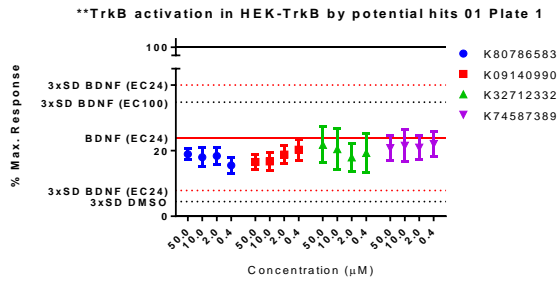
1.7.2 Pilot screen



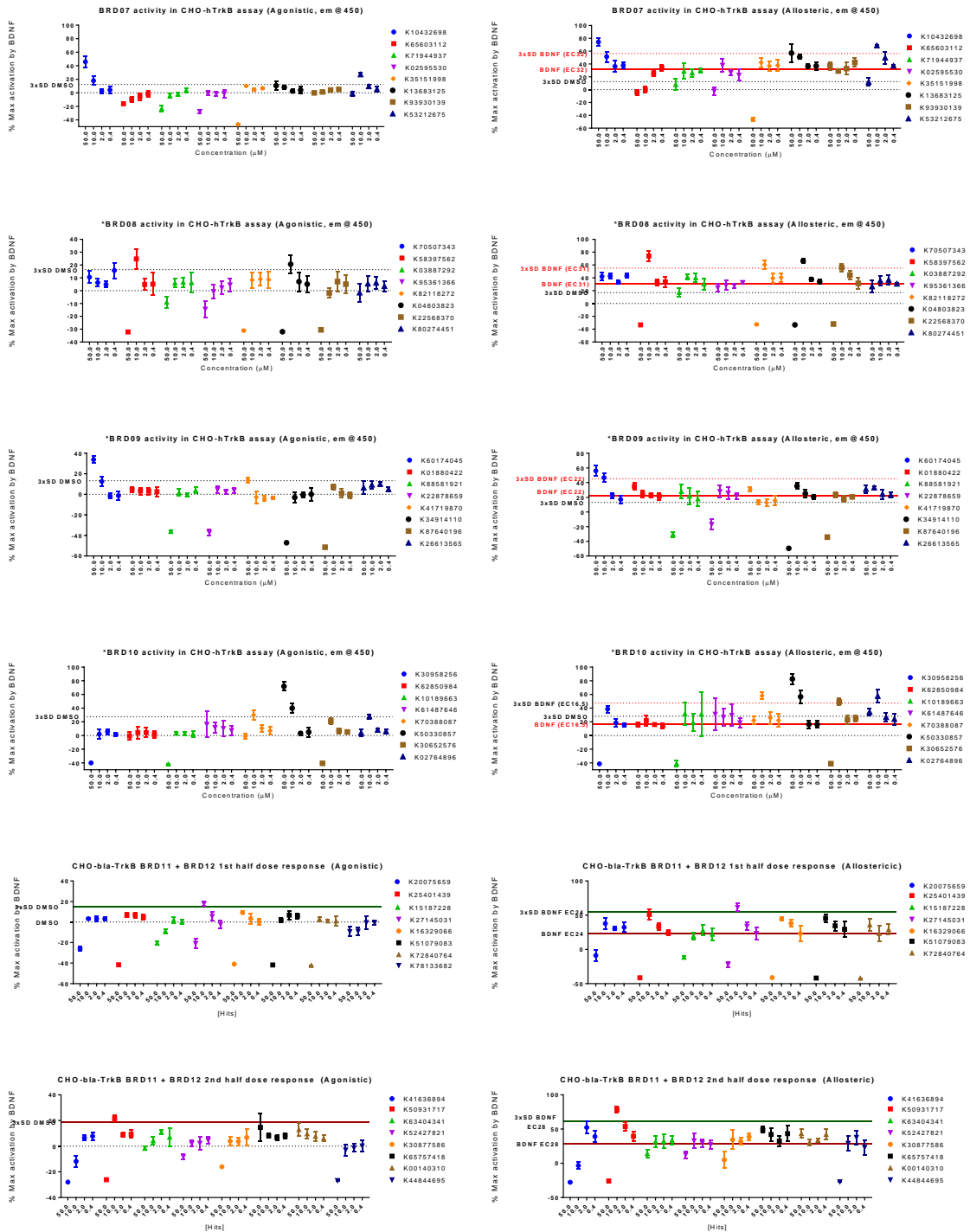
1.7.3 HEK-TrkB screen

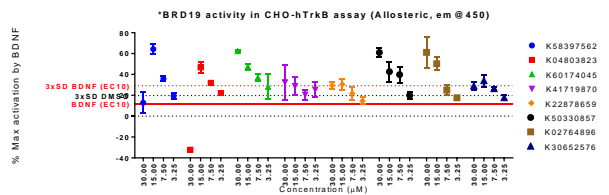
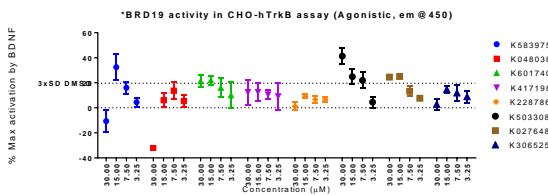
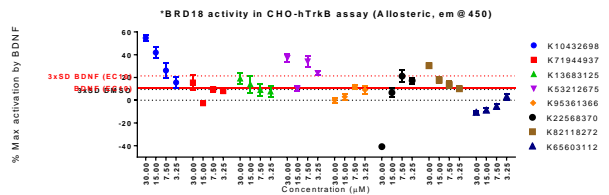
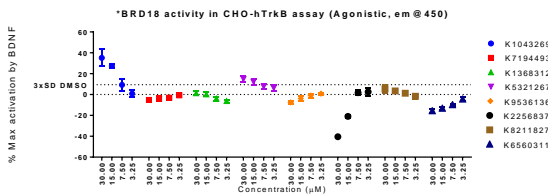
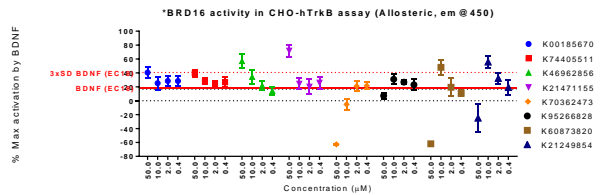
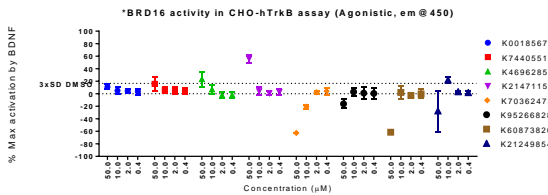
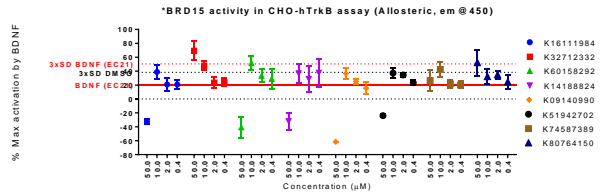
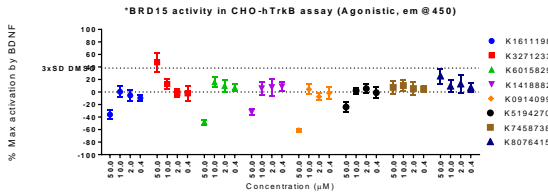
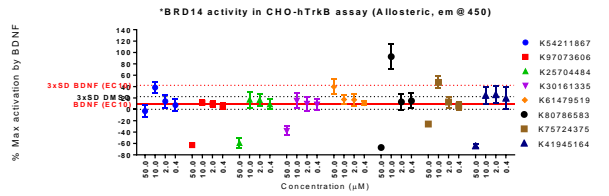
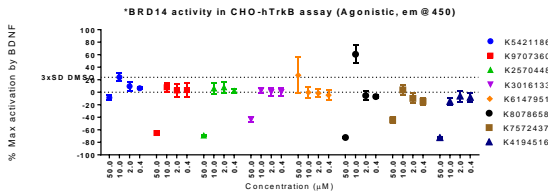
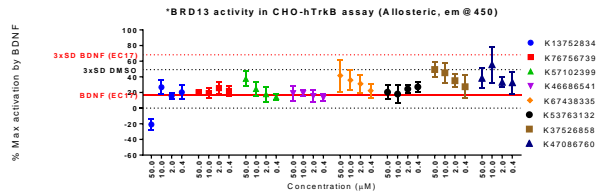
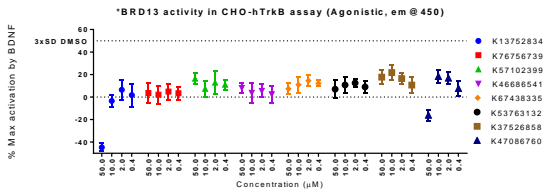


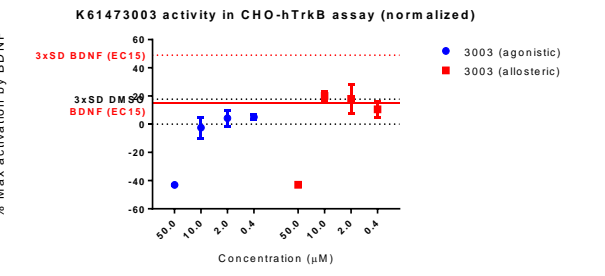
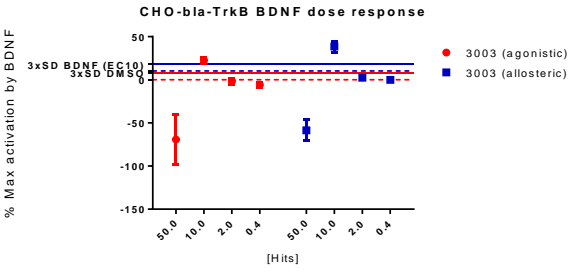
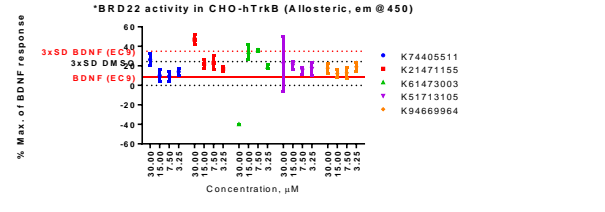
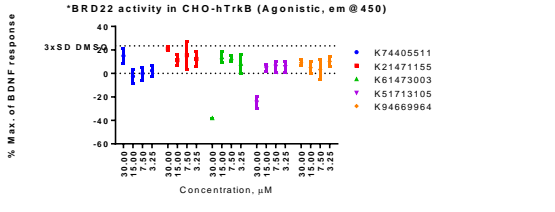
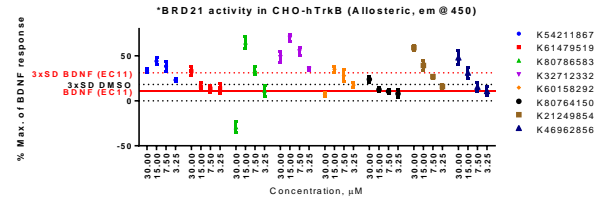
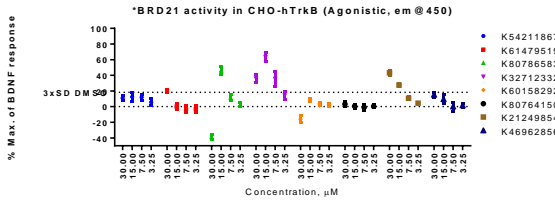
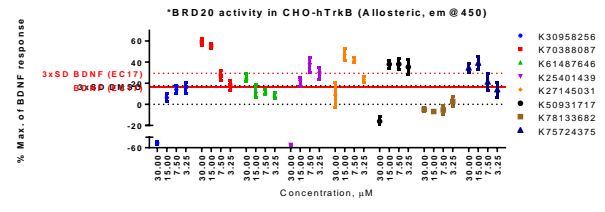
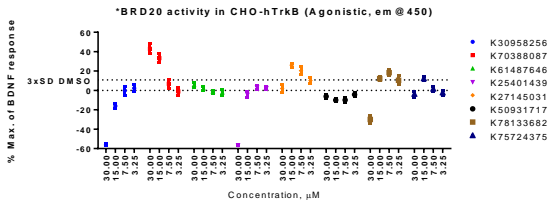




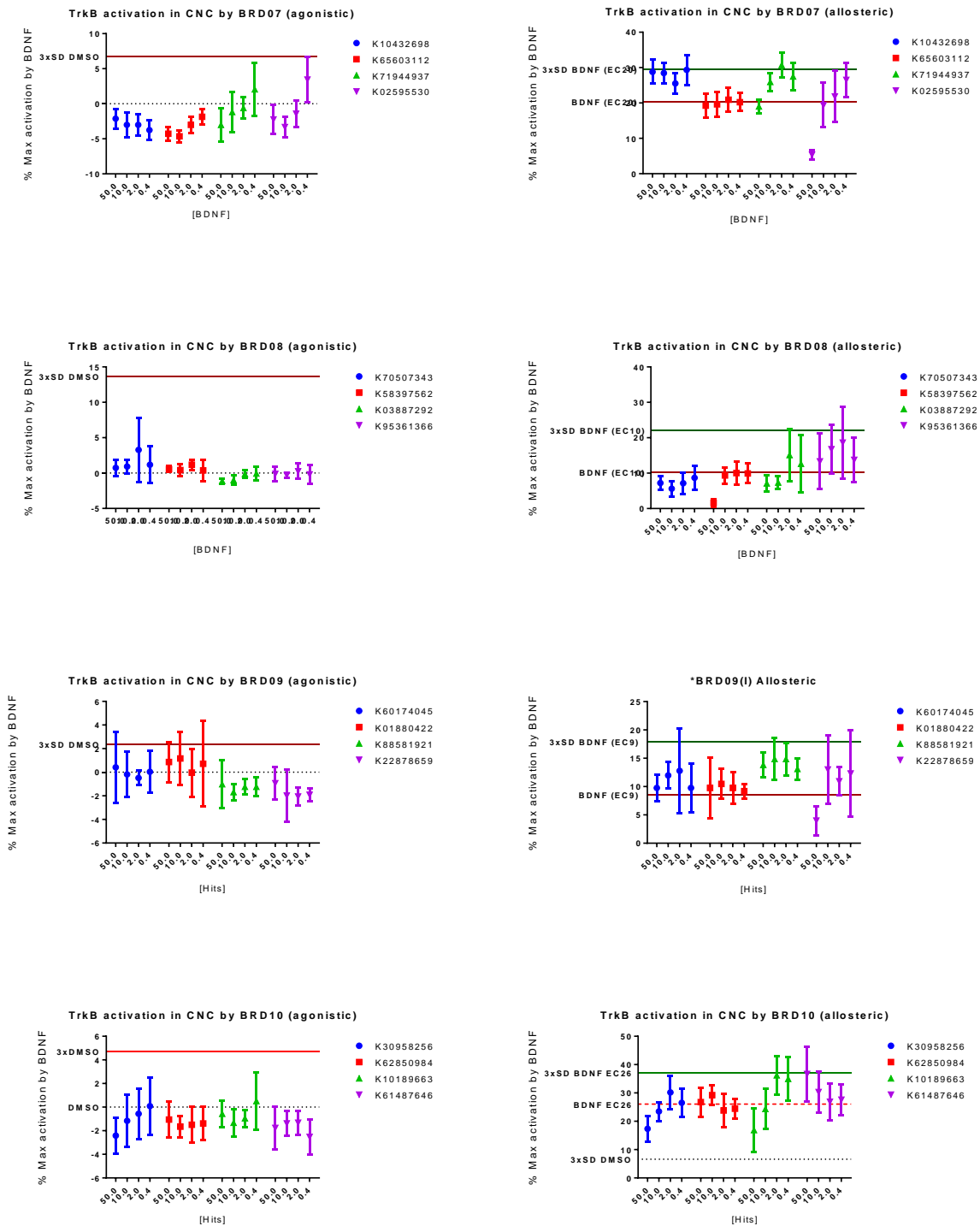
1.7.4 CellSensor screen



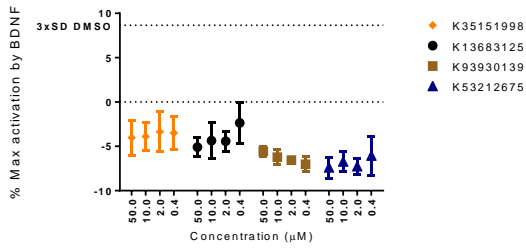




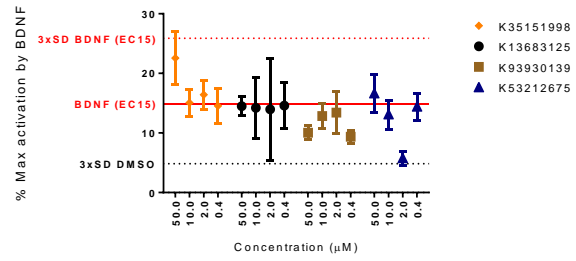
1.7.5 CNC screen



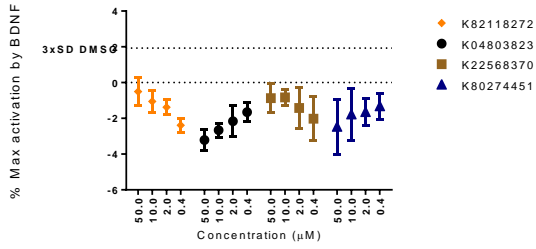
*TrkB Activation in CNC (DIV13) by BRD07 (agonistic)



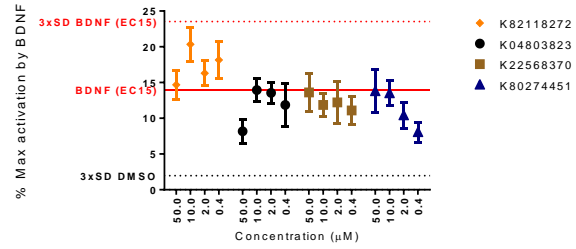
*TrkB Activation in CNC (DIV13) by BRD07 (allosteric)



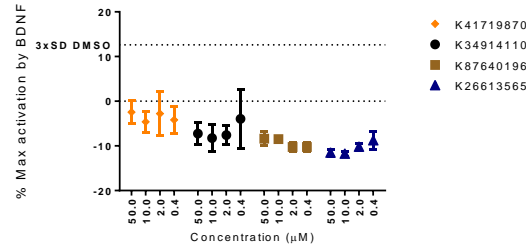
*TrkB activation in CNC (DIV13) by BRD08 (agonistic)



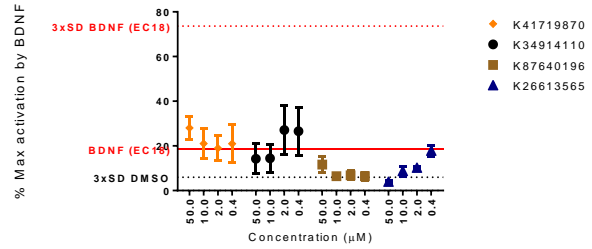
*TrkB activation in CNC (DIV13) by BRD08 (allosteric)



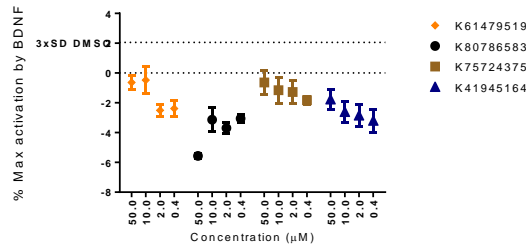
*TrkB activation in CNC (DIV14) by BRD09 (agonistic)



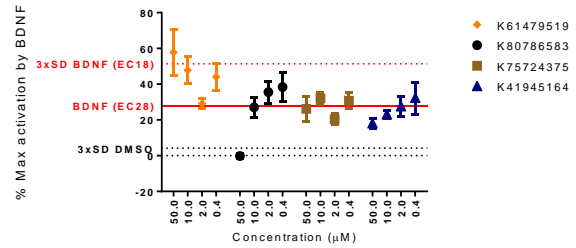
*TrkB activation in CNC (DIV14) by BRD09 (allosteric)

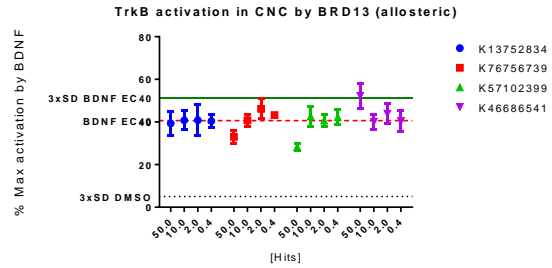
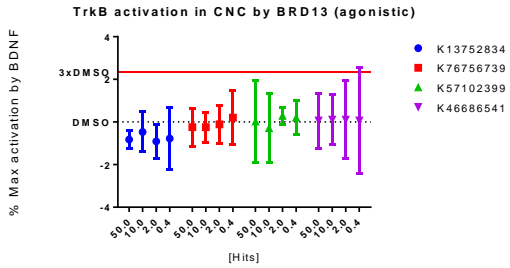
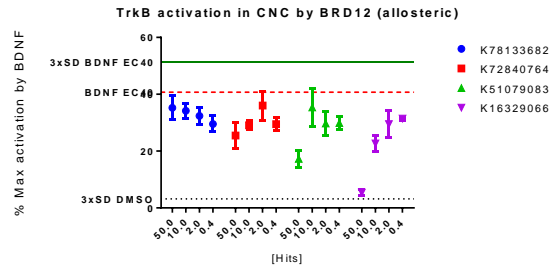
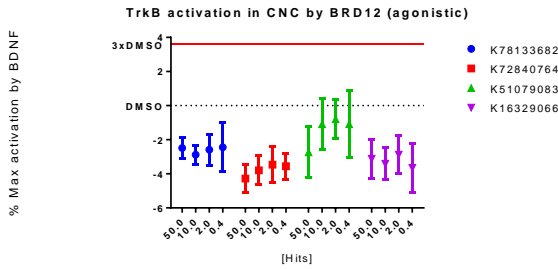
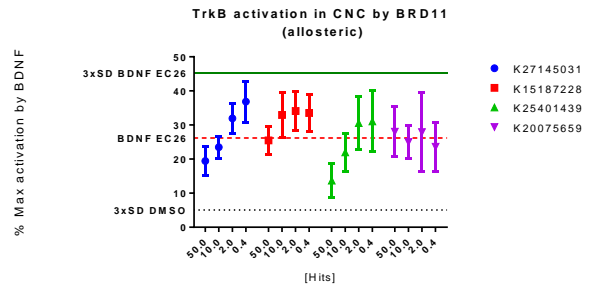
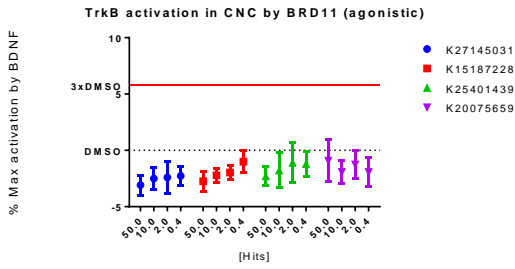


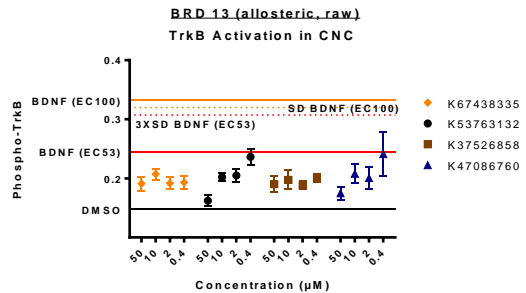
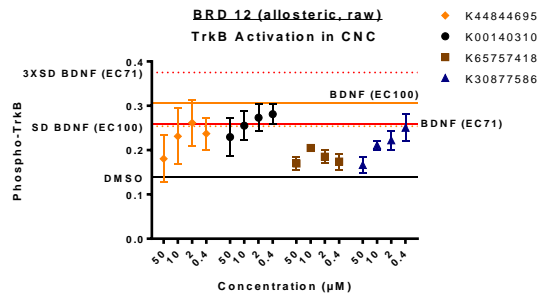
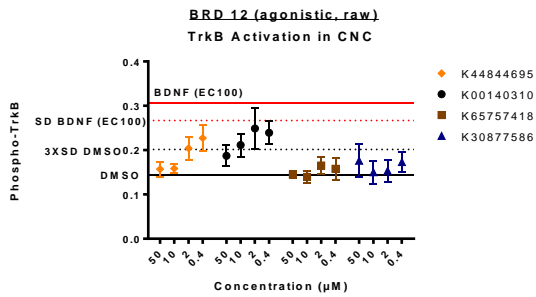
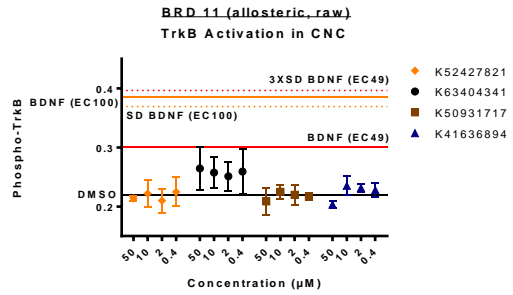
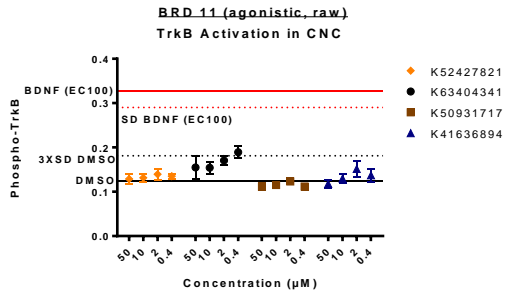
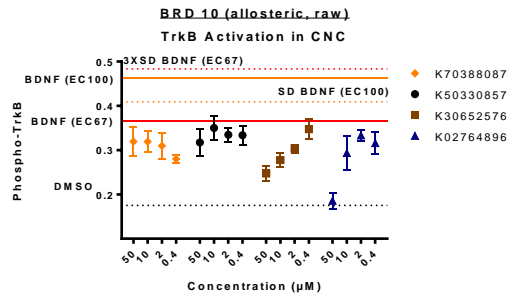
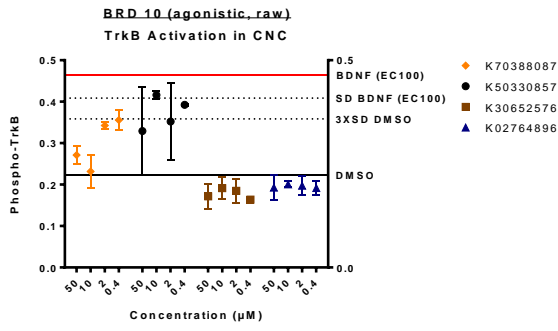
*TrkB activation by BRD14 (II) in CNC (agonistic)

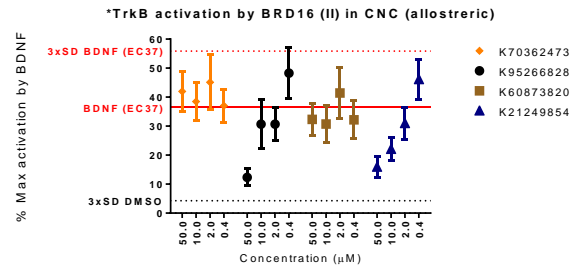
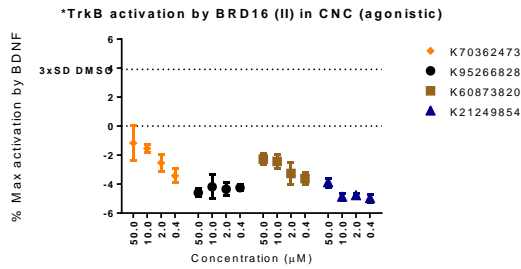
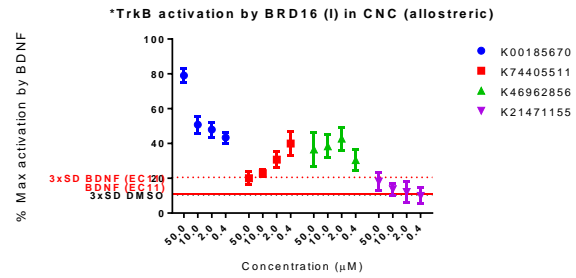
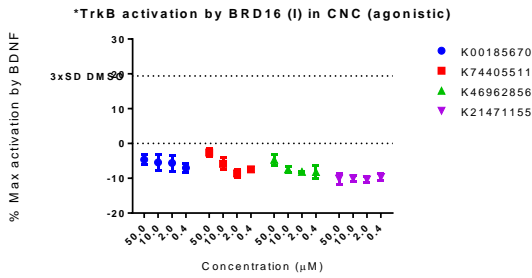
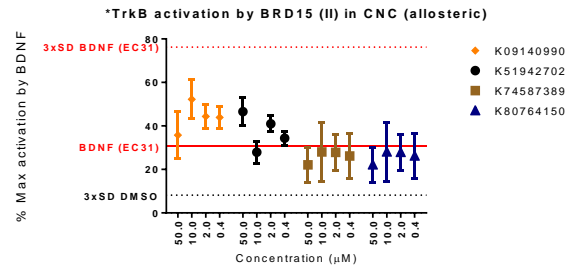
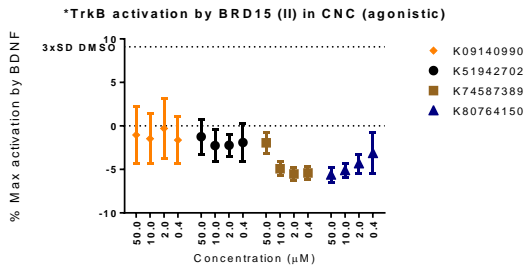
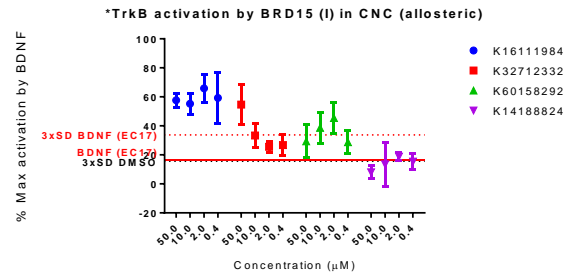
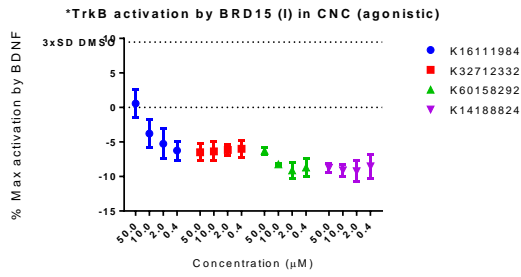


*TrkB activation by BRD14 (II) in CNC (allosteric)









2 Chapter II: Targeting neurons through screening platforms

2.1 Introduction

One of the challenges in neuroscience, neurology, and neurosurgery has been to gain the ability to identify pathological cell phenotypes and target therapy on a neuronal cell level. The brain is highly complex in its anatomy and physiology. A great progress has been made to image and measure brain activity on a macroscopic level using different techniques, like computed tomography (CT), functional magnetic resonance imaging (fMRI), electroencephalogram (EEG), and positron emission tomography (PET). However, it still remains challenging to visualize brain on cellular and molecular levels underlying the circuits and connections.

2.1.1 Central nervous system diversity of neurons and synapses

The central nervous system (CNS) is one of the most complex structures in a human body. The mature male brain has been found to have 170 billion cells, of which 86 billion has been identified as neuronal cells through immunoreactivity of the neuronal nuclear protein (NeuN) (1, 2). Distribution of neurons has been shown to be non-uniform across different brain structures; for example, 80% of the neurons have been localized to the cerebellum and 19% to the cerebral cortex (1). Interestingly, the distribution of the non-neuronal cells has been found to be inverse, with 72% of total number in cerebral cortex and 19% in the cerebellum. In cortical grey matter, 12 billion neuronal bodies and 17 billion non-neuronal cell bodies have been identified giving the ratio of non-neuronal/neuronal number close 1.5. In the white matter non-neuronal cells have been found to be much more abundant with 40 billion against 2.6 billion of neuronal cells increasing the ratio up to 15 non-neuronal to 1 neuronal cell body (1).

Classification of the neurons has also been an important goal in understating the functional activity of the brain areas. For example, cerebral cortex, which has been estimated to have 180 different areas responsible for motor, sensory, and high-order executive functions, has been shown to have two major classes of neurons: glutamatergic excitatory neurons and GABAergic inhibitory neurons (3). However, to provide diverse functional activities of the cortex, each area must contain different types of neurons. Indeed, RNA sequence profiling revealed 19 distinctive excitatory neuronal types and 23

interneuron types under the four main subclasses in the adult mouse visual cortex (4). In rat somatosensory neocortex, approximately 207 neuronal types have been identified based on morphological and electrophysiological properties (5).

To identify the different types of neurons morphological and electrophysiological properties have been studied in-depth, but perhaps a more useful approach has been employment of biochemical markers that are expressed in the neuron of interest, which could be used to genetically tag these neurons. The molecular classification has also been used to classify cells, for example, GABAergic parvalbumin-expressing neurons, or somatostatin-expressing neurons were named after the specific protein expressed in these cells (6).

Such diversity of neurons should also produce large diversity of the synaptic connections. Indeed, simulation of a small volume of rat neocortex containing 31,000 neurons predicted 184 million synapses with an average of 1,145 synapses per neuron and each neurons innervating 255 other neurons belonging to 32% of total number of neuron types present the area (5). Overall, synapses have been classified based on the neurotransmitters that are released during the signal transduction, as well as microanatomical (e.g. connectivity, size and number of synaptic vesicles, dimensions of the synaptic cleft and postsynaptic density), electrophysiological (e.g. excitatory or inhibitory postsynaptic potentials), and molecular (different ligand-gated ion channels) features (7, 8). Therefore, although the basic molecular machinery required for NT release is similar, it could be hypothesized that some neurochemical markers specific to certain neuronal types may also distinguish the synapses formed by these cells.

2.1.2 Neurons and synapses in pathologies

Synaptic connections have been shown to be altered in different pathologies (9, 10). For example, the mutation in cell adhesion molecules neuroligin and neurexin that form trans-synaptic complex along with synaptic scaffolding proteins were found in individuals with autistic spectrum disorders. Interestingly, mice with neuroligin or neuroxin knock-out have shown impaired synaptic transmission with no change in the number of synapses (11). Moreover, mice bearing mutations in these genes have found to exhibit a shift in the excitatory and inhibitory signals with enhancements in GABA_A receptor-mediated synaptic transmission (12). To measure such intricate changes in signaling would require detection of the neurotransmitter release, or action potential in certain cell types, which would be

possible with probes that have a homing potential to the cells of interest. On the other hand, in neurodegenerative diseases synaptic loss is seen together with synaptic function dysfunction

2.1.3 Genetic methods

To monitor synaptic activities various genetic methods have been developed based on pH or calcium sensitive fluorescent proteins. For example, a fusion protein of vesicle-associated membrane protein and a pH sensitive form of green fluorescent protein (pHluorin), where pHluorin is located in lumen of the synaptic vesicle, has been successfully used to indirectly measure the neurotransmitter release/exocytosis during the stimulation (13). In another construct, a genetically encoded calcium indicator GCaMP has been fused to the cytoplasmic C-terminus of the synaptic vesicle protein synaptophysin, which yielded a robust reporter gene of the calcium influx in the presynaptic termini during the action potential (14).

An intriguing approach to visualize synapses has been reported where a GFP-fused intrabody, an antibody-like protein, for postsynaptic density protein 95 and gephyrin (a component of the postsynaptic protein network of inhibitory synapses) has been transfected into neurons with self-regulated expression allowing to achieve high signal-to-background ratio (15). In other words, using such construct has provided opportunity to perform an immunofluorescence assay inside the living cells.

To directly detect the neurotransmitter release, a FRET based construct has been engineered where a bacterial glutamate-binding protein GltI has been sandwiched between two FRET partner proteins, CFP and citrine. The binding of the glutamate to the GltI causes a disruption of FRET between the fluorescent protein reaching a 10% FRET ratio change upon the glutamate release (16). An improved version of this sensor has taken advantage of the circularly permuted GFP, which has been shown report on the release of glutamate in vivo in mice (17).

All these methods are powerful enough to detect a single neurotransmission event, however, they require genetic manipulations and viral transductions, which always raises the question of genetic alterations and phenotypic consequences. Moreover, these constructs have limited application for diagnostics and treatments due to invasive natures of the methods. Thus, developing the chemical approach to detect and measure synaptic transmissions and neuronal composition of the brain has a potential to be used beyond the preclinical research purposes.

2.1.4 Chemical methods

There are only a few chemical probes developed to report on neurotransmission-related physiological processes. These include FM dyes and voltage sensitive dyes (VSDs). There is only one class of chemical probes that are both targeted to specific neuronal cell/synapse types and report on neurotransmission: the FFN probes (see below).

The FM dyes, based on the styryl-pyridinium fluorescent core, provide membrane staining due to the lipophilic character of the probe, however these compounds do not readily cross the cell membranes owing to the two charges (Figure 2.1.1 A) (18, 19). This structure also provides an environmental sensitivity to the dye with two orders of magnitude larger quantum yield in the non-polar solvents. It has been largely used for staining active synapses. However, the method of staining has not been simple, where the dye must be loaded into the synaptic vesicle through the recycling of the vesicles, which requires electrical or high K⁺ concentration stimulation of the neurons (18). Even though any type of synapses could be labeled by these dyes, staining procedure and lack of specificity to the neuronal plasma membrane have restricted the utility of these dyes mostly to in vitro application.

Structurally similar to FM dyes, naphthylstyryl class of the fluorophore has been found to have electrochromic properties, a shift in excitation and emission spectra caused by the change in the external electric field, which allowed to optically measure changes in cell membrane potential (Figure 2.1.1 B) (20). These dyes opened the opportunity to image membrane potential changes with millisecond temporal resolution, which classified them as fast VSDs. Following a different structural design, a new class of VSDs has been developed based on a bright fluorophore and an orthogonal π -wire containing the aniline group at its end (Figure 2.1.1 C). This design was guided by the idea of electric field induced modulation of the photo-induced electron transfer (PeT) from the aniline electron lone pair to the fluorophore (21). This class of VSDs produce better optical sensitivity and structural flexibility while retaining the temporal resolution. In addition to the fast VSD, alternative structural and mechanistic designs have been developed such as fluorophore repartitioning, reorientation, or aggregation with various spatial and temporal resolutions. However, one of the major limitation of the VSD has been the lack of cell specificity in brain tissue (22–24).

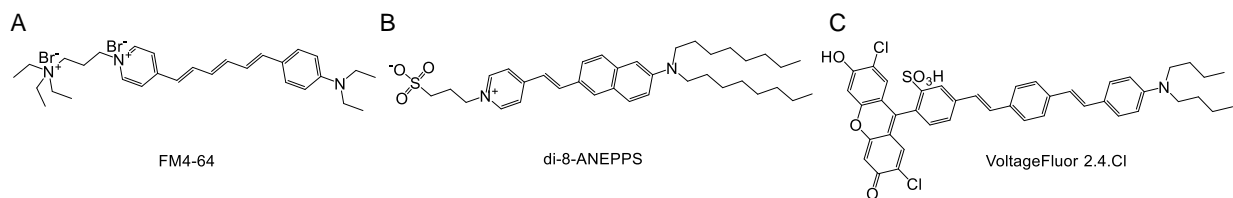


Figure 2.1.1 Structure of synaptic and voltage sensitive dyes.
 A. Structure of FM4-64, example of endocytic dyes. B. Structure of di-8-ANEPPS, an electrochromic fluorophore.
 C. A voltage sensitive dye VF2.4 based on PeT sensing mechanism.

An interesting approach to detecting and reporting on neurotransmitter release has been developed in our laboratory, based on the idea of designing the fluorophore by mimicking the neurotransmitter structure (Figure 2.1.2) (25, 26). This class of probes, named fluorescent false neurotransmitters (FFNs), is characterized by several design features, most notably the probe acts as a fluorescent substrate of both the plasma membrane and vesicular transporters. In some instances, FFN probes were also designed as pH sensors with the pKa values in the relevant physiological range between the pH of the vesicle lumen and cytoplasm (from 5.5-7.4). For example, FFN102 is a dopamine transporter and vesicular monoamine transported substrate, as well as a pH sensor, which has been successfully used to image individual dopaminergic terminals *in vivo* and report on changes in vesicular pH and neurotransmitter release (Figure 2.1.2) (27, 28). Another probe, FFN200, has revealed the existence of silent synapses in striatal dopamine axons (Figure 2.1.2) (29). FFNs has also been instrumental in the study of pharmacological mechanisms of psychostimulants in intact brain circuitry (30). Even though FFNs has provided high specificity and functional activity at specific synapses, they have so far been limited to the monoaminergic neuronal systems.

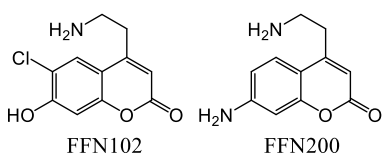


Figure 2.1.2 FFN structure
 FFN102, a pH sensitive dye specific to dopaminergic terminals. FFN200, specific to dopaminergic terminals.

Chemical targeting of living neurons (even in the absence of any sensing capabilities) has limited precedent. A neuron specific probe, named NeuO (Figure 2.1.3), has been developed in Dr. Chang's laboratory (POSTECH) through the high content screening (HCS) of a diversity-oriented

fluorescence library (DOFL) (31). This dye demonstrated a high selectivity to neuronal cell bodies *in vitro* and *in vivo*, allowing to differentiate neurons from glia and other non-neuronal cells without affecting the functional integrity of the neurons. Mechanistically, it is yet to be uncovered how NeuO achieves such a high specificity.

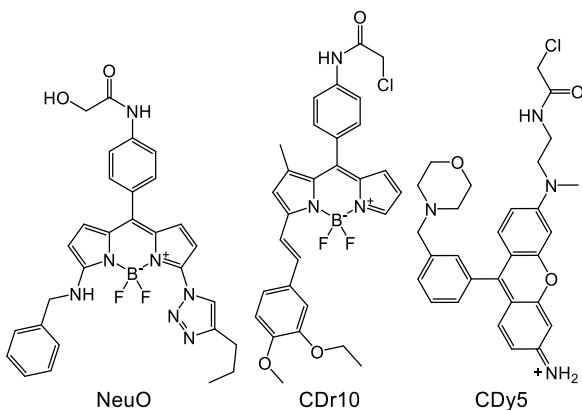


Figure 2.1.3 Structures of NeuO, CDr10, and CDy5
 NeuO, a neuron specific dye. CDr10, a microglia specific dye. CDy5, a neural stem/progenitor cell specific dye.

The DOFL approach seems to be a promising method for identifying similar probes for different cell types (32). For example, a microglia specific probe, CDr10, which has also been found through the HCS, allowed to quantitatively isolate microglia by flow cytometry and label the cells for a long period of time (33). Interestingly, CDr10 and NeuO are based on the same BODIPY fluorescent core (Figure 2.1.3),

however, the difference in the side groups has been sufficient to grant the specificity to two distinct cell lines. Perhaps, one of the most exciting success of DOFL approach could be exemplified by the neural stem/progenitor cell probe, CDy5 (Figure 2.1.3), which visualized the symmetric and asymmetric cell division of the stem cells by staining both or one of the daughter cells (34). Given the diversity of the neuronal cells in the brain, DOFL approach may be a very promising method in identifying probes that would specifically label the cells of interest.

2.1.5 Phage display

An alternative approach for finding a cell specific probe could be phage display of peptides or proteins. The success of this methods could be exemplified by the in vivo screens conducted by Dr. Ruoslahti (35). By targeting various tumors in vivo, it has become apparent that each tumor influences the protein expression on the membrane surface of the vasculature, which then creates a sort of molecular ZIP code of the area, which can be targeted with homing peptides found in the phage display. Similar idea could be applied to any cell type, under the assumption that each cell type has a unique protein profile expressed on the plasma membrane, and that could afford a target specificity. In other words, a gene expression profile is reflected on the cell surface, and thus, similar to a gene promoter providing genetic targeting of the cell, a cell surface could provide a platform for the chemical targeting.

Phage display provides a diverse library of peptides, from which some could bind to the membrane protein specific to the neurons. However, due to blood-brain barrier (BBB) that physically

restricts the access to the neurons in the brain, most of the efforts focused on finding peptidic probes has been focused on the discovery of ligands that could penetrate the BBB (36).

To deliver a payload to the brain parenchyma, one of the approaches has been to mimic tetanus toxins, which has been shown to selectively bind and penetrate axon terminals of the peripheral nervous system and then undergo retrograde transport. For this purpose, a two-tier selection method for a peptide with affinity to a tetanus toxin receptor using M13 phage display has been developed, in which *in vitro* biopanning on the trisialogangliosides (GT1b), an oligosaccharide-derivative important for functional activity of the tetanus toxin, has been performed followed by the biopanning on NGF-differentiated PC12 cells. The identified CX7C peptide, Tet.C7C.1, with CKGTINPFC sequence, has shown to have affinity to the dorsal root ganglia and lower motor neurons (37). Another peptide, Tet1 with HLNILSTLWKYR sequence, found through phage display of immobilized GT1b (38) has been shown to deliver nanoparticles into the brain parenchyma following intracarotid artery injection (39). However, it has not been demonstrated whether this peptide stains any specific neurons in CNS (40).

In another attempt to address BBB penetration, Wan et al. have examined the nasal passage of therapeutics as an approach to bypass BBB (41). Using Ph.D. – C7C library in M13 bacteriophages researchers identified an 11-aa long sequence, ACTTPHAWLCG, that displayed increased homing into the brains of live rats as compared to distribution to other organs or tissues (liver, spleen, blood). This method displays a potential to improve brain specificity as well as pharmacokinetics of peptidic drugs.

There have been efforts to target neuronal cells as well. Staquicini et al. have applied phage display method (CX₇C: C, cysteine; X, any residue) to characterize the mechanisms involved in neuronal stem cells (NSCs) proliferation and migration, as well as astrocytic-neuronal crosstalk, in development of murine olfactory system (42). Out of 5 most selective sequences, the authors have selected one, CGLPYSSVC, which showed superior efficacy in inducing proliferation, migration and adhesion in comparison to other peptides. The method has helped the authors to identify some of the key molecular players, netrin-4/laminin γ 1chain/ α 6 β 1 integrin, in olfactory bulb development and maturation. Another lab, Hou et al, has employed M-13 phage display in attempt to improve targeted gene delivery to mouse cerebellar granule neurons (CGNs) (43). Although a careful analysis of 4 most promising compounds *in vitro* did not confirm significantly superior selectivity to neurons, the authors have emphasized the utility of

phage display method for post-mitotic neurons identification. Taking it a step further Schmidt et al. have used M-13 phage library to identify a peptide that would guide adenoviral internalization into neuronal precursor cells (NPCs) neurospheres for targeted gene delivery (44). Upon identification of selective sequences, QTRFLLH, VPTQSSG, and HTFEPGV, the two former sequences were covalently linked to adenoviral red fluorescent protein (AdRFP) and injected the AdRFP.QTRFLLH and AdRFP.VPTQSSD viral particles into hippocampi of young adult pNestin-GFP transgenic mice, to verify NPCs selective delivery. Authors concluded that although they were able to demonstrate NPC selectivity in vitro, considering the variability of NPCs in different brain regions, further improvements will need to be achieved for each brain region.

Emphasizing the versatility of phage display derived peptides, Whitney et al. have employed the method for fluorescent tagging of peripheral nerves to reduce adverse events during surgical procedures. In their in vivo studies, authors have identified a sequence, NP41, NTQTLAKAPEHT, which selectively localized to sciatic nerve and its branches post IV injection as compared to surrounding tissue (45). Further analysis, however, showed that the peptide was specific to epineurium and, to some extent, to perineurium and endoneurium, as opposed to axons and/or myelin. Still, the study represents an example of versatile application of phage display method for therapeutic targeting and selective modulation.

2.2 Results

2.2.1 Overview

To address the shortage of the specific chemical probes for glutamatergic and GABAergic synapses, or other parts of the neurons, like axons and dendrites, or even for different neuronal types, we set out to develop new methods for finding these molecules. DOFL coupled with the HCS has shown promise for finding cell type specific fluorescent probes. An HCS platform was developed in collaboration with Dr. Waites (CUMC), Dr. Chang (Pohang University), and Dr. Karan (CUMC), to explore the possibility of finding molecular probes for glutamatergic synapses or neurons. In addition, a phage display method was developed to find peptides that could specifically bind to the striatal neurons in collaboration with Dr. Ruoslahti (SBP MRI), Dr. Teesalu (SBP MRI), and Dr. Sulzer (CUMC).

2.2.2 High content screening assay

To find fluorescent compounds that would specifically stain synapses, a high content screening strategy was developed where compound labeling patterns were compared to a well-characterized synaptic marker. The primary parameter to compare these patterns was the colocalization values of synaptic marker and fluorescent compounds. Other parameters were also measured (see below). The synaptic marker was either the expression of GFP-Synapsin1a (GFP-Syn) or mCherry-Rab3 (mCh-Rab3) to provide optically compatible control to the different library groups (see below). Synapsin1a is a cytoplasmic protein that has been hypothesized to regulate the synaptic vesicle reserve pools by tethering them to cytoskeleton, and thus, it is primarily localized in presynaptic boutons (46). The GFP-Syn construct has been shown to be localized in the synapses, making it a good synaptic marker (47). Rab3 is a small GTPase protein that regulates Ca²⁺-dependent neurotransmitter release (48, 49). It has been shown to be located in glutamatergic and GABAergic terminals, making it another good synaptic marker (50). To perform a high content screening, it was necessary to conduct imaging on readily available and abundant neuronal cells. We used cortical neuronal cultures (CNC) due to the high number of neurons in the cortex and a simpler harvesting procedure (compared to other neuronal cultures). In addition, CNC could be maintained for a long time and consisted of predominantly glutamatergic and GABAergic synapses (51). CNC were lentivirally transduced with the one of the synaptic marker at days in vitro (DIV) 3 and cultured until DIV 14-16 to allow for synapse formation and maturation in 96-well plates. More than 60% of neurons expressed the synaptic markers, which formed fluorescent puncta readily detectable in the imaging system (Figure 2.2.1 A-B).

The cell imaging system in the Columbia Genome Center high-throughput screening core (IN Cell Analyzer 2000, GE Healthcare; 2048 x 2048 pixel CCD camera) allowed imaging of a whole 96-well plate in 2 channels within minutes. CNC were treated with the library for 20 min and then washed before imaging. Images then were analyzed using an algorithm developed in the image analysis software (IN Cell Developer Toolbox).

To develop the algorithm, screening plates were immunostained with antibodies against known synaptic (synaptic vesicle glycoprotein 2, SV2; vesicular glutamate transporter 1, VGLUT1; Synaptophysin; and Synapsin) and non-synaptic (microtubule associated protein 2, MAP2; and lysosomal

associated membrane protein 1, LAMP1) markers (Figure 2.2.1). Thresholding of images to select synaptic puncta and exclude background signals was optimized empirically, using images of neurons immunostained with the GFP or mCh antibody, which should exhibit ~100% colocalization with GFP-Syn and mCh-Rab3, respectively. Colocalization values were expressed as the fraction of GFP-Syn or mCh-Rab3 puncta that exhibited overlap with the immunostained protein. With the software parameters established using the above-mentioned criteria, the algorithm could reliably distinguish synaptic proteins (avg. colocalization of 0.67) from non-synaptic proteins (Figure 2.2.1 C-D).

To test a small molecule in the assay, screening plates were stained with FM4-64, a lipophilic dye taken up by recycling synaptic vesicles that is an established marker for active presynaptic boutons (19). FM4-64 required stimulation of cortical neuronal culture with 90 mM KCl, followed by washing. While, FM4-64 exhibited a lower signal-to-noise ratio than immunostained synaptic proteins due to its non-

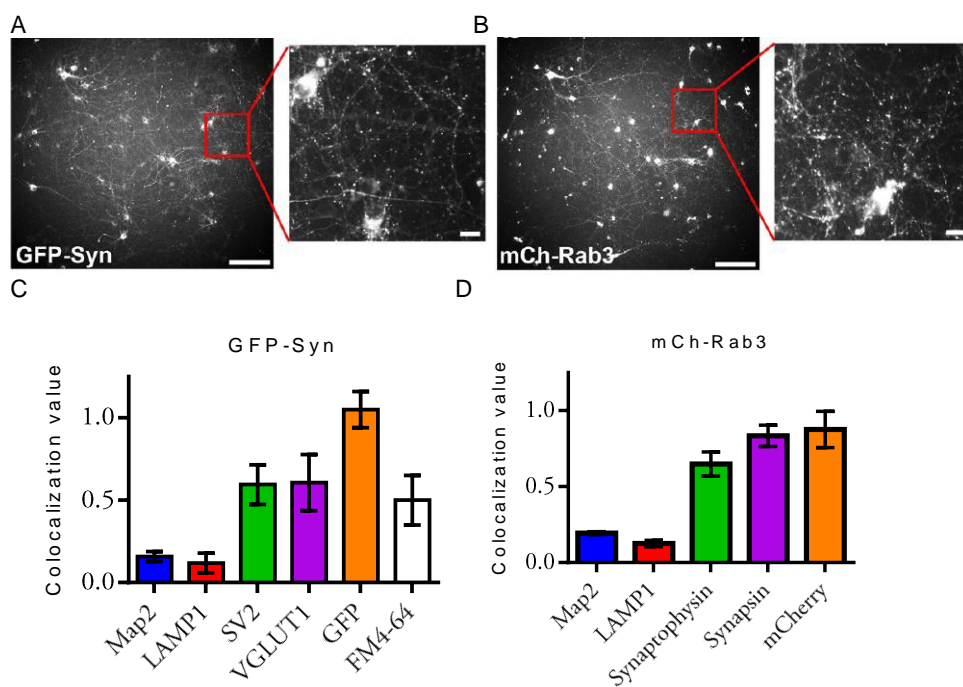


Figure 2.2.1 Characterization of synaptic markers for HCS

A. A representative image (original and zoomed) images of GFP-Syn expressing cortical neurons in 96-well plate format, acquired via high-throughput screening microscope. Scale bar is 100 μ m for original image, 10 μ m for zoomed image. B. Same as (A), but neurons are expressing mCh-Rab3. C. Colocalization values of various markers and FM4-64 with GFP-Syn construct. Non-synaptic markers, MAP2 and LAMP1, had low colocalization with the construct at 0.16 ± 0.03 and 0.12 ± 0.06 respectively, while synaptic markers, SV2 and VGLUT1, had higher colocalization at 0.6 ± 0.1 and 0.6 ± 0.2 respectively. FM4-64 had similar colocalization as synaptic markers with 0.5 ± 0.2 . GFP antibody had 1.1 ± 0.1 colocalization with the GFP construct. D. Colocalization values of various markers with mCh-Rab3 construct. Non-synaptic markers, MAP2 and LAMP1, had low colocalization with the construct at 0.19 ± 0.01 and 0.13 ± 0.03 respectively, while synaptic markers, Synaptophysin and synapsin, had higher colocalization at 0.65 ± 0.08 and 0.83 ± 0.07 respectively. mCherry antibody had 0.9 ± 0.1 colocalization with the construct

specific labeling of cellular membranes, it served as a good test case (and the only available chemical tool-based positive control) for the colocalization algorithm in live neurons. Although the colocalization values for FM4-64 were lower than those for immunostained synaptic proteins, the average value (Figure 2.2.1 C) was still significantly higher than that seen for non-synaptic proteins.

2.2.2.1 Fluorescent library

The library for this screen, which contained 7 different structural fluorescent cores, was provided by Dr. Y. T. Chang. One of the main cores presented in the library was BODIPY-triazole structure that exhibited a very large Stokes shift (up to 160 nm), as well as environment-dependent fluorescence (Figure 2.2.2 A) (52). NeuO dye was found using this sub-library (31). Other chemosensing fluorescent structures were based on benzimidazolium dyes, which were used to find a turn-on fluorescent GTP sensor (Figure 2.2.2 B) (53). Similar to benzimidazolium structures, a quinaldine scaffold based sub-library was also used in our HCS, providing the library with a broad range of excitation/emission wavelengths from 315/480 nm to 600/720 nm and a broad range of Stokes shifts from 530/555 nm to 485/720 nm (Figure 2.2.2 C) (54). A chalcone amide sub-library was also used in our HCS (Figure 2.2.2 D). This sub-library exhibited absorbance at 430 nm and emission at 560 nm with quantum yield at 0.2. A green mouse embryonic stem cell probe, CDg4, was derived from this sub-library, which stains embryonic stem cells and was used both for imaging and flow cytometry (55). The rosamine based sub-library

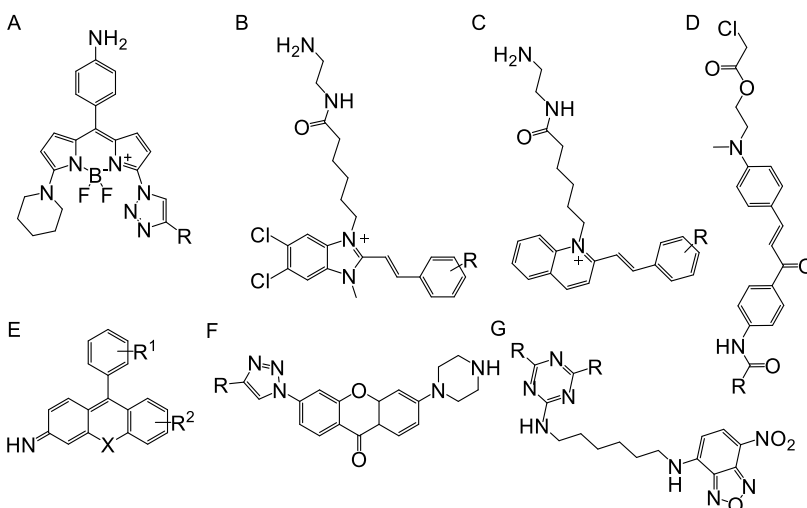


Figure 2.2.2 Structural cores of the fluorescent library.

A. BODIPY-triazole structure. B. Benzimidazolium structures. C. Quinaldine structure. D. Diaminochalcone structure. E. Rosamine structure. F. Xanthone structures. G. Nitrobenzoxadiazole conjugate triazine structure.

provided compounds with excellent photophysical properties, which was used to identify a yellow stem cell marker, CDy1 (Figure 2.2.2 E) (56). To cover blue range of wavelengths, xanthone scaffold based sub-library, which was used to find blue embryonic stem cell marker CDb8, were also provided

(Figure 2.2.2 F) (57). Nitrobenzoxadiazole tagged triazine derivatives (Figure 2.2.2 G) were included where triazine structures could provide biological activity (58) while nitrobenzoxadiazole was used as one of the smallest fluorescent cores

Table 2.1 List of the groups for HCS

Filter combination	Number of compounds	Number of 96wells plates	Synaptic marker used for this group
CFP:YFP (430±12/535±15)	503	6	mCherry-Rab3 (587/610)
DAPI:Cy3 (350±25/605±32)	80	1	mCherry-Rab3
DAPI:FITC (350±25/525±18)	961	12	mCherry-Rab3
FITC:Cy3 (490±10/605±32)	669	8	mCherry-Rab3
FITC:FITC (490±10/525±18)	633	8	mCherry-Rab3
FITC:YFP (490±10/535±15)	831	10	mCherry-Rab3
YFP:YFP (500±10/535±15)	38	1	mCherry-Rab3
CFP:Cy3 (430±12/605±32)	324	4	GFP-Synapsin (475/509)
Cy3:Cy3 (543±11/605±32)	311	4	GFP-Synapsin
DAPI:CFP (350±25/470±12)	401	5	GFP-Synapsin
DAPI:DAPI (350±25/455±25)	401	5	GFP-Synapsin
dsRed:dsRed (555±12/602±26)	968	12	GFP-Synapsin
FITC:TexasRed (490±10/624±20)	82	1	GFP-Synapsin
TexasRed:Cy5 (579±17/705±36)	125	3	GFP-Synapsin
TexasRed:TexasRed (579±17/624±20)	665	9	GFP-Synapsin

The fluorescent library was received as powders in 6992 wells across 80 plates. Compounds were then dissolved in DMSO to yield 200 μ M stock solutions, which were distributed into 89 plates. Based on their photophysical properties, and the available filters on the imaging system, compounds were divided into 15 groups with appropriate filter combinations, which served as a name of the group (excitation filter_ emission filter, Table 2.1). The size of the group varied from 968 compounds in dsRed_Cy3 to 38 compounds in YFP_YFP. Synaptic markers were assigned to each group based on the minimum overlap of excitation and emission wavelengths with 7 groups imaged against mCh-Rab and 8 groups against GFP-Syn. With an optimized platform for detecting synaptic labeling, the entire fluorescent dye library was screened. During screening, neurons were incubated with the compounds at 2 μ M concentration, washed, and imaged on the HTS microscope with 4 fields of view per well. A pilot screen on one of the DAPI_DAPI plates was performed to assess the screening platform. A primary screen of 89 plates was then performed following the outlined procedure (Figure 2.2.3), with 31 plates were re-screened due to technical issues of the control channel. Based on the analysis described below, cherry-picked the most promising compounds from the DAPI_DAPI plates were then screened at 8

concentrations from 31 nM to 2 μ M using the same protocol to determine concentration dependence (Figure 2.2.3).

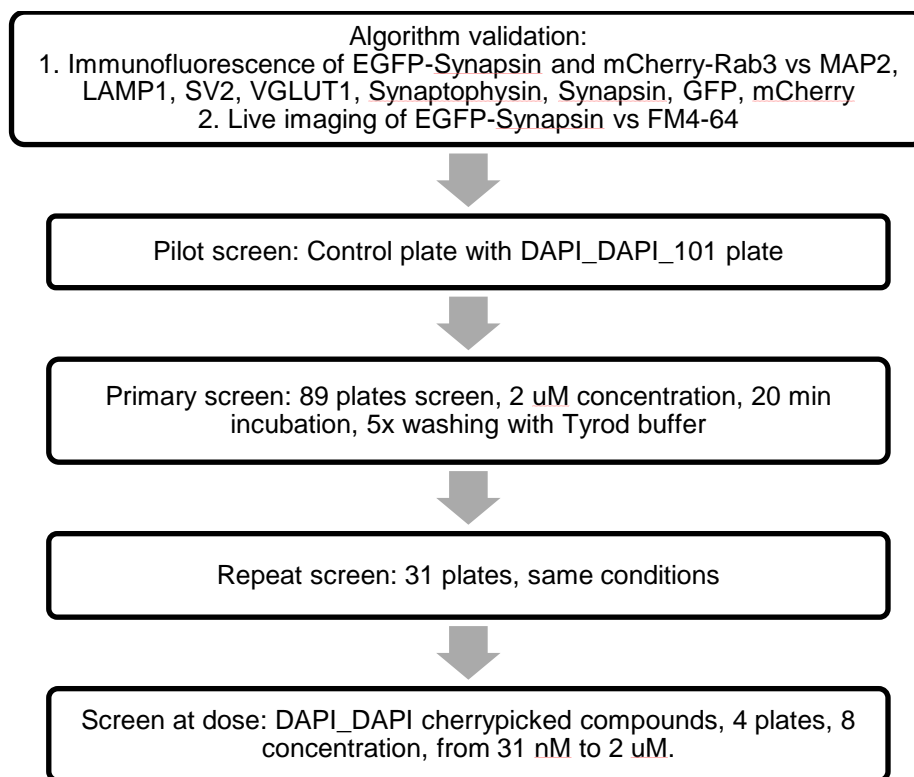


Figure 2.2.3 HCS outline

2.2.2.2 Image analysis

2.2.2.2.1 Parameters

To analyze the images, a segmentation algorithm was used to differentiate areas with either puncta or a cell bodies. As previously reported (59), the Vesicle Segmentation algorithm provided by the IN Cell Developer Toolbox (v.1.9) software was used to threshold images based on average size of GFP-Synapsin and mCh-Rab3 puncta (1–2 pixels; only objects in range of 0.5–5 μ m² were selected) and intensity (average intensity higher than 2–2.5 standard deviation over the background) (Figure 2.2.4 A). Thresholding of images to select synaptic puncta or cell bodies and exclude background signals was optimized empirically, using images of neurons immunostained with the GFP or mCh antibody for puncta, which should exhibit ~100% colocalization with GFP-Syn and mCh-Rab3, respectively. For the

immunostained images, puncta positive for a synaptic marker were collected by size and intensity (excluding pixels with intensities below 175 value). Compound channels were not thresholded.

For cell body identification, built-in Cytoplasm Segmentation algorithm has been used with filters on area and form factor of the objects (Figure 2.2.4 B). Specific values were chosen empirically using MAP2 immunostained screening plates; if the area of the selection was larger than $50 \mu\text{m}^2$ and form factor was greater than 0.2, then the large, round (form factor = 1-0.9) to oblong (form factor = 0.9-0.2) forms were selected as the cell bodies.

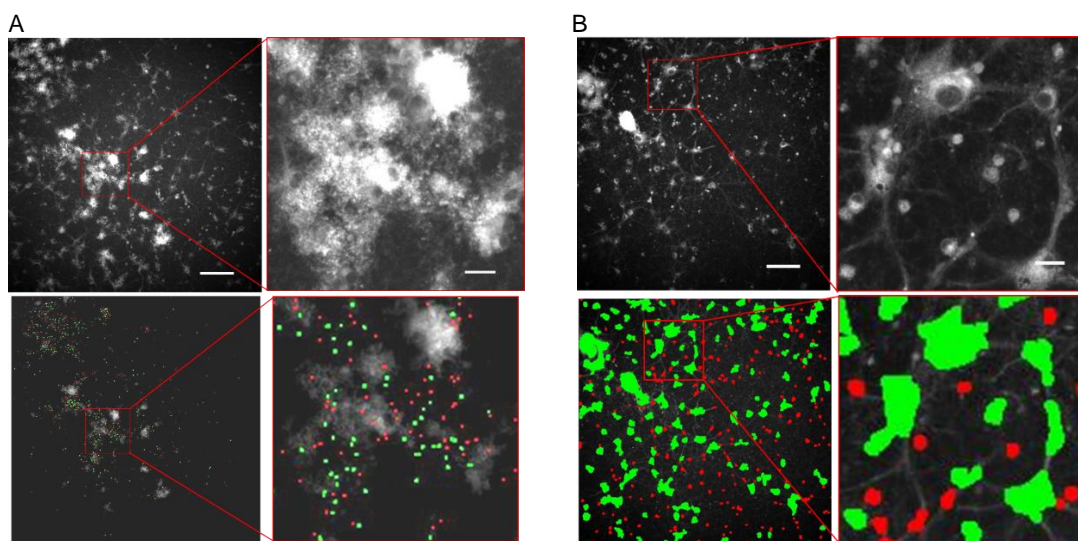


Figure 2.2.4 Segmentation of the representative image

A. Puncta identification using vesicle segmentation developed through IN Cell Developer Toolbox. B. Cell body identification using cytoplasm segmentation developed through IN Cell Developer Toolbox. Top image presents raw file, bottom presents segmentation pattern. Green mask represents selected ROI (puncta for A, and cell body for B) for measurement, red mask represents discarded ROI. Images on the left show full field of view (scale bar $100 \mu\text{m}$), images on the right show zoomed area (scale bar $20 \mu\text{m}$).

For each channel, the number of objects and the sum of object intensities were counted, and colocalization between channels were calculated based on the number of overlapping pixels. Fraction of the GFP-Syn or mCh-Rab3 region of interest (ROI) that colocalized with the immunostained proteins and later with each compound was referred to as overlap. Colocalization values expressed as the fraction of immunostained proteins or compound ROI overlapping with synaptic markers were referred to as coverage. As initial characterization, average overlap value for each group of compounds was calculated, and hits were defined as compounds with overlap values > 2.5 standard deviations above the group mean.

In addition to the number of objects and colocalization values, intensities as percentage of total image intensity were also used to characterize every plate to find promising compounds. Relative intensity provided additional information on compound distribution in the neuronal culture. For example, compounds that stain synapses had higher relative intensities in the puncta. In the dose response experiment, relative intensities of the puncta were higher at the lower concentration of the dye, presumably because the non-specific binding decreased while the specific staining remained the same or decreased with a slower rate (e.g., Figure 2.2.8 B).

To characterize the plates, these parameters were plotted against each other. The puncta overlap versus coverage plot would demonstrate the degree of colocalization of the compounds with the synaptic markers. Hit compounds were assumed to have high overlap and coverage, and thus should be positioned in the upper right side of the plot. As expected the synaptic proteins, VGLUT1 and SV2, were found in the upper right corner of the plot, whereas non-synaptic proteins, MAP2, LAMP1, and charged multivesicular body protein 2b (CHMP2b), were located in the lower left corner for puncta segmentation analysis (Figure 2.2.5 A). The observed reduced coverage of GFP could be explained by thresholding of the control channel, which reduced the number of puncta. Relative intensity of the hit compound in the puncta or the cell bodies would be expected to be high, while the number of the objects (puncta or cell bodies) would be within the certain limits, which based on the synaptic proteins colocalization should be between 1000-2000 puncta per image (Figure 2.2.5 B). High number of puncta or cell bodies indicated high non-specific staining and/or false segmentation (GFP in Figure 2.2.5B). Similar pattern is observed for cell body segmentation analysis showed in Figure 2.2.5 C and D. Puncta overlap and coverage versus cell bodies overlap and coverage would reveal compound distribution in the cell culture. Hit compounds that stain synapses would have higher overlap and coverage in synapses and lower overlap and coverage in cell bodies locating them in the upper left side of the plot (Figure 2.2.5 E, F). The inverse statement was assumed to be true for the cell body staining compounds. Similar information could be extracted from puncta number versus cell body number plot (Figure 2.2.5 G). Some of these plots do not

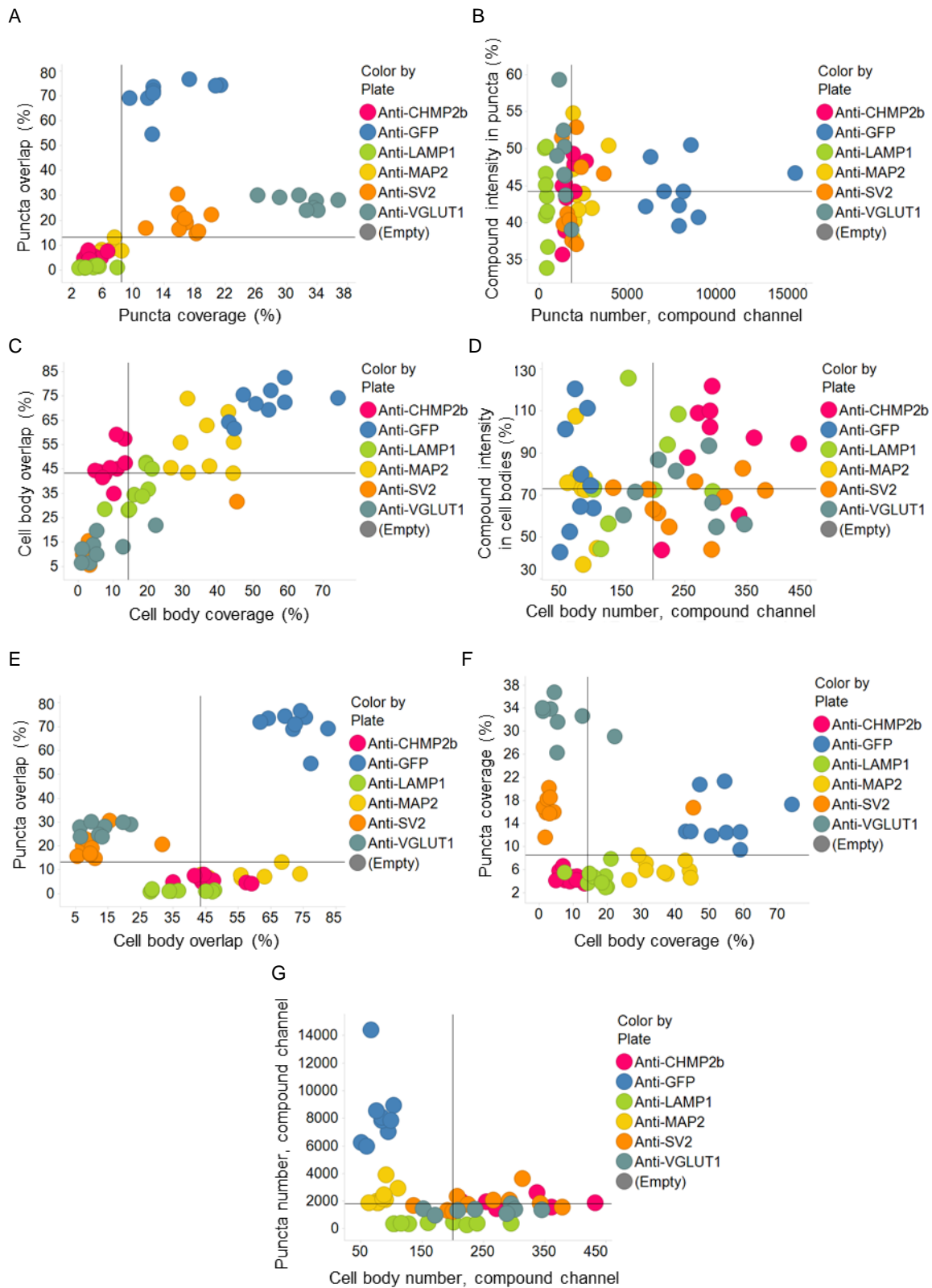


Figure 2.2.5 Control plate plots

A and C. Overlap versus coverage plot of the puncta segmentation (A) and cell body segmentation (C) of GFP-Syn and immunostained synaptic markers (VGLUT1, SV2), neuronal cell body marker (MAP2), and endosomal markers (CHMP2b, LAMP1). B and D. Average intensity in the puncta (B) or cell body (D) versus the number of

puncta and cell bodies in immunostained channel (referred to as compound). E-F. Overlap (E) and coverage (F) values of puncta and cell body segmentation plotted against each other. G. Raw puncta number versus cell body number in immunostained channel.

depend on the control channel and provide information of the staining patterns of the compounds.

All the plots of 29 analyzed plates, as well as representative images of the wells in the plate, are presented in the Appendix.

2.2.2.2.2 Quality control

As expected, a substantial amount of the compounds produced poor and inconsistent staining. To identify these compounds, and exclude them from the analysis, the relative standard deviation of any parameter value was measured, which should not exceed 100%. Hits that fell under this designation were manually checked for further inspection. For example, a compound in A8 well of CFP_FITC_101_Q3 plate was excluded because the relative standard deviation of the cell body number exceeded 100% (Figure 2.2.6 A). Upon inspection of these images, it was obvious that the staining was poor with low intensity, which probably created false segmentation.

On the other hand, some compounds at the screened concentration produced oversaturated images, which also could not be used to correctly characterize them. To identify compounds that resulted in poor images, a histogram analysis was used. The pixel histogram from each image was plotted, and then divided into 3 sections: bottom 10% (0-410 intensity), from bottom 10% to middle point (410-2048 intensities), from middle point to top (2048-4096). Then the number of pixels in each section was calculated using areas under the curve of the image histogram. By comparing these percentages, it was decided whether the well was bad, good, saturated, or oversaturated: if intensity of all pixels were smaller than 10% of maximal intensity, then it was a bad image (Figure 2.2.6 B); if the number of pixel with intensities in the top 50% was larger than the number of pixels with intensities in the bottom 10%, then the well was labeled saturated (Figure 2.2.6 D); if the number of pixel with the intensities in top 50% was larger than in the middle intensities, then well was considered oversaturated (Figure 2.2.6 E); every other condition was considered to be good (Figure 1.2.6 C). The average values of 3 quadrants were calculated to decide how to characterize a given well in the plate. The third quadrant was excluded from the

analysis, because it would contain inconsistent images probably due to close proximity to washing needle.

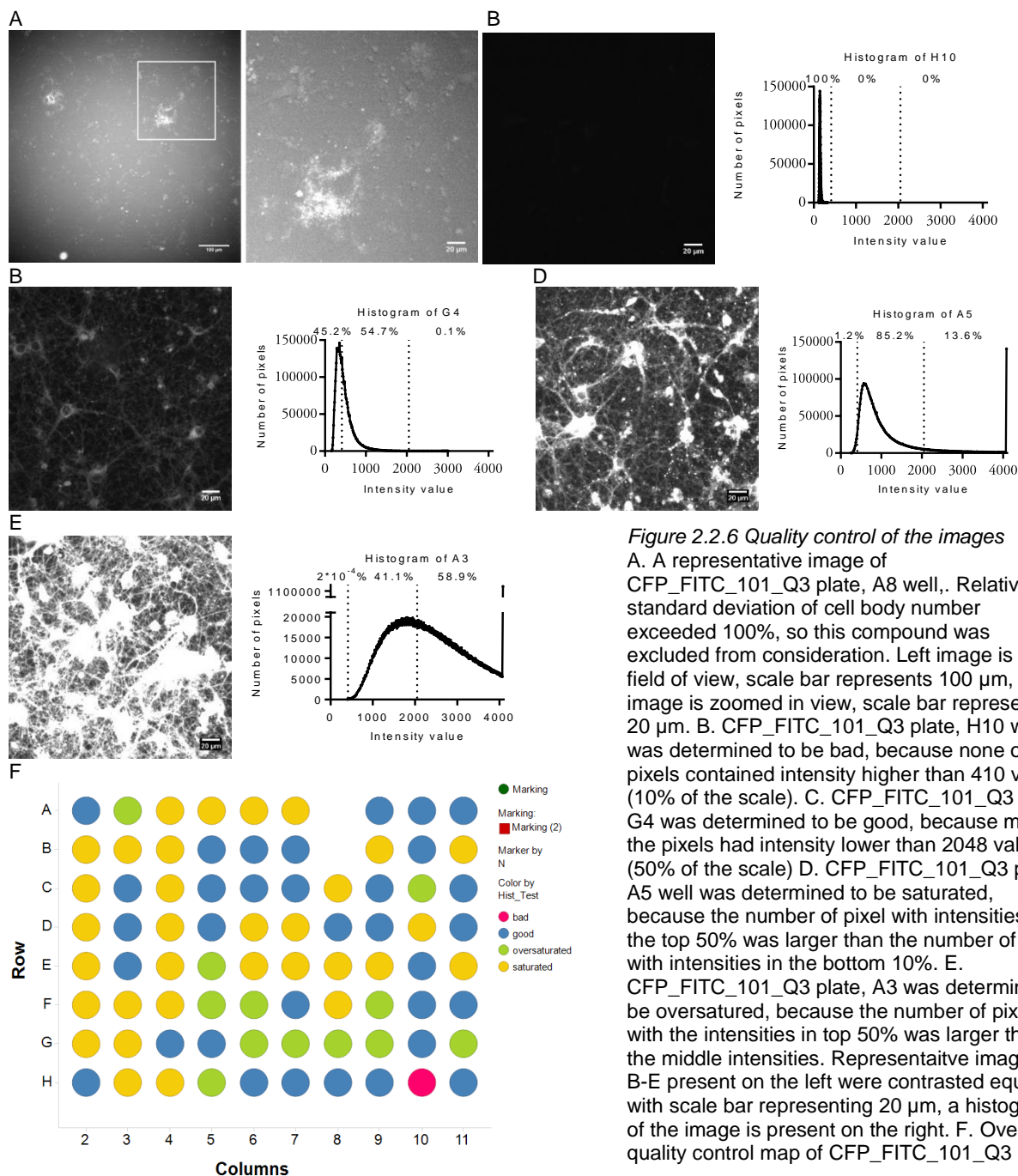


Figure 2.2.6 Quality control of the images

A. A representative image of CFP_FITC_101_Q3 plate, A8 well. Relative standard deviation of cell body number exceeded 100%, so this compound was excluded from consideration. Left image is full field of view, scale bar represents 100 μm, right image is zoomed in view, scale bar represents 20 μm. B. CFP_FITC_101_Q3 plate, H10 well was determined to be bad, because none of the pixels contained intensity higher than 410 value (10% of the scale). C. CFP_FITC_101_Q3 plate, G4 was determined to be good, because most of the pixels had intensity lower than 2048 value (50% of the scale). D. CFP_FITC_101_Q3 plate, A5 well was determined to be saturated, because the number of pixel with intensities in the top 50% was larger than the number of pixels with intensities in the bottom 10%. E. CFP_FITC_101_Q3 plate, A3 was determined to be oversaturated, because the number of pixel with the intensities in top 50% was larger than in the middle intensities. Representative images in B-E present on the left were contrasted equally, with scale bar representing 20 μm, a histogram of the image is present on the right. F. Overall quality control map of CFP_FITC_101_Q3 plate.

These filters identified compounds that produced good images, which were then examined first.

For example, in CFP_FITC_101_Q3 plate, 2 wells (A8 and B8) possessed bad statistics, 33 wells were labeled as good, 33 wells were saturated, and 12 wells were oversaturated (Figure 2.2.6 F). The overall

quality of all plates varied depending on the type of fluorophore and ranged from all good wells to only couple of good wells. The quality control maps of 29 analyzed plates are presented in the Appendix.

2.2.2.3 *Screening pitfalls*

2.2.2.4 *Signal cross-contamination issue*

The other issue in the screening was the bleed through of the compound emission into the control channel. To solve this issue, a MATLAB algorithm was developed based on the assumptions listed below:

1. The first assumption was that the control channels containing signals from the compound channel retained the same image contour of the compound channel
2. This compound image contour could be subtracted from the control image if the percentage of the bleed-through was known
3. There is at least one pixel in the bleed-through control channel that is purely compound signal.

Then the intensity of each pixel in the bleed-through control channel could be expressed with the following equation:

$$C = Cnt + n \times Cpd$$

where C is the intensity of the bleed-through control channel, Cnt – pure intensity of the control, n – bleed-through factor, Cpd – intensity of the compound channel. Therefore, the equation

$$Cnt = C - n \times Cpd$$

should restore the control image (Figure 2.2.7 A). To use this equation, n value must be found. To this end, a MATLAB algorithm for finding the n value and then generating the bleed-through subtracted control image was developed.

These new corrected images then were analyzed in IN Cell Analyzer 2000 algorithm again. As expected overlap and coverage values were reduced (Figure 2.2.7 B). The n value provided information about the bleed-through level of compounds into control channel. Some compounds had a quite substantial bleed through level with about 75% of their fluorescent signal in the compound channel (Figure 2.2.7 C).

Despite this success, corrected images seemed to still contain staining pattern of the compound channel and not characteristic of synaptic markers. A closer inspection revealed a small shift of the

stained objects between control and compound channels, possibly due to movements of the internal organelles visible on certain images (e.g. Figure 2.2.7 D). Aligning images using an X/Y registration component further improved n values by 10%. However, aligning did not correct for any fast-moving puncta and other movements that altered relative positions of the stained objects between the imaging of the two channels (Figure 2.2.7 D). Due to these issues, the correction algorithm was not run on the entire HCS images, but only used to identify possible hit compounds using the previously outlined parameters (see Parameters section above).

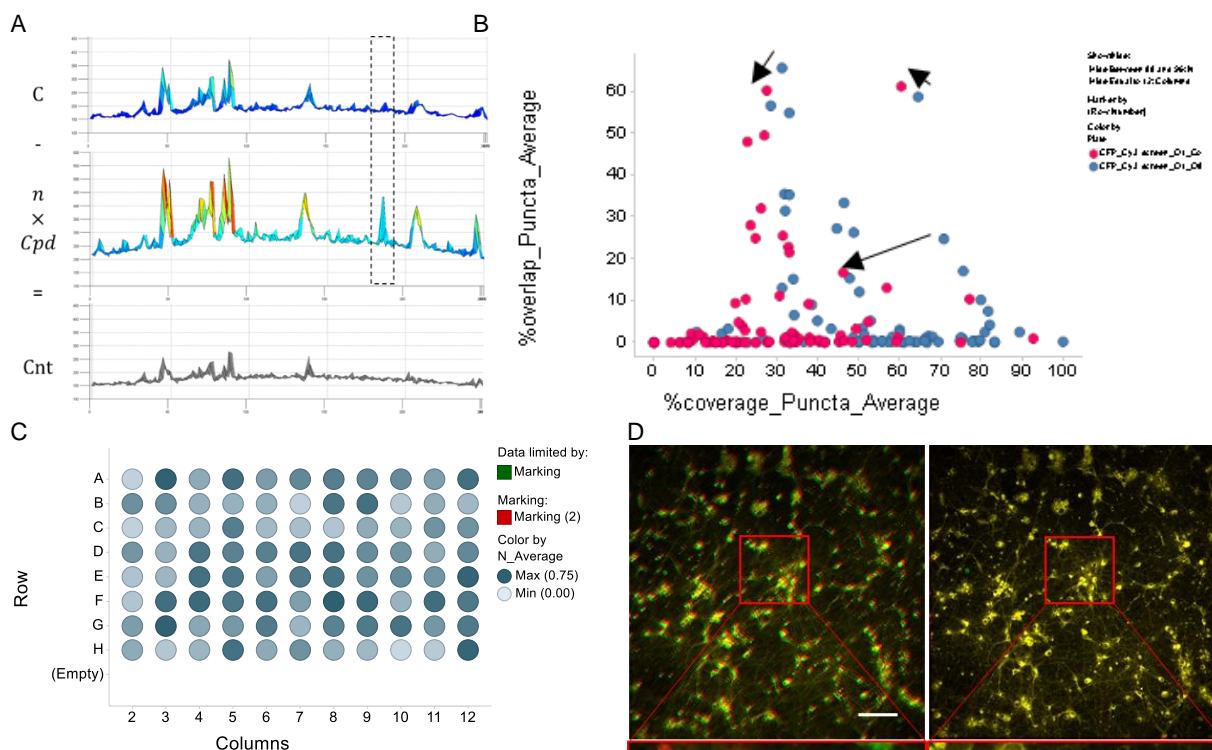


Figure 2.2.7 Bleed through correction

A. An example of image contours of the bleed through control image, compound image, and corrected control image. Dashed box indicates an example of the third assumption. B. Bleed-through correction influence on overlap and coverage values of the representative plate, arrows indicate the change of the overlap and coverage values for some compounds. C. A plate map of bleed-through factor calculated using the MATLAB algorithm. D. An example of the mismatch between the control and the compound images (top image – full field of view, scale bar 100 μm; bottom image – zoomed in view, scale bar 20 μm). Dashed boxes highlight displaced puncta

2.2.2.5 DAPI-DAPI plates

As the primary selection criteria, average overlap value was calculated for each compound group, and hits were defined as compounds with overlap values >2.5 standard deviations above the group mean. This selection method led to the identification of 53 hits across 11 of the compound groups (Table 2.2). Images of each hit compound were manually inspected to evaluate synaptic labeling. Sixteen were excluded due to bleed through into the control channel, as some of the compound groups exhibited broader excitation and/or emission spectra (indicated by Table 2.2). Of the remaining 37 hits, the 22 most promising (Figure 2.2.8 A) were from a single plate (Q4) of the compound group designated 'DAPI:DAPI' due to its excitation/emission profile in the 4',6-diamidino-2-phenylindole (DAPI) range (~360 nm excitation, 460 nm emission).

Table 2.2 Analysis of the overlap value per library groups

Filter combination	Overlap mean with synaptic marker	Hit threshold (with 2.5 StdDev)	Number of hits (with 2.5 StdDev)
FITC: Cy3**	33.8 %	86.8 %	4
Cy3: Cy3**	29 %	73.0 %	2
dsRed: dsRed	24.9 %	67.4 %	-
CFP: Cy3**	14.5 %	63.5 %	4
TexasRed: TexasRed	24.7 %	62.2 %	1
FITC: YFP**	18.6 %	59.6 %	3
Cy5: Cy5	25.5 %	58.7 %	-
FITC: FITC	15.3 %	56.2 %	-
TexasRed: Cy5	27.4 %	56.2 %	-
YFP: YFP	16.2 %	52.6 %	-
DAPI: FITC	12.4 %	49.8 %	1
CFP: YFP**	13.9 %	47.9 %	3
DAPI: Cy3	13.3 %	44.6 %	3
DAPI: CFP	8.6 %	27.8 %	8
FITC: TexasRed	3.1 %	25.8 %	2
DAPI: DAPI	4.1 %	25.1 %	22

To validate these findings, screening of the Q4 plate was repeated twice and selected compounds were imaged in a dose-dependent manner. The overlap values at the 2 μ M concentration were consistent across three experiments, averaging 0.30-0.40 for the top 10 hits (Table S4), similar to the colocalization of FM dye with GFP-Syn (0.50 +/- 0.15). The percentage of compound intensity in puncta increased with decreasing concentration of the dye indicating specificity toward puncta over other

cellular structures (Figure 2.2.8 B). Coverage remained at the same level, while overlap was smaller at lower concentration due to lowering of overall puncta number in the compound channel (Figure 2.2.8 C-D).

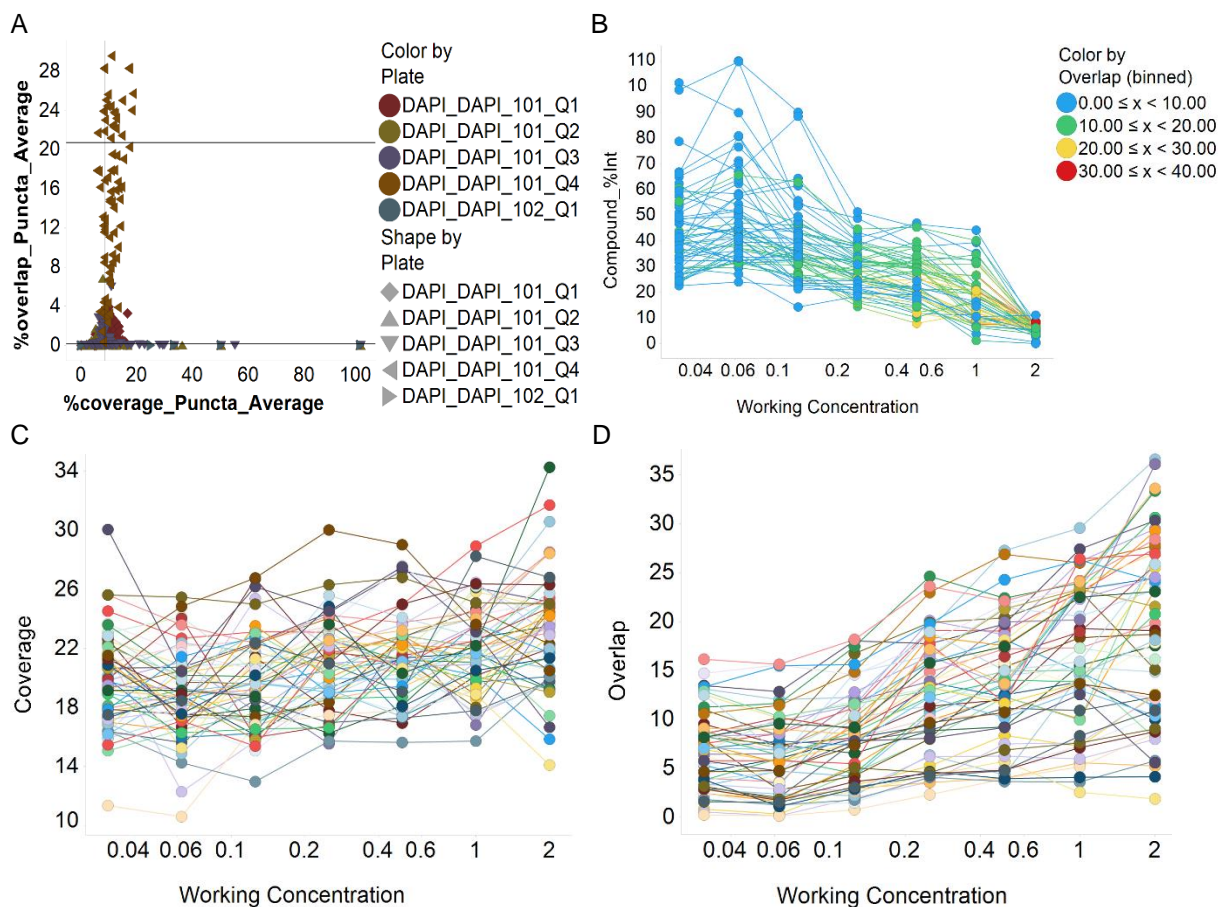


Figure 2.2.8 Parameters of the DAPI_DAPI plate

A. Overlap versus coverage plot of the DAPI_DAPI group, 5 plates. A horizontal line represents a cut-off level of the overlap value. Each point represents an average value of individual compound. B. Relative intensity versus concentration plot of the cherry-picked compounds. Overlap values are color-coded. C-D. Coverage and overlap versus concentration plot of the cherry-picked compounds.

2.2.2.5.1 Staining pattern

As we previously reported (59) an identified hit compound with highest overlap value at 36% at 2 μ M was CX-G3 compound. The puncta intensities of the compound increased by 14% to 50% at 125 nM, while overlap dropped to 7% and coverage reached 19% (Figure 2.2.9 A). To further characterize compound staining, CX-G3 was imaged and the colocalized against immunostained vesicular associated membrane protein (VAMP2) and VGLUT1. Since CX-G3 could not be fixed, a special grid dish was used to image the same field of view before and after fixation. Images then were retrospectively aligned for

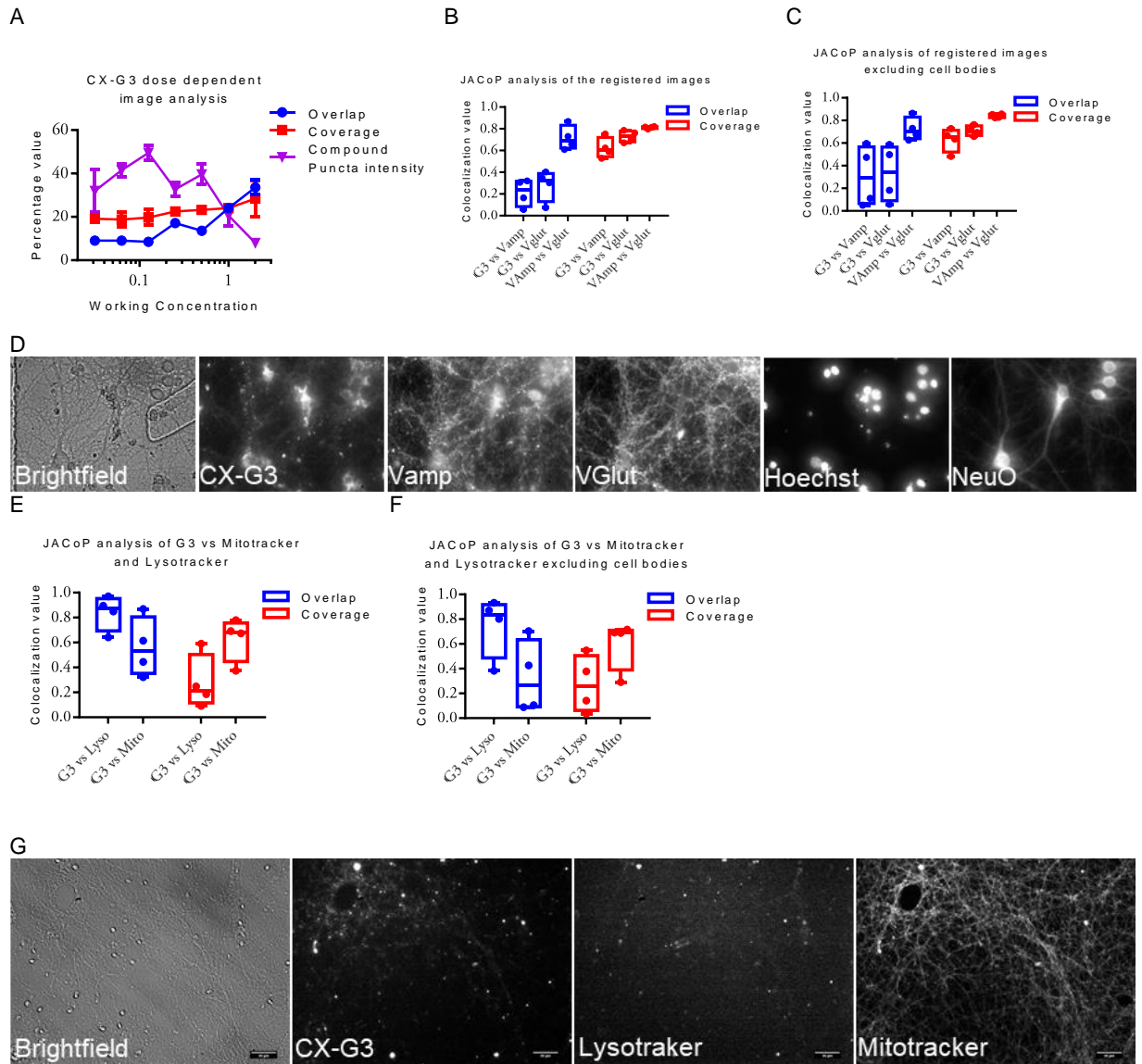


Figure 2.2.9 Colocalization of CX-G3 with immunostained markers, Lysotracker, Mitotracker
 A. Overlap, coverage, and relative intensity versus concentration plot of CX-G3. B-C. Colocalization analysis of immunostained synaptic markers and CX-G3 retroactively aligned. D. A representative images of live and immunofluorescent staining aligned retroactively. NeuO and CX-G3 were imaged live, while Vamp, VGlut, and Hoechst were imaged through the immunofluorescence. E-F. Colocalization analysis of Lysotracker and Mitotracker against CX-G3. G. A representative image of Lysotracker and Mitotracker with CX-G3. All images were taken in our laboratory. The scale bar represents 20 μ m.

colocalization analysis using the ImageJ Just Another Colocalization Plugin (JACoP) (60). Overlap value of CX-G3 compound was at 20-30% against VAMP2 and VGLUT1, while coverage reached 60-70% (Figure 2.2.9 B). Since cell periphery staining was more meaningful for synaptic markers, the analysis was repeated excluding cell bodies. Overlap value improved in this analysis reaching 35% values for both markers, while coverage remained the same (Figure 2.2.9 C). As a positive

control, the colocalization value of Vamp staining against VGLUT1 (labeled as overlap) was at 75%, while 82% of VGLUT1 (labeled coverage) colocalized with VAMP2 in both analysis approaches. When inspecting the image, it became apparent that CX-G3 also stained large puncta mostly in the cell bodies. CX-G3 also stained non-neuronal cells, which could be exemplified by comparing compound staining and NeuO, a neuron specific dye (Figure 2.2.9 D).

In addition to synaptic markers, it was important to identify whether any of the CX-G3 stained puncta were lysosomes and/or mitochondria. For this purpose, CX-G3 was co-stained with spectrally compatible LysoTracker and Mitotracker (Figure 2.2.9 E). The colocalization of LysoTracker with the compound (labeled overlap) was high at 85%, while Mitotracker had 53%. On the other, CX-G3 colocalized against LysoTracker (labeled coverage) with 21% of stained pixels, while against Mitotracker with 69% of pixels. Excluding cell bodies, CX-G3 vs LysoTracker colocalization values in both directions, and the percent of CX-G3 colocalized with Mitotracker, did not change, while about 26% of Mitotracker colocalized with the compound (Figure 2.2.9 F). On further analysis LysoTracker puncta showed high overlap with CX-G3, while CX-G3 stained more cells than LysoTracker, resulting in low coverage values (Figure 2.2.9 G).

To create higher quality of the CX-G3 staining of neuronal culture, imaging was performed on a microscope in Dr. Waites's laboratory (CUMC). To this end, a similar experiment was conducted, however, more detailed images were acquired could be captured for LysoTracker and CX-G3 (Figure 2.2.10 A). Colocalization values were calculated using an in-house developed algorithm (described in (59)) in ImageJ. In short, this involved selecting G3 puncta using a multiple threshold analysis, and then quantifying the percentage of pixels within each punctum that overlapped with the marker. Puncta which contained more than 50% overlapped pixels were considered to have a positive colocalization. The number of CX-G3 puncta that colocalized with LysoTracker reached 50% (0.45 ± 0.06 , Figure 2.2.10 B), while with Mitotracker colocalization was only 30% (0.29 ± 0.08 , Figure 2.2.10 B). Since the dye is not fixable, we also performed these experiments by live imaging in 14–16 DIV neurons lentivirally transduced on 3 DIV with mCh-tagged VAMP2 or Rab3. Again, we found that CX-G3 exhibited a high degree of colocalization with both VAMP2-mCh (0.57 ± 0.06 , Figure 2.2.10 B). and mCh-Rab3 (0.61 ± 0.09 ; Figure 2.2.10 B), comparable to colocalization values measured between mCh-Rab3 and

endogenous VAMP2 (0.51 ± 0.05 ; Figure 2.2.10 B). CX-G3 also strongly colocalized with FM4-64 in hippocampal cultures (0.45 ± 0.05 ; Figure 2.2.10 B).

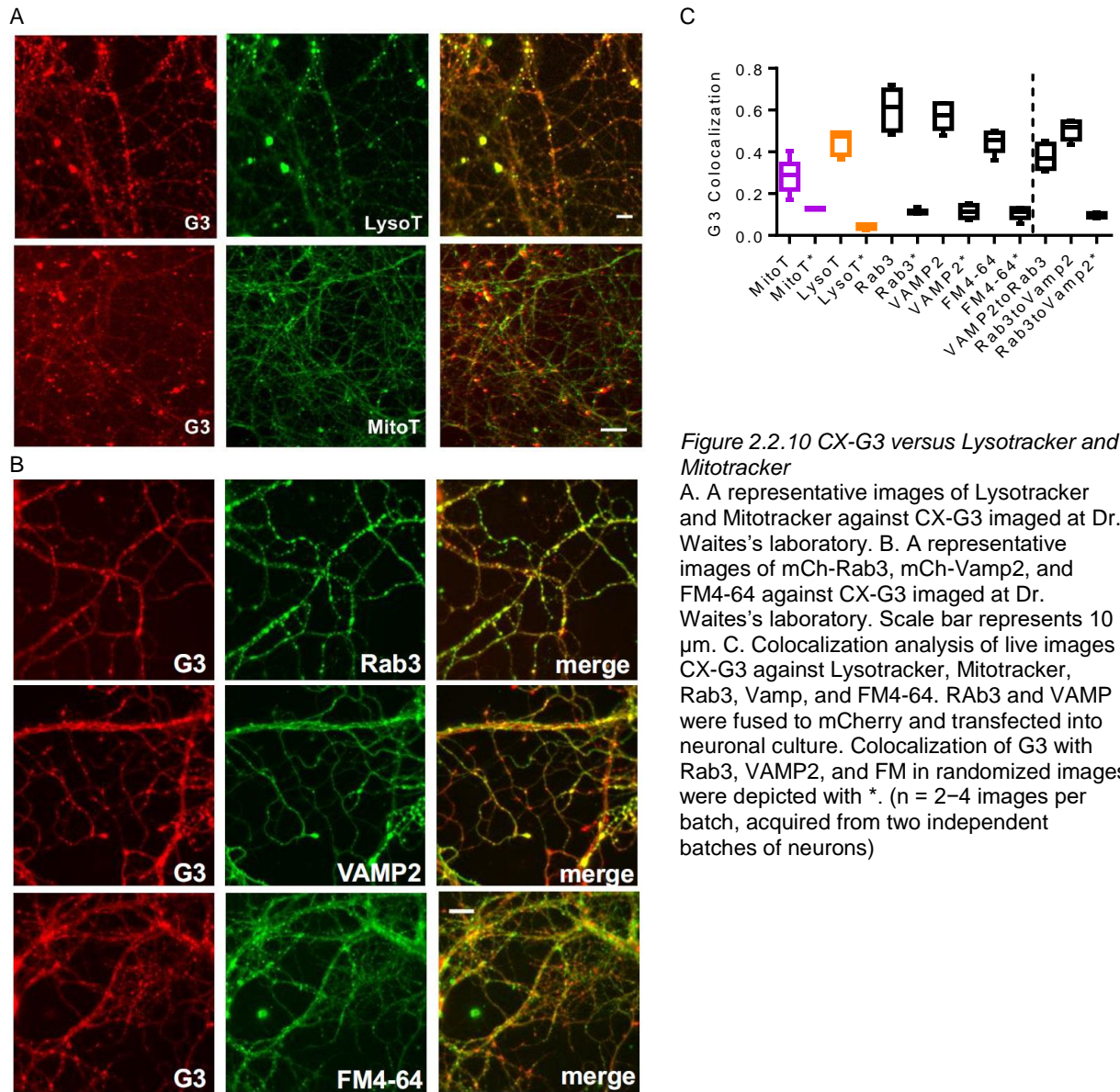


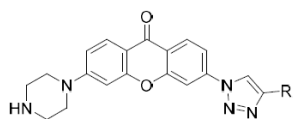
Figure 2.2.10 CX-G3 versus LysoTracker and Mitotracker

A. A representative images of LysoTracker and Mitotracker against CX-G3 imaged at Dr. Waite's laboratory. B. A representative images of mCh-Rab3, mCh-Vamp2, and FM4-64 against CX-G3 imaged at Dr. Waite's laboratory. Scale bar represents 10 μ m. C. Colocalization analysis of live images CX-G3 against LysoTracker, Mitotracker, Rab3, Vamp, and FM4-64. Rab3 and VAMP were fused to mCherry and transfected into neuronal culture. Colocalization of G3 with Rab3, VAMP2, and FM in randomized images were depicted with *. (n = 2-4 images per batch, acquired from two independent batches of neurons)

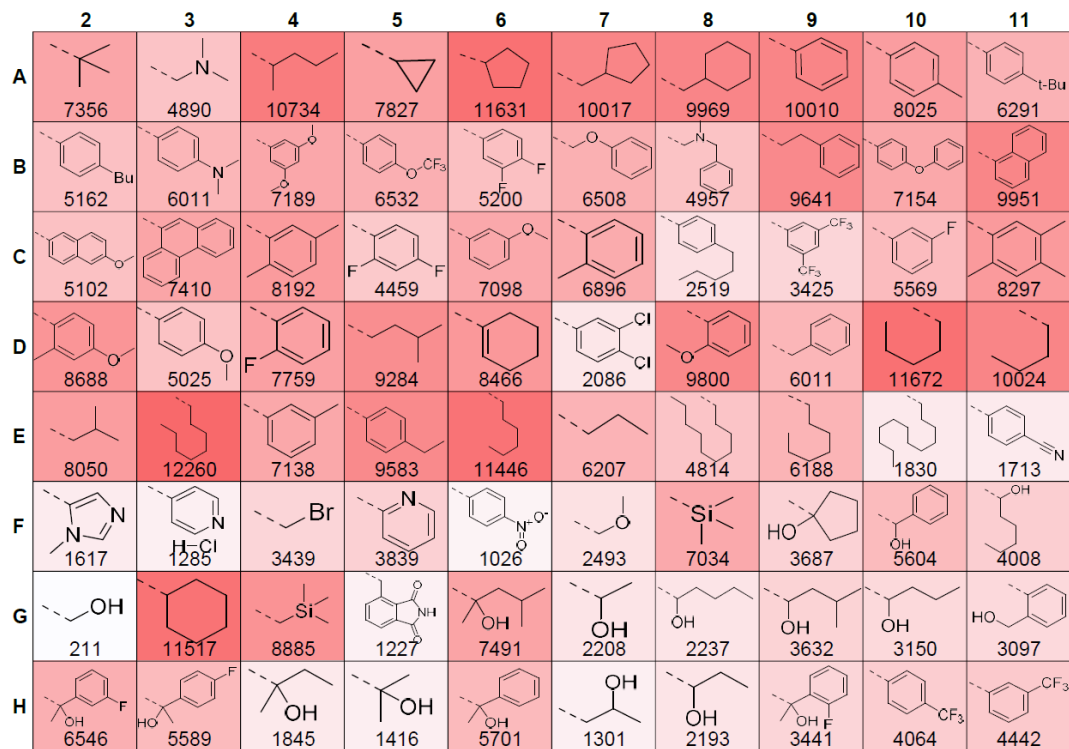
2.2.2.5.2 Photophysical properties

Dyes from the Q4 plate are based on the xanthone scaffold (Figure 2.2.11 A), with peak excitation and emission values between 360 and 380 nm and 480–520 nm, respectively (57). The

A
General Structure



Side Chains



B

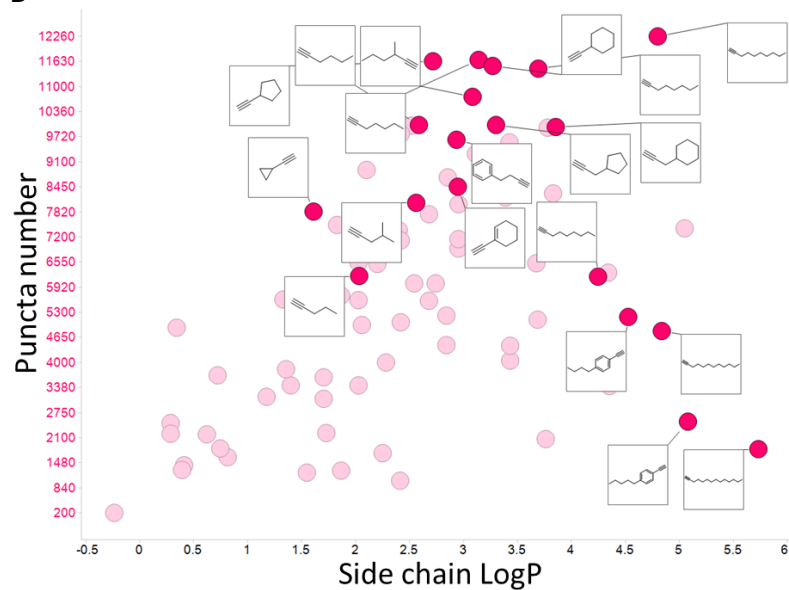


Figure 2.2.11 DAPI_DAPI_101_Q4 structures and properties

A. Structures and overlap heat map of the compounds in DAPI_DAPI_101_Q4 plate. B. Puncta number and side chain relationship.

compound diversity was achieved through various side chains attached through the azide-alkyne cycloaddition. Analyzing compounds using the overlap and total puncta number parameters and criteria discussed above, it became apparent that the aliphatic side chains gave better parameters than the aromatic ones (Figure 2.2.11 A). This observation prompted calculation of LogP values of the side chains to examine the lipophilicity in terms of puncta staining. Indeed, the puncta number versus LogP value plot revealed a bell-shaped distribution, which indicated an optimal lipophilicity range for high puncta staining (Figure 2.2.11 B). For example, cyclohexyl (CX-G3), cyclopentyl, isopentyl, pentyl, octanyl, butyl, hexyl side chains produced the highest number of puncta, while hydroxymethyl, 1-methyl-1H-imidazol-5-yl, 4-nitrophenyl as well as dodecanyl and 4-pentylphenyl side chain containing compounds were on the lower end

Since CX-G3 colocalized with lysotracker, it was important to measure fluorescent properties of the dye at different pH. To this end, CX-G3 was dissolved at 1 μ M in Tyrod's buffer equilibrated at different pH, and the excitation and emission spectra were recorded (Figure 2.2.12 A). Both the excitation and emission intensities were higher at the acidic pH. The emission intensity at pH 3 was 3.7x higher than at pH 9. At more physiologically relevant pH values, the dye was twice brighter at pH 5 than at pH 7.4. The pK_a value was approximated at 6.5 (Figure 2.2.12 B).

Of note, CX-A4 and CX-A6 had similar properties as CX-G3, CX-A6 was brighter than the other two dyes. Dr. Cheng sent us other analog compounds to test along with these hit compounds (Figure 2.2.12 C). CXAC series compounds contained acetyl groups on piperazine moiety, and CXPi contained piperidine residue. CXAC family was previously reported to selectively label mouse embryonic stem cells and to exhibit minimal cellular toxicity over multiple days of incubation, thus indicating the suitability of the CX family for use as probes in living cells. These compounds were brighter than their related CX series dyes (Figure 2.2.12 D-E). For example, at 1 μ M at pH 7.4 CXAC-G3 was 2.6x brighter than CX-G3. However, the CXAC-A4 did not show any affinity to neurons in CNC with limited staining of the cell bodies, while CXPi-A4 stained all the cell bodies in pan-cytoplasmic manner (Figure 2.2.12 F). This posed a question about the functional role of second amino group of the piperazine ring in CX-G3's ability to selectively localize to acidic compartments within the cell, potentially due to basifying ability of the molecule.

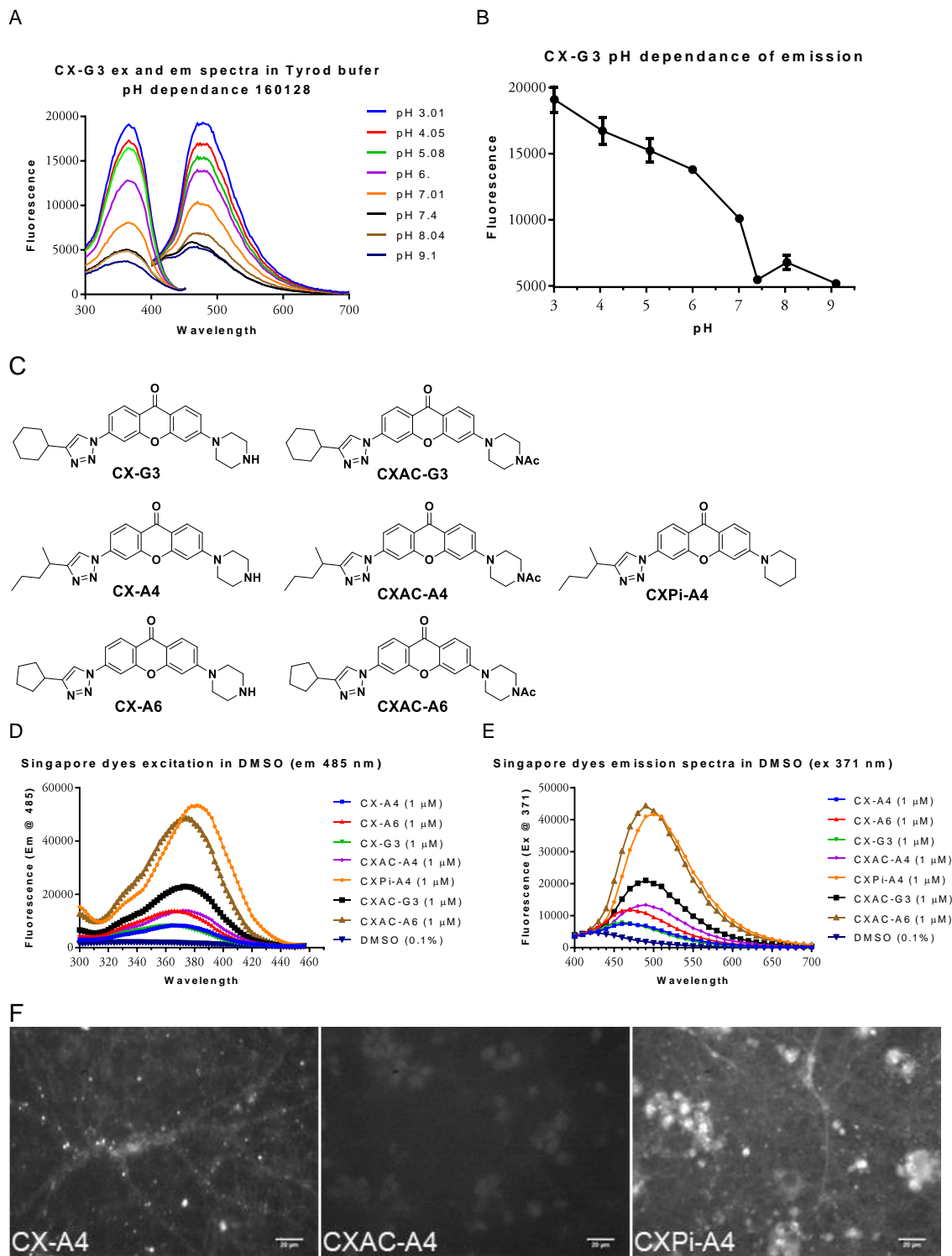


Figure 2.2.12 Spectral properties of CX-G3 and its analogs

A. Excitation and emission spectra of CX-G3 at different pH (ex @ 371 nm, em @ 485 nm). B. Emission versus pH plot of CX-G3 (ex @ 371 nm, em @ 485 nm) C. CX-G3 and its analogs structures. D-E. Excitation and emission spectra of CX-G3 and its analogs in Tyrod buffer. F. Representative images of CX-A4, CXAC-A4, and CXPi-A4 at 250 nM in cortical neuronal culture.

2.2.2.5.3 Mechanism of action

Taken together the, pH dependence of the dyes and the photophysical properties of the acetylated compounds, we hypothesized that the outer piperazine amino group quenches compounds' fluorescence through photoinduced electron transfer (PeT), which provided the CX family with pH sensing properties. Combined with our colocalization results, it is possible that the CX-G3 compound penetrates the majority of the soma due to lipophilicity of the structure, then concentrates and appears brighter in acidic vesicles, including lysosomes, endosomes, and synaptic vesicles. This would be a similar mechanism of action to that of LysoTracker dyes, with the key difference between these compounds being their photophysical properties and CX-G3's preferential distribution into synapses within the cells.

2.2.2.5.4 Stimulation of the cells

To confirm the proposed mechanism of action, it was necessary to show pH-dependent staining in the neuronal culture. To this end, two approaches were chosen for this purpose, using bafilomycin and NH_4Cl medium. Bafilomycin is a macrolide antibiotic which prevents re-acidification of the synaptic vesicles (61). It does not penetrate cell membrane and enters the vesicles through endocytosis. On the other hand, NH_4Cl penetrates the cells and basifies all vesicles. LysoTracker was used as the control for vesicle de-acidification.

Experimental protocols were optimized to reduce LysoTracker bleed-through, by reducing its concentration to 10 nM, and CX-G3 photobleaching, by modulating imaging conditions (Figure 2.2.13 A). Next, LysoTracker at 10 nM and CX-G3 at 250 nM were co-imaged before and after NH_4Cl treatment. LysoTracker images contained bright puncta, primarily in the cell bodies, and dim puncta in the periphery. CX-G3 images, on the other hand, contained puncta both in the cell bodies and on the periphery with a much lower difference in intensity between these regions (Figure 2.2.13 B). Colocalization in the cell bodies between LysoTracker and CX-G3 was high, however, in the periphery there were CX-G3 puncta that did not appear in LysoTracker staining, consistent with our colocalization data. Upon NH_4Cl treatment, puncta staining decreased for both LysoTracker and CX-G3.

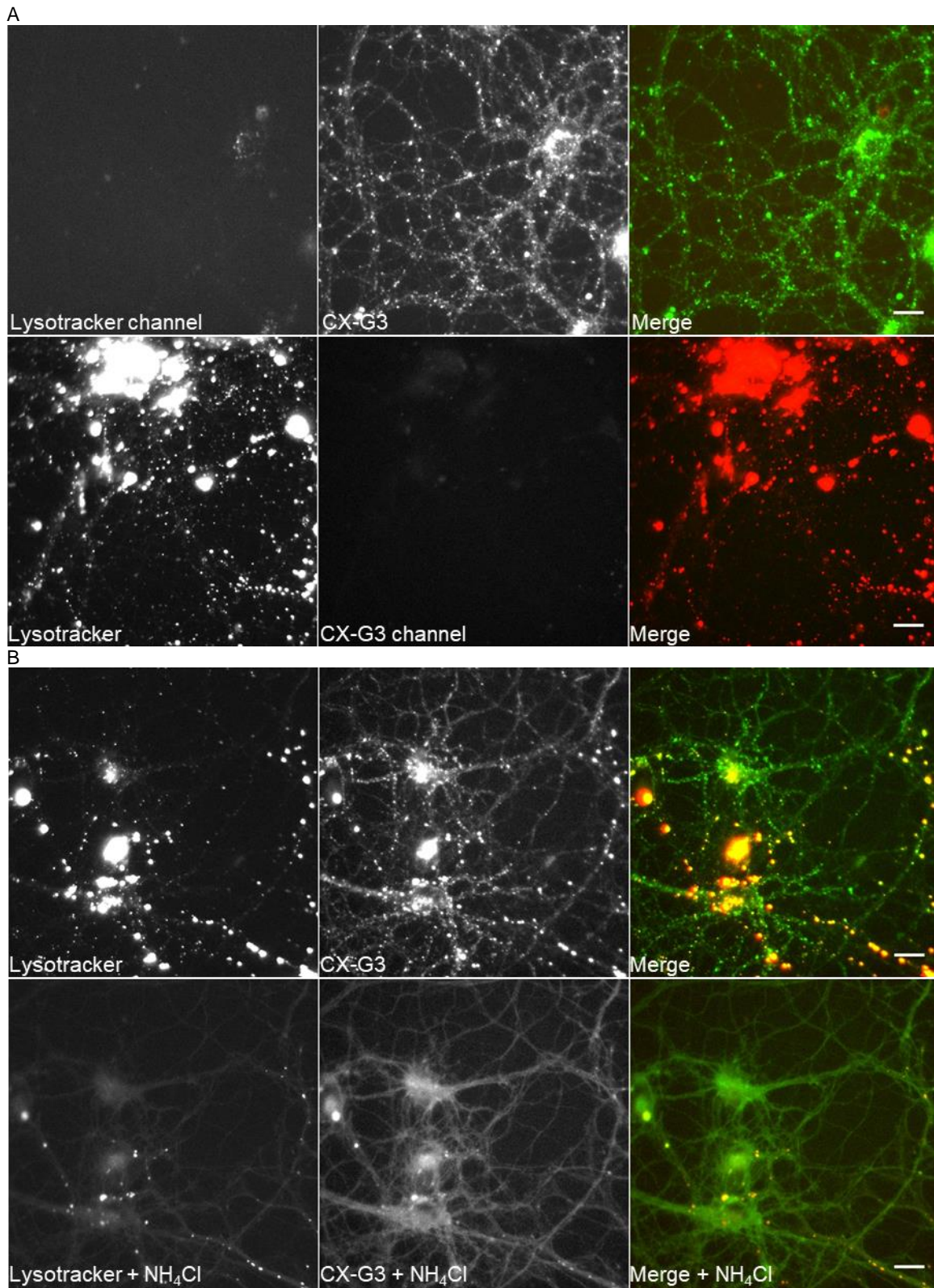


Figure 2.2.13 Representative images of CX-G3 and Lysotracker
 A. An example of the images taken at the optimized conditions. B. CX-G3 and Lysotracker staining before (top) and after (bottom) NH₄Cl treatment. Scale bar represents 20 μ m

Since CX-G3 exhibited high colocalization with synaptic markers, then upon neuronal stimulation fluorescence of the dye should be reduced or disappear in the synapses. However, electric stimulation of the cells did not induce dramatic destaining of CX-G3 in hippocampal culture (59), possibly due to association with the vesicular proteins or lipid that maintain the dye in protonated bright form. To determine whether pH of the synaptic vesicle was the only driving force for the staining, or if CX-G3 may bind to vesicular molecules, we performed a series of bafilomycin experiments. Bafilomycin treatment could indicate which case is more likely, since this compound can specifically collapse the pH-gradient in synaptic vesicles. If fluorescence signal remains after the collapse, there is likely a binding interaction between CX-G3 and an intravesicular partner. In order to load bafilomycin into synaptic vesicles, it was necessary to stimulate neurons to induce recycling of the vesicles. To this end, cells were stained with CX-G3, stimulated with an electrical field (10 Hz, 30 sec) and imaged before, during, and after the stimulation. SynaptopHluorin (spH), a fusion protein of the transmembrane synaptic vesicle protein VAMP2 and a pH-sensitive EGFP, was transfected into neuronal culture and used as the control. Stimulating spH expressing neurons resulted in an increase of fluorescence intensity that decayed over time due to recycling of the vesicles, since pHluorin becomes brighter at neutral pH. In the presence of the bafilomycin spH should remain bright after stimulation. Cell stimulation of the neurons indeed induced increase in fluorescence of spH along the neuronal processes which decayed overtime (Figure 2.2.14 A). To measure the intensity of the responsive neuronal processes, trainable WEKA segmentation, a combination of machine learning algorithms tailored for pixel-based segmentation, was performed to select the ROI. It could be argued that WEKA provided a superior identification of puncta than traditional algorithms because background identifier uses human defined features and thus puncta could be detected with different backgrounds. For example, WEKA identified puncta in the cell bodies with high background as well as in the periphery with low background. Treating the same cells with bafilomycin and stimulating them attenuated the stimulation-dependent fluorescence signal decrease as expected (Figure 2.2.14 B). Interestingly the spH produced largely a stringy staining pattern most likely due to cell membrane localization of the spH sensor, especially after the electrical stimulation (Figure 2.2.14 C-D).

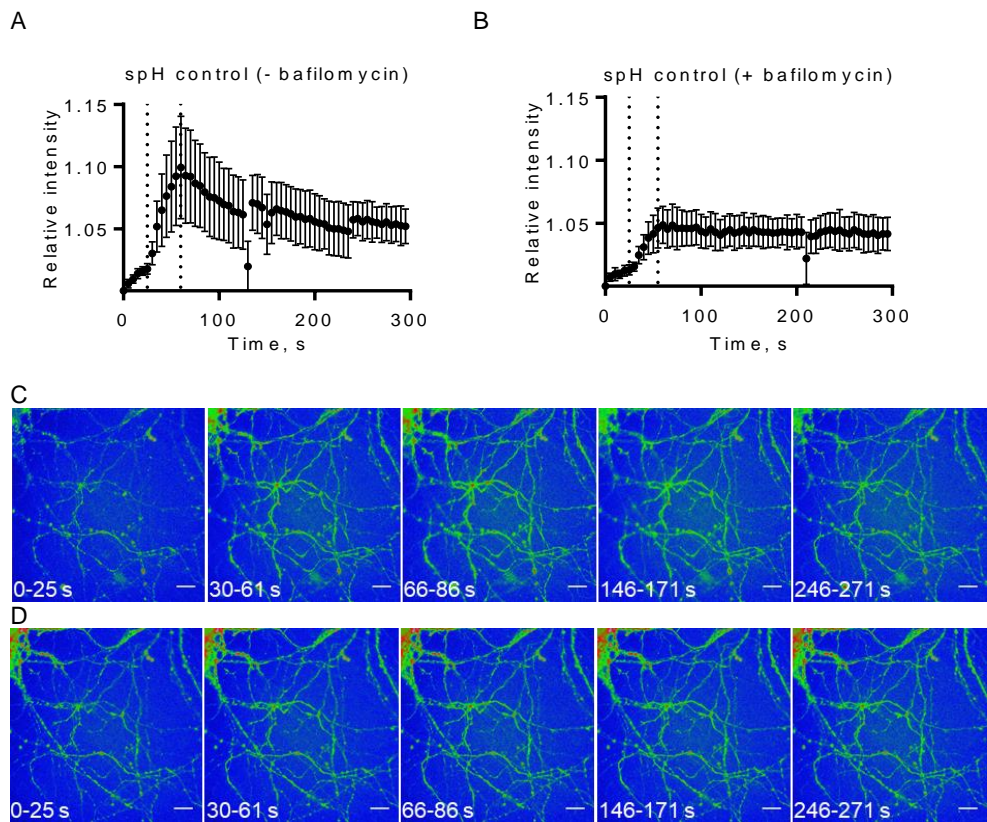


Figure 2.2.14 spH imaging with and without bafilomycin

A. Relative intensity change of spH over time in hippocampal culture in the absence of bafilomycin. To analyze the image, an axon classifier (developed based on spH processes) of WEKA segmentation was used to select ROI and measure the intensities across the frames. B. Relative intensity change of spH over time in the presence of 1 μ M bafilomycin. Dotted lines indicate the start and end of the stimulation (10 Hz, 30 s). Data represents mean \pm SD of 12 ROI C. Averaged frames of spH in the absence of bafilomycin. D. Averaged frames of spH in the presence of bafilomycin

Since changes in spH indicate an area of the cell which has undergone vesicle fusion, this signal could be used as a marker for release sites where CX-G3 signal may be decreasing. To this end, spH expressing cells were treated with CX-G3 and electrically stimulated in Tyrod buffer. Using the same WEKA axon classifier to segment the spH channel we measured the fluorescence changes in both channels over time (Figure 2.2.15 C). One interesting observation was that spH emission did not decay after stimulation ended as previously recorded, suggesting that CX-G3 could act as a lipophilic base (Figure 2.2.15 A). Instead, overall background fluorescence of the sample increased, which was not observed in the control experiment (Figure 2.2.15 D). The CX-G3 fluorescent signal did not significantly decrease due to the stimulus (Figure 2.2.15 B). In other words, coincubation of spH with CX_G3 resulted in amplified spH signal. Considering the pH determinants of spH fluorescence, the lipophilic base activity

of CX-G3 could have driven the amplified signal of spH, which was almost twice as high than in the absence of CX-G3 (Figure 2.2.14 A). Further investigation must be conducted to verify the presented hypothesis.

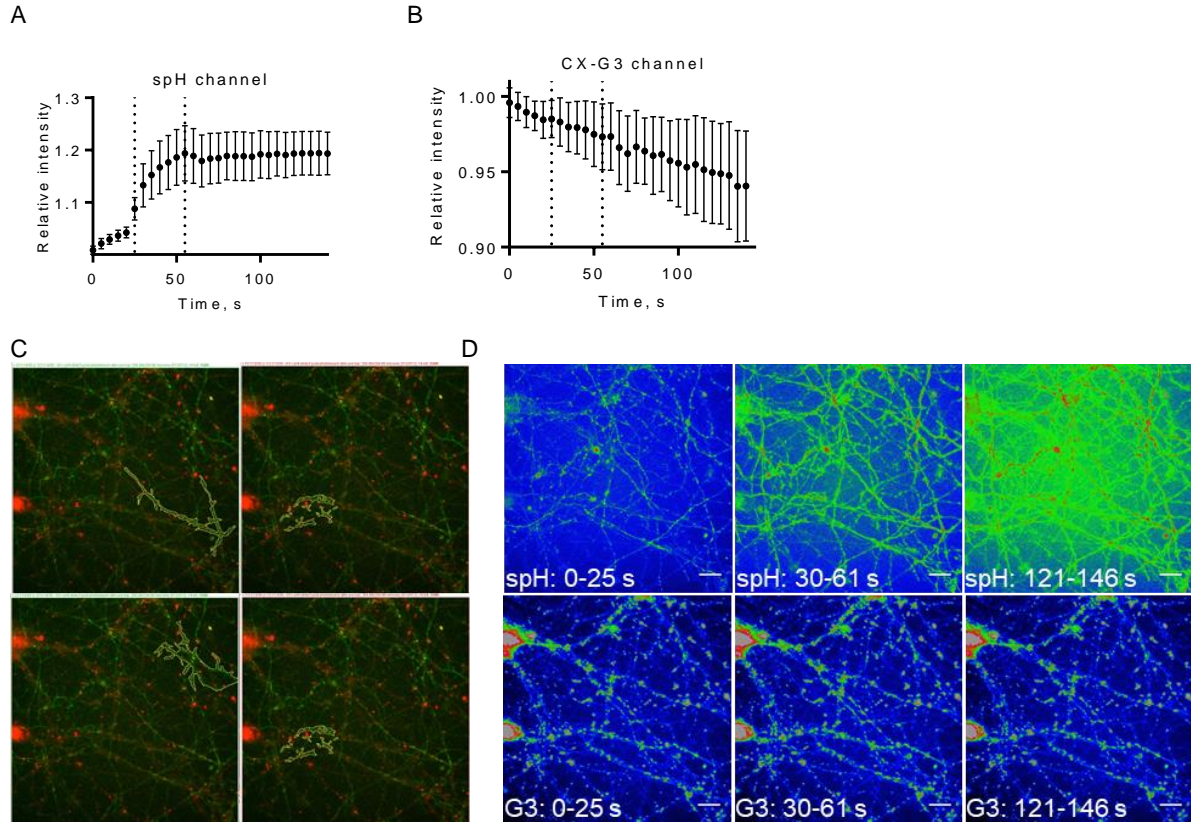


Figure 2.2.15 spH and CX-G3 response to electrical stimulation in spH expressing hippocampal neuronal culture incubated with CX-G3.

A. Relative intensity change in spH channel over time of CX-G3 (250 nM) treated hippocampal culture transfected with spH in the absence of bafilomycin upon stimulation. B. Relative intensity change in CX-G3 channel over time of the same sample. The stimulation (10 Hz, 30 s) starting and ending points are present with dotted lines. Data represents mean \pm SD of 75 ROI. C. An example of 4 ROI segmented through WEKA axon classifier. Green is spH, red is CX-G3, ROI is highlighted in yellow. D. Averaged frames of the same sample in the absence of bafilomycin upon stimulation, top - spH response, bottom - CX-G3 response.

An earlier experiment of electrical stimulation of CX-G3 stained neuronal culture demonstrated that some puncta disappeared upon stimulation without bafilomycin (Figure 2.2.16 A). Thus, analysis method of spH filaments may not be ideal for analysis of CX-G3 puncta properties. To quantify the changes of CX-G3 staining, first approach was to count the number of the puncta. However, there were drastic variations in the number of puncta between the frames because of the puncta movements and a shift in z-plane of the objective.

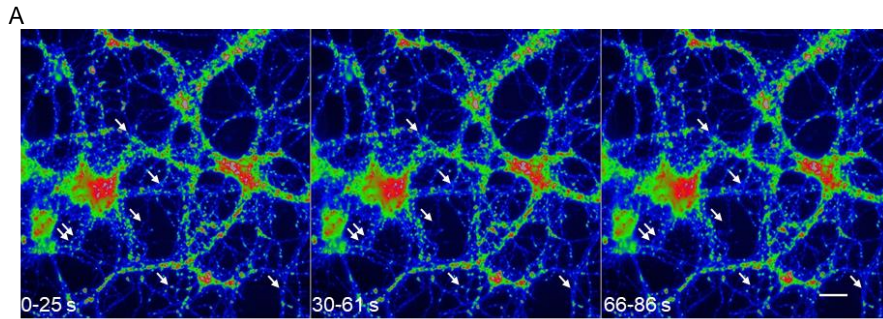
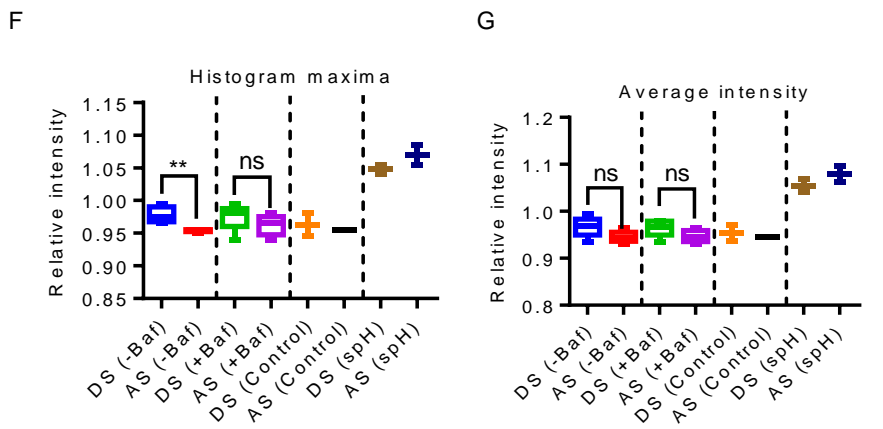
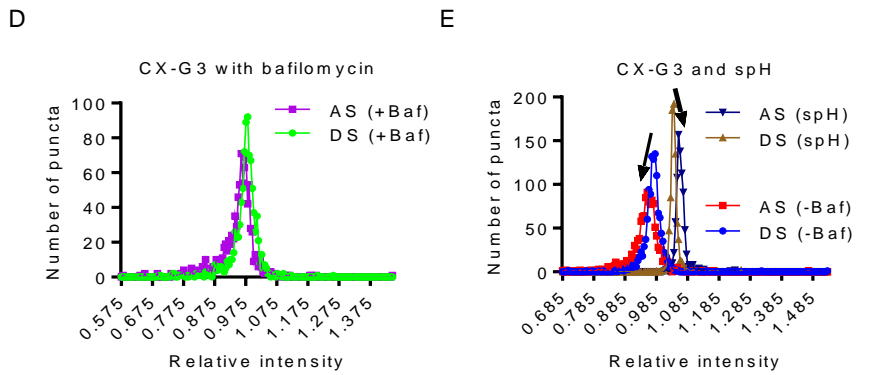
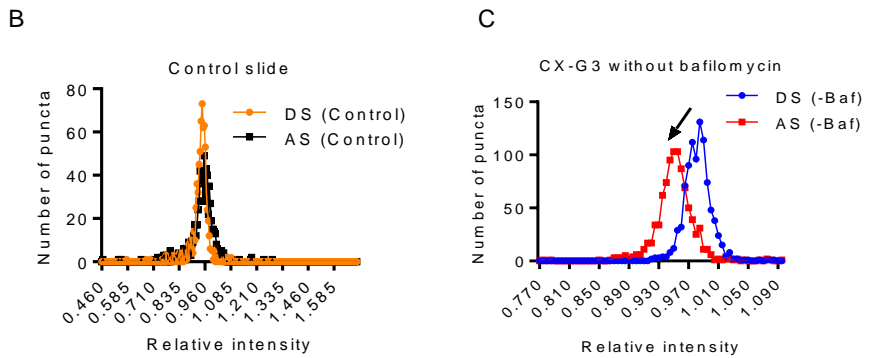


Figure 2.2.16
Representative CX-G3
image analysis approaches



A. An example of the puncta disappearance. B-E. Representative histograms of the control sample CX-G3 (250 nM) stained hippocampal slide without stimulation (B), the stimulated slide in the absence of bafilomycin (C), the stimulated slides of spH expressing neurons in the absence of bafilomycin (E). Arrow indicate the shift in the histogram over time. F. Statistical analysis of the histogram maxima, data represents mean \pm SD of n=5 for CX-G3 samples, n=2 for spH and control samples. G. Statistical analysis of the average intensity of the puncta, data represents mean \pm SD of n=5 for CX-G3 samples, n=2 for spH and control samples. DS – during stimulation, AS – after stimulation, Baf – bafilomycin. Intensities were normalized to the average intensities before the stimulation for each punctum.

Since the number of puncta could not be reliably counted, it was attempted to measure changes of the fluorescence of the ROI. To this end, image stacks were divided into several frames corresponding to the before (BS), during (DS), and after (AS) stimulation time periods, and subsequently were averaged

through t-projection images by averaging pixel intensities. Image corresponding to before stimulation period was used to create puncta segmentation using WEKA puncta classifier (developed based on CX-G3 staining), and intensities of these segments were measured in all images. Intensities then were normalized to first image (corresponding to before stimulation period), and data was used to create histograms to detect if the overall intensity distribution changed. In this analysis, if puncta intensities did not change over time, then histogram should not change as a function of time, which was observed for control slides of CX-G3 without stimulation (Figure 2.2.16 B). Histogram maxima of CX-G3 stained cells stimulated in the absence of bafilomycin significantly shifted to the right, indicating the decrease in the number of puncta with the same intensity after the stimulation (Figure 2.2.16 C, F). Surprisingly, CX-G3 stained cells treated with bafilomycin did not show significant shift in the histogram maxima (Figure 2.2.16 D, F). In comparison, spH histogram shifted to the left as expected, however, the number of samples precluded the statistical analysis of the data (Figure 2.2.16 E, F). Change in average intensity of the puncta in CX-G3 samples with and without bafilomycin was not significantly different (Figure 2.2.16 G)

2.2.2.5.4.1 Image analysis algorithm

Even though histogram analysis of the puncta intensities indicated the decrease of fluorescence of CX-G3 after the stimulation, it was unclear what percent of puncta responded to stimulation and what was the percent of the fluorescence change. To more accurately analyze these images, a new analysis algorithm was developed where each individual punctum signal was measured to find whether the fluorescence changes were due to the stimulation. To this end, each frame was segmented using WEKA puncta classifier, and all the ROI were then combined across the frames (before, during and after the stimulation for a total of 30 frames), which created a sort of Z-projection of the segmentation. This allowed for confining moving puncta to one ROI and preventing them from falsely appearing as responsive to the stimulus. On the other hand, some closely located puncta were grouped into one ROI. In the next step, fluorescence of all ROI was measured over time. Fluorescence of the destaining punctum (responsive puncta) was assumed to follow exponential decay, as it has been exemplified with FM1-43 unloading under the similar conditions (62). Thus, to identify puncta responsive to the stimulus, measured intensities

over time were fitted to 'Plateau followed by one phase decay' function in GraphPad, parameters of which allowed to distinguish these puncta.

Applying this algorithm to a sample with spH expressing cells treated with CX-G3 and stimulated in the absence of bafilomycin revealed that out of 925 identified puncta (Figure 2.2.17 A) in CX-G3 channel only 112 puncta or 12.1 satisfied the selection criteria (Figure 2.2.17 B, see 2.5.11 section). The response varied greatly from about 20% to 4% decrease in fluorescence to cumulatively giving $10\pm 4\%$ decrease (Figure 2.2.17 C). Some of the unresponsive puncta displayed linear decay and were excluded from the consideration (Figure 2.2.17 D). Z-drift had limited influence on identification and measurement

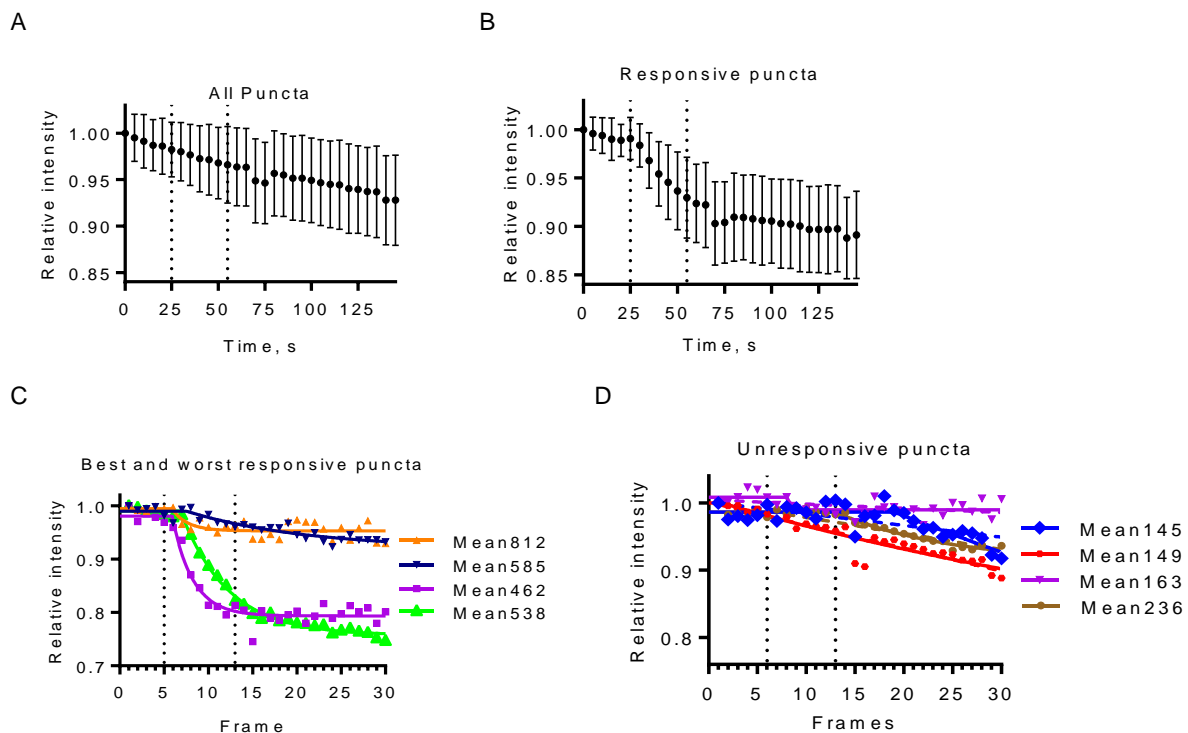


Figure 2.2.17 Individual punctum analysis

A. Intensity plot over time of 925 puncta, identified through puncta classifier (developed based on CX-G3 staining) of WEKA segmentation in the CX-G3 channel of CX-G3 (250 nM) stained hippocampal culture transfected with spH stimulated in the absence of bafilomycin. The stimulation (10 Hz, 30 s) starting and ending points are present with dotted lines. Data represents mean \pm SD of 925 ROI B. Intensity plot over time of puncta responsive to stimulation identified using data filters. Data represents mean \pm SD of 112 ROI C. An example of best and worst responsive puncta fitted to 'Plateau followed by one phase decay'. D. Examples of the curve fitting results to unresponsive puncta intensity plots

of the puncta in this algorithm. These results indicate that CX-G3 could indeed be released upon the stimulation. For a more definitive answer, more images, including controls, must be further analyzed.

2.2.2.6 Conclusion of HCS

Using the DOFL approach in HCS of synaptic and neuronal probes, approximately 7000 fluorophores were imaged in CNC providing a powerful platform for finding specific dyes. As the result of initial data analysis, a xanthone based probe was discovered that also labeled presynaptic terminals. These probes being lipophilic and pH-sensitive dyes that consistently colocalized with synaptic markers and stained releasable synaptic vesicles. These probes could be used for quick staining of synaptic vesicle in variety of preparations (cultured neurons, brain slices, in vivo). The accumulated image repository could be further used to find new probes.

2.2.3 Phage Display

While HCS provided an opportunity to find fluorescent small molecules that stain synapses and cell bodies, the diversity of the library was still limited (~ 8,000 compounds). Moreover, this library was unlikely to produce a molecule that could be used for delivery of other sensors or actuators/drugs. Given the diversity of the cells in the CNS, it was also important to find probes specific to the neuronal cell surface markers. To address this issue, a phage display targeted at neurons was developed. While phage display was successfully used with cancer cells, little success has been achieved in targeting neurons in vivo.

2.2.3.1 Phage display on cultured neurons

Using T7 bacteriophage and CX7C and CX8C phage libraries, the biopanning was performed on neuron-glia co-culture with glia culture as parallel control screen. In the initial trials, cells were treated with phage library at 4°C for 3h, then washed and lysed for phage analysis. The output-to-input ratio (O/I) was about 3% for both libraries indicating high background most likely due to non-specific binding of the phage to the plastic. To avoid this background, two alternative approaches were explored. In the first one, after biopanning for 2 h at 37°C cells were detached from the plate with papain. This approach produced 0.4% O/I for CX7C library which was 2.5 times higher than G7 O/I. Despite providing better O/I, it was still high for the initial round, as well as papain could compromise the phages. As the second approach, mature neuronal-glia co-culture was detached with papain before biopanning for 2 h on ice in the tube with rocking. The O/I was at 0.004% with 12 times higher value than G7 O/I for neuron-glia co-culture. Meanwhile, glia culture produced O/I at 0.0002% with 3.5 times higher O/I than that of G7. The output

result of the second approach was considered successful and thus was used for the screen. One thing must be noted that detaching the cells from the culture most likely kept only cell bodies while neurons processes were washed away. Also, detaching the neurons could have induced membrane damage through which phages could penetrate the cells. Nevertheless, this method was the best in-vitro phage display option on mature neurons.

The first round of selection was conducted on striatal neurons isolated from neonatal mouse pups co-cultured with rat embryonic glia derived from the cortex (established procedure in Dr. Sulzer group). CX7C and CX8C O/I value for neurons were 0.002% and 0.004% respectively, while G7 O/I was 0.0003%. For glia culture, O/I for both CX7C and CX8C were lower at 0.0007% and 0.0015%, respectively, with G7 O/I reaching $7 \times 10^{-5}\%$. However, the second round of selection could not be performed, because new striatal cultures contained a low number of neurons, which raised the questions whether the selection would produce any peptide with neuron homing properties and whether striatal cultures were consistent in producing the same neuronal markers. Moreover, the cell surface protein markers of cultured neurons may be drastically different from the in vivo ones, as well as not all neuronal subtypes could survive in vitro conditions. Based on these concerns, the attempts to conduct phage display on the cultured neurons were abandoned.

2.2.3.2 Ex-vivo phage display

To perform selection on neurons with the closest conditions to in vivo, ex vivo phage display protocol was developed. Biopanning could not be performed in the tissue due to limited penetration of the phage into the tissue, as well as the concerns of washing inefficiency. Moreover, neurons could not be separated from glia without tissue disintegration. To use striatal tissue

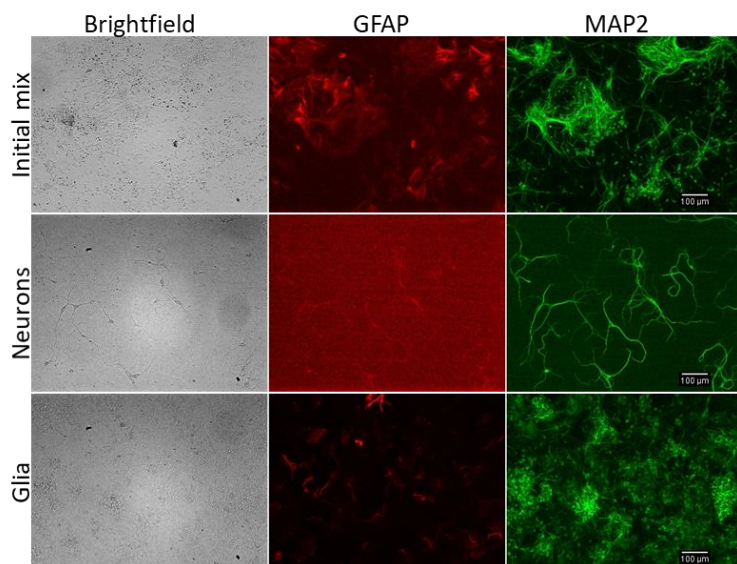


Figure 2.2.18 Immunofluorescence of isolated neuron and glia cultures Initial single cell suspension (initial mix), isolated neurons, and isolated glia were cultured and immunostained with neuronal (MAP2, green) and glia (GFAP, red) markers.

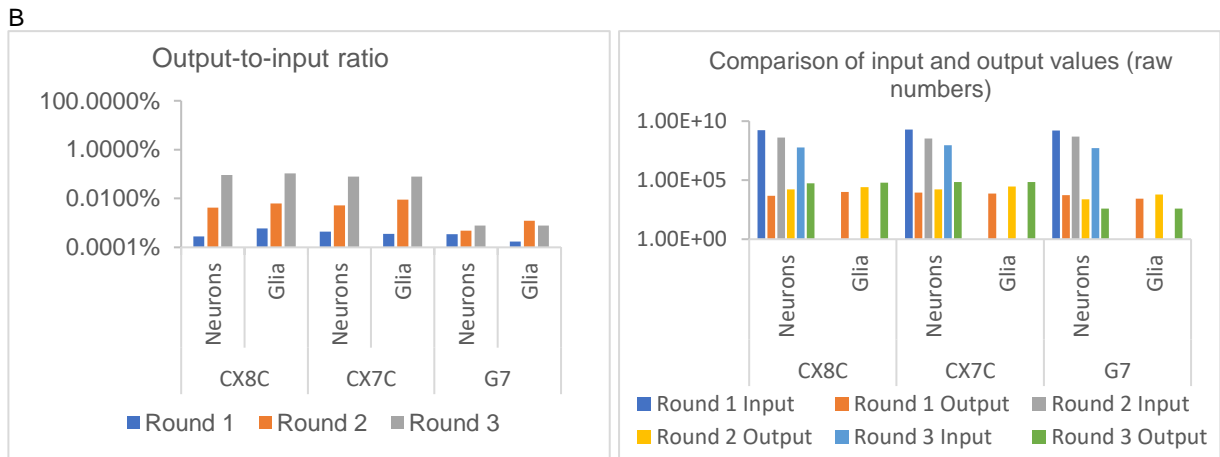
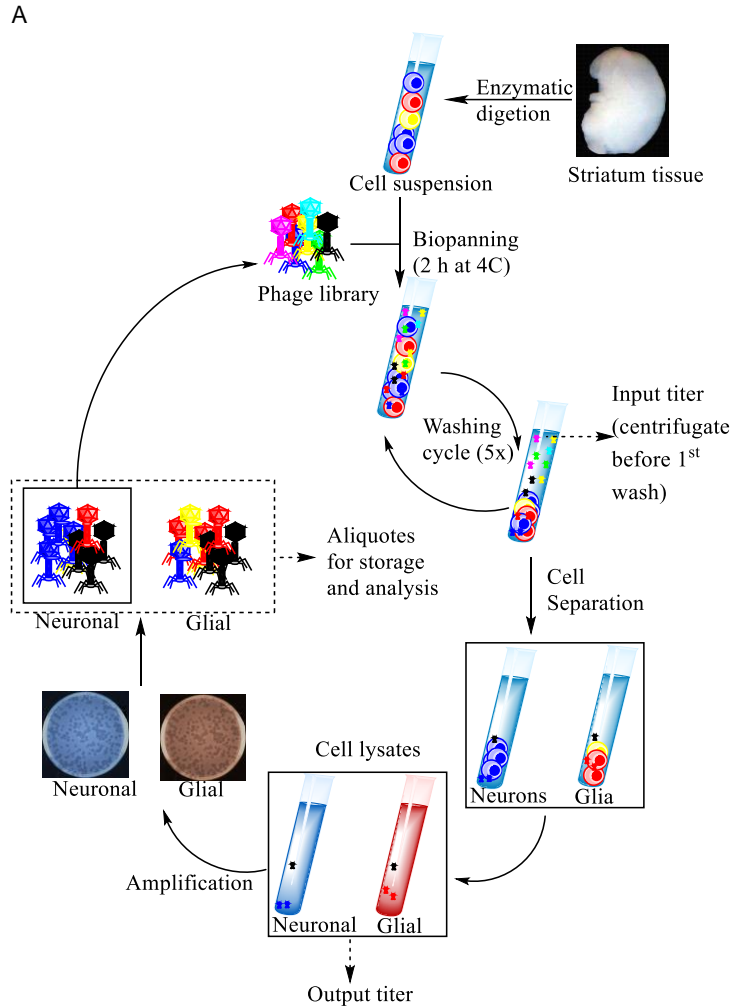


Figure 2.2.19 Ex vivo phage display scheme and outcome

A. A phage display protocol scheme. Striatum tissue was digested and triturated into a single cell suspension, treated with phage library for 2 h at 4°C, washed 5 times with centrifugation and resuspension in a new tube. Then neurons and glia were separated using magnetic beads, and lysed. Collected phages from both fractions were titered and amplified for sequencing. Neuronal phage library was then used for the next round of selection. **B.** The output-to-input ratio and fraction of each round measured by titring. **C.** Raw number and fraction of phage input and output for each round.

for selection, cells needed to be separated into single cell suspension, where biopanning could be performed, and then neuronal cells needed to be isolated from glia to achieve enrichment for neuron specific peptides. This approach would provide equilibrium in binding to neurons and glia for phage, which should increase probability for selection of neuron homing peptides. For this purpose, Miltenyi neuron isolation kit and magnetic labeling of glia were employed. To isolate the neurons from the glia, striatal tissue was digested and triturated using the kit to achieve the single cell suspension. Then cells were treated with antibody cocktail for glial markers and tagged with magnetic beads. Then glia were separated from the neurons on the column in the magnetic field. In other words, flow through contained neurons, while glia remained on the column. Neuronal fraction contained 79% of the total cells, while glia fraction had 17% (In human striatum neuron to glia ratio has been found to be 1.07 (63)). To confirm the composition, neuron and glia fraction were seeded along with initial cell suspension and cultured for two weeks. Immunofluorescence revealed that neuronal fraction contained mostly neurons, while glia fraction was made up mostly of glia, confirming successful isolation of neurons (Figure 2.2.18).

Since successful isolation of the neurons could be achieved using the magnetic beads, a new phage display protocol was developed. Cell suspension prepared from the striatal tissue (with both neurons and glia) was treated with phage for 1.5 h on ice with rocking. Cells then were washed five times, and neurons were isolated from glia and lysed (Figure 2.2.19 A). The same protocol was used for two more rounds with the decreasing amount of the phage input amplified from neuronal fraction of previous round of selection. The output number of phages, on the other hand, increased with each round indicating a successful enrichment, while the G7 output decreased with decreasing input number of phages. The O/I value for the libraries reached 0.1% up from 0.0003% (Figure 2.2.19 B-C).

2.2.3.2.1 CX7C library sequence analysis and characterization

Collected libraries were sequenced using Ion Torrent sequencing. In CX7C library collected in the first round of selection the number of unique phages had been reduced from 4.14×10^6 in the naïve library to 6426 (0.16% of unique phages of naïve library) in the neuron fraction, and 5709 (0.14% of unique phages from naïve library) in the glia fraction, giving a ratio of 1.1 between the samples. Surprisingly, the total number of phages recovered was 26934 and 97576 in neuron and glia fraction respectively, with

0.28 ratio between the samples. These numbers did not take into account phages that expressed non-cyclic peptides and the ones that do not start with C amino acid, and thus these numbers could not be accurately compared with values found by titering during the screening.

In the second round the number of unique phages was reduced to 2720 and 4471 with total number of phages reaching 55512 and 54300 in neuronal and glial fractions respectively. The top 20 abundant phages are presented in Table 2.3. The most abundant sequence, CPPFLETIC, amounted to 7% of total phage number in neuronal fraction and 2% in glial fraction, providing a selection ratio of 3.5. Selection ratio for the top 20 phages was 3 ± 1 , while the total unique phage number in neuronal fraction was 2 times less than in glial fraction.

Table 2.3 Top 20 sequence in CX7C libraries identified by IonTorrent

Round 2					Round 3				
Peptides	Count		% of total		Peptides	Count		% of total	
	Neuron	Glia	Neuron	Glia		Neuron	Glia	Neuron	Glia
CPPFLETIC	3650	1202	6.6%	2.2%	CPPFLETIC	29415	10498	35.4%	24.3%
CPPLLRELC	1246	447	2.2%	0.8%	CPPLLRELC	3784	1554	4.5%	3.6%
CEDFECAVL SLRPSS	1056	535	1.9%	1.0%	CPPWIETVC	2915	985	3.5%	2.3%
CPALMATLC	791	202	1.4%	0.4%	CEDFECAVL SLRPSS	2264	1102	2.7%	2.6%
CPPWIETVC	782	209	1.4%	0.4%	CPALMATLC	1798	652	2.2%	1.5%
CEIGRLMGIEC	699	246	1.3%	0.5%	CPELLRGLC	1159	520	1.4%	1.2%
CPELLRGLC	578	209	1.0%	0.4%	CEIGRLMGIEC	1057	452	1.3%	1.0%
CGLSVQGIC	561	420	1.0%	0.8%	CPTFMNSLC	911	337	1.1%	0.8%
CTLWEGASC	559	216	1.0%	0.4%	CTLWEGASC	893	386	1.1%	0.9%
CGDAFPYIC	548	185	1.0%	0.3%	CGLSVQGIC	866	564	1.0%	1.3%
CPTFMNSLC	527	205	0.9%	0.4%	CGDAFPYIC	831	379	1.0%	0.9%
CDFRGNAIC	344	164	0.6%	0.3%	CDFRGNAIC	753	460	0.9%	1.1%
CDLDRNMLC	297	60	0.5%	0.1%	CDVRGNAIC	606	401	0.7%	0.9%
CPEFLVNIC	260	121	0.5%	0.2%	CPDFLSEFC	461	147	0.6%	0.3%
CDVRGNAIC	259	70	0.5%	0.1%	CSDYSNEVC	435	297	0.5%	0.7%
CLGPTDSPC	240	158	0.4%	0.3%	CGREFPYIC	399	159	0.5%	0.4%
CSPGGNAIC	236	104	0.4%	0.2%	CYMSNNVNC	393	207	0.5%	0.5%
CGREFPYIC	235	43	0.4%	0.1%	CPEFLVNIC	367	142	0.4%	0.3%
CYMSNNVNC	225	117	0.4%	0.2%	CSPGGNAIC	326	353	0.4%	0.8%
CPNWLKDIC	201	66	0.4%	0.1%	CPSFIASLC	319	106	0.4%	0.2%
Total peptides	55512	54300	-	-	Total peptides	83173	43124	-	-
Unique peptides	2720	4471	-	-	Unique peptides	2396	2033	-	-

In the third round the number of unique phages was 2396 and 2033 and the total number of phages was 83173 and 43124 in neuronal and glial fractions respectively. Over the course of phage display, the number of unique phages reduced drastically in round 1 and round 2 collapsing the diversity of the library. Interestingly, the total number of phages increased in neuronal fraction, while reverse trend

was observed in glial fraction indicating enrichment of neuron specific phages (Figure 2.2.20 C). The most abundant sequence, CPPFLETIC, reached 35% and 24% of total phage number in neuronal and glial fraction respectively (the second most abundant sequence amounted to 4.5%), with selection ratio of 1.5 reducing the difference between the fractions. Among top 20 phages in round 3 specificity for neuronal fraction was reduced to 1.2 ± 0.3 . The higher than expected number of phages in the glial fraction could be attributed to less stringent biopanning condition of the third round. However, in glial fraction the difference in number of unique sequences between round 2 and 3 was larger than that of round 1 and 2, which did not support the abovementioned stringency concern.

Table 2.4 Sequences of CX7C round 3 library identified by Sanger sequencing

Sequence	Number
CPPFLETIC	3
CPPLLRELC	1
CEDFECAVLSLRPHSS	1
CPDFLSEFC	1
CSDYSNEVC	1
CLQVDAF	1
CLSVESF	2
CLTVAPSC	1
CPELLRGLC	1
CRGGYEADC	1
CSLNNNVVC	1
CSRTGGSAC	1
CVPRQSTLC	1
CVXXEDRW	1
Total	46

Sequence analysis of the round two library top 20 CX7C peptides (excluding peptides with less than 7 amino acids between C) (Figure 2.2.20 A) showed a prevalence of hydrophobic amino acids at 2-5 and 7 and 8 positions, respectively in the neuronal fraction. Amino acids were arbitrarily color coded as follows: DE, RHK, CGSTY, NQ, AFILMPVW. The sequence made up from the most frequently occurring amino acids in round 2 and round 3 libraries was CPPFLNAIC, which had high homology to the most abundant sequence, CPPFLETIC (Figure 2.2.20 A-B). Glial fraction

sequences from round 2 less frequently contained hydrophobic amino acids, however, the composition at 2, 6, and 8 positions was similar to neuronal fraction library. Glial fraction sequences from round 3 were quite similar to the neuronal fraction. These preliminary results did not reflect our expectations. Further analysis must be performed with the detailed sequence comparison of the two fractions in order to find peptides specific to neurons.

For Sanger sequencing random phage plaques from amplified plates of round three neuronal fraction library were collected and submitted to sequencing (Table 2.4). CPPFLETIC phage was in 6.5% of all selected plaques. Sanger sequencing results contained only 5 out of 20 peptides from top 20 of the Ion Torrent sequencing outcome. At the initial characterization of the sequences, the most abundant phage, CPPFLETIC, was amplified for further testing.

2.2.3.2.2 CX8C library sequence analysis and characterization

Collected libraries were sequenced in Ion Torrent sequencing. In CX8C library, collected in the first round of selection, the number of unique phages had been reduced from 2×10^8 in the naïve library to 5814 (0.003% of unique phages from naïve library) in the neuronal fraction, and 7106 (0.004% of unique phages from naïve library) in the glial fraction, giving a ratio of 0.82 between the samples. The total number of phages recovered was 194083 and 49447 in neuronal and glial fractions respectively, with selection ratio of 4 between the samples. The total phage number for the first round was unusually high when compared to other phage display results and it was a complete reverse result when compared to CX7C library results. Also, total number of individual phages was 10 times than that of CX7C round 1 library.

In the second round the number of unique phages was reduced to 2065 and 2429 with the total number of phages reaching 36628 and 41061 in neuronal and glial fractions respectively. The top 20 abundant phages are presented in Table 2.5. The most abundant sequence, CTLWDEAQIC, amounted to 4.4% of total phage number in neuronal fraction and 1.9% in glial fraction, providing a selection ratio of 2.3, while the next two sequences, CFNSLEFPDC and CQLWDEAIVC, reached 3% and 1% in neuronal and glial fractions respectively. Selection ratio for the top 20 phages was 1.8 ± 0.9 .

In the third round, the number of the unique phages was 2033 and 2396 and the total number of phages was 47107 and 62445 in neuronal and glial fractions respectively. The number of unique phages and total number of phages in neuronal

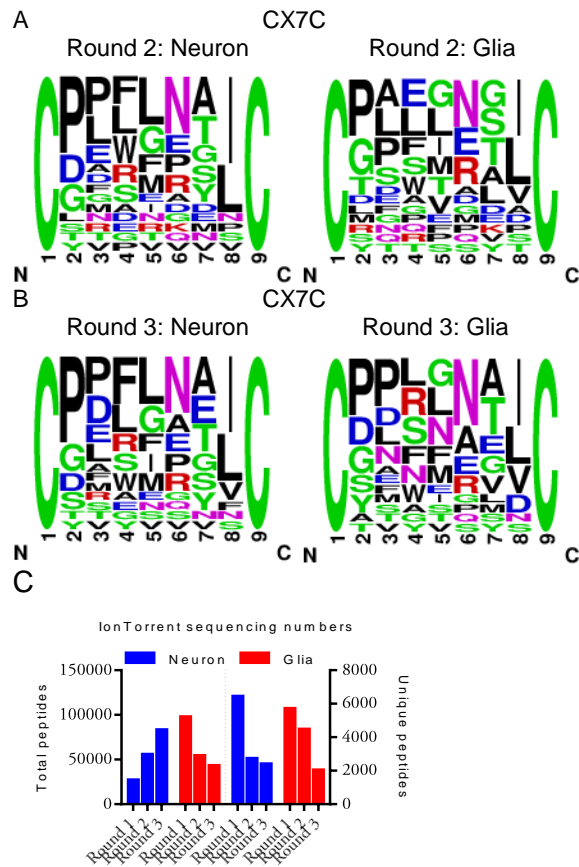


Figure 2.2.20 CX7C sequences and numbers from the neuronal versus glia screen

A-B. Sequence logo representation of round 2 (A) and round 3 (B) CX7C library. Amino acids were arbitrarily color coded as follows: DE, RHK, CGSTY, NQ, AFILMPVW. C. Number of unique phages and total number of phages measured by IonTorrent

fraction were drastically reduced in round 1 and round 2 collapsing the diversity of the library. However, round 3 did not improve the enrichment. The glial fraction mirrored the outcome of neuronal fraction (Figure 2.2.21 C). While the top peptide in round 2, CTLWDEAQIC, dropped to fourth position in round 3 keeping the abundance at 5%, CFNSLEFPDC and CQLWDEAIVC assumed the top positions in round 3 reaching 18% and 9% of total phage number. Among top 20 phages in round 3 specificity for neuronal fraction dropped to 1.1 ± 0.6 . The round 3 of selection did not improve the numbers overall, while it changed the abundance of the sequences.

Table 2.5 Top 20 sequence in CX8C libraries identified by IonTorrent

Peptides	Count		% of total	
	Neuron	Glia	Neuron	Glia
CTLWDEAQIC	1602	793	4.4%	1.9%
CFNSLEFPDC	1118	591	3.1%	1.4%
CQLWDEAIVC	1098	491	3.0%	1.2%
CLVLESLSDC	1005	1020	2.7%	2.5%
CFGLILENDC	495	522	1.4%	1.3%
CENTIFDGIC	440	203	1.2%	0.5%
CPANLKGIVC	439	239	1.2%	0.6%
CATGNRVKLC	393	279	1.1%	0.7%
CQLWPGSKVC	316	118	0.9%	0.3%
CLQVSNLTSC	290	299	0.8%	0.7%
CDMMRNLGVDC	285	73	0.8%	0.2%
CRGLTVEGTC	284	369	0.8%	0.9%
CNEDMFPYMC	274	182	0.7%	0.4%
CASNARTRC	259	116	0.7%	0.3%
LLVNDTEC	251	139	0.7%	0.3%
CSDRSYMDEC	237	676	0.6%	1.6%
CNNATTSDEC	208	256	0.6%	0.6%
CEEDYHSTTC	188	302	0.5%	0.7%
CMTLGELTIC	187	117	0.5%	0.3%
CKSNRTNAIC	186	225	0.5%	0.5%
Total peptides	36628	41061	-	-
Unique peptides	2065	2429	-	-

Peptides	Count		% of total	
	Neuron	Glia	Neuron	Glia
CFNSLEFPDC	8499	7122	18.0%	11.4%
CQLWDEAIVC	4089	3705	8.7%	5.9%
CENTIFDGIC	3617	2155	7.7%	3.5%
CTLWDEAQIC	2448	1987	5.2%	3.2%
CDMMRNLGVDC	1568	1526	3.3%	2.4%
CPANLKGIVC	1143	1614	2.4%	2.6%
CLVLESLSDC	790	1630	1.7%	2.6%
CQLWPGSKVC	727	584	1.5%	0.9%
CNEDMFPYMC	684	538	1.5%	0.9%
CNMYANSCQS				
GLTIEPF	667	945	1.4%	1.5%
CFGLILENDC	621	1142	1.3%	1.8%
CSDRSYMDEC	475	2806	1.0%	4.5%
CEEDYHSTTC	465	1530	1.0%	2.5%
CVGTLFSSIC	431	250	0.9%	0.4%
CKSNRTNAIC	399	706	0.8%	1.1%
CASNARTRC	390	513	0.8%	0.8%
CKWKGLNDAC	341	925	0.7%	1.5%
CRGLTVEGTC	328	836	0.7%	1.3%
CLQVSNLTSC	282	313	0.6%	0.5%
CKLWDEVRLC	273	324	0.6%	0.5%
Total peptides	47107	62445	-	-
Unique peptides	2033	2396	-	-

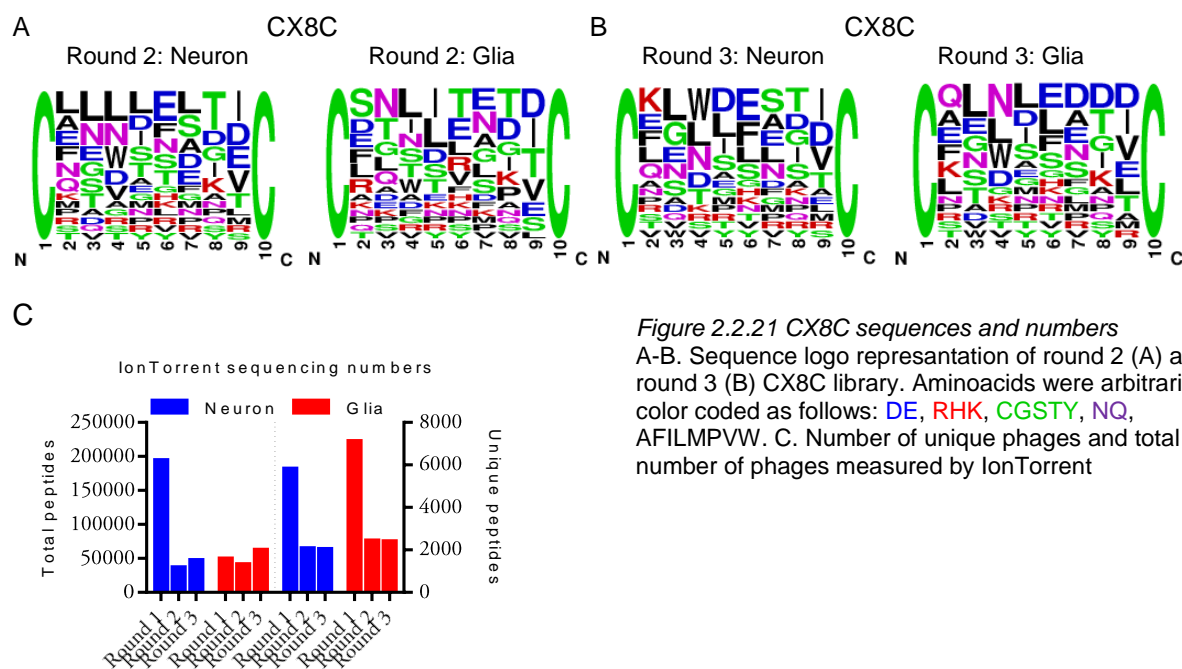
Sequence analysis of top 20 CX7C peptides from round 2 library (excluding peptides with less than 7 amino acids between C) (Figure 2.2.21 A) showed a prevalence of Leu amino acids at 2-5 and 7 positions in neuronal fraction, while glial fraction amino acid composition was more varied. In the round three, the frequency changed drastically with different hydrophobic amino acids at 3-6 and 9 positions in neuronal fraction, while negatively charged amino acids become more frequent in glial fraction (Figure 2.2.21 B). Amino acids were arbitrarily color coded as follows: DE, RHK, CGSTY, NQ, AFILMPVW. The sequence made up from the most frequently occurring amino acids in round three of the neuronal fraction, CKLWDESTIC, was homologous to the second most abundant peptide, CQLWDEAIVC.

Table 2.6 Sequences of CX8C round 3 library identified by Sanger sequencing

Sequence	Number
CQLWDEAIVC	3
CFNSLEFPDC	3
CTLWDEAQIC	1
CRLRSNSIQC	1
CLVLESLSDC	1
CLTVKDF	1
CKSNRTNAIC	2
CGMLHPNAMC	1
CFGLILENDC	1
CENTIFDGIIC	1
CDQSLTNDIC	1
CDMMRNLGVDC	1
Total	48

For Sanger sequencing random phage plaques from amplified plates of round 3 of neuronal fraction library were collected and submitted for sequencing (Table 2.6). CFNSLEFPDC and CQLWDEAIVC phage were in 6.3% of all selected plaques. Sanger sequencing results mirrored the peptides found through the Ion Torrent sequencing. At the initial characterization of the sequences, the most

abundant phages, CFNSLEFPDC and CQLWDEAIVC, were amplified for further testing.



2.2.3.2.3 In vitro characterization of the phages

Striatal neurons were cultured to test the collected phages (Figure 2.2.22 A). This culture was treated with CX7C libraries for 2 h at 37°C and then fixed for immunofluorescence. Naïve library did not stain neurons or glia and rather had 1-2 pixel size puncta staining pattern with occasional bright spots, which did not colocalize with any of the cell body proteins. Round three library, on the other hand, stained

some cell bodies in the neuronal fraction along with a similar staining pattern as naïve library. To quantify the cell bodies stained by the phages, a WEKA segmentation was used, which revealed the number of cell bodies stained was the highest by the round three CX7C library (Figure 2.2.22 B-C). Interestingly, round two phages stained less number of cell bodies than round one. Similar staining pattern was observed for CX8C libraries. Stained cell bodies did not create any extensive processes. Most likely, the library stained a neuronal cell subtype that did not grow in vitro. Since phage display was performed on the cell bodies of freshly isolated neurons, protein expression profile could be completely different from cultured neurons. Thus, in vitro culturing could not be used to test isolated phages.

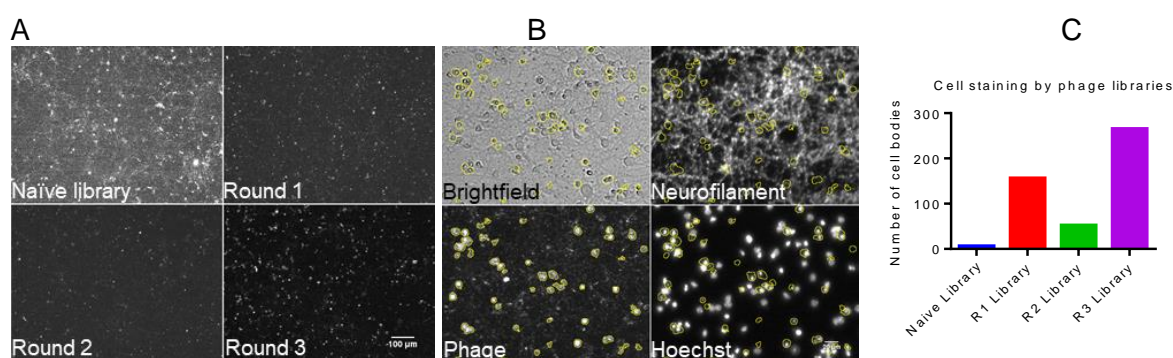


Figure 2.2.22 Immunofluorescent analysis of phage specificity

A. Staining pattern of the naïve, round one, round two, and round three CX7C libraries in striatal cultures. Scale bar represents 100 μm . B. WEKA segmentation of the CX7C round three library puncta overlaid on other control channels in striatal culture. Scale bar represents 20 μm . C. The number of the cell bodies stained by the CX7C libraries measured with the WEKA segmentation.

2.2.3.3 Conclusion of Phage Display

The initial selection conditions indicated a possibility of selecting phages specific to neurons reflected in the diversity collapse of the naïve library and enrichment of specific sequences. Moving forward, a more detailed analysis of the sequences must be performed to find promising contenders, and peptide characterization must be performed on neuron preparations that are close to in vivo conditions. Further optimization and improvement of phage display protocols should increase the probability of finding selective, neuron specific peptides.

2.3 Discussion

High content screening is a powerful approach for finding new probes and one that can generate a lot of information from a library of diverse compounds. The advantage of this approach could be highlighted by the intrinsic multiple screening opportunities of different targets. For example, our primary

target of HCS was the glutamatergic synapses, the acquired images could still be used to search for probes that specifically stain cell bodies, or axons, or dendrites without necessity to develop new screening assay. In addition to the probe, molecules that grant the specificity towards the target of the screen could lead to a better understanding of the gene expression profile of the cells of interest.

One of the primary challenges of HCS is the image analysis algorithms. Currently, most of the image analyses are based on the models built in a software. Even though these models can do an excellent job in identifying the necessary structures, the rate of false positives and false negatives could be high depending on the quality of the images. Moreover, variations in the background, saturation of the images, and the irregularities in the staining patterns create a big challenge for these models to perform well. Progress in the artificial intelligence and the machine learning technology has created new algorithms in recognizing different patterns in the image, which is getting close to the human level of recognition. These algorithms may be employed and lead to a much superior platform for image analysis.

Another challenge of HCS is the logistics of the project. Since the images could be analyzed multiple times and must be empirically examined, it becomes important to have an easy access to the images. Given the number of images (the total number we acquired was 40,000 images) it was not a trivial task to share images between the labs, an issue that was not thoroughly addressed in the beginning of the project. An open-source software, OMERO sever, was used to help ameliorate the situation and provide a structure to image storage. Future screening project must plan the logistics of data storage to avoid these pitfalls.

Quality control also becomes an important aspect of the logistics. Such control gives an opportunity to recognize poor quality images for potential re-screening with adjusted conditions, as well as excluding such images from analysis to save time. In our screen multiple quality issues, such as bleed through between the channels, low fluorescent signal of the dyes, oversaturation of the images, became apparent during the analysis. Implementing quality control analysis during the image acquisition may provide the opportunity for early intervention and adjustments of the conditions to improve the quality of the screen in general. Implementation of these logistical goals, however, may require software development skills.

Primary selection criterion that was built into the design of the HCS identified a new probe, CX-G3, that stained acidic cellular compartments, including synaptic vesicles. Even though mechanistically, CX-G3 is likely similar to LysoTrackers, it stained more vesicles in the neuronal projections, while cell body staining was not as bright as LysoTracker, thus providing a more selective staining of the synaptic vesicles. Early attempts to detect the release of the synaptic vesicles did not show definitive results. However, a more detailed analysis of individual synapses showed that approximately 10% of all stained puncta were released under the stimulation. Given this little number of the releasable puncta stained by CX-G3, it should not be surprising that little significant change in fluorescence on average could be detected, especially since the intensities of the synaptic vesicles were low and contributed little to the total intensity of the image. CX-G3 also stained puncta in brain slices ex-vivo, as well as in-vivo, with high colocalization with synaptic markers (not discussed in this thesis, but recently published (59)).

Using other selection criteria, new probes could be found in the HCS. Several promising compounds have been identified, which still require further assessment. Overall, HCS provided an opportunity to find new promising probes that label different parts of neurons.

To provide an alternative approach to finding the probes specific to neuronal cell bodies or synapses, a peptide phage display method was developed. Such selective molecules could provide homing properties for molecular materials bearing other functional probes, like VSD. As the proof of concept of the cell surface signature for different cell types, we have aimed at finding peptides that would selectively bind to neurons in the presence of the other non-neuronal cells. The outcome of the phage display was promising, reaching high enrichment of the peptides at later rounds. Further analysis is required to confirm the success of the selection. For this purpose, peptides must be tested using ex vivo samples, which would require additional optimizations of the conditions.

When proven successful, phage display could be then used to find specific peptides to synapses and different neuronal types using new exciting approaches, such as individual cell or synapse picking by an automated system. Moreover, a new dual functional phage display system could be developed, where phages could penetrate the BBB for in vivo biopanning. Such construct is being developed in collaboration with Dr. Ruoslahti and Dr. Teesalu, which may open new exciting avenues of the discovery of the neuron specific probes.

2.4 Conclusion

Though at these early stages HCS and phage display methods pose a lot of challenges, the intrinsic potential of these approaches cannot be underestimated. The ability to target systems on single neuronal, or even single synaptic, levels provides an unprecedented and exciting opportunity to diagnose and modify various neurological conditions, which to date pose the biggest challenge to fields of medical and biochemical science. In our attempts to identify probes that have a potential to selectively label specific neurons and neuronal compartments, new compounds have been uncovered which stain synapses, in vitro and in vivo, as well as new platforms have been created allowing for future discovery of numerous novel probes. The extent of potential application of these approaches is being expanded every day and the opportunities for translational application are becoming more realistic with each new step of their optimization. These novel methods possess a great potential which will undeniably be one of the integral parts of future neuroscience.

2.5 Materials and Methods

2.5.1 DNA constructs and AAV production

Lentiviral constructs to express EGFP-Synapsin1a, mCh-Rab3, and VAMP2-EGFP/mCh have been previously described (47, 48). For AAV experiments, *Rattus norvegicus* synaptophysin (GenBank accession number NM_012664.3) tagged at its C-terminus with mCherry was synthesized (Genewiz) and subcloned into the pAAV-CaMKIIa-EGFP expression vector (gift from Ed Boyden; Addgene plasmid #64545) at the BamHI and EcoRI sites, replacing the EGFP cassette. This construct was sent to the University of North Carolina viral vector core for custom AAV8 production. Synaptophluorin construct was from Addgene plasmid #24478 (deposited by Leon Lagnado), in which synaptophysin-pHluorin was subcloned from pEGFP-C1 vector backbone (using Nhe1/Mfe1 digest) into the FUGWm vector backbone (for lentiviral production) using EcoRI/XbaI digest.

2.5.2 Neuronal culture and lentiviral transduction

Cortical neurons were prepared from E18 Sprague-Dawley rat embryos of both sexes, dissociated in TrypLE Express (Fisher/Life Technologies) for 20 minutes, washed 3X in Hank's Balanced Salt Solution (Sigma), and plated in Neurobasal medium with B27 supplement and Glutamax (all Fisher/Life Technologies) at a density of 10,000 cells/well in 96 well plates coated with poly-L-lysine (Sigma). On 3 days in vitro (DIV), neurons were transduced with lentivirus (2 μ l/well), prepared as previously described (48), to express either GFP-Syn or mCh-Rab3. Hippocampal neurons were prepared in the same way but plated onto 22x22 mm coverslips at a density of 250,000 neurons per coverslip. Coverslips were lentivirally transduced with mCh-Rab3 or VAMP2-mCh on 5-7 DIV.

2.5.3 Immunofluorescence on HTS microscope

GFP-Synapsin or mCh-Rab3-expressing cortical cultures in 96-well plates were fixed with 4% formaldehyde in PBS for 15 min, washed 3X in PBS, then incubated with primary antibodies in blocking buffer (2% glycine, 2% BSA, 0.2% gelatin, 50mM NH₄Cl in 1X PBS) for 1 hour. The following antibodies were used: MAP2 (Sigma, ap-20 m1406), LAMP1, SV2A (Developmental Studies Hybridoma Bank), VGLUT1 (SySy, #135 302), GFP. Following 3X PBS washes, cells were incubated with Alexa Fluor 488 or 568-conjugated secondary antibodies for 1 hour, washed 3X in PBS, and imaged using the high-throughput screening microscope (IN Cell Analyzer; GE Healthcare, 20X objective) in the Columbia Genome Center. Colocalization of FP-tagged Synapsin or Rab3 with the synaptic and non-synaptic markers was calculated as described below (colocalization algorithm).

2.5.4 Screening

The compound library was formatted into groups of 96-well plates based on excitation/emission spectra (Table 2.2). Screening was performed in batches of 12-15 plates, with each compound group screened in the same batch. The compounds (prepared in DMSO as 100 μ M stock solutions) were added to the medium of 14-16 DIV neurons via automated liquid handling system (Cell Explorer; Perkin Elmer) for a final concentration of 2 μ M. Following 20-minute incubation at 37°C, plates were washed 3X at room temperature in normal Tyrodes solution (119mM NaCl, 2.5 mM KCl, 2 mM CaCl₂, 2 mM MgCl₂, 30 mM

glucose, 25 mM Hepes pH 7.4), and images were acquired at room temperature in 4 fields of view/well using the high-throughput screening microscope (IN Cell Analyzer; GE Healthcare, 20X objective) and CCD camera (2048 x 2048 pixels) in the Columbia Genome Center HTS facility. Following screening, plates were fixed with 4% formaldehyde in PBS, washed once in PBS, and stored in the dark at 4°C.

2.5.5 Colocalization algorithm and hit selection

The vesicle segmentation algorithm of IN Cell Developer Toolbox (v.1.9) was used to identify puncta through thresholding images based on average size of GFP-Synapsin and mCh-Rab3 puncta (1-2 pixels; only objects in range of 0.5-5 μm^2 selected) and intensity (average intensity 2-2.5X over background). Cytoplasm Segmentation algorithm has been used with filters on area >0.2 (arbitrary units) and form factor > 0.2, the kernel size 19, sensitivity 50 was used identify cell bodies. Specific values were chosen empirically using MAP2 immunostained screening plates. For each channel, thresholded objects were counted, and colocalization between channels calculated based on number of overlapping pixels. Colocalization was calculated for each compound with GFP-Syn or mCh-Rab3. For each group of compounds, average colocalization with the synaptic marker was calculated, and hits were defined as compounds with colocalization values >2.5 standard deviations above the group mean.

2.5.6 Serial dilutions

Serial dilution was performed in 96-well plates of neurons or glia for the CX Q4 plate of compounds, using the following concentrations: 2, 1, 0.5, 0.25, 0.125, 0.0625, 0.03125 μM . Signal-to-noise ratio of the compounds was determined by comparing their average intensity at GFP-Syn puncta to their average intensity across the entire plate.

2.5.7 Determination of excitation/emission spectra and lipophilicity

Spectral analysis of the compounds was performed on BioTek Synergy H1 Hybrid reader. Compounds were in DMSO or normal Tyrodes buffer at pH ranging from 3 to 9 to yield final concentration of 1 μM . Excitation spectra were measured by recording emission at 485 nm; emission spectra were

recorded by exciting at 371 nm. Theoretic LogP values of the side chains of CX Q4 library compounds were calculated using PerkinElmer ChemDraw 14.0 software.

2.5.8 Live imaging in cultured hippocampal and cortical neurons

Imaging experiments of CX-G3 with mCh-Rab3, VAMP2-mCh, and FM4-64 were performed with 18-20 DIV hippocampal neurons using a custom chamber designed for liquid perfusion and electrical stimulation. For FM4-64 loading, neurons were incubated with FM4-64 (15 μ M) in high potassium Tyrodes solution (like normal Tyrodes except for 90 mM KCl, 31.5 mM NaCl) for 45 seconds to stimulate FM dye uptake, then washed for ~5 minutes in normal Tyrodes to eliminate excess dye prior to 2-minute incubation with 0.5 μ M CX-G3, 2 min washing in Tyrodes, and image acquisition. For mCh-Rab3 and VAMP2-mCh imaging, neurons were placed in normal Tyrodes solution with 0.5 μ M CX-G3, washed for 2 minutes in Tyrodes solution, then imaged. Images were acquired with a 40X objective (Neofluar, NA 1.3) or a 63X objective (Neofluar, NA 1.4) on an epifluorescence microscope (Axio Observer Z1, Zeiss) with Colibri LED light source, EMCCD camera (Hamamatsu) and Zen 2012 (blue edition) software. MitoTracker experiments were performed in 19-21 DIV cortical neurons after incubation with 100 nM MitoTracker (MitoTracker Deep Red FM; Thermofisher) for 30 min. Imaging was performed using a Leica DMI4000 imaging system.

2.5.9 Quantification of CX-G3 colocalization with synaptic markers in cultured hippocampal neurons

CX-G3 images were first background subtracted (3 μ m rolling ball) using ImageJ software (National Institutes of Health). Clearly visible cell bodies were then manually excluded from the image analysis. CX-G3-positive puncta were then identified using the Multiple Thresholds plug-in (created by Damon Poburko, Simon Fraser University, Burnaby, BC, Canada) for ImageJ with the selection criteria: >1 standard deviation above background, 6-50 pixels in size, and min. circularity of 0.6. Puncta were then considered positive for the respective synaptic markers if at least 6 pixels (>0.95 μ m²) of the ROI colocalized with fluorescence >1 standard deviation above background from the corresponding fluorescent marker. As a control, the analysis was repeated on randomized image pairs. For the MitoTracker images, which were collected on a separate microscope with different resolution, this

analysis was not possible. Instead these images were analyzed using the Just Another Colocalization Plugin (JACoP) (60) setting the threshold to the >1 standard deviation and recording the Manders' overlap coefficient.

2.5.10 Immunofluorescence in cortical neuronal cells cultured in the grid dish

Cortical cells were seeded on PDL-coated μ -Dish 33 mm (ibidi, 81166) and grown until DIV 12-20. Cells were incubated with CX-G3 (250 nM) and NeuO (500 nM) for 30 min to 1h, then imaged, fixed, and immunostained with VAMP2 (SySy, #104 211) and VGLUT1 (SySy, #135 302) antibodies with Hoechst staining. Images were taken at the exact location of live imaging. Images then were registered and aligned using ImageJ TrackEM 2 plugin. Colocalization analysis was performed using JACoP plugin.

2.5.11 Electrical stimulation of CX-G3-labeled hippocampal neurons

Following 30 min incubation in 0.25 μ M CX-G3, 10 nM LysoTracker (DND-99) and washes, 14-16 DIV neurons lentivirally transduced with synaptopHluorin at DIV 4-6 were imaged in normal Tyrodes solution in a custom-built imaging chamber as described previously. Images were acquired every 5 seconds over a 5 min time course, under baseline conditions or in the presence of electrical stimulation (10Hz, 30 seconds; 10 mAmp current, 1 ms pulse width), administered following the first 5 images (25 sec into time course). To calculate the change in CX-G3 fluorescence intensity over time, WEKA segmentation was applied using puncta, axon, and background classifiers trained on spH and CX-G3 images. Number of puncta and intensities were measured and normalized to the first frame. Individual puncta time course intensity changes were fitted to functions in GraphPad and the results were analyzed in TIBCO Spotfire software.

Intensity over time plot of each individual punctum was fitted to 'Plateau followed by one phase decay' function in GraphPad. Parameters of the function were: X_0 – time at which decay starts; Y_0 – average Y value up to time X_0 ; Plateau – is the Y value at infinite times. To select the responsive puncta following conditions must be satisfied:

$25 \text{ s} \leq X_0 \leq 55 \text{ s}$, where 25-55 s corresponds to stimulation duration;

$[Y_0 - 3 \cdot \text{SD}] > [\text{Plateau} + 3 \cdot \text{SD}]$, where SD – standard deviation calculated by fitting function;

$[\mu_{0-25\text{s}} - 3 \cdot \text{SD}_{0-25\text{s}}] > [\mu_{55-150\text{s}} - 3 \cdot \text{SD}_{55-150\text{s}}]$, where μ is average intensity, SD – standard deviation, 0-25s and

55-150s indicate frames (time period) used;

R^2 of 'Plateau followed by one phase decay' function > R^2 of 'Line' function

2.5.12 Data repository and analysis.

All the images were uploaded onto custom build OMERO server. Data analysis of the HCS results was performed in TIBCO Spotfire software. Parameters were averaged using quadrant 1, 2, and 4 results. Quadrant 3 results were discarded due to inconsistent staining, presumably influence by the close proximity to the delivery needle of the imaging station.

2.5.13 Striatal cultures for phage display

Striatal glia co-culture was prepared using protocol developed in Dr. Sulzer lab. Glia derived from embryonic rat cortex were seeded on PDL and laminin coated dishes in custom made glia medium, followed by cold wash next day, and treatment with FDU when cells reached 70% confluency. A day before seeding neurons, glia was once again washed on cold medium and replaced with custom made neuronal culture. Striatal tissue was provided by Ms. Kanter, Dr. Choi, Dr. Mosharov. Tissue was digested in papain solution, then seeded on top of the glia monolayer and grown until DIV 13. On the day of the experiment, cells were digested with papain, resuspended in 1% BSA PBS medium, treated with phage at 4°C for 1-3 h, then washed 3 times with cold neuron medium, lysed and scrapped for phage titering.

For culturing, striatal tissue was digested in enzymatic solution of the Miltneyi Neuronal isolation kit, triturated, filtered in 70 μ m mesh, resuspended in 80 μ L of the 1% BSA PBS solution and treated with 20 μ L of antibody cocktail for 5 min at 4°C. Then cells were washed, resuspended in 80 μ L of the 1% BSA PBS medium, treated with 20 μ L of antibiotin conjugated magnetic beads, and applied to the LD column in magnetic field. Neurons that were washed from the column by 2x 1 mL of 1% BSA PBS were collected, Glia then were collected by flushing from the column in absence of the magnetic field with 3 ml of the 1% BSA PBS. Cell fractions then seeded on PDL coated 12-well plate in glia growth medium. Next day, cells were washed and fed with neurobasal medium to increase survivability of the neurons. Cells were then cultured until DIV 12.

.For phage display, tissue was treated as describe above, but before applying glia antibody, cells were treated with the phage library for 2-4h at 4°C with rocking, and then washed 5 times with 1% BSA

PBS solution. Upon the collection of the fractions, cells were centrifuged and lysed for phage titering and amplification.

For immunofluorescence experiments, cells were incubated with phage for 30-2h at 37°C or 4°C, then washed and fixed. T7 (provided by Dr. E. Ruoslahti), Neurofilament (Cell Signaling), VGLUT1 antibodies were used to stain the cells.

2.6 References

1. Azevedo, F. A. C., L. R. B. Carvalho, L. T. Grinberg, J. M. Farfel, R. E. L. Ferretti, R. E. P. Leite, W. J. Filho, R. Lent, and S. Herculano-Houzel. 2009. Equal numbers of neuronal and nonneuronal cells make the human brain an isometrically scaled-up primate brain. *J. Comp. Neurol.* 513: 532–541.
2. Herculano-Houzel, S. 2014. The glia/neuron ratio: How it varies uniformly across brain structures and species and what that means for brain physiology and evolution. *Glia* 62: 1377–1391.
3. Glasser, M. F., T. S. Coalson, E. C. Robinson, C. D. Hacker, J. Harwell, E. Yacoub, K. Ugurbil, J. Andersson, C. F. Beckmann, M. Jenkinson, S. M. Smith, and D. C. Van Essen. 2016. A multi-modal parcellation of human cerebral cortex. *Nature* 536: 171–178.
4. Tasic, B., V. Menon, T. N. Nguyen, T. K. Kim, T. Jarsky, Z. Yao, B. Levi, L. T. Gray, S. A. Sorensen, T. Dolbeare, D. Bertagnoli, J. Goldy, N. Shapovalova, S. Parry, C. Lee, K. Smith, A. Bernard, L. Madisen, S. M. Sunkin, M. Hawrylycz, C. Koch, and H. Zeng. 2016. Adult mouse cortical cell taxonomy revealed by single cell transcriptomics. *Nat. Neurosci.* 19: 335–346.
5. Markram, H., E. Muller, S. Ramaswamy, M. W. Reimann, M. Abdellah, C. A. Sanchez, A. Ailamaki, L. Alonso-Nanclares, N. Antille, S. Arsever, G. A. A. Kahou, T. K. Berger, A. Bilgili, N. Buncic, A. Chalimourda, G. Chindemi, J.-D. Courcol, F. Delalondre, V. Delattre, S. Druckmann, R. Dumusc, J. Dynes, S. Eilemann, E. Gal, M. E. Gevaert, J.-P. Ghobril, A. Gidon, J. W. Graham, A. Gupta, V. Haenel, E. Hay, T. Heinis, J. B. Hernando, M. Hines, L. Kanari, D. Keller, J. Kenyon, G. Khazen, Y. Kim, J. G. King, Z. Kisvarday, P. Kumbhar, S. Lasserre, J.-V. Le Bé, B. R. C. Magalhães, A. Merchán-Pérez, J. Meystre, B. R. Morrice, J. Muller, A. Muñoz-Céspedes, S. Muralidhar, K. Muthurasa, D. Nachbaur, T. H. Newton, M. Nolte, A. Ovcharenko, J. Palacios, L. Pastor, R. Perin, R. Ranjan, I. Riachi, J.-R. Rodríguez, J. L. Riquelme, C. Rössert, K. Sfyarakis, Y. Shi, J. C. Shillcock, G. Silberberg, R. Silva, F. Tauheed, M. Telefont, M. Toledo-Rodriguez, T. Tränkler, W. Van Geit, J. V. Díaz, R. Walker, Y. Wang, S. M. Zaninetta, J. DeFelipe, S. L. Hill, I. Segev, and F. Schürmann. 2015. Reconstruction and Simulation of Neocortical Microcircuitry. *Cell* 163: 456–492.
6. Zeng, H., and J. R. Sanes. 2017. Neuronal cell-type classification: Challenges, opportunities and the path forward. *Nat. Rev. Neurosci.* 18: 530–546.
7. O'Rourke, N. A., N. C. Weiler, K. D. Micheva, and S. J. Smith. 2012. Deep molecular diversity of mammalian synapses: why it matters and how to measure it. *Nat. Rev. Neurosci.* 13: 365–79.
8. Busse, B., and S. Smith. 2013. Automated analysis of a diverse synapse population. *PLoS Comput. Biol.* 9: e1002976.
9. van Spronsen, M., and C. C. Hoogenraad. 2010. Synapse Pathology in Psychiatric and Neurologic Disease. *Curr. Neurol. Neurosci. Rep.* 10: 207–214.
10. Waites, C. L., and C. C. Garner. 2011. Presynaptic function in health and disease. *Trends Neurosci.* 34: 326–37.
11. Südhof, T. C. 2008. Neuroligins and neurexins link synaptic function to cognitive disease. *Nature* 455: 903–911.
12. Tabuchi, K., J. Blundell, M. R. Etherton, R. E. Hammer, X. Liu, C. M. Powell, and T. C. Südhof. 2007. A Neuroligin-3 Mutation Implicated in Autism Increases Inhibitory Synaptic Transmission in Mice. *Science* (80-.). 318: 71–76.
13. Miesenböck, G., D. A. De Angelis, and J. E. Rothman. 1998. Visualizing secretion and synaptic transmission with pH-sensitive green fluorescent proteins. *Nature* 394: 192–195.
14. Li, H., S. M. Foss, Y. L. Dobryy, C. K. Park, S. A. Hires, N. C. Shaner, R. Y. Tsien, L. C. Osborne, and S. M. Voglmaier. 2011. Concurrent imaging of synaptic vesicle recycling and calcium dynamics. *Front. Mol. Neurosci.* 4: 34.
15. Gross, G. G., J. A. Junge, R. J. Mora, H.-B. Kwon, C. A. Olson, T. T. Takahashi, E. R. Liman, G. C. R. Ellis-Davies, A. W. McGee, B. L. Sabatini, R. W. Roberts, and D. B. Arnold. 2013. Recombinant probes for visualizing endogenous synaptic proteins in living neurons. *Neuron* 78: 971–85.
16. Hires, S. A., Y. Zhu, and R. Y. Tsien. 2008. Optical measurement of synaptic glutamate spillover and reuptake by linker optimized glutamate-sensitive fluorescent reporters. *Proc. Natl. Acad. Sci.* 105: 4411–4416.

17. Marvin, J. S., B. G. Borghuis, L. Tian, J. Cichon, M. T. Harnett, J. Akerboom, A. Gordus, S. L. Renninger, T.-W. Chen, C. I. Bargmann, M. B. Orger, E. R. Schreiter, J. B. Demb, W.-B. Gan, S. A. Hires, and L. L. Looger. 2013. An optimized fluorescent probe for visualizing glutamate neurotransmission. *Nat. Methods* 10: 162–170.
18. Gaffield, M. A., and W. J. Betz. 2007. Imaging synaptic vesicle exocytosis and endocytosis with FM dyes. *Nat. Protoc.* 1: 2916–2921.
19. Hoopmann, P., S. O. Rizzoli, and W. J. Betz. 2012. Imaging Synaptic Vesicle Recycling by Staining and Destaining Vesicles with FM Dyes. *Cold Spring Harb. Protoc.* 2012: pdb.prot067603-pdb.prot067603.
20. Manno, C., L. Figueroa, R. Fitts, and E. Ríos. 2013. Confocal imaging of transmembrane voltage by SEER of di-8-ANEPPS. *J. Gen. Physiol.* 141: 371–387.
21. Miller, E. W., J. Y. Lin, E. P. Frady, P. A. Steinbach, W. B. Kristan, and R. Y. Tsien. 2012. Optically monitoring voltage in neurons by photo-induced electron transfer through molecular wires. *Proc. Natl. Acad. Sci. U. S. A.* 109: 2114–9.
22. Ebner, T. J., and G. Chen. 1995. Use of voltage-sensitive dyes and optical recordings in the central nervous system. *Prog. Neurobiol.* 46: 463–506.
23. Peterka, D. S., H. Takahashi, and R. Yuste. 2011. Imaging Voltage in Neurons. *Neuron* 69: 9–21.
24. Tsytsarev, V., L.-D. Liao, K. V. Kong, Y.-H. Liu, R. S. Erzurumlu, M. Olivo, and N. V. Thakor. 2014. Recent progress in voltage-sensitive dye imaging for neuroscience. *J. Nanosci. Nanotechnol.* 14: 4733–44.
25. Gubernator, N. G., H. Zhang, R. G. W. Staal, E. V Mosharov, D. B. Pereira, M. Yue, V. Balsanek, P. A. Vadola, B. Mukherjee, R. H. Edwards, D. Sulzer, and D. Sames. 2009. Fluorescent false neurotransmitters visualize dopamine release from individual presynaptic terminals. *Science* 324: 1441–4.
26. Merchant, P., D. Sulzer, and D. Sames. 2015. Synaptic optical imaging platforms: Examining pharmacological modulation of neurotransmitter release at discrete synapses. *Neuropharmacology* 98: 90–4.
27. Lee, M., N. G. Gubernator, D. Sulzer, and D. Sames. 2010. Development of pH-Responsive Fluorescent False Neurotransmitters. *J. Am. Chem. Soc.* 132: 8828–8830.
28. Rodriguez, P. C., D. B. Pereira, A. Borgkvist, M. Y. Wong, C. Barnard, M. S. Sonders, H. Zhang, D. Sames, and D. Sulzer. 2013. Fluorescent dopamine tracer resolves individual dopaminergic synapses and their activity in the brain. *Proc. Natl. Acad. Sci. U. S. A.* 110: 870–5.
29. Pereira, D. B., Y. Schmitz, J. Mészáros, P. Merchant, G. Hu, S. Li, A. Henke, J. E. Lizardi-Ortiz, R. J. Karpowicz, T. J. Morgenstern, M. S. Sonders, E. Kanter, P. C. Rodriguez, E. V Mosharov, D. Sames, and D. Sulzer. 2016. Fluorescent false neurotransmitter reveals functionally silent dopamine vesicle clusters in the striatum. *Nat. Neurosci.* 19: 578–586.
30. Federici, M., E. C. Latagliata, A. Ledonne, F. R. Rizzo, M. Feligioni, D. Sulzer, M. Dunn, D. Sames, H. Gu, R. Nisticò, S. Puglisi-Allegra, and N. B. Mercuri. 2014. Paradoxical Abatement of Striatal Dopaminergic Transmission by Cocaine and Methylphenidate. *J. Biol. Chem.* 289: 264–274.
31. Er, J. C., C. Leong, C. L. Teoh, Q. Yuan, P. Merchant, M. Dunn, D. Sulzer, D. Sames, A. Bhinge, D. Kim, S.-M. Kim, M.-H. Yoon, L. W. Stanton, S. H. Je, S.-W. Yun, and Y.-T. Chang. 2015. NeuO: a Fluorescent Chemical Probe for Live Neuron Labeling. *Angew. Chemie Int. Ed.* 54: 2442–2446.
32. Yun, S. W., N. Y. Kang, S. J. Park, H. H. Ha, Y. K. Kim, J. S. Lee, and Y.-T. Chang. 2014. Diversity oriented fluorescence library approach (DOFLA) for live cell imaging probe development. *Acc. Chem. Res.* 47: 1277–1286.
33. Leong, C., S. C. Lee, J. Ock, X. Li, P. See, S. J. Park, F. Ginhoux, S.-W. Yun, and Y.-T. Chang. 2014. Microglia specific fluorescent probes for live cell imaging. *Chem. Commun.* 50: 1089–1091.
34. Yun, S.-W., C. Leong, X. Bi, H.-H. Ha, Y. H. Yu, Y. L. Tan, G. Narayanan, S. Sankaran, J.-Y. Kim, S. Hariharan, S. Ahmed, and Y.-T. Chang. 2014. A fluorescent probe for imaging symmetric and asymmetric cell division in neurosphere formation. *Chem. Commun. (Camb).* 50: 7492–4.
35. Teesalu, T., K. N. Sugahara, and E. Ruoslahti. 2012. Mapping of vascular ZIP codes by phage display. *Methods Enzymol.* 503: 35–56.
36. Gray, B. P., and K. C. Brown. 2014. Combinatorial peptide libraries: Mining for cell-binding peptides. *Chem. Rev.* 114: 1020–1081.
37. Federici, T., J. K. Liu, Q. Teng, M. Garrity-Moses, J. Yang, and N. M. Boulis. 2006. Neuronal affinity of a C7C loop peptide identified through phage display. *J. Drug Target.* 14: 263–71.
38. Liu, J. K., Q. Teng, M. Garrity-Moses, T. Federici, D. Tanase, M. J. Imperiale, and N. M. Boulis. 2005. A novel peptide defined through phage display for therapeutic protein and vector neuronal targeting. *Neurobiol. Dis.* 19: 407–18.
39. Georgieva, J. V., R. P. Brinkhuis, K. Stojanov, C. A. G. M. Weijers, H. Zuilhof, F. P. J. T. Rutjes, D. Hoekstra, J. C. M. Van Hest, and I. S. Zuhorn. 2012. Peptide-mediated blood-brain barrier transport of polymersomes. *Angew. Chemie - Int. Ed.* 51: 8339–8342.
40. Georgieva, J., D. Hoekstra, and I. Zuhorn. 2014. Smuggling Drugs into the Brain: An Overview of Ligands Targeting Transcytosis for Drug Delivery across the Blood–Brain Barrier. *Pharmaceutics* 6: 557–583.
41. Wan, X. M., Y. P. Chen, W. R. Xu, W. Jun Yang, and L. P. Wen. 2009. Identification of nose-to-brain homing peptide through phage display. *Peptides* 30: 343–350.

42. Staquicini, F. I., E. Dias-Neto, J. Li, E. Y. Snyder, R. L. Sidman, R. Pasqualini, and W. Arap. 2009. Discovery of a functional protein complex of netrin-4, laminin gamma1 chain, and integrin alpha6beta1 in mouse neural stem cells. *Proc. Natl. Acad. Sci. U. S. A.* 106: 2903–8.
43. Hou, S. T., M. Dove, E. Anderson, J. Zhang, and C. R. MacKenzie. 2004. Identification of polypeptides with selective affinity to intact mouse cerebellar granule neurons from a random peptide-presenting phage library. *J. Neurosci. Methods* 138: 39–44.
44. Schmidt, A., S. J.-P. Haas, S. Hildebrandt, J. Scheibe, B. Eckhoff, T. Racek, G. Kempermann, A. Wree, and B. M. Pützer. 2007. Selective targeting of adenoviral vectors to neural precursor cells in the hippocampus of adult mice: new prospects for in situ gene therapy. *Stem Cells* 25: 2910–8.
45. Whitney, M. a, J. L. Crisp, L. T. Nguyen, B. Friedman, L. a Gross, P. Steinbach, R. Y. Tsien, and Q. T. Nguyen. 2011. Fluorescent peptides highlight peripheral nerves during surgery in mice. *Nat. Biotechnol.* 29: 352–6.
46. Fornasiero, E. F., D. Bonanomi, F. Benfenati, and F. Valtorta. 2010. The role of synapsins in neuronal development. *Cell. Mol. Life Sci.* 67: 1383–1396.
47. Leal-Ortiz, S., C. L. Waites, R. Terry-Lorenzo, P. Zamorano, E. D. Gundelfinger, and C. C. Garner. 2008. Piccolo modulation of Synapsin1a dynamics regulates synaptic vesicle exocytosis. *J. Cell Biol.* 181: 831–46.
48. Sheehan, P., M. Zhu, A. Beskow, C. Vollmer, and C. L. Waites. 2016. Activity-Dependent Degradation of Synaptic Vesicle Proteins Requires Rab35 and the ESCRT Pathway. *J. Neurosci.* 36: 8668–86.
49. Tanaka, M., J. Miyoshi, H. Ishizaki, A. Togawa, K. Ohnishi, K. Endo, K. Matsubara, A. Mizoguchi, T. Nagano, M. Sato, T. Sasaki, and Y. Takai. 2001. Role of Rab3 GDP/GTP exchange protein in synaptic vesicle trafficking at the mouse neuromuscular junction. *Mol. Biol. Cell* 12: 1421–30.
50. Bragina, L., G. Fattorini, S. Giovedí, M. Melone, F. Bosco, F. Benfenati, and F. Conti. 2011. Analysis of Synaptotagmin, SV2, and Rab3 Expression in Cortical Glutamatergic and GABAergic Axon Terminals. *Front. Cell. Neurosci.* 5: 32.
51. Beaudoin, G. M. J., S.-H. Lee, D. Singh, Y. Yuan, Y.-G. Ng, L. F. Reichardt, and J. Arikath. 2012. Culturing pyramidal neurons from the early postnatal mouse hippocampus and cortex. *Nat. Protoc.* 7: 1741–1754.
52. Er, J. C., M. K. Tang, C. G. Chia, H. Liew, M. Vendrell, and Y.-T. Chang. 2013. MegaStokes BODIPY-triazoles as environmentally sensitive turn-on fluorescent dyes. *Chem. Sci.* 4: 2168.
53. Wang, S., and Y. Chang. 2006. Combinatorial Synthesis of Benzimidazolium Dyes and Its Diversity Directed Application toward GTP-Selective Fluorescent Chemosensors. 10380–10381.
54. Wang, S., K. K. Yun, and Y.-T. Chang. 2008. Diversity-oriented fluorescence library approach (DOFLA) to the discovery of chymotrypsin sensor. *J. Comb. Chem.* 10: 460–465.
55. Lee, S.-C., N.-Y. Kang, S.-J. Park, S.-W. Yun, Y. Chandran, and Y.-T. Chang. 2012. Development of a fluorescent chalcone library and its application in the discovery of a mouse embryonic stem cell probe. *Chem. Commun.* 48: 6681.
56. Im, C. N., N. Y. Kang, H. H. Ha, X. Bi, J. J. Lee, S. J. Park, S. Y. Lee, M. Vendrell, Y. K. Kim, J. S. Lee, J. Li, Y. H. Ahn, B. Feng, H. H. Ng, S. W. Yun, and Y.-T. Chang. 2010. A fluorescent rosamine compound selectively stains pluripotent stem cells. *Angew. Chemie - Int. Ed.* 49: 7497–7500.
57. Ghosh, K. K., H.-H. Ha, N.-Y. Kang, Y. Chandran, and Y.-T. Chang. 2011. Solid phase combinatorial synthesis of a xanthone library using click chemistry and its application to an embryonic stem cell probe. *Chem. Commun.* 47: 7488.
58. Jung, D.-W., J. Kim, Z. M. Che, E.-S. Oh, G. Kim, S. H. Eom, S.-H. Im, H.-H. Ha, Y.-T. Chang, D. R. Williams, and J. Kim. 2011. A Triazine Compound S06 Inhibits Proinvasive Crosstalk between Carcinoma Cells and Stromal Fibroblasts via Binding to Heat Shock Protein 90. *Chem. Biol.* 18: 1581–1590.
59. Dunn, M., U. Boltaev, A. Beskow, S. Pampou, R. Realubit, T. Meira, J. V. Silva, R. Reeb, C. Karan, S. Jockusch, D. Sulzer, Y. T. Chang, D. Sames, and C. L. Waites. 2018. Identification of Fluorescent Small Molecule Compounds for Synaptic Labeling by Image-Based, High-Content Screening. *ACS Chem. Neurosci.* 9: 673–683.
60. Bolte, S., and F. P. Cordelières. 2006. A guided tour into subcellular colocalization analysis in light microscopy. *J. Microsc.* 224: 213–232.
61. Yoshimori, T., A. Yamamoto, Y. Moriyama, M. Futai, and Y. Tashiro. 1991. Bafilomycin A1, a specific inhibitor of vacuolar-type H(+)-ATPase, inhibits acidification and protein degradation in lysosomes of cultured cells. *J. Biol. Chem.* 266: 17707–12.
62. Waters, J., and S. J. Smith. 2002. Vesicle pool partitioning influences presynaptic diversity and weighting in rat hippocampal synapses. *J. Physiol.* 541: 811–23.
63. Weise, C. M., P. R. Mouton, J. Eschbacher, S. W. Coons, and J. Krakoff. 2015. A post-mortem stereological study of striatal cell number in human obesity. *Obesity* 23: 100–104.

2.7 Appendix: HCS plates

Parameters plots of 29 plates are present: as follows:

- A. Puncta overlap versus coverage plot
- B. Cell body overlap versus coverage plot
- C. Relative intensity in puncta vs cell body plot
- D. Number of puncta vs number of cell body un compound channel
- E. Puncta relative intensity vs puncta number in compound channel
- F. Cell body relative intensity vs cell body number in compound channel
- G. Puncta overlap vs cell body overlap
- H. Puncta vs cell body coverage
- I. Legend of the plots
- J. Quality control map
- K. 4 selected images from the plate. Scale bar is 20 μm

